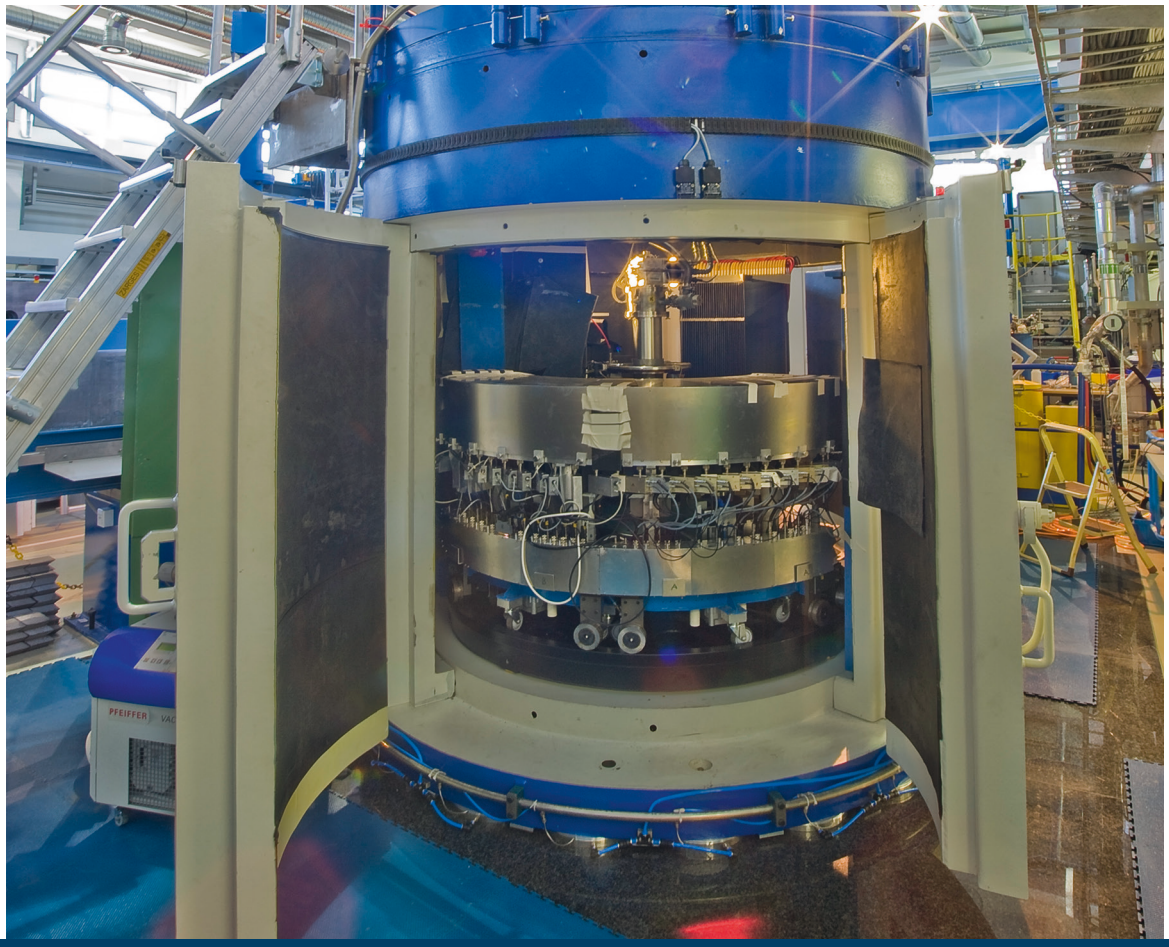

Laboratory Course

Neutron Scattering

Experimental Manuals

Thomas Brückel, Stephan Förster, Karen Friese, Margarita Kruteva,
Mirijam Zobel, and Reiner Zorn (Editors)

Schlüsseltechnologien / Key Technologies
Band / Volume 271
ISBN 978-3-95806-705-9

RWTH AACHEN UNIVERSITY

JÜLICH Forschungszentrum

Schriften des Forschungszentrums Jülich
Reihe Schlüsseltechnologien / Key Technologies Band / Volume 271

Forschungszentrum Jülich GmbH
Jülich Centre For Neutron Science (JCNS)

Thomas Brückel, Stephan Förster, Karen Friese,
Margarita Kruteva, Mirijam Zobel, and Reiner Zorn (Editors)

Neutron Scattering

Experimental Manuals of the JCNS Laboratory Course
held at Forschungszentrum Jülich and
at the Heinz-Maier-Leibnitz Zentrum Garching
In cooperation with RWTH Aachen

Schriften des Forschungszentrums Jülich
Reihe Schlüsseltechnologien / Key Technologies Band / Volume 271

ISSN 1866-1807 ISBN 978-3-95806-705-9

Bibliografische Information der Deutschen Nationalbibliothek.
Die Deutsche Nationalbibliothek verzeichnet diese Publikation in der
Deutschen Nationalbibliografie; detaillierte Bibliografische Daten
sind im Internet über http://dnb.d-nb.de abrufbar.

Herausgeber und Vertrieb:	Forschungszentrum Jülich GmbH Zentralbibliothek, Verlag 52425 Jülich Tel.: +49 2461 61-5368 Fax: +49 2461 61-6103 zb-publikation@fz-juelich.de www.fz-juelich.de/zb
Umschlaggestaltung:	Grafische Medien, Forschungszentrum Jülich GmbH
Druck:	Frank Druck + Medien GmbH & Co. KG
Copyright:	Forschungszentrum Jülich 2023

Schriften des Forschungszentrums Jülich
Reihe Schlüsseltechnologien / Key Technologies, Band / Volume 271

ISSN 1866-1807
ISBN 978-3-95806-705-9

Vollständig frei verfügbar über das Publikationsportal des Forschungszentrums Jülich (JuSER)
unter www.fz-juelich.de/zb/openaccess.

Contents

PUMA

Thermal Triple Axis Spectrometer

Oleg Sobolev, Anke Teichert, Norbert Jünke

Forschungsneutronenquelle Heinz Maier-Leibnitz (FRM II)
Technische Universität München

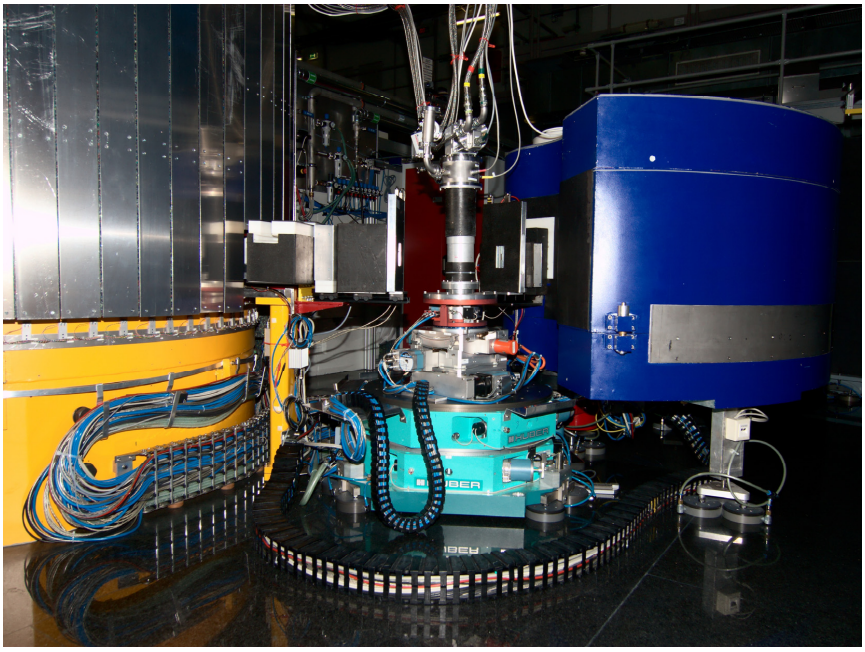

Manual of the JCNS Laboratory Course Neutron Scattering

Contents

1. Introduction

Excitations in crystals can be described using formalism of dispersion relations of the normal modes or quasi-particles (phonons, magnons, etc.). These relations contain the most detailed information on the intermolecular interactions in solids.

The result of a neutron scattering experiment is the distribution of neutrons that have undergone an energy exchange $\hbar\omega = E_i - E_f$, and a wave vector transfer, $\mathbf{Q} = \mathbf{k_i} - \mathbf{k_f}$, after scattering by the sample.:

$$\frac{d^2\sigma}{d\Omega d\omega}(2\theta,\omega) = N\frac{k_f}{k_i}\left\{\frac{\sigma_{coh}}{4\pi}S_{coh}(\mathbf{Q},\omega)+\frac{\sigma_{inc}}{4\pi}S_{inc}(\mathbf{Q},\omega)\right\} \quad (1)$$

σ_{coh} is coherent scattering cross section, σ_{inc} is incoherent scattering cross section. They are constants that can be found in tables (http://www.ncnr.nist.gov/resources/n-lengths/). $S(\mathbf{Q},\omega)$ functions depend only on the structure and dynamics of the sample and do not depend on the interaction between neutrons and the sample. $S_{inc}(\mathbf{Q},\omega)$ reflects individual motions of atoms. $S_{coh}(\mathbf{Q},\omega)$ provides the information on the structure and collective excitations in the sample.

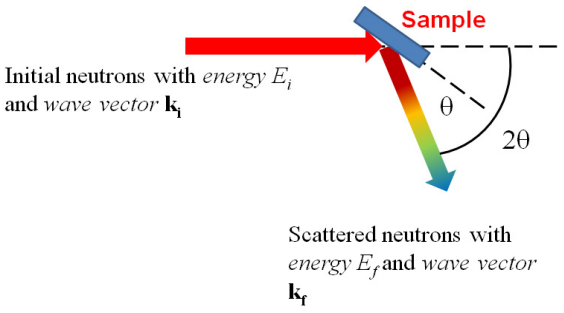

Energy transfer

$\hbar\omega = E_i - E_f$

Momentum transfer

$\mathbf{Q} = \mathbf{k_0} - \mathbf{k_f}$

$$k = \frac{\sqrt{2mE}}{\hbar} = \frac{2\pi}{\lambda}$$

$$Q = \sqrt{k_i^2 + k_f^2 - 2k_i k_f \cos 2\theta}$$

If $k_i = k_f$

$$Q = 2k_i \sin\theta = \frac{4\pi}{\lambda}\sin\theta$$

The triple axis spectrometer is designed for measuring the $S_{coh}(\mathbf{Q},\omega)$ in monocrystals. Therefore this function is of special interest for us.

2. Elastic scattering and Structure of Crystals

In the case of coherent *elastic scattering,* when $\omega = 0$ ($k_i = k_f$) only neutrons, that fulfill the Brags law are scattered by the sample:

$$n\lambda = 2d_{hkl}\sin\theta_{hkl}, \tag{2}$$

where λ is a wavelength of neutron, d_{hkl} is a distance between crystal planes described by corresponding Miller indexes *hkl*. θ_{hkl} denotes the angle between incoming (outgoing) scattering beam and the (hkl) plane.

For the analysis of the scattering processes in crystals it is convenient to use the concept of the *reciprocal space*. For an infinite three dimensional lattice, defined by its primitive vectors $\boldsymbol{a}_1$, $\boldsymbol{a}_2$ and $\boldsymbol{a}_3$, its reciprocal lattice can be determined by generating three reciprocal primitive vectors, through the formulae:

$$\begin{aligned}
\mathbf{g}_1 &= 2\pi \frac{\mathbf{a}_2 \times \mathbf{a}_3}{\mathbf{a}_1 \cdot \mathbf{a}_2 \times \mathbf{a}_3} \\
\mathbf{g}_2 &= 2\pi \frac{\mathbf{a}_1 \times \mathbf{a}_3}{\mathbf{a}_2 \cdot \mathbf{a}_1 \times \mathbf{a}_3} \\
\mathbf{g}_3 &= 2\pi \frac{\mathbf{a}_1 \times \mathbf{a}_2}{\mathbf{a}_3 \cdot \mathbf{a}_1 \times \mathbf{a}_2}
\end{aligned} \tag{3}$$

Note the denominator is the scalar triple product. Geometrically, the scalar triple product $\mathbf{a_1(a_2 \times a_3)}$ is the volume of the parallelepiped defined by the three vectors.

Let us imagine the lattice of points given by the vectors $\mathbf{g_1}$, $\mathbf{g_2}$ and $\mathbf{g_3}$ such that $\boldsymbol{\tau}$ is an arbitrary linear combination of these vectors:

$$\boldsymbol{\tau} = h\mathbf{g}_1 + k\mathbf{g}_2 + l\mathbf{g}_3 , \tag{4}$$

where *h,k,l* are integers. Every point of the reciprocal lattice, characterized by $\boldsymbol{\tau}$ corresponds in the position space to the equidistant set of planes with Miller indices (*h,k,l*) perpendicular to the vector $\boldsymbol{\tau}$. These planes are separated by the distance

$$d_{hkl} = \frac{2\pi}{|\boldsymbol{\tau}_{hkl}|} \tag{6}$$

The Brag's condition for diffraction can be expressed in the following vector form:

$$\mathbf{Q} = \boldsymbol{\tau}_{hkl} \tag{7}$$

A useful construction for work with wave vectors in reciprocal space is the Brillouin zone (BZ). The BZ is the smallest unit in reciprocal space over which physical quantities such as phonon or electron dispersions repeat themselves. It is constructed by drawing vectors from one reciprocal lattice points to another and then constructing lines perpendicular to these vectors at the midpoints. The smallest enclosed volume is the BZ.

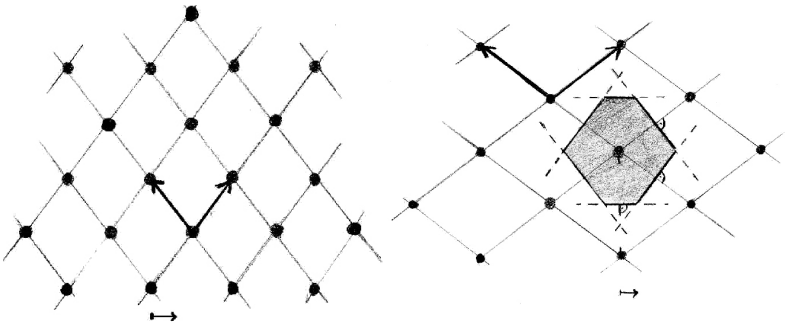

Fig.1 Real (left) and reciprocal (right) two dimensional lattices and BZ (gray area)

3. Inelastic Neutron Scattering and Phonons

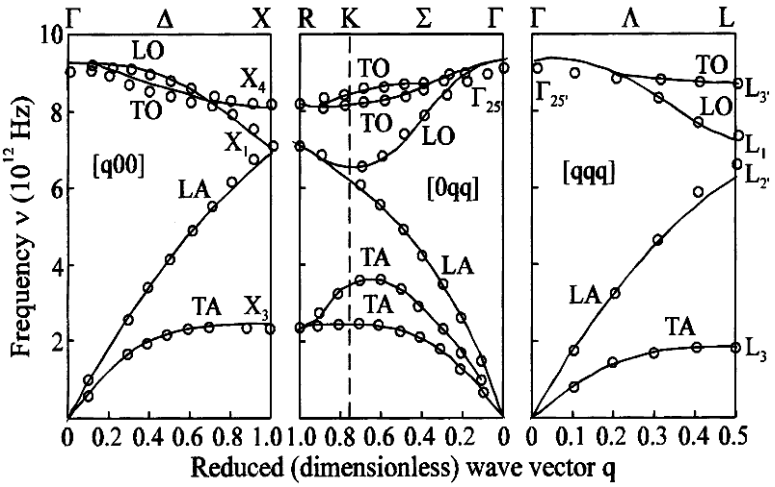

Fig.2 Phonon dispersion curves for Ge.

Atomic vibrations in a crystal can be analyzed in terms of lattice waves which are the normal modes of the crystal. The frequencies of normal modes ω are related to their wave vectors $\mathbf{q}$ ($q = 2\pi/\lambda$) by the dispersion relations

$$\omega = \omega_j(\mathbf{q}), \tag{7}$$

where the index j denotes a particular branch. For a crystal with N atoms per primitive unit cell there are $3N$ branches of the frequency spectrum. Three branches are acoustic ones for which $\omega \to 0$ as $\mathbf{q} \to 0$; the other $3N$-3 are branches are optical branches for which ω tends to a finite value as $\mathbf{q} \to 0$. In certain directions of high symmetry the normal vibrations are strictly transverse or longitudinal. The energy quantum $\hbar\omega$ is called *phonon* in analogy to the phonon for electromagnetic waves.

If we want to measure the frequency of a phonon ω for a certain **q**, the basic scattering conditions must fulfil the energy and momentum conservation laws:

$$E_i - E_f = \frac{\hbar}{2m_n}(k_i^2 - k_f^2) = \pm\hbar\omega(\mathbf{q}) \qquad (9)$$

$$\mathbf{Q} = \mathbf{k_i} - \mathbf{k_f} = \mathbf{G} \pm \mathbf{q}$$

When the above conditions are fulfilled, the function $S_{coh}(\mathbf{Q},\omega)$ shows a peak. We can held **Q** constant and vary $\mathbf{k_i}$ ($\mathbf{k_f}$) to measure intensity of scattered neutrons at different energy transfers. In order to keep **Q**, and thus **q**, constant while varying $\mathbf{k_i}$, the scattering angle must change as well as the relative orientation of the crystal with respect to $\mathbf{k_f}$.

The intensity of neutrons scattered by phonon is proportional to the square of the dynamical structure factor $F(\mathbf{Q})$:

$$S_{coh}(\mathbf{Q},\omega) \sim |F(\mathbf{Q})|^2 = \left| \sum_\kappa b_\kappa \frac{\mathbf{Q}\cdot\mathbf{e}_\kappa(\mathbf{q}_j)}{\sqrt{m_\kappa}} \exp(-W_k)\exp(-i\mathbf{q}\mathbf{r}_\kappa) \right|^2, \qquad (10)$$

Where sum is taken over all atoms in unit cell with coordinates $\mathbf{r}_k$, exp(-W) is a Debye-Waller factor, $\mathbf{e}_k$ denotes the polarization vector of the phonon. The scalar product $\mathbf{Q}\cdot\mathbf{e}_\kappa(\mathbf{q}_j)$ means that only lattice vibrations polarized along the momentum transfer are visible. This makes possible to distinguish transverse (TA) and longitudinal (LA) acoustic modes. For TA modes $\mathbf{e}\perp\mathbf{q}$, and therefore **Q** must be perpendicular to **q**, while for a LA mode, one must take $\mathbf{Q} \,||\, \mathbf{q}$ (Fig. 3)

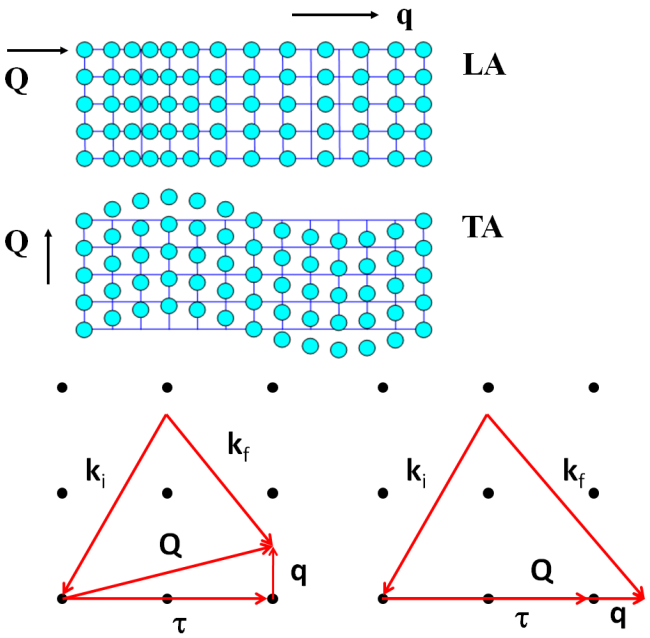

Fig. 3 Top: LA and TA phonons. Bottom: Neutron scattering diagram in the reciprocal space for TA (left) and LA phonons

4. Triple Axis Spectrometer PUMA

The three-axis instrument is the most versatile instrument for use in inelastic scattering because it allows one to probe nearly any coordinates in energy and momentum space in a precisely controlled manner. The three axes correspond to the axes of rotation of the *monochromator* (axis1), *the sample* (axis2), and *the analyzer* (axis3). The monochromator crystal selects neutrons with a certain energy from the white neutron beam emanating from the reactor. The monochromatic beam is then scattered off from the sample (second axis). The neutrons scattered by the sample can have a different energy from those incident on the sample. The energy of these scattered neutrons is then determined by the analyzer crystal (third axis). All three angles (θ_M, θ_S, θ_A) can vary during an experiment, the sample table and analyzer are equipped with air pads, so that they can glide over the "Tanzboden" (dancing floor). Below, we describe in detail each component of a triple-axis spectrometer.

Monochromator

A crystal monochromator is used to select neutrons with a specific wavelength. Neutrons with this wavelength interact with the sample and are scattered off at a similar (elastic) or different wavelength (inelastic). The energy of the neutrons both incident on and scattered from the sample is determined by Bragg reflection from the monochromator and analyzer crystals, respectively. For a specific Bragg plane (hkl) characterized by an interplanar spacing d_{hkl}, the crystal is rotated about a vertical axis. A pyrolytic graphite with d_{002} = 3.35 Å (PG(002)) and a copper with d_{220} = 1.28 Å (Cu(220)) monochromators are available at PUMA. The angular range of the monochromator $2\theta_M$ is of 15° - 115°. The PG(002) is usually used for energies below 50meV (λ>1.3Å). For higher incident energies the Cu(220) can be used.

Sample table

The sample table from the company Huber provides a possibility to vary independently both $2\theta_S$ and θ_S. It is equipped with a goniometer moving the sample in the three translation axes *x*, *y* and *z* and tilting. The tilt angle is ±15°. Single crystal experiments can be performed with an Euler cradle at PUMA. The sample environment includes magnets, pressure cells, cryostats and high temperature furnace.

Analyzer

Like the monochromator, the PG(002) analyzer consist of 20x5 separate analyzer crystal plates are mounted in an aluminum frame. There is an option to measure with the flat or horisontaly and verticaly focused analyser. The angular range of the analysator $2\theta_M$ is of -130° - 130°.

Detector and monitor

The detector consists of five counter tubes which are filled with a ^{3}He pressure of 5 bar. To be able to monitor the neutron flux incident on the sample, a low-efficiency neutron counter monitor is usually placed before the sample. Such a monitor is required so that flux variation caused by, for example, the reactor power fluctuations and the change in reflectivity of the monochromator with neutron wavelength can be automatically corrected for.

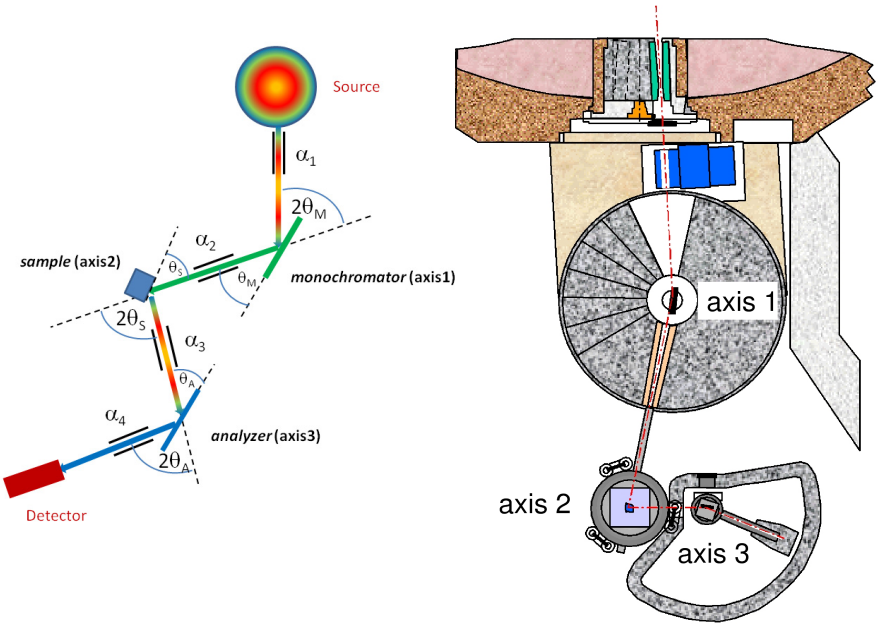

Fig.4 PUMA spectrometer.

Slits, Collimators, Filter

Additional components like slits or collimators are used to define the beam cross section. Collimators (α1- α4) are used for the improvement of the resolution and to specify the beam divergence. They consist of multiple parallel arranged Gd_2O_3 coated foils with a defined angle to the beam. The angular divergence of the collimator in the horizontal plane α is defined by the distance between foils Δd and the length of the collimator l ($\tan \alpha = \Delta d / l$). Different collimators with a horizontal divergence between 10' and 60' are available at the instrument.

One of the problems of the TAS method is the possible presence of higher harmonics in the neutron beam. Higher harmonics arise from higher order (hkl) in Bragg's law (2). This means that if the monochromator (analyzer) crystal is set to reflect neutrons with a wavelength of λ from a given (hkl) plane, it will also reflect neutrons with wavelength λ/n. This leads to the appearance of several types of spurious peaks in the observed signal. Different filters are used to eliminate the high-order neutrons and to reduce the background. There are a sapphire filter (Al_2O_3) and an erbium filter (Er) at PUMA. They are installed in front of the monochromator. Sapphire filter is used wavelengths $\lambda > 1$ Å and reduce the background inducing by the epithermal neutrons. Erbium filter is suitable as $\lambda/2$ filter for λ between 0.5 and 1Å as well as $\lambda/3$ filter for λ between 0.7 and 1.6Å.

Components	Axis	PUMAs notation	Description
Monochromator M	θ_M	mth	Monochromator Theta
	$2\theta_M$	mtt	Monochromator 2Theta
		mtx, mty	Monochromator Translation x-, y- direction
		mgx, mgy	Monochromator Goniometer x-, y- direction
		mfh, mfv	Monochromator Focus horizontal, vertical
Sample S	θ_S	psi	Sample Theta
	$2\theta_S$	phi	Sample 2Theta
		stx, sty, stz	Sample Translation x-, y-, z- direction
		sgx, sgy	Sample Goniometer x-, y- direction
Analyzer A	θ_A	ath	Analyzer Theta
	$2\theta_A$	att	Analyzer 2Theta
		atx, aty	Analyzer Translation x-, y- direction
		agx, agy	Analyzer Goniometer x-, y- direction
		afh	Analyzer Focus horizontal
Collimators		alpha1 – alpha4	Collimation

5. Experiment Procedure

The aim of the experiment is to measure acoustic phonons in a germanium sample. The phonons will be measured for [110] (LA) and [001] (TA) directions in [220] BZ.
The experimental procedure shall contain the following steps:

Sample alignment

It is very difficult to align a sample with triple axis spectrometer, if the sample orientation is absolutely unknown. A sample must be pre-aligned, this means that the vertical axis of the sample must be known and roughly perpendicular to the 'Tanzboden'. Than we shall do the following steps:
- Inform the control program of the spectrometer about a scattering plane of the sample. One must set two reciprocal vectors (in our case [110] and [001]) laying in the scattering plane.
- Drive spectrometer (θ_M, $2\theta_M$, θ_S, $2\theta_S$, θ_A, $2\theta_A$,) to the position corresponding to [220] reflection.
- Scan θ_S and find the Brag's peak.
- Scan corresponding goniometer axes to maximize intensity of the peak.
- Do the same for other reflection [004].
- Change the offset of the θ_S so that the nominal θ_S values correspond to intensity maxima for the above reflections.

Phonons measurements

For our measurements we will chose the const-k_f configuration with $k_f = 2.662$ Å^{-1} ($E_f = 14.68$ meV). This means that we will scan the energy transfer $\hbar\omega = E_i - E_f$ by varying incident energy E_i (k_i). We are going to use PG(002) monochromator.

For LA phonon we will do constant-**Q** scans in the energy transfer range $\hbar\omega$ = 0 – 21 meV (0 – 8 THz) for the following points:
Q(r.l.u.) = (2.1, 2.1, 0), (2.2, 2.2, 0), (2.3, 2.3, 0), (2.4, 2.4, 0), (2.5, 2.5, 0), (2.6, 2.6, 0), (2.7, 2.7, 0), (2.75, 2.75, 0).

For TA phonon we will do constant-**Q** scans in the energy transfer range $\hbar\omega$ = 0 – 15 meV (0 – 3.6 THz) for the following points:
Q(r.l.u.) = (2, 2, 0.2), (2, 2, 0.3), (2, 2, 0.4), (2, 2, 0.5), (2, 2, 0.7), (2, 2, 0.8), (2, 2, 0.9), (2, 2, 1).

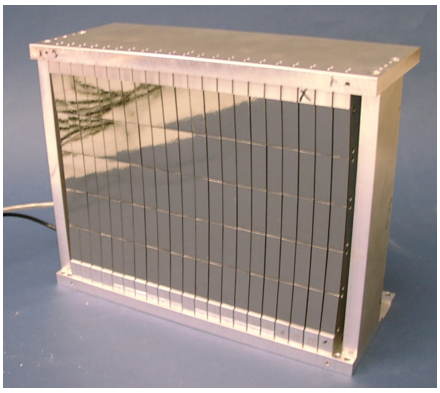

a) PG Analyzer

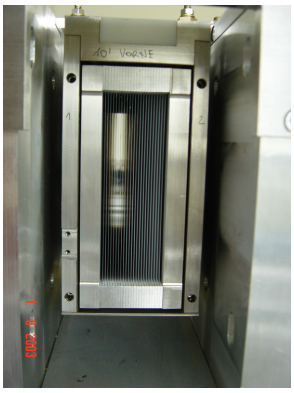

b) Soller collimator

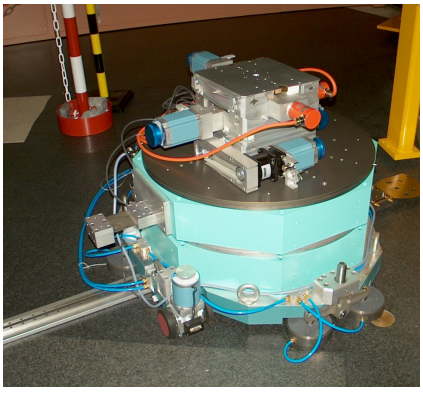

c) Sample table

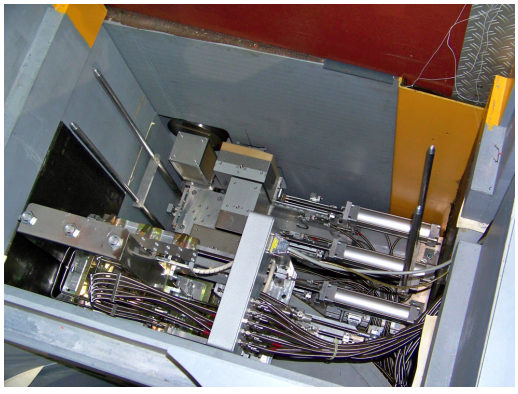

d) Shutter, filters and collimators

e) Analyzer and Detector

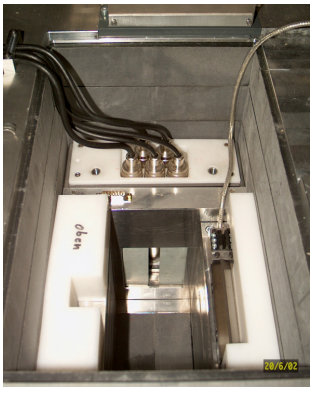

f) Detector, consists of 5 ^{3}He tubes

Fig 5 Elements of PUMA

6. Preparatory Exercises

1. Calculate angles θ_M, $2\theta_M$, θ_S, $2\theta_S$ for the reflections [220] and [004] of *germanium* (cubic-diamond, a = 5.66 Å), supposing that $k_f = 2.662$ Å^{-1} = const, monochromator is PG(002), and check, if this reflections are measurable with our experimental setup.

2. Before doing a scan it is important to check that all point in **Q** - $\hbar\omega$ space are available, instrument angles do not exceed high or low limits. Also, an experimental scientist must be sure that the moving instrument will not hit walls or any equipment. Calculate instrument parameters (θ_M, $2\theta_M$, θ_S, $2\theta_S$) for the momentum transfers **Q** (r.l.u.) = (2.1, 2.1, 0), (2.75, 2.75, 0) and energy transfers $\hbar\omega$ = 0 and 21 meV. This can be done using an online triple-axis simulator:
http://www.ill.eu/instruments-support/computing-for-science/cs-software/all-software/vtas/

7. Experiment-Related Exercises

1. Plot obtained spectra for each **Q** as a function of energy (THz). Fit the spectra with Gaussian function and find centers of the phopon peaks. The obtained phonon energies plot as a function of **q.**
2. Why triple-axis spectrometer is the best instrument to study excitations in single crystals?
3. During this practicum we do not consider some problems that are very important for planning experiments with a triple axis instrument such as *resolution* and *intensity zones* [2]. Persons who have a strong interest to the triple-axis spectroscopy should study these topics by oneself. Advanced students should be able to explain our choice of Brillouin zone and parameters of scans for the phonon measurements.

Useful formula and conversions

1 THz = 4.1.4 meV

$n\lambda = 2d_{hkl}\sin\theta_{hkl}$,

$$d_{hkl} = \frac{2\pi}{|\boldsymbol{\tau}_{hkl}|}$$

$$\mathbf{Q} = \mathbf{k_0} - \mathbf{k_f}$$

$$Q = \sqrt{k_i^2 + k_f^2 - 2k_i k_f \cos 2\theta}$$

If $k_i = k_f$ (elastic scattering) $Q = 2k_i \sin\theta = \frac{4\pi}{\lambda}\sin\theta$

E [meV] = 2.072 k^2 [Å^{-1}]

References

[1] Ch. Kittel, Einführung in die Festkörperphysik, Oldenburg, 14th ed., 2006
[2] G. Shirane, S.M. Shapiro, J.M. Tranquada, Neutron Scattering with a Triple-Axis Spektrometer, Cambridge University Press, 2002
[4] G. Eckold, P. Link, J. Neuhaus, Physica B, 276-278 (2000) 122- 123
[5] B.N.Brockhouse and P.K. Iyengar, Physikal Review 111 (1958) 747-754
[6] *http://www.ill.eu/instruments-support/computing-for-science/cs-software/all-software/vtas/*

Contact

PUMA

Phone: 089/289-14914
Web: http://www.mlz-garching.de/puma

Avishek Maity

IPC, University of Göttingen
Outstation at PUMA@FRMII, MLZ

Phone: 089/289-54835
e-Mail: avishek.Maity@frm2.tum.de

Jitae Park

Forschungsneutronenquelle Heinz Maier-Leibnitz
ZWE FRM II

Phone: 089/289-13983
e-Mail: jitae.park@frm2.tum.de

HEiDi

Hot Single Crystal Diffractometer for Structure Analysis with Neutrons

Martin Meven

Institut für Kristallographie, RWTH Aachen
and
Jülich Centre for Neutron Science
Forschungszentrum Jülich

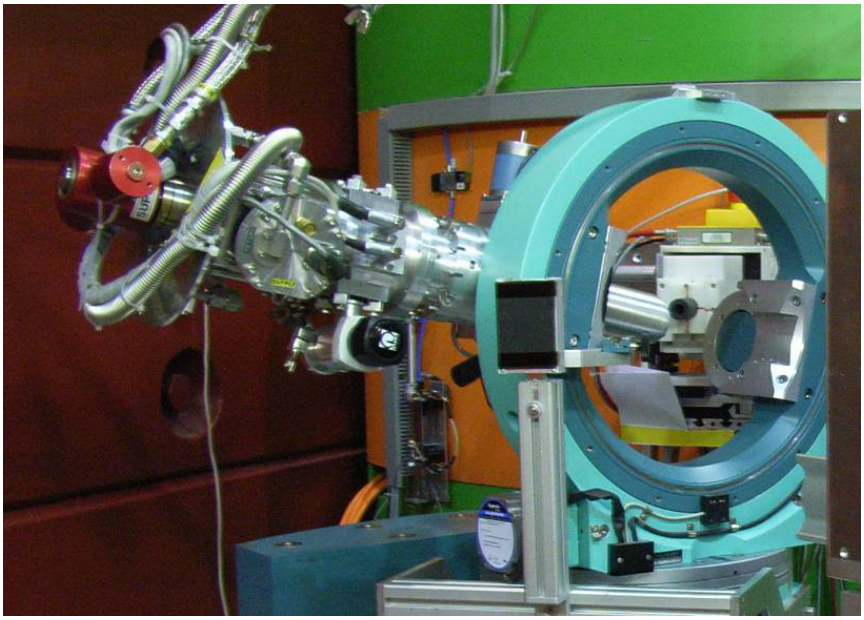

Contents

1 Introduction

Many properties of solid matter like their mechanical, thermal, optical, electrical and magnetic properties depend strongly on their atomic structure. Therefore, a good understanding of the physical properties needs not only the knowledge about the particles inside (atoms, ions, molecules) but also about their spatial arrangement. For most cases diffraction is *the* tool to answer questions about the atomic and/or magnetic structure of a system. Beyond this, neutron diffraction allows to answer questions where other techniques fail.

2 Crystallographic Basics

In the ideal case a complete solid matter consists of small identical units (same content, same size, same orientation like sugar pieces in a box). These units are called unit cells. A solid matter made of these cells is called a single crystal. The shape of a unit cell is equivalent to a parallelepiped that is defined by its base vectors $\mathbf{a_1}$, $\mathbf{a_2}$ und $\mathbf{a_3}$ and that can be described by its lattice constants a, b, c; α, β and γ (pic. 1). Typical lengths of the edges of such cells are between a few and a few ten Ångström (1Å=10^{-10} m). The combination of various restrictions of the lattice constants between $a \neq b \neq c$; $\alpha \neq \beta \neq \gamma \neq 90°$ (triclinic) and $a = b = c$; $\alpha = \beta = \gamma = 90°$ (cubic) yields seven crystal systems. The request to choose the system with the highest symmetry to describe the crystal structure yields fourteen Bravais lattices, seven primitive and seven centered lattices.

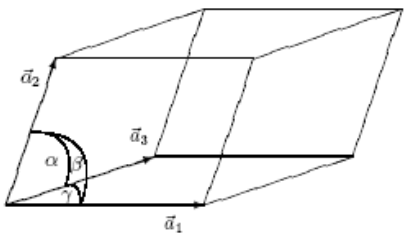

Fig. 1: Unit cell with $|\mathbf{a_1}|=a$, $|\mathbf{a_2}|=b$, $|\mathbf{a_3}|=c$, α, β, γ

Each unit cell contains one or more particles i. The referring atomic positions $\mathbf{x_i}=x_i*\mathbf{a_1} + y_i*\mathbf{a_2} + z_i*\mathbf{a_3}$ are described in relative coordinates $0 \leq x_i; y_i; z_i < 1$. The application of different symmetry operations (mirrors, rotations, glide mirrors, screw axes) on the atoms in one cell yield the 230 different space groups (see [1]).

The description of a crystal using identical unit cells allows the representation as a threedimensional lattice network. Each lattice point can be described as the lattice vector $\mathbf{t} = u*\mathbf{a_1} + v*\mathbf{a_2} + w*\mathbf{a_3}$; $u, v, w \in \mathbf{Z}$. From this picture we get the central word for diffraction in crystals; the *lattice plane* or *diffraction plane*. The orientations of these planes in the crystal are described by the so called *Miller indices* h, k and l with $h, k, l \in \mathbf{Z}$ (see pic. 2). The reciprocal base vectors $\mathbf{a^*_1}$, $\mathbf{a^*_2}$, $\mathbf{a^*_3}$ create the reciprocal space with: $\mathbf{a^*_i} * \mathbf{a_j} = \delta_{ij}$ with $\delta_{ij}=1$ for $i=j$ and $\delta_{ij}=0$ for $i \neq j$. Each point $\mathbf{Q}=h*\mathbf{a^*_1} + k*\mathbf{a^*_2} + l*\mathbf{a^*_3}$ represents the normal vector of

a (*hkl*) Plane. Each plane cuts the crystal lattice along its base vectors $\mathbf{a_1}$, $\mathbf{a_2}$ and $\mathbf{a_3}$ at $1/h^*\mathbf{a_1}$, $1/k^*\mathbf{a_2}$ and $1/l^*\mathbf{a_3}$. A Miller index of zero means that the referring axis will be cut in infinity. Thus, the lattice plane is parallel to this axis.

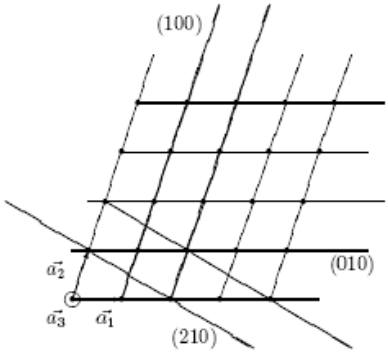

Fig. 2: Different lattice planes in a crystal lattice, $\mathbf{a_3}$ = viewing direction

The atoms in a unit cell are not rigidly fixed at their positions. They oscillate around their positions (e.g. thermal excitation). A simple description for this is the model of coupled springs. In this model atoms are connected via springs whose forces describe the binding forces between the atoms (e.g. van der Waals, Coulomb, valence). The back driving forces of the springs are proportional to the deviation x_i of the atoms from their mean positions and to the force constant D, thus. $F = -D^*\Delta x$ (harmonic approximation).
Therefore, the atoms oscillate with $x_i = A_i^*\sin(\nu^*t)$ around their mean positions with the frequency ν and the amplitude A_i. Both, ν and A_i are influenced by the force constant D_j of the springs and the atomic masses m_i of the neighbouring atoms. The resulting lattice oscillations are called phonons in reference to the photons (light particles) in optics, which as well transport energy in dependence of their frequency. A more complex and detailed description of phonons in dependence on the lattice structure and the atomic reciprocal effects is given in lattice dynamics. In the harmonic approximation the displacements of an atom can be described with an oszillation ellipsoid. This ellipsoid describes the preferred spacial volume in which the atom is placed. Its so called mean square displacements (MSD) U^i_{jk} represent the different sizes of the ellipsoid along the different main directions *j, k* in the crystal. The simplest case is a sphere with the isotrope MSD B_i. In the next paragraph MSD are discussed from the point of view of diffraction analysis.
A full description of a single crystal contains information about lattice class, lattice constants and unit cell, space group and all atomic positions and their MSD. If the occupancy of one or more positions is not exactly 100%, e.g. for a mixed crystal or a crystal with deficiencies there has to be used also an occupancy factor.

3 Structure Determination with Diffraction

3.1 Introduction

Diffraction means coherent elastic scattering of a wave on a crystal. Because of the quantum mechanical wave/particle dualism x-rays as well as neutron beams offer the requested wave properties:

Electrons: $E = h\nu$; $\lambda = c/\nu$
Neutrons: $E_{kin} = 1/2 * m_n * v^2 = h\nu = p^2/2m_n$; $\lambda = h/p$; $p \sim \sqrt{(m_n k_B T)}$

h: Planck's constant; ν: oscillation frequency; λ: wavelength; c: light speed; p: impact; m_n: neutron mass; k_B: Boltzmann constant; T: temperature

Only the cross section partners are different (x-rays: scattering on the electron shell of the atoms, neutrons: core (and magnetic) scattering) as explained in detail below. In scattering experiments informations about structural properties are hidden in the scattering intensities I.
In the following pages we will discuss only elastic scattering ($\lambda_{in}=\lambda_{out}$). The cross section of the radiation with the crystal lattice can be described as following:
Parallel waves of the incoming radiation with constant λ are diffracted by lattice planes which are ordered parallel with a constant distance of d. This is very similar to a light beam reflected by a mirror. The angle of the diffracted beam is equal to the angle of the incoming beam, thus the total angle between incoming and outgoing beam is 2Θ (see fig. 3).

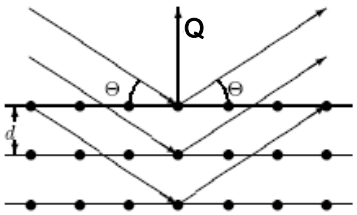

Fig. 3: Scattering on lattice planes

The overlap of all beams diffracted by a single lattice plane results in constructive interference only if the combination of the angle Θ, lattice plane distance d and wavelength λ meet Braggs law:

$$\mathbf{2}d\ \mathbf{sin}\Theta = \lambda$$

The largest distance $d_{hkl} = |\mathbf{Q}|$ of neighboured parallel lattice planes in a crystal is never larger than the largest lattice constant $d_{hkl} \leq \max(a; b; c)$. Therefore, it can only be a few Å or less. For a cubic unit cell ($a = b = c$; $\alpha = \beta = \gamma = 90°$) this means:
$d_{hkl} = a/\sqrt{(h^2+k^2+l^2)}$

With increasing scattering angle also the indices (hkl) increase while the lattice plane distances shrink with a lower limit of $d_{min} = \lambda/2$. Therefore, scattering experiments need

wavelengths λ in the same order of magnitude of the lattice constants or below. This is equal to x-ray energies of about 10 keV or neutron energies about 25 meV (thermal neutrons).

Ewald Construction: In reciprocal space each Bragg reflex is represented by a point $\mathbf{Q} = h\mathbf{a}^*_1 + k\mathbf{a}^*_2 + l\mathbf{a}^*_3$. A scattered beam with the wave vector $\mathbf{k}$ fulfills Braggs law if the relationship $\mathbf{k} = \mathbf{k_0} + \mathbf{Q}$, $|\mathbf{k}|=|\mathbf{k_0}|=1/\lambda$ is true, as shown in fig. 4. During an experiment the available reciprocal space can be described by an Ewald sphere with a diameter of $2/\lambda$ and the (000)-point as cross point of $\mathbf{k_0}$ direction and the centre of the diameter of the sphere. The rotation of the crystal lattice during the diffraction experiment is equal to a synchronous movement of the reciprocal lattice around the (000)-point. If Braggs law is fulfilled, one point (h k l) of the reciprocal lattices lies exactly on the Ewald sphere. The angle between the $\mathbf{k}$-vektor and the $\mathbf{k_0}$-vektor is 2Θ. The limited radius of $1/\lambda$ of the Ewald sphere limits also the visibility of (h k l) reflections to $|\mathbf{Q}| < 2/\lambda$.

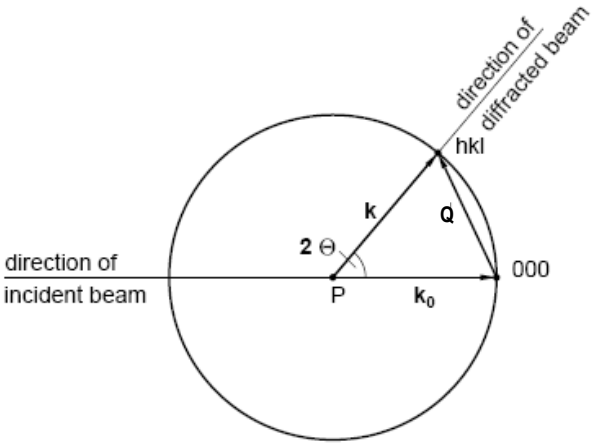

Fig. 4: Ewald construction

Determination of the Unit Cell: Following Braggs law the scattering angle 2Θ varies (for λ=const.) according to the lattice distance d_{hkl}. Thus for a given λ and known scattering angles 2Θ one can calculate the different d values of the different layers in the lattice of a crystal. With this knowledge is is possible to determine the lattice system and the lattice constants of the unit cell (although not always unambigously!).

Atomic Positions in the Unit Cell: The outer shape of a unit cell does not tell anything about the atomic positions $\mathbf{x_i}=(x_i\ y_i\ z_i)$ of each atom in this cell. To determine the atomic positions one has to measure also the quantities of the different reflection intensities of a crystal. This works because of the relationship between the intensities of Bragg reflections and the specific cross section of the selected radiation with each element in a unit cell. Generally one can use the following formula for the intensity of a Bragg reflection (h k l) with $\mathbf{Q}$ (kinetic scattering theory):

$$I_{hkl} \sim |F_{hkl}|^2 \text{ with } F_{hkl} = \sum^{n}_{i=1} s_i(\mathbf{Q}) \exp(2\pi\imath(hx_i+ky_i+lz_i))$$

The scattering factor F is a complex function describing the overlap of the scattering waves of each atom i (n per unit cell). $s_i(\mathbf{Q})$ describes the scattering strength of the i-th atom on its position $\mathbf{x}_i$ in dependence of the scattering vector $\mathbf{Q}$, which depends on the character of cross section as described below.
In this context one remark concerning statistics: For measurements of radiation the statistical error σ is the square root of the number of measured events, e.g. x-ray or neutron particles. Thus, 100 events yield an error of 10% while 10,000 events yield an error of only 1%!

Mean Square Displacements (MSD): Thermal movement of atoms around their average positions reduce the Bragg intensities during a diffraction experiment. The cause for this effect is the reduced probability density and therefore reduced cross section probability at the average positions. For higher temperatures (above a few Kelvin) the MSD B_i of the atoms increase linearly to the temperature T, this means $B \sim T$. Near a temperature of 0 K the MSD become constant with values larger than zero (zero point oscillation of the quantum mechanical harmonic oscillator).
Thus, the true scattering capability s_i of the i-th atom in a structure has to be corrected by an angle-dependent factor (the so called Debye-Waller factor):

$$s_i(\mathbf{Q}) \rightarrow s_i(\mathbf{Q}) * \exp(-B_i(\sin \Theta_\mathbf{Q}/\lambda)^2)$$

This Debye-Waller factor decreases with increasing temperatures and yields an attenuation of the Bragg reflection intensities. At the same time this factor becomes significantly smaller with larger $\sin\Theta/\lambda \sim |\mathbf{Q}|$. Therefore, especially reflections with large indices loose a lot of intensity. The formula for anisotropic oscillations around their average positions looks like this:

$$s_i(\mathbf{Q}) \rightarrow s_i(\mathbf{Q}) * \exp(-2\pi^2(U^i_{11} h^2a^{*2} + U^i_{22} k^2b^{*2} + U^i_{33} l^2c^{*2} + 2U^i_{13} hl\, a^*c^* + 2U^i_{12} hk\, a^*b^* + 2U^i_{23} kl\, b^*c^*))$$

The transformation between B and U_{eq} (from the U_{ij} calculated isotropic MSD for a sphere with identical volume) yields $B = 8\pi^2 U_{eq}$.
For some structures the experimentally determined MSD are significantly larger than from the harmonic calculations of the thermal movement of the atoms expected. Such deviations can have different reasons: Static local deformations like point defects, mixed compounds, anharmonic oscillations or double well potentials where two energetically equal atomic positions are very near to each other and therefore distribute the same atom over the crystal with a 50%/50% chance to one or the other position. In all those cases an additional contribution to the pure Debye-Waller factor can be found which yields an increased MSD. Therefore in the following text only the term MSD will be used to avoid misunderstandings.

3.2 Comparison of X-ray and Neutron Radiation

X-Ray Radiation interacts as electromagnetic radiation only with the electron density in a crystal. This means the shell electrons of the atoms as well as the chemical binding. The scattering capability s (atomic form factor $f(\sin\Theta/\lambda)$) of an atom depends on the number Z of its shell electrons ($f(\sin(\Theta=0)/\lambda) = Z$). To be exact, $f(\sin(\Theta)/\lambda)$ is the Fourier transform of the radial electron density distribution $n_e(r)$: $f(\sin(\Theta)/\lambda) = s \int_0^\infty 4\pi^2 n_e(r) \sin(\mu r)/\mu r \, dr$ with $\mu = 4\pi\sin(\Theta)/\lambda$. Heavy atoms with many electrons contribute much stronger to reflection

intensities ($I \sim Z^2$) than light atoms with less electrons. The reason for the $\sin\Theta/\lambda$-dependence of f is the diameter of the electron shell, which has the same order of magnitude as the wavelength λ. Because of this there is no pointlike scattering centre. Thus, for large scattering angles the atomic form factors vanish and also the reflection intensities relying on them. The atomic form factors are derived from theoretical spherical electron density functions (e. g. Hartree-Fock). The resulting $f(\sin\Theta/\lambda)$-curves of all elements (separated for free atoms and ions) are listed in the international tables. Their analytical approximation can be described by seven coefficients (c; a_i; b_i; $1 \leq i \leq 3$) , see [1].

Neutron Radiation radiation interacts with the cores and the magnetic moments of atoms. The analogon to the x-ray form factor (the scattering length b) is therefore not only dependent on the element but the isotope. At the same time b-values of elements neighboured in the periodic table can differ significantly. Nevertheless, the scattering lengths do not differ around several orders of magnitude like in the case of the atomic form factors f . Therefore, in a compound with light and heavy atoms the heavy atoms do not dominate necessarily the Bragg intensities. Furthermore the core potential with a diameter about 10^{-15}Å is a pointlike scattering centre and thus the scattering lengths b_n become independent of the Bragg angle and $\sin\Theta/\lambda$ respectively. This results in large intensities even at large scattering angles. The magnetic scattering lengths b_m can generate magnetic Bragg intensities comparable in their order of magnitude to the intensities of core scattering. On the other hand side the magnetic scattering lengths are strongly dependent on the $\sin\Theta/\lambda$ value due to the large spacial distribution of magnetic fields in a crystal. Therefore, it is easy to measure magnetic structures with neutrons and to separate them from the atomic structure.

Comparison: In summary in the same diffraction experiment the different character of x-ray and neutron radiation yield different pieces of information that can be combined. x-rays yield electron densities in a crystal while neutron scattering reveals the exact atomic positions. This fact is important because for polarised atoms the core position and the centre of gravity of electron densities are not identical any more. In compounds with light an heavy atoms structural changes driven by light elements need additional diffraction experiments with neutrons to reveal their influence and accurate atomic positions respectively. One has to take into account also that for x-rays intensitied depend twice on $\sin\Theta/\lambda$. Once bye the atomic form factor f, and twice by the temperature dependent Debye-Waller factor (see above). The first dependence vanishes if using neutron diffraction with b=const. and decouples the structure factors from the influence of the MSD. In general this yields much more accurate MSD U_{ij} especially for the light atoms and might be helpful to reveal double well potentials.

3.3 Special Effects

From the relation $I \sim |F|^2$ one can derive that the scattering intensities of a homogenous illuminated sample increases with its volume. But there are other effects than MSD that can attenuate intensities. These effects can be absorption, extinction, polarization and the Lorentz factor:

Absorption can be described by the Lambert-Beer law:

$I = I_0 \exp(-\mu x)$, μ/cm^{-1} = linear absorption coefficient, x/cm = mean path through sample

The linear absorption coefficient is an isotropic property of matter and depends on the wavelength and kind of radiation. For x-rays penetration depths are only a few millimetre or below (e.g. for silicon with $\mu_{MoK\alpha}$=1.546 mm^{-1}, $\mu_{CuK\alpha}$=14.84 mm^{-1} with penetration depths of 3 mm and 0.3 mm respectively). This limits transmission experiments to sample diameter of typically below 0.3 mm. To correct bias of intensities due to different scattering paths through the sample one has to measure accurately the sample size in all directions. Even for sphere liek samples the mean path lenghts depend on 2Θ! In addition the sample environment must have an extraordinary small absorption
Thermal neutrons have for most elements a penetration depth of several centimeters. Thus, sample diameters of several millimeters and large and complex sample environments (furnaces, magnets, etc.) can be used. On the other hand side one needs sufficiently large samples for neutron diffraction which is often a delicate problem.

Extinction reduces also radiation intensities. But the character is completely different form that of absorption. In principle extinction can be explained quite easily by taking into account that each diffracted beam can be seen as a new primary beam for the neighbouring lattice planes. Therefore, the diffracted beam becomes partially backscattered towards the direction of the very first primary beam (Switch from kinetic to dynamic scattering theory!). Especially for very strong reflections this effect can reduce intensities dramatically (up to 50% and more). Condition for this effect is a merely perfect crystal.
Theoretical models which include a quantitative description of the extinction effect were developed from Zachariasen (1962) and Becker and Coppens [2, 3, 4, 5, 6]. These models base on an ideal spherical mosaic crystal with a very perfect single crystal (primary Extinction) or different mosaic blocks with almost perfect alignment (secundary Extinction) to describe the strength of the extinction effect. In addition, it is possible to take into account anisotropic extinction effect if the crystal quality is also anisotropic. Nowadays extinction correction is included in most refinement programs [7]. In general extinction is a problem of sample quality and size and therefore more commonly a problem for neutron diffraction and not so often for x-ray diffraction with much smaller samples and larger absorption.

Polarisation*:* X-ray radiation is electromagnetic radiation. Therefore, the primary beam of an x-ray tube is not polarized. The radiation hits the sample under an diffraction angle of Θ where it can be separated into two waves of same intensity, firstly with an electrical field vector parallel $E_{||}$ and secondly perpendicular $E_{\perp}$ towards the Θ-axis. Whilst the radiation with $E_{||}$ will not be attenuated the radiation with $E_{\perp}$ will be attenuated with $E_{\perp} \rightarrow \cos(2\Theta)\, E_{\perp}$. The polarization factor P for the attenuation has then the following formula ($I \sim E^2$):

$$P = (1+\cos(2\Theta)^2)/2$$

Additional optical components like monochromator crystals also have an impact on the polarization and have to be taken into account accordingly.

Lorentz factor: The Lorentz factor L is a purely geometrical factor. It describes that during an ω- and Θ-scan respectively of Bragg reflections towards higher 2Θ values for the same angular speed $\Delta\omega/\Delta t$ an effectively elongated stay of the sample in the reflection position results.:

$$L = 1/\sin(2\Theta)$$

This has to be taken into account for any kind of radiation in an diffraction experiment.

3.4 Summary of Theory of Method

The different interactions of x-ray and neutron radiation with the atoms in a crystal make neutrons in general the better choice for a diffraction experiment. But on the other hand one has to take into account the available flux of x-rays and neutrons respectively. The flux of modern neutron sources like the Heinz Maier-Leibnitz neutron source (FRM II) is spread around a broad spectrum of neutron energies. In a sharp band of energies/wavelengths, e.g. $\Delta\lambda/\lambda<10^{-3}$, there is the flux of neutrons several order of magnitude smaller than the flux of x-rays of a corresponding synchtrotron source or x-ray tube in the laboratory. The reason for this is the fact that in an x-ray tube most x-rays are generated in a small energy band, the characteristic lines of the tube target (K_α, K_β, etc.). Additional metal foil used as filter allow to cut off unwanted characteristic lines which yields quasi monochromatic radiation of a single wavelength.
To use neutrons around a small energy band one has to use monochromator crystals. This reduces significantly the number of available neutrons for the diffraction experiment. Thus, the weak flux of neutrons and the weak cross section of neutrons with matter has to be compensated with large sample sizes of several millimeters. For the same reason the monochromatization of the neutrons is normally chosen to be not too sharp (resolution about $\Delta\lambda/\lambda\approx10^{-2}$ for neutrons, $\Delta\lambda/\lambda\approx10^{-5} - 10^{-6}$ for synchrotron).

3.5 From Measurement to Model

To get a structural model from the experimentally collected integral Bragg intensities one needs several steps in advance. Firstly on has to make sure that all reflections are measured properly (no shading, no $\lambda/2$-contamination, no Umweganregung (Renninger-effect)). Damaged reflections have to be excluded from further treatment.
During data refinement not only the quantities of the relative intensities but also their errors are taken into account. The total statistical error σ of an integral intensity I_{obs} of a single reflection is calculated as following:

$$\sigma^2 = I_{obs} + I_{background} + (k\, I_{total})^2$$

The part $\sigma_0^2 = I_{total}$, $I_{total} = I_{obs} + I_{background}$ refers to the error caused by counting statistics. It contains as well the effective intensity Iobs as well as the contribution of the background. But there are other effects that influence the reproducibility of a measurement (and thus the total error), e.g. specific errors of the instrumental adjustment. Those errors are collected in the so called *McCandlish-Factor k* and contribute to the total error. Therefore, the total error cannot drop below the physically correct limit of the experiment and thus the impact of strong reflections does not become exaggerated in the refinement. The determination of *k* is done by measurent the same set of reflections several times during an experiment (the so called standard reflections). The mean variation of the averaged value represents *k*. In addition, the repeated measurement of standard reflections offers the opportunity to notice unwanted changes during experiment like structural changes or release from the sample holder.

To make sure the comparisability of all reflections with each other, all intensities and errors are normalized to the same time of measurement (or monitor count rate) and undergo the Lorentz and (in the x-ray case) polarization correction.
Finally in advance of the data refinement there can be done an numerical (e.g. with DataP, [8]) or an empirical absoprtion if necessary. The quality of a measurement is checked in advance of the data refinement by comparing symmetry equivalent reflections and systematic extinctions to confirm the Laue group and space group symmetry. The result is written as internal *R*-value:

$$R_{\mathrm{int}} = (\sum_{k=1}^{m}(\sum_{j=1}^{n}{}_{k} (<I_k>- I_j)^2))/ (\sum_{k=1}\sum_{j=1}^{n}{}_{k}(I_j^2)_k)$$

R_{int} represents the mean error of a single reflection j of a group k of n_k symmetry equivalent reflections, corresponding to its group and the total number m of all symmetrically independent groups. Therefore R_{int} is also a good mark to check the absorption correction. After these preliminary steps one can start the final data refinement.
At the beginning one has to develop a structural model. The problem with that is that we measure only the absolut values $|F_{\mathrm{hkl}}|$ and not the complete structure factor $F_{\mathrm{hkl}} = |F_{hkl}|\exp(\iota\phi)$ including its phase ϕ. Therefore, generally the direct fouriertransform of the reflection information F_{hkl} from reciprocal space into the density information ρ in the direct space (electron density for x-rays, probability density of atomic cores for neutrons) with

$$\rho(\mathbf{x}) \sim \sum_h\sum_k\sum_l F_{hkl} \exp(-2\pi(hx+ky+lz))$$

not possible. This can be done only by direct methods like patterson, heavy atom method or anomal dispersion for x-rays.
In the so called refinement program a given structural model (space group, lattice constants, atomic form factors, MSD, etc.) are compared with the experimental data and fitted. In a leas squares routine those programs try to optimize (typically over several cycles) the free parameters to reduce the difference between the calculated structure factors F_{calc} and intensities $|F_{calc}|^2$ respectively and the experimentally found F_{obs} and $|F_{\mathrm{obs}}|^2$ respectively. To quantisize the quality of measurement there are several values in use:

1. *unweighted R*-value: $R_{\mathrm{u}} = \sum_{hkl} |F_{\mathrm{obs}}{}^2-F_{\mathrm{calc}}{}^2|/\sum_{hkl} F_{\mathrm{obs}}{}^2$
This value gives the alignment of the whole number of reflections without their specific errors.

2. weighted *R*-value: $R_{\mathrm{w}} = (\sum_{hkl} w\ (F_{\mathrm{obs}}{}^2-F_{\mathrm{calc}}{}^2)^2)/\sum_{hkl} w\ F_{\mathrm{obs}}{}^4$
This value represents the alignment of the whole number of reflections including their specific errors or weights (w~$1/\sigma^2$). Sometimes weights are adopted in a way to suppress unwanted influence of the refinement algorithm by weak or badly defined reflections. Be aware that such corrections have to be done extremely carefully because otherwise the refinement adopts the data to the selected structural model and not the model to the experimental data!

3. *Goodness of Fit S*: $S^2 =(\sum_{hkl} w\ (F_{\mathrm{obs}}{}^2-F_{\mathrm{calc}}{}^2)/(n_{\mathrm{hkl\text{-}reflections}} - n_{\mathrm{free\ parameter}})$

S should have a value near one if the weighting scheme and the structure model fit to the experimental data set.

4 Sample Section

4.1 Introduction

$La_{2-x}Sr_xCuO_4$ is one of the cuprate superconductors with K_2NiF_4- structure for whose discovery the noble prize was granted in 1988 (Bednorz and Müller [9]) . Pure La_2CuO_4 is an isolator. Doping with earth alcali metals (Ca^{2+}, Sr^{2+}, Ba^{2+}) on the La^{3+} lattice positions generates in dependence of the degree of doping superconductivity. Sr doping of x=0.15 yields a maximum T_c of 38 K.

Pure La_2CuO_4 undergoes at $T_{t\text{-}o}$=530 K a structural phase transition from the tetragonal high temperature phase (HTT)

F4/mmm: a=b=5.384 Å, c=13.204 Å, α=β=γ=90° at T=540 K

to the orthorhombic low temperature phase (LTO)

Abma: a=5.409 Å, b=5.357 Å, c=13.144 Å, α=β=γ=90° at room temperature.

The phase transition temperature $T_{t\text{-}o}$ drops for $La_{2-x}Sr_xCuO_4$ with increased doping and disappears above x=0.2.

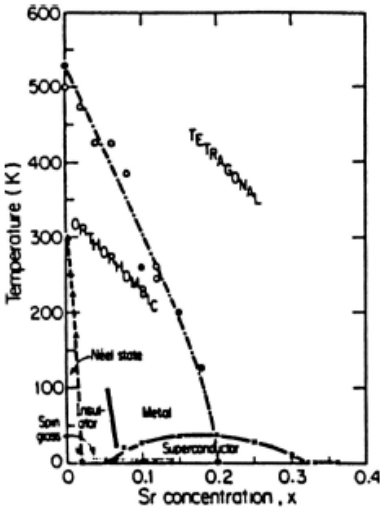

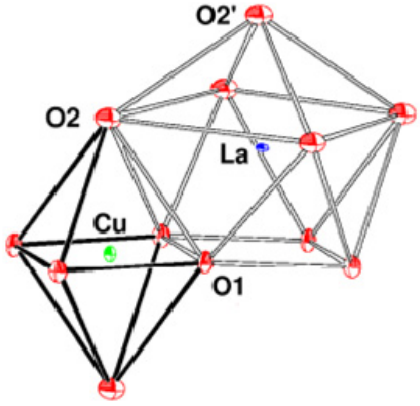

Fig.. 6 left: J. Birgenau, G. Shirane, HTC Superconductors I, World Scientific (1989)
Fig.. 6 right: Stuctural parts of La_2CuO_4 in the LTO phase

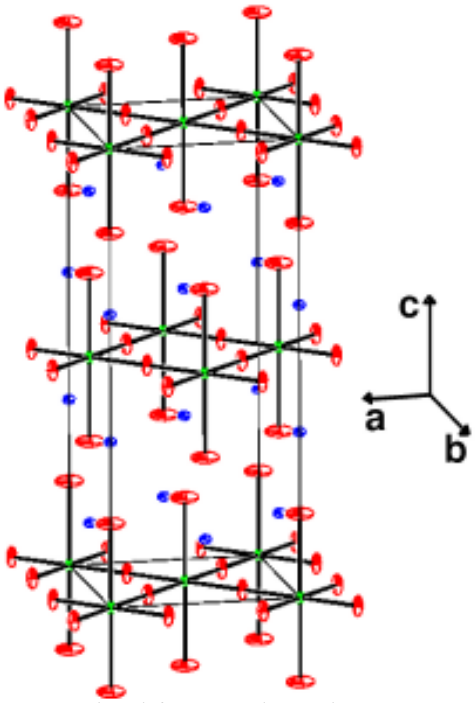

Fig. 7 left: tetragonal HTT phase

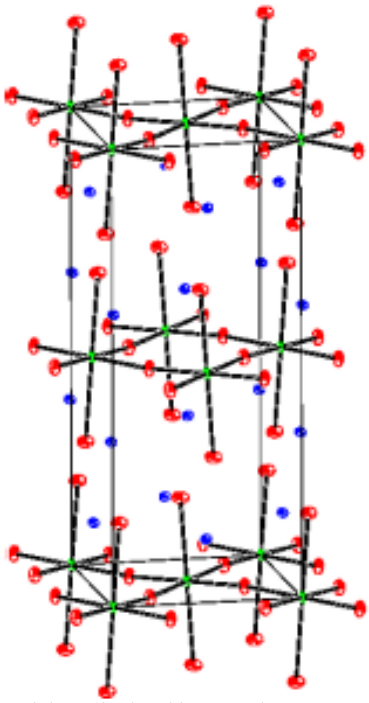

Fig. 7 right: orthorhombic´LTO phase

4.2 Twinning

During the transition into the low temperature phase the CuO_6 octahedrons are tilted around their [010] axis. Thus, the two axes of identical length in the HTT phase, a_1 and a_2, are not equal in the LTO phase anymore. Instead, the longer one becomes the new *a* axis, the shorter one becomes the *b* axis. Whether a_1 or a_2 becomes the new a axis depends only on the real structure of the crystal, for instance grain boundaries or point defects. Therefore, one can find two equivalent crystallographic space groups in the LTO phase:

Abma ($a_1 \rightarrow a$, $a_2 \rightarrow b$) and B*mab* ($a_1 \rightarrow b$, $a_2 \rightarrow a$)

For the structure factors in the LTO is valid:

$F_{\mathrm{Abma}}(hkl)=F_{\mathrm{Bmab}}(khl)$

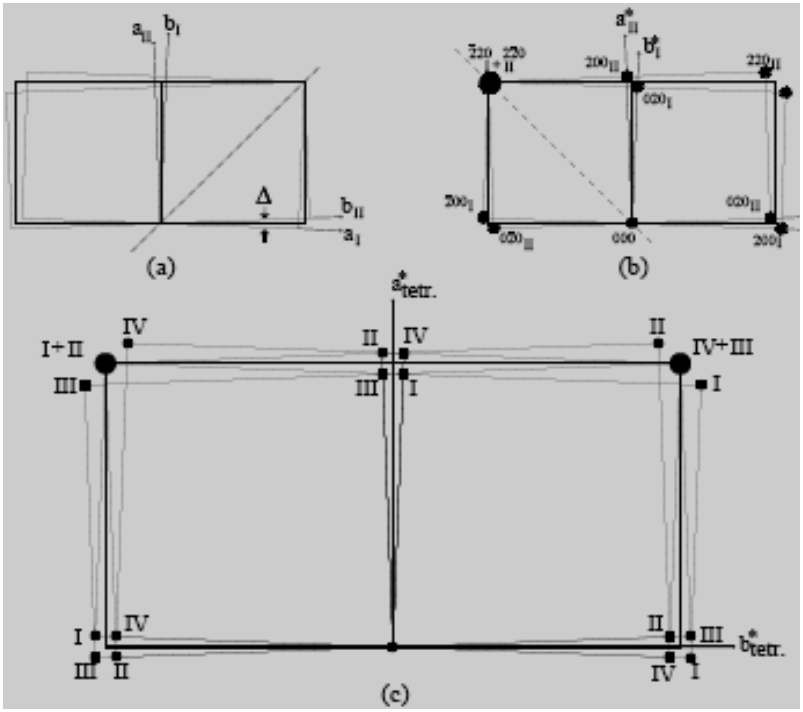

Fig. 8
(a) orthorhombic distortion with twinning correspondint to a (1-10) mirroring
(b) corresponding reciprocal lattice
(c) Overlay of (110)- and (1-10)-mirroring in reciprocal space

In the HTT phase only reflections with *h, k, l* of equal parity (*g* for even, *u* for uneven) are allowed - (*uuu*) and (*ggg*). They are called in the following main structrure reflections.
In the LTO phase additional reflections occur, called super structure reflections: In the *Abma*-Structure (*ugg*), l≠0 and (*guu*), in the *Bmab* structure (*gug*), l≠0 and(*ugu*).
Forbidden in both the HTT and the LTO phase are (*uug*), (*ggu*), (*ug*0) and (*gu*0).
These extinction rules will become important later.
In the real structure of the crystal there exist four domain types in total. They are separated into two pairs with the couple $Abma_1/Bmab_1$ (I/II) with the (1-10) mirror plane as grain boundary and the couple $Abma_2/Bmab_2$ (III/IV) with the (110) mirror plane as grain boundary (fig. 8).

The following overlaps of reflections result from this twinning:

- No splitting of the (00l) reflections,
- triple splitting of the (hh0) reflections
- fourfold splitting of the (h00) reflections.

An equal distribution of the volumetric portion of each single domain yields a ratio of intensities of 1:2:1 for the triple splitting. The distance $\Delta\omega$ between the centre and the side

peaks of a (*hkl*) reflex gives because of $(a+b)/2 = a_{1/2}$ an information about the orthorhombic *a/b* splitting. For the triple splitting of a (*hh*0) reflex is valid:

$\Delta\omega = 90°\text{-}2\arctan(b/a)$

Thus, although the real crystal is twinned, one can quantify the orthorhombic distortion.

The intensity contribution of the single domains corresponding to the whole intensity of a reflection can be described (taking into account the incoherent overlap of single intensities and the volumetric portions V_{A1} to V_{B2} of the domains) as follows:

$$I_{obs}(hkl) = I_{Abma1}(hkl) + I_{Bmab1}(hkl) + I_{Abma2}(hkl) + I_{Bmab2}(khl) \text{ or}$$

$$V_{total}|F_{obs}(hkl)|^2 = V_{A1}|F_{Abma1}(hkl)|^2 + V_{B1}|F_{Bmab1}(hkl)|^2 + V_{A2}|F_{Abma2}(hkl)|^2 + V_{B2}|F_{Bmab2}(hkl)|^2$$

$$= (V_{A1} + V_{A2})|F_{Abma1}(hkl)|^2 + (V_{B1}| + V_{B2})|F_{Bmab1}(hkl)|^2$$

$$= V_{total}\ \{\alpha|F_{Abma}(hkl)|^2 + (1\text{-}\alpha)\ |F_{Abma}(khl)|^2\ \}$$

with α being the relative portion of the volume of *Abma* domains to the crystal..

Because of the extinction rules in the LTO phase for the super structure reflections is valid: $I_{obs}(hkl) \sim \alpha|F_{Abma}(hkl)|^2$ for *Abma* and $I_{obs}(hkl) \sim (1\text{-}\alpha)|F_{Abma}(khl)|^2$ for *Bmab*. Thus, one can classify directly intensities to the volumetric portions of the domain types *Abma* and *Bmab* respectively. Therefore, by using one single additional parameter α to describe the relation between the twins in the structure one can determine the orthorhombic single crystal structure! This holds true although the Bragg reflections contain contributions of up to four different domains.

4.3 Oxygen Position

The oxygen atoms undergo the largest shift of their positions during the transition to the LTO phase. For the structure factor of a any Bragg reflection forbidden in *F4/mmm* is valid:

$$F(hkl) \sim \sum_i s_i \exp(-2\pi\imath(hx_i+ky_i+lz_i) = F(hkl)_{\text{apex oxygen}}+F(hkl)_{\text{in plane oxygen}}+F(hkl)_{\text{structure w/o O}}$$
$$\rightarrow F(hkl)_{\text{apex oxygen}}+F(hkl)_{\text{in plane oxygen}}$$

In the LTO phase the atomic position of the apex oxygens is (x 0 z), the atomic position for the in-plane oxygens is (1/4 1/4 -z). This yields the following intensities for the superstructure reflections:

$F(hkl)_{\text{apex oxygen}} = \cos(2\pi hx)\cos(2\pi lz)$ for h even or
$F(hkl)_{\text{apex oxygen}} = \sin(2\pi hx)\cos(2\pi lz)$ for h uneven

In the case of x-rays the form factor $f_i \sim Z_i$, Z_i=order number is much smaller for oxygen (Z=16) than for Cu (Z=29) and La (Z=57). Because of $I_{\text{obs}}(hkl) \sim |F(hkl)|^2$ the oxygen shift is hardly measurable. In the case of neutrons the scattering lengths b_i of all atoms are in the same order of magnitude (b_O=5.803 barn, b_{Cu}= barn, b_{La}= barn, 1 barn = 10^{-24} cm^{-2}). Therefore, the intensity contribution of the oxygen atoms increeases in relation to the other elements in the structure and allows a much more precise determination of the structural change of the oxygen positions

5 Preparatory Exercises

1. What is the fundamental difference between powder/single crystal diffraction and what are the advantages and disadvantages of both techniques (Compare d-values and orientations of different reflections in a cubic structure)?
2. What is wrong with fig. 2?
3. Which reflections are not allowed in a face centered structure (structure factor)?
4. There is no space group F4/mmm in the international tables. Why (Which other space group in the international tables yields the same pattern in direct space)?

6 Experiment Procedure

During this practical course not all physical and technical aspects of structure analysis with neutrons can be discussed in detail. Nevertheless this course is supposed point out the basic similarities and dissimilarities of x-rays and neutron radiation as well as their specific advantages and disadvantages in general and referring to single crystal diffraction. The sample selected for this practical course is most suitable for this purpose because of its special crystallographic peculiarities.

6.1 The Instrument

Fig. 5 shows the typical setup of a single crystal diffractometer with a single detector. Outgoing from the radiation source a primary beam defined by primary optics (in our case the beam tube) reaches the single crystal sample. If one lattice plane (*hkl*) fulfills Braggs laws, the scattered beam, called secondary beam, leaves the sample under an angle 2Θ to the primary beam. The exact direction of this beam depends only on the relative orientation of the sample to the primary beam.
For the diffractometer shown in fig. 5 the movement of the neutron detector is limited to a horizontal rotation around the 2Θ axis. Thus, only those reflections can be measured, whose scattering vector **Q** lies exactly in the plane defined by the source, the sample and detector circle. This plane is also called scattering plane.

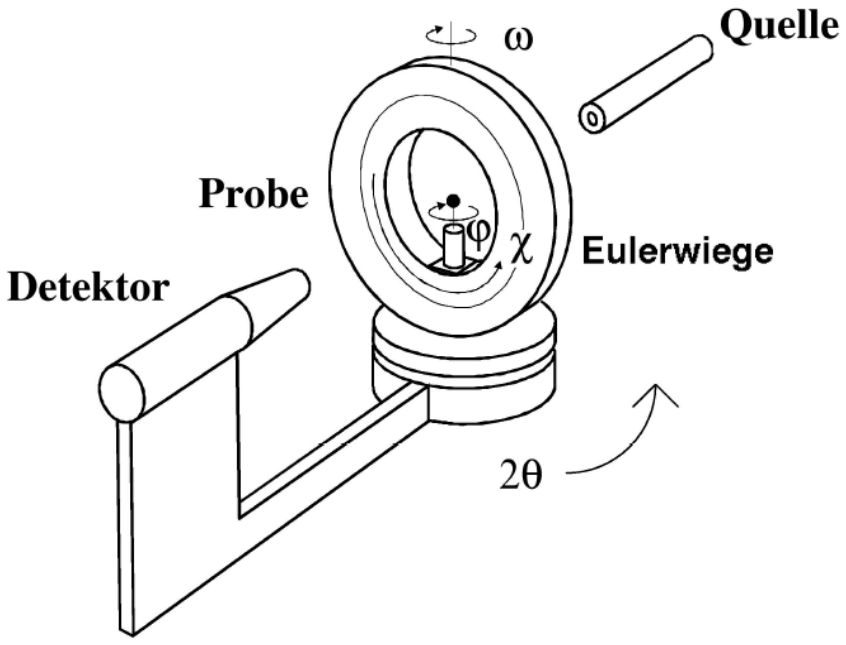

Fig. 5: Scheme of a single crystal diffractometer

To direct the secondary beam towards the detector position one has to orient the sample around the three axes ω, χ and ϕ. These three axes allow a virtually random orientation of the crystal in the primary beam. During the experiment the sample has to stay exactly in the cross point of all four axes (2Θ, ω, χ and ϕ) and the primary beam. Additionally, for $2\Theta = \omega = \chi = \phi = 0°$ the primary beam direction and the χ axis on one hand side and the 2Θ-, ω- and ϕ-axes on the other hand side are identical while the angle between the primary beam and the 2Θ-is exactly 90°. Because of the four rotational axes (2Θ, ω, χ, ϕ) this kind of single crystal diffractometer is often called four circle diffractometer. Another often used geometry - the so called κ-Geometrie - will not be discussed in detail here.

Further details of the experimental setup:

1. Beam source and primary optics: The primary beam is generated by a suitable source (x-rays: x-ray tube, synchrotron; neutrons: nuclear fission, spallation source). The primary optics defines the path of the beam to the sample in the Eulerian cradle. Furthermore, the primary optics defines the beam diameter using slits to make it fit to the sample size for homogeneous illumination. This homogeneity is very important because the quality of the data refinement relies on the comparison of the intensity ratios between the different reflections measured during an experiment. Wrong ratios caused by inhomogeneous illumination can yield wrong structural details! Other components of the primary optics are collimators defining beam divergence and filters or monochromators which define the wavelength λ of the radiation.

2. Sample and sample environment: The sample position is fixed by the centre of the Eulerian cradle which is defined by the cross point of the axes ω, χ and ϕ. As described above, the cradle itself has in combination with the ω-circle the task to orient the sample according to the observed reflection in a way that it hits the detector. The sample itself is mounted on a goniometer head. This head allows the adjustment of the sample in all three directions **x**; **y**; **z**, via microscope or camera. To avoid scattering from the sample environment and goniometer head the sample is usually connected to the head via a thin glass fibre (x-rays) or aluminum pin (neutrons). This reduces significantly background scattering. For experiments at high or low temperatures adjustable cooling or heating devices can be mounted into the Eulerian cradle.

3. Secondary optics and detector: The 2Θ arm of the instrument hold the detector which – in the ideal case – catches only radiation scattered from the sample and transforms it to an electrical signal. There exists a variety of detectors, single detectors and position sensitive 1D and 2D detectors. Area detectors have a large sensitive area that allows the accurate observation of spatial distribution of radiation. Other components of the secondary optics are slits and collimators or analyser (as optional units). They fulfil the task to shield the detector from unwanted radiation like scattering from sample environment, scattering in air, wrong wavelengths or flourescence

6.2 Sequence of measurement in Theory

1. Centering: In advance of the planned scientific program (profile analysis, Bragg data collection) the orientation of the sample in relation to the coordinate system of the diffractometer has to be determined. First of all the sample has to be centered optically to assure a homogeneous illumination of the sample. Afterwards, a reflection search routine has to be started to optimize the intensity of a found reflection by moving several angles after each other.
In many cases there are some structural informations like the unit cell and hkl values of strong reflections available from previous studies, e.g. from powder diffraction, thus, one can limit the reflection search to 2Θ values around these strong reflections to spare some time and to classify manually the found reflections with the correct indices.

2. Determination of orienting matrix and lattice constants: The comparison of the **Q** vectors of the found and centered reflections yields generally one or more suggestions for a suitable unit cell. This is done by a least squares routine minimizing the error bars between the calculated and measured **Q** vectors. This method allows to determine accurately the orientation matrix $\mathbf{M_o} = (\mathbf{a^*}\ \mathbf{b^*}\ \mathbf{c^*})^T$ of the sample relative to the coordinate system of the diffractometer and the lattice constants of the unit cell.

On HEiDi the axes are defined as following: **x**=primary beam, **z** || 2Θ axis, **y**=**z** x **x**.
A proposed unit cell is only acceptable if all experimentally found reflections can be indexed with integer *hkl* , this means $\mathbf{Q} = (h\ k\ l)^*\mathbf{M_o}$. In addition the found reflection intensities *I* offer a course check, e.g. whether extinction rules are followed or intensities of symmetrically identical reflections are identical.

3. Profile analyses and scan types: During profile analysis reflex profiles are analysed via so called ω scans. During this scan the sample is turned for *n* steps around a center position ω_0. This scan makes different crystallites in one large sample visible. In addition one has to take into account that even in perfectly grown crystals there are grain boundaries and slight mismatches of the crystallites. These mosaic blocks are perfect crystals whose orientations are misaligned only a few tenths of a degree or less. By the way, the axis position $2\Theta/2=\Theta=\omega$ is called the bisecting orientation of the Eulerian cradle.
As long as the vertical aperture is large enough, a rotation of the crystal around a ω_0, that is equivalent to the ideal Θ_0 Bragg angle of a reflex allows to catch the intensity portion of each crystallite in the sample in the neutron detector on the fixed 2Θ position, even those that can only be found for slightly differing ω. Therefore, a crystal with large mosaicity gives measurable intensities over a broader ω area than a perfect crystal. Thus it gives a broader reflex profile. Also the tearing and cracking of a crystal creates broad but unregular profiles.
Beside the crystal quality also the instrumental resolution limits the measurable profile widths in the following sense: The divergence of a primary beam in real experiment is limited, for instance to 0.2°.
If a reflection fulfills Bragg's Law at Θ, the total divergence is a convolution of the divergence of the primary beam *and* the mosaicity/divergence of the sample. Thus, the reflection profile will never be sharper than the divergence of the primary beam itself.
In addition one has to take into account that for larger diffraction angles a fixed detector window will not be sufficient to catch the whole reflection intensities during a rocking scan.

For a given spectrum $\Delta\lambda/\lambda$ of the primary beam, with increasing scattering angle Θ angular range $\Delta\Theta$ increases with $\sin(\Delta\Theta/2)=\tan(\Theta)*\Delta\lambda/\lambda$ for which all wavelengths in the interval $\lambda\pm\Delta\lambda/2$ fulfilling Bragg's law are distributed. Because of the limited width of the detector window this yields a cut off of intensities for larger scattering angles for ω-scans.
To compensate this cut off effect it is necessary to begin at a certain 2Θ-angle to move the detector window with the ω-angle.. This can be done by so called $\omega/2\Theta$-scans. The start position of this 2Θ range depends on the primary beam divergence and sample quality and has to be checked individually for each sample.

4. Collection of Bragg reflections: If a sample was found good after the described preliminary studies one can start with the Bragg data collection. In this data collection all (or selected) reflections in a given 2Θ intervall are collected automatically. The usual strategy follows the rule „Only as many as necessary". This means the following: On one hand side the quality of the measured reflections has to fulfil certain standards (like small standard deviations σ and a good shape of the profiles) to reach an acceptable accuracy. On the other side there is only a limited amount of time available for each reflection due to the huge number of them (up to several thousands). and the limited beam time. A rule of thumb is therefore to measure about 10 non symmetry equivalent reflections for each free parameter used in the data refinement to get the correct structure. To achieve this goal a typical algorithm is to do a prescan with t_{min} per point of measurement in combination with a given larger (e.g. I/σ=4 and 25%, respectively) and a smaller (e.g. I/σ=20 and 5%, respectively) relative error limit. t_{min} is chosen in a way that the statistics of strong reflections is fine already after the prescan. Weak reflections are also noticed in the prescan and stored as weak reflections without additional treatment. Reflections in between get an additional chance to improve their statistics by performing a second scan with a limited amount of time up to t_{max}-t_{min}. This method avoids to spend unreasonable beam time to weak reflections which will not help to improve the quality of the structure model.

6.3 and in Practice

1. **Adjust optically the sample in the neutron beam :** Alignment of the sample in the rotational centre of the instrument. This is necessary for a homogeneous illumination of the sample for all possible orientations.

2. **Search for Bragg reflections and center them, , "Reflex centering**": Sample and detector position are controlled by a special diffractometer software. The main goal is to find suitable angular positions for the detector first and afterwards for the sample to get a measurable signal. Afterwards the orientation of the sample in the Eulerian cradle have to be optimized for maximum intensity.

3. **Analyse profiles of selected reflections:** Study different reflex profiles and reveal the impact of twinning

4. **Determine the orthorhombic lattice parameters a, b and c**: Estimate the misalignment of a and b in reference to $a_{1/2}$ in the real tetragonal cell.

5. **Determine the average tetragonal unit cell**: The centering of different reflections allows the calculation of all lattice constants including the averaged tetragonal parameters.

6. **Observe super structure reflections:** Measuring pairs of (*hkl*)/(*khl*) allows the estimation of the volumetric contribution of each single domain to the whole crystal.

7. **Select measurement parameters for Bragg data collection:** In order to optimize the number and statistical quality of collected Bragg reflections suitable scan parameters (time/step, no. of steps, stepwidths, etc.) have to be determined.

8. **Collect a Bragg data set**

6.4 Data analysis

After having measured a Bragg data set one has to do the final step, the alignment of model and measurement:

1. **Data Reduction:** In this process the measured reflection profiles are analysed and reduced to a simple list of all measured reflections and their integrated intensities including error bars and some other useful information. This so-called *hkl*-list is the base for the next step:

2. **Structure refinement:** Here the measured *hkl*-list and our structure model are combined to determine structural details like atomic positions and mean square displacements.

7 Experiment-Related Exercises

1. Why is the optical adjustment of the sample so important?
2. How large is the *a/b*-splitting at room temperature (=|*a*-*b*|/(*a*+*b*))?
3. What is the benefit/enhancement of studying the room temperature structure with neutrons instead of X-rays?

References

[1] Th. Hahn (ed.), Space-group symmetry, International Tables for Crystallography Vol. A, Kluver Academic Publishers (2006).
[2] W.H. Zachariasen, Acta Cryst. 18 703 (1965).

[3] W.H. Zachariasen, Acta Cryst. 18 705 (1965).

[4] P. Coppens and W.C. Hamilton, Acta Cryst. A 26 71-83 (1970).

[5] P.J. Becker and P. Coppens, Acta Cryst. A 30 129-147 (1974).

[6] P.J. Becker and P. Coppens, Acta Cryst. A 30 148-153 (1974).

[7] U.H. Zucker, E. Perrenthaler, W.F. Kuhs, R. Bachmann and H. Schulz J. of Appl. Crystallogr., 16 358 (1983).
[8] P. Coppens, W.C. Hamilton, S. Wilkins, M.S. Lehmann and Savariault, Datap, http://www.ill.fr/data treat/diftreat.html#single (1999).
[9] J. Bednorz and K. Müller, Z. Phys. B 64 189 (1986).

Literature

N.W. Ashcroft and N.D. Mermin, Festkörperphysik, Oldenbourg 2001.

H. Ibach and H. Lüth, Festkörperphysik, Einführung in die Grundlagen, 6. Edition Springer 2002.

C. Kittel, Einführung in die Festkörperphysik, 10. Edition, Oldenbourg 1993.

W. Borchardt-Ott, Kristallographie. Eine Einführung für Naturwissenschaftler, 6. Auflage Springer 2002.

W. Kleber, Einführung in die Kristallographie, Oldenbourg 1998

H. Dachs, Neutron Diffraction, Springer (1978)

D.J. Dyson, X-Ray and Electron Diffraction Studies in Material Science, Maney Pub 2004.

C. Giacovazzo, Fundamentals of Crystallography, 2nd Ed., Oxford University Press 2002.

L.A. Aslanov, Crystallographic Instrumentation, Oxford University Press 1998.

M.T. Dove, Structure and Dynamics. An Atomic View of Materials, Oxford University Press 2003. W. Clegg, Crystal Structure Analysis. Principles and Practice, Oxford University Press 2001.

Appendix (Tables and space groups from [1])

3.1. SPACE-GROUP DETERMINATION AND DIFFRACTION SYMBOLS

Table 3.1.4.1. *Reflection conditions, diffraction symbols and possible space groups* (*cont.*)

ORTHORHOMBIC, Laue class *mmm* ($2/m\ 2/m\ 2/m$) (*cont.*)

Reflection conditions								Laue class *mmm* ($2/m\ 2/m\ 2/m$)		
								Point group		
hkl	0*kl*	*h*0*l*	*hk*0	*h*00	0*k*0	00*l*	Extinction symbol	222	*mm*2 *m*2*m* 2*mm*	*mmm*
	$k+l$	l	k		k	l	*Pncb*			*Pncb* (50)
	$k+l$	l	$h+k$	h	k	l	*Pncn*			*Pncn* (52)
	$k+l$	$h+l$		h	k	l	*Pnn* –		***Pnn*2** (34)	***Pnnm*** (58)
	$k+l$	$h+l$	h	h	k	l	*Pnna*			***Pnna*** (52)
	$k+l$	$h+l$	k	h	k	l	*Pnnb*			*Pnnb* (52)
	$k+l$	$h+l$	$h+k$	h	k	l	*Pnnn*			***Pnnn*** (48)
$h+k$	k	h	$h+k$	h	k		*C* – – –	***C*222** (21)	***Cmm*2** (35) *Cm*2*m* (38) *C*2*mm* (38)	***Cmmm*** (65)
$h+k$	k	h	$h+k$	h	k	l	*C*– –2_1	***C*222$_1$** (20)		
$h+k$	k	h	h, k	h	k		*C*– –(*ab*)		*Cm*2*e* (39) *C*2*me* (39)	***Cmme*** (67)
$h+k$	k	h, l	$h+k$	h	k	l	*C*–*c* –		***Cmc*2$_1$** (36) *C*2*cm* (40)	***Cmcm*** (63)
$h+k$	k	h, l	h, k	h	k	l	*C*–*c*(*ab*)		*C*2*ce* (41)	***Cmce*** (64)
$h+k$	k, l	h	$h+k$	h	k	l	*Cc* – –		*Ccm*2$_1$ (36) *Cc*2*m* (40)	*Ccmm* (63)
$h+k$	k, l	h	h, k	h	k	l	*Cc* –(*ab*)		*Cc*2*e* (41)	*Ccme* (64)
$h+k$	k, l	h, l	$h+k$	h	k	l	*Ccc* –		***Ccc*2** (37)	***Cccm*** (66)
$h+k$	k, l	h, l	h, k	h	k	l	*Ccc*(*ab*)			***Ccce*** (68)
$h+l$	l	$h+l$	h	h		l	*B* – – –	*B*222 (21)	*Bmm*2 (38) *Bm*2*m* (35) *B*2*mm* (38)	*Bmmm* (65)
$h+l$	l	$h+l$	h	h	k	l	*B*–2_1–	*B*22_12 (20)		
$h+l$	l	$h+l$	h, k	h	k	l	*B*– –*b*		*Bm*2_1*b* (36) *B*2*mb* (40)	*Bmmb* (63)
$h+l$	l	h, l	h	h		l	*B* –(*ac*)–		*Bme*2 (39) *B*2*em* (39)	*Bmem* (67)
$h+l$	l	h, l	h, k	h	k	l	*B* –(*ac*)*b*		*B*2*eb* (41)	*Bmeb* (64)
$h+l$	k, l	$h+l$	h	h	k	l	*Bb* – –		*Bbm*2 (40) *Bb*2_1*m* (36)	*Bbmm* (63)
$h+l$	k, l	$h+l$	h, k	h	k	l	*Bb*–*b*		*Bb*2*b* (37)	*Bbmb* (66)
$h+l$	k, l	h, l	h	h	k	l	*Bb*(*ac*)–		*Bbe*2 (41)	*Bbem* (64)
$h+l$	k, l	h, l	h, k	h	k	l	*Bb*(*ac*)*b*			*Bbeb* (68)
$k+l$	$k+l$	l	k		k	l	*A* – – –	*A*222 (21)	***Amm*2** (38) *Am*2*m* (38) *A*2*mm* (35)	*Ammm* (65)
$k+l$	$k+l$	l	k	h	k	l	*A*2$_1$– –	*A*2_122 (20)		
$k+l$	$k+l$	l	h, k	h	k	l	*A*– –*a*		***Am*2*a*** (40) *A*2_1*ma* (36)	*Amma* (63)
$k+l$	$k+l$	h, l	k	h	k	l	*A*–*a* –		***Ama*2** (40) *A*2_1*am* (36)	*Amam* (63)
$k+l$	$k+l$	h, l	h, k	h	k	l	*A*–*aa*		*A*2*aa* (37)	*Amaa* (66)
$k+l$	k, l	l	k		k	l	*A*(*bc*)– –		***Aem*2** (39) *Ae*2*m* (39)	*Aemm* (67)
$k+l$	k, l	l	h, k	h	k	l	*A*(*bc*)– *a*		*Ae*2*a* (41)	*Aema* (64)
$k+l$	k, l	h, l	k	h	k	l	*A*(*bc*)*a* –		***Aea*2** (41)	*Aeam* (64)
$k+l$	k, l	h, l	h, k	h	k	l	*A*(*bc*)*aa*			*Aeaa* (68)
$h+k+l$	$k+l$	$h+l$	$h+k$	h	k	l	*I* – – –	[***I*222** (23) ***I*2$_1$2$_1$2$_1$** (24)]*	***Imm*2** (44) *Im*2*m* (44)	***Immm*** (71)

3. DETERMINATION OF SPACE GROUPS

Table 3.1.4.1. *Reflection conditions, diffraction symbols and possible space groups (cont.)*

ORTHORHOMBIC, Laue class *mmm* ($2/m\ 2/m\ 2/m$) (*cont.*)

Reflection conditions								Laue class *mmm* ($2/m\ 2/m\ 2/m$)		
								Point group		
hkl	0*kl*	*h*0*l*	*hk*0	*h*00	0*k*0	00*l*	Extinction symbol	222	*mm*2 *m*2*m* 2*mm*	*mmm*
									*I*2*mm* (44)	
$h+k+l$	$k+l$	$h+l$	h, k	h	k	l	$I--(ab)$		*Im*2*a* (46)	***Imma*** (74)
									*I*2*mb* (46)	*Immb* (74)
$h+k+l$	$k+l$	h, l	$h+k$	h	k	l	$I-(ac)-$		***Ima*2** (46)	*Imam* (74)
									*I*2*cm* (46)	*Imcm* (74)
$h+k+l$	$k+l$	h, l	h, k	h	k	l	$I-cb$		*I*2*cb* (45)	*Imcb* (72)
$h+k+l$	k, l	$h+l$	$h+k$	h	k	l	$I(bc)--$		*Iem*2 (46)	*Iemm* (74)
									*Ie*2*m* (46)	
$h+k+l$	k, l	$h+l$	h, k	h	k	l	$Ic-a$		*Ic*2*a* (45)	*Icma* (72)
$h+k+l$	k, l	h, l	$h+k$	h	k	l	$Iba-$		***Iba*2** (45)	***Ibam*** (72)
$h+k+l$	k, l	h, l	h, k	h	k	l	$Ibca$			***Ibca*** (73)
										Icab (73)
$h+k, h+l, k+l$	k, l	h, l	h, k	h	k	l	$F---$	***F*222** (22)	***Fmm*2** (42)	***Fmmm*** (69)
									*Fm*2*m* (42)	
									*F*2*mm* (42)	
$h+k, h+l, k+l$	k, l	$h+l=4n$; h, l	$h+k=4n$; h, k	$h=4n$	$k=4n$	$l=4n$	$F-dd$		*F*2*dd* (43)	
$h+k, h+l, k+l$	$k+l=4n$; k, l	h, l	$h+k=4n$; h, k	$h=4n$	$k=4n$	$l=4n$	$Fd-d$		*Fd*2*d* (43)	
$h+k, h+l, k+l$	$k+l=4n$; k, l	$h+l=4n$; h, l	h, k	$h=4n$	$k=4n$	$l=4n$	$Fdd-$		***Fdd*2** (43)	
$h+k, h+l, k+l$	$k+l=4n$; k, l	$h+l=4n$; h, l	$h+k=4n$; h, k	$h=4n$	$k=4n$	$l=4n$	$Fddd$			***Fddd*** (70)

* Pair of space groups with common point group and symmetry elements but differing in the relative location of these elements.

3.1. SPACE-GROUP DETERMINATION AND DIFFRACTION SYMBOLS

Table 3.1.4.1. *Reflection conditions, diffraction symbols and possible space groups (cont.)*

TETRAGONAL, Laue classes $4/m$ and $4/mmm$ (*cont.*)

Reflection conditions							Extinction symbol	Laue class						
								$4/m$			$4/mmm$ ($4/m\ 2/m\ 2/m$)			
								Point group						
hkl	*hk*0	0*kl*	*hhl*	00*l*	0*k*0	*hh*0		4	$\bar{4}$	$4/m$	422	4*mm*	$\bar{4}2m$ $\bar{4}m2$	$4/mmm$
	$h+k$	k			k		*Pnb* –							*P*4/*nbm* (125)
	$h+k$	k	l	l	k		*Pnbc*							*P*4$_2$/*nbc* (133)
	$h+k$	l		l	k		*Pnc* –							*P*4$_2$/*ncm* (138)
	$h+k$	l	l	l	k		*Pncc*							*P*4/*ncc* (130)
	$h+k$	$k+l$		l	k		*Pnn* –							*P*4$_2$/*nnm* (134)
	$h+k$	$k+l$	l	l	k		*Pnnc*							*P*4/*nnc* (126)
$h+k+l$	$h+k$	$k+l$	l	l	k		$I---$	*I*4 (79)	*I*$\bar{4}$ (82)	*I*4/*m* (87)	*I*422 (97)	*I*4*mm* (107)	*I*$\bar{4}$2*m* (121)	*I*4/*mmm* (139)
													I$\bar{4}$*m*2 (119)	
$h+k+l$	$h+k$	$k+l$	l	$l=4n$	k		$I4_1--$	*I*4$_1$ (80)			*I*4$_1$22 (98)			
$h+k+l$	$h+k$	$k+l$	‡	$l=4n$	k	h	$I--d$					*I*4$_1$*md* (109)	*I*$\bar{4}$2*d* (122)	
$h+k+l$	$h+k$	k, l	l	l	k		$I-c-$					*I*4*cm* (108)	*I*4*c*2 (120)	*I*4/*mcm* (140)
$h+k+l$	$h+k$	k, l	‡	$l=4n$	k	h	$I-cd$					*I*4$_1$*cd* (110)		
$h+k+l$	h, k	$k+l$	l	$l=4n$	k		$I4_1/a--$			*I*4$_1$/*a* (88)				
$h+k+l$	h, k	$k+l$	‡	$l=4n$	k	h	$Ia-d$							*I*4$_1$/*amd* (141)
$h+k+l$	h, k	k, l	‡	$l=4n$	k	h	$Iacd$							*I*4$_1$/*acd* (142)

† Pair of enantiomorphic space groups, *cf.* Section 3.1.5.
‡ Condition: $2h+l=4n$; l.

International Tables for Crystallography (2006). Vol. A, Space group 139, pp. 478–479.

$I4/mmm$ D_{4h}^{17} $4/mmm$ Tetragonal

No. 139 $I\ 4/m\ 2/m\ 2/m$ Patterson symmetry $I4/mmm$

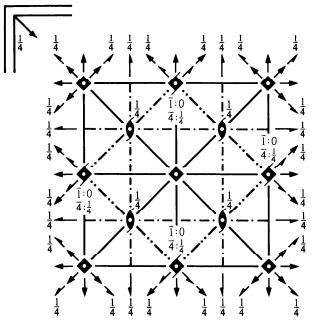

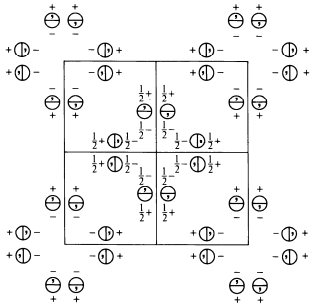

Origin at centre $(4/mmm)$

Asymmetric unit $0 \le x \le \frac{1}{2};\quad 0 \le y \le \frac{1}{2};\quad 0 \le z \le \frac{1}{4};\quad x \le y$

Symmetry operations

For $(0,0,0)+$ set

(1) 1	(2) 2 $0,0,z$	(3) 4^+ $0,0,z$	(4) 4^- $0,0,z$
(5) 2 $0,y,0$	(6) 2 $x,0,0$	(7) 2 $x,x,0$	(8) 2 $x,\bar{x},0$
(9) $\bar{1}$ $0,0,0$	(10) m $x,y,0$	(11) $\bar{4}^+$ $0,0,z$; $0,0,0$	(12) 4^- $0,0,z$; $0,0,0$
(13) m $x,0,z$	(14) m $0,y,z$	(15) m $x,\bar{x},z$	(16) m x,x,z

For $(\frac{1}{2},\frac{1}{2},\frac{1}{2})+$ set

(1) $t(\frac{1}{2},\frac{1}{2},\frac{1}{2})$	(2) $2(0,0,\frac{1}{2})$ $\frac{1}{4},\frac{1}{4},z$	(3) $4^+(0,0,\frac{1}{2})$ $0,\frac{1}{2},z$	(4) $4^-(0,0,\frac{1}{2})$ $\frac{1}{2},0,z$
(5) $2(0,\frac{1}{2},0)$ $\frac{1}{4},y,\frac{1}{4}$	(6) $2(\frac{1}{2},0,0)$ $x,\frac{1}{4},\frac{1}{4}$	(7) $2(\frac{1}{2},\frac{1}{2},0)$ $x,x,\frac{1}{4}$	(8) 2 $x,\bar{x}+\frac{1}{2},\frac{1}{4}$
(9) $\bar{1}$ $\frac{1}{4},\frac{1}{4},\frac{1}{4}$	(10) $n(\frac{1}{2},\frac{1}{2},0)$ $x,y,\frac{1}{4}$	(11) $\bar{4}^+$ $\frac{1}{2},0,z$; $\frac{1}{2},0,\frac{1}{4}$	(12) $\bar{4}^-$ $0,\frac{1}{2},z$; $0,\frac{1}{2},\frac{1}{4}$
(13) $n(\frac{1}{2},0,\frac{1}{2})$ $x,\frac{1}{4},z$	(14) $n(0,\frac{1}{2},\frac{1}{2})$ $\frac{1}{4},y,z$	(15) c $x+\frac{1}{2},\bar{x},z$	(16) $n(\frac{1}{2},\frac{1}{2},\frac{1}{2})$ x,x,z

---

Maximal non-isomorphic subgroups *(continued)*

IIa
[2] $P4_2/nmc$ (137) 1; 2; 7; 8; 11; 12; 13; 14; (3; 4; 5; 6; 9; 10; 15; 16) + $(\frac{1}{2},\frac{1}{2},\frac{1}{2})$
[2] $P4_2/mnm$ (136) 1; 2; 7; 8; 9; 10; 15; 16; (3; 4; 5; 6; 11; 12; 13; 14) + $(\frac{1}{2},\frac{1}{2},\frac{1}{2})$
[2] $P4_2/nnm$ (134) 1; 2; 5; 6; 11; 12; 15; 16; (3; 4; 7; 8; 9; 10; 13; 14) + $(\frac{1}{2},\frac{1}{2},\frac{1}{2})$
[2] $P4_2/mmc$ (131) 1; 2; 5; 6; 9; 10; 13; 14; (3; 4; 7; 8; 11; 12; 15; 16) + $(\frac{1}{2},\frac{1}{2},\frac{1}{2})$
[2] $P4/nmm$ (129) 1; 2; 3; 4; 13; 14; 15; 16; (5; 6; 7; 8; 9; 10; 11; 12) + $(\frac{1}{2},\frac{1}{2},\frac{1}{2})$
[2] $P4/mnc$ (128) 1; 2; 3; 4; 9; 10; 11; 12; (5; 6; 7; 8; 13; 14; 15; 16) + $(\frac{1}{2},\frac{1}{2},\frac{1}{2})$
[2] $P4/nnc$ (126) 1; 2; 3; 4; 5; 6; 7; 8; (9; 10; 11; 12; 13; 14; 15; 16) + $(\frac{1}{2},\frac{1}{2},\frac{1}{2})$
[2] $P4/mmm$ (123) 1; 2; 3; 4; 5; 6; 7; 8; 9; 10; 11; 12; 13; 14; 15; 16

IIb none

Maximal isomorphic subgroups of lowest index

IIc [3] $I4/mmm$ ($\mathbf{c}' = 3\mathbf{c}$) (139); [9] $I4/mmm$ ($\mathbf{a}' = 3\mathbf{a}, \mathbf{b}' = 3\mathbf{b}$) (139)

Minimal non-isomorphic supergroups

I [3] $Fm\bar{3}m$ (225); [3] $Im\bar{3}m$ (229)

II [2] $C4/mmm$ ($\mathbf{c}' = \frac{1}{2}\mathbf{c}$) ($P4/mmm$, 123)

CONTINUED **No. 139** $I4/mmm$

Generators selected (1); $t(1,0,0)$; $t(0,1,0)$; $t(0,0,1)$; $t(\frac{1}{2},\frac{1}{2},\frac{1}{2})$; (2); (3); (5); (9)

Positions

Multiplicity, Wyckoff letter, Site symmetry			Coordinates $(0,0,0)+$ $(\frac{1}{2},\frac{1}{2},\frac{1}{2})+$				Reflection conditions
							General:
32	o	1	(1) x,y,z (5) $\bar{x},y,\bar{z}$ (9) $\bar{x},\bar{y},\bar{z}$ (13) $x,\bar{y},z$	(2) $\bar{x},\bar{y},z$ (6) $x,\bar{y},\bar{z}$ (10) $x,y,\bar{z}$ (14) $\bar{x},y,z$	(3) $\bar{y},x,z$ (7) $y,x,\bar{z}$ (11) $y,\bar{x},\bar{z}$ (15) $\bar{y},\bar{x},z$	(4) $y,\bar{x},z$ (8) $\bar{y},\bar{x},\bar{z}$ (12) $\bar{y},x,\bar{z}$ (16) y,x,z	hkl : $h+k+l=2n$ $hk0$: $h+k=2n$ $0kl$: $k+l=2n$ hhl : $l=2n$ $00l$: $l=2n$ $h00$: $h=2n$
							Special: as above, plus
16	n	$.m.$	$0,y,z$ $0,y,\bar{z}$	$0,\bar{y},z$ $0,\bar{y},\bar{z}$	$\bar{y},0,z$ $y,0,\bar{z}$	$y,0,z$ $\bar{y},0,\bar{z}$	no extra conditions
16	m	$..m$	x,x,z $\bar{x},x,\bar{z}$	$\bar{x},\bar{x},z$ $x,\bar{x},\bar{z}$	$\bar{x},x,z$ $x,x,\bar{z}$	$x,\bar{x},z$ $\bar{x},\bar{x},\bar{z}$	no extra conditions
16	l	$m..$	$x,y,0$ $\bar{x},y,0$	$\bar{x},\bar{y},0$ $x,\bar{y},0$	$\bar{y},x,0$ $y,x,0$	$y,\bar{x},0$ $\bar{y},\bar{x},0$	no extra conditions
16	k	$..2$	$x,x+\frac{1}{2},\frac{1}{4}$ $\bar{x},\bar{x}+\frac{1}{2},\frac{3}{4}$	$\bar{x},\bar{x}+\frac{1}{2},\frac{1}{4}$ $x,x+\frac{1}{2},\frac{3}{4}$	$\bar{x}+\frac{1}{2},x,\frac{1}{4}$ $x+\frac{1}{2},\bar{x},\frac{3}{4}$	$x+\frac{1}{2},\bar{x},\frac{1}{4}$ $\bar{x}+\frac{1}{2},x,\frac{3}{4}$	hkl : $l=2n$
8	j	$m2m.$	$x,\frac{1}{2},0$	$\bar{x},\frac{1}{2},0$	$\frac{1}{2},x,0$	$\frac{1}{2},\bar{x},0$	no extra conditions
8	i	$m2m.$	$x,0,0$	$\bar{x},0,0$	$0,x,0$	$0,\bar{x},0$	no extra conditions
8	h	$m.2m$	$x,x,0$	$\bar{x},\bar{x},0$	$\bar{x},x,0$	$x,\bar{x},0$	no extra conditions
8	g	$2mm.$	$0,\frac{1}{2},z$	$\frac{1}{2},0,z$	$0,\frac{1}{2},\bar{z}$	$\frac{1}{2},0,\bar{z}$	hkl : $l=2n$
8	f	$..2/m$	$\frac{1}{4},\frac{1}{4},\frac{1}{4}$	$\frac{3}{4},\frac{3}{4},\frac{1}{4}$	$\frac{3}{4},\frac{1}{4},\frac{1}{4}$	$\frac{1}{4},\frac{3}{4},\frac{1}{4}$	hkl : $k,l=2n$
4	e	$4mm$	$0,0,z$	$0,0,\bar{z}$			no extra conditions
4	d	$\bar{4}m2$	$0,\frac{1}{2},\frac{1}{4}$	$\frac{1}{2},0,\frac{1}{4}$			hkl : $l=2n$
4	c	$mmm.$	$0,\frac{1}{2},0$	$\frac{1}{2},0,0$			hkl : $l=2n$
2	b	$4/mmm$	$0,0,\frac{1}{2}$				no extra conditions
2	a	$4/mmm$	$0,0,0$				no extra conditions

Symmetry of special projections

Along [001] $p4mm$
$\mathbf{a}' = \frac{1}{2}(\mathbf{a}-\mathbf{b})$ $\mathbf{b}' = \frac{1}{2}(\mathbf{a}+\mathbf{b})$
Origin at $0,0,z$

Along [100] $c2mm$
$\mathbf{a}' = \mathbf{b}$ $\mathbf{b}' = \mathbf{c}$
Origin at $x,0,0$

Along [110] $p2mm$
$\mathbf{a}' = \frac{1}{2}(-\mathbf{a}+\mathbf{b})$ $\mathbf{b}' = \frac{1}{2}\mathbf{c}$
Origin at $x,x,0$

Maximal non-isomorphic subgroups

I	[2] $I\bar{4}2m$ (121)	(1; 2; 5; 6; 11; 12; 15; 16)+
	[2] $I\bar{4}m2$ (119)	(1; 2; 7; 8; 11; 12; 13; 14)+
	[2] $I4mm$ (107)	(1; 2; 3; 4; 13; 14; 15; 16)+
	[2] $I422$ (97)	(1; 2; 3; 4; 5; 6; 7; 8)+
	[2] $I4/m11$ ($I4/m$, 87)	(1; 2; 3; 4; 9; 10; 11; 12)+
	[2] $I2/m2/m1$ ($Immm$, 71)	(1; 2; 5; 6; 9; 10; 13; 14)+
	[2] $I2/m12/m$ ($Fmmm$, 69)	(1; 2; 7; 8; 9; 10; 15; 16)+

(*Continued on preceding page*)

International Tables for Crystallography (2006). Vol. A, Space group 69, pp. 316–318.

$F\,mmm$ D_{2h}^{23} mmm Orthorhombic

No. 69 $F\ 2/m\ 2/m\ 2/m$ Patterson symmetry $F\,mmm$

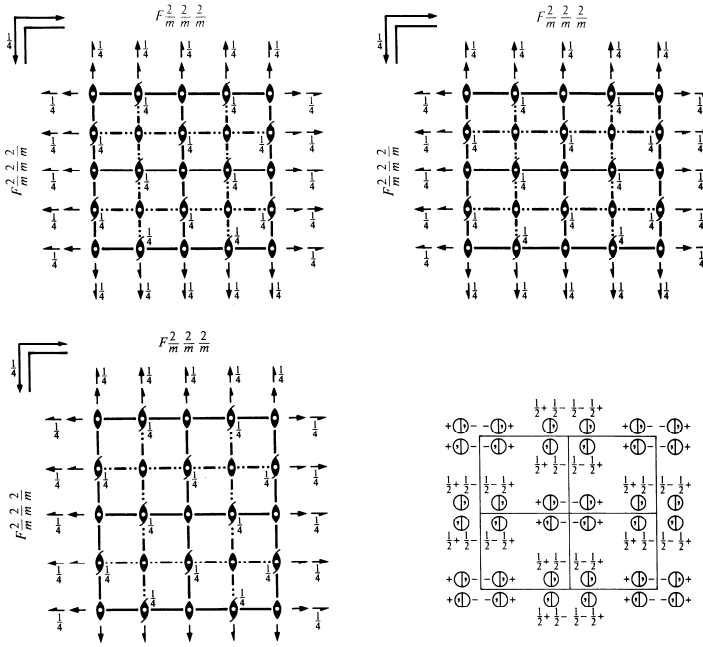

Origin at centre (mmm)

Asymmetric unit $0 \le x \le \frac{1}{4};\quad 0 \le y \le \frac{1}{4};\quad 0 \le z \le \frac{1}{2}$

Symmetry operations

For $(0,0,0)+$ set

(1) 1 (2) 2 $0,0,z$ (3) 2 $0,y,0$ (4) 2 $x,0,0$
(5) $\bar{1}$ $0,0,0$ (6) m $x,y,0$ (7) m $x,0,z$ (8) m $0,y,z$

For $(0,\frac{1}{2},\frac{1}{2})+$ set

(1) $t(0,\frac{1}{2},\frac{1}{2})$ (2) $2(0,0,\frac{1}{2})$ $0,\frac{1}{4},z$ (3) $2(0,\frac{1}{2},0)$ $0,y,\frac{1}{4}$ (4) 2 $x,\frac{1}{4},\frac{1}{4}$
(5) $\bar{1}$ $0,\frac{1}{4},\frac{1}{4}$ (6) b $x,y,\frac{1}{4}$ (7) c $x,\frac{1}{4},z$ (8) $n(0,\frac{1}{2},\frac{1}{2})$ $0,y,z$

For $(\frac{1}{2},0,\frac{1}{2})+$ set

(1) $t(\frac{1}{2},0,\frac{1}{2})$ (2) $2(0,0,\frac{1}{2})$ $\frac{1}{4},0,z$ (3) 2 $\frac{1}{4},y,\frac{1}{4}$ (4) $2(\frac{1}{2},0,0)$ $x,0,\frac{1}{4}$
(5) $\bar{1}$ $\frac{1}{4},0,\frac{1}{4}$ (6) a $x,y,\frac{1}{4}$ (7) $n(\frac{1}{2},0,\frac{1}{2})$ $x,0,z$ (8) c $\frac{1}{4},y,z$

For $(\frac{1}{2},\frac{1}{2},0)+$ set

(1) $t(\frac{1}{2},\frac{1}{2},0)$ (2) 2 $\frac{1}{4},\frac{1}{4},z$ (3) $2(0,\frac{1}{2},0)$ $\frac{1}{4},y,0$ (4) $2(\frac{1}{2},0,0)$ $x,\frac{1}{4},0$
(5) $\bar{1}$ $\frac{1}{4},\frac{1}{4},0$ (6) $n(\frac{1}{2},\frac{1}{2},0)$ $x,y,0$ (7) a $x,\frac{1}{4},z$ (8) b $\frac{1}{4},y,z$

CONTINUED **No. 69** ***F m m m***

Generators selected (1); $t(1,0,0)$; $t(0,1,0)$; $t(0,0,1)$; $t(0,\frac{1}{2},\frac{1}{2})$; $t(\frac{1}{2},0,\frac{1}{2})$; (2); (3); (5)

Positions

Multiplicity, Wyckoff letter, Site symmetry			Coordinates $(0,0,0)+$	$(0,\frac{1}{2},\frac{1}{2})+$	$(\frac{1}{2},0,\frac{1}{2})+$	$(\frac{1}{2},\frac{1}{2},0)+$	Reflection conditions
							General:
32	*p*	1	(1) x,y,z (5) $\bar{x},\bar{y},\bar{z}$	(2) $\bar{x},\bar{y},z$ (6) $x,y,\bar{z}$	(3) $\bar{x},y,\bar{z}$ (7) $x,\bar{y},z$	(4) $x,\bar{y},\bar{z}$ (8) $\bar{x},y,z$	hkl : $h+k,h+l,k+l=2n$ $0kl$: $k,l=2n$ $h0l$: $h,l=2n$ $hk0$: $h,k=2n$ $h00$: $h=2n$ $0k0$: $k=2n$ $00l$: $l=2n$
							Special: as above, plus
16	*o*	. . *m*	$x,y,0$	$x,y,0$	$x,y,0$	$x,y,0$	no extra conditions
16	*n*	. *m* .	$x,0,z$	$\bar{x},0,z$	$\bar{x},0,\bar{z}$	$x,0,\bar{z}$	no extra conditions
16	*m*	*m* . .	$0,y,z$	$0,\bar{y},z$	$0,y,\bar{z}$	$0,\bar{y},\bar{z}$	no extra conditions
16	*l*	2 . .	$x,\frac{1}{4},\frac{1}{4}$	$\bar{x},\frac{3}{4},\frac{1}{4}$	$\bar{x},\frac{3}{4},\frac{3}{4}$	$x,\frac{1}{4},\frac{3}{4}$	hkl : $h=2n$
16	*k*	. 2 .	$\frac{1}{4},y,\frac{1}{4}$	$\frac{3}{4},\bar{y},\frac{1}{4}$	$\frac{3}{4},\bar{y},\frac{3}{4}$	$\frac{1}{4},y,\frac{3}{4}$	hkl : $h=2n$
16	*j*	. . 2	$\frac{1}{4},\frac{1}{4},z$	$\frac{3}{4},\frac{1}{4},\bar{z}$	$\frac{3}{4},\frac{3}{4},\bar{z}$	$\frac{1}{4},\frac{3}{4},z$	hkl : $h=2n$
8	*i*	*m m* 2	$0,0,z$	$0,0,\bar{z}$			no extra conditions
8	*h*	*m* 2 *m*	$0,y,0$	$0,\bar{y},0$			no extra conditions
8	*g*	2 *m m*	$x,0,0$	$\bar{x},0,0$			no extra conditions
8	*f*	2 2 2	$\frac{1}{4},\frac{1}{4},\frac{1}{4}$	$\frac{3}{4},\frac{3}{4},\frac{3}{4}$			hkl : $h=2n$
8	*e*	. . 2/*m*	$\frac{1}{4},\frac{1}{4},0$	$\frac{3}{4},\frac{1}{4},0$			hkl : $h=2n$
8	*d*	. 2/*m* .	$\frac{1}{4},0,\frac{1}{4}$	$\frac{3}{4},0,\frac{1}{4}$			hkl : $h=2n$
8	*c*	2/*m* . .	$0,\frac{1}{4},\frac{1}{4}$	$0,\frac{3}{4},\frac{1}{4}$			hkl : $h=2n$
4	*b*	*m m m*	$0,0,\frac{1}{2}$				no extra conditions
4	*a*	*m m m*	$0,0,0$				no extra conditions

Symmetry of special projections

Along [001] $p2mm$
$\mathbf{a}' = \frac{1}{2}\mathbf{a}$ $\mathbf{b}' = \frac{1}{2}\mathbf{b}$
Origin at $0,0,z$

Along [100] $p2mm$
$\mathbf{a}' = \frac{1}{2}\mathbf{b}$ $\mathbf{b}' = \frac{1}{2}\mathbf{c}$
Origin at $x,0,0$

Along [010] $p2mm$
$\mathbf{a}' = \frac{1}{2}\mathbf{c}$ $\mathbf{b}' = \frac{1}{2}\mathbf{a}$
Origin at $0,y,0$

International Tables for Crystallography (2006). Vol. A, Space group 64, pp. 302–303.

$Cmce$ D_{2h}^{18} mmm Orthorhombic

No. 64 $C\ 2/m\ 2/c\ 2_1/e$ Patterson symmetry $Cmmm$

Former space-group symbol $Cmca$; *cf.* Chapter 1.3

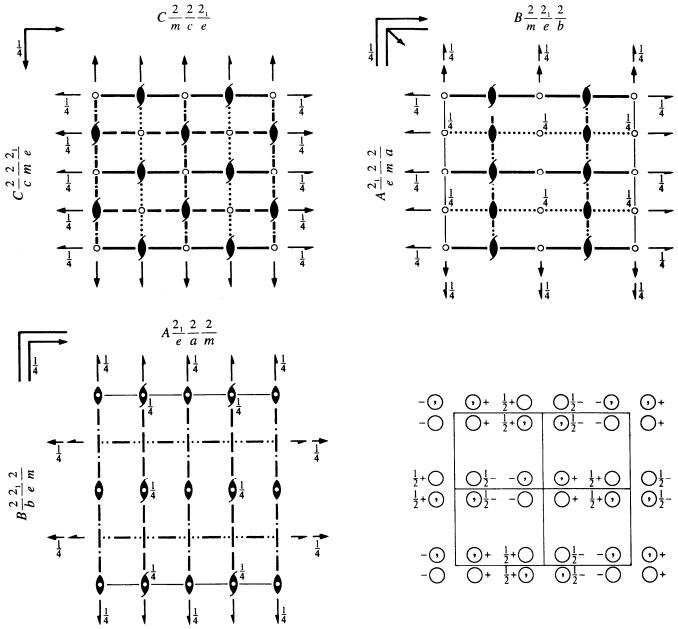

Origin at centre $(2/m)$ at $2/mn1$

Asymmetric unit $0 \le x \le \frac{1}{4}$; $0 \le y \le \frac{1}{2}$; $0 \le z \le \frac{1}{2}$

Symmetry operations

For $(0,0,0)+$ set

(1) 1 (2) $2(0,0,\frac{1}{2})$ $0,\frac{1}{4},z$ (3) $2(0,\frac{1}{2},0)$ $0,y,\frac{1}{4}$ (4) 2 $x,0,0$
(5) $\bar{1}$ $0,0,0$ (6) b $x,y,\frac{1}{4}$ (7) c $x,\frac{1}{4},z$ (8) m $0,y,z$

For $(\frac{1}{2},\frac{1}{2},0)+$ set

(1) $t(\frac{1}{2},\frac{1}{2},0)$ (2) $2(0,0,\frac{1}{2})$ $\frac{1}{4},0,z$ (3) 2 $\frac{1}{4},y,\frac{1}{4}$ (4) $2(\frac{1}{2},0,0)$ $x,\frac{1}{4},0$
(5) $\bar{1}$ $\frac{1}{4},\frac{1}{4},0$ (6) a $x,y,\frac{1}{4}$ (7) $n(\frac{1}{2},0,\frac{1}{2})$ $x,0,z$ (8) b $\frac{1}{4},y,z$

CONTINUED **No. 64** *Cmce*

Generators selected (1); $t(1,0,0)$; $t(0,1,0)$; $t(0,0,1)$; $t(\frac{1}{2},\frac{1}{2},0)$; (2); (3); (5)

Positions

Multiplicity, Wyckoff letter, Site symmetry			Coordinates $(0,0,0)+$ $(\frac{1}{2},\frac{1}{2},0)+$				Reflection conditions
							General:
16	*g*	1	(1) x,y,z (5) $\bar{x},\bar{y},\bar{z}$	(2) $\bar{x},\bar{y}+\frac{1}{2},z+\frac{1}{2}$ (6) $x,y+\frac{1}{2},\bar{z}+\frac{1}{2}$	(3) $\bar{x},y+\frac{1}{2},\bar{z}+\frac{1}{2}$ (7) $x,\bar{y}+\frac{1}{2},z+\frac{1}{2}$	(4) $x,\bar{y},\bar{z}$ (8) $\bar{x},y,z$	hkl : $h+k=2n$ $0kl$: $k=2n$ $h0l$: $h,l=2n$ $hk0$: $h,k=2n$ $h00$: $h=2n$ $0k0$: $k=2n$ $00l$: $l=2n$
							Special: as above, plus
8	*f*	*m* . .	$0,y,z$	$0,\bar{y}+\frac{1}{2},z+\frac{1}{2}$	$0,y+\frac{1}{2},\bar{z}+\frac{1}{2}$	$0,\bar{y},\bar{z}$	no extra conditions
8	*e*	. 2 .	$\frac{1}{4},y,\frac{1}{4}$	$\frac{3}{4},\bar{y}+\frac{1}{2},\frac{3}{4}$	$\frac{3}{4},\bar{y},\frac{3}{4}$	$\frac{1}{4},y+\frac{1}{2},\frac{1}{4}$	hkl : $h=2n$
8	*d*	2 . .	$x,0,0$	$\bar{x},\frac{1}{2},\frac{1}{2}$	$\bar{x},0,0$	$x,\frac{1}{2},\frac{1}{2}$	hkl : $k+l=2n$
8	*c*	$\bar{1}$	$\frac{1}{4},\frac{1}{4},0$	$\frac{3}{4},\frac{1}{4},\frac{1}{2}$	$\frac{3}{4},\frac{3}{4},\frac{1}{2}$	$\frac{1}{4},\frac{3}{4},0$	hkl : $k,l=2n$
4	*b*	$2/m$ . .	$\frac{1}{2},0,0$	$\frac{1}{2},\frac{1}{2},\frac{1}{2}$			hkl : $k+l=2n$
4	*a*	$2/m$ . .	$0,0,0$	$0,\frac{1}{2},\frac{1}{2}$			hkl : $k+l=2n$

Symmetry of special projections

Along [001] $p2mm$
$\mathbf{a}' = \frac{1}{2}\mathbf{a}$ $\mathbf{b}' = \frac{1}{2}\mathbf{b}$
Origin at $0,0,z$

Along [100] $p2gm$
$\mathbf{a}' = \frac{1}{2}\mathbf{b}$ $\mathbf{b}' = \mathbf{c}$
Origin at $x,0,0$

Along [010] $p2mm$
$\mathbf{a}' = \frac{1}{2}\mathbf{c}$ $\mathbf{b}' = \frac{1}{2}\mathbf{a}$
Origin at $0,y,0$

Maximal non-isomorphic subgroups

I	[2] $C2ce$ ($Aea2$, 41)	(1; 4; 6; 7)+
	[2] $Cm2e$ ($Aem2$, 39)	(1; 3; 6; 8)+
	[2] $Cmc2_1$ (36)	(1; 2; 7; 8)+
	[2] $C222_1$ (20)	(1; 2; 3; 4)+
	[2] $C12/c1$ ($C2/c$, 15)	(1; 3; 5; 7)+
	[2] $C112_1/e$ ($P2_1/c$, 14)	(1; 2; 5; 6)+
	[2] $C2/m11$ ($C2/m$, 12)	(1; 4; 5; 8)+
IIa	[2] $Pmnb$ ($Pnma$, 62)	1; 3; 6; 8; (2; 4; 5; 7) + $(\frac{1}{2},\frac{1}{2},0)$
	[2] $Pbca$ (61)	1; 3; 5; 7; (2; 4; 6; 8) + $(\frac{1}{2},\frac{1}{2},0)$
	[2] $Pbna$ ($Pbcn$, 60)	1; 2; 3; 4; (5; 6; 7; 8) + $(\frac{1}{2},\frac{1}{2},0)$
	[2] $Pmca$ ($Pbcm$, 57)	1; 2; 7; 8; (3; 4; 5; 6) + $(\frac{1}{2},\frac{1}{2},0)$
	[2] $Pbnb$ ($Pccn$, 56)	1; 2; 5; 6; (3; 4; 7; 8) + $(\frac{1}{2},\frac{1}{2},0)$
	[2] $Pmcb$ ($Pbam$, 55)	1; 2; 3; 4; 5; 6; 7; 8
	[2] $Pbcb$ ($Pcca$, 54)	1; 4; 6; 7; (2; 3; 5; 8) + $(\frac{1}{2},\frac{1}{2},0)$
	[2] $Pmna$ (53)	1; 4; 5; 8; (2; 3; 6; 7) + $(\frac{1}{2},\frac{1}{2},0)$
IIb	none	

Maximal isomorphic subgroups of lowest index

IIc [3] $Cmce$ ($\mathbf{a}' = 3\mathbf{a}$) (64); [3] $Cmce$ ($\mathbf{b}' = 3\mathbf{b}$) (64); [3] $Cmce$ ($\mathbf{c}' = 3\mathbf{c}$) (64)

Minimal non-isomorphic supergroups

I none

II [2] $Fmmm$ (69); [2] $Pmcm$ ($\mathbf{a}' = \frac{1}{2}\mathbf{a}, \mathbf{b}' = \frac{1}{2}\mathbf{b}$) ($Pmma$, 51); [2] $Cmme$ ($\mathbf{c}' = \frac{1}{2}\mathbf{c}$) (67)

Contact

HEiDi

Phone: 089/289-14828
Web: http://www.mlz-garching.de/heidi

Martin Meven
Institut für Kristallographie Aachen, RWTH Aachen
JCNS Outstation at Forschungsneutronenquelle Heinz Maier-Leibnitz (FRM II)
Phone: 089/289-14727
e-Mail: Martin.Meven@frm2.tum.de

SPODI

High-resolution powder diffractometer

Markus Hoelzel, Anatoliy Senyshyn, Volodymyr Baran

Heinz Maier-Leibnitz Zentrum (MLZ)
Technische Universität München

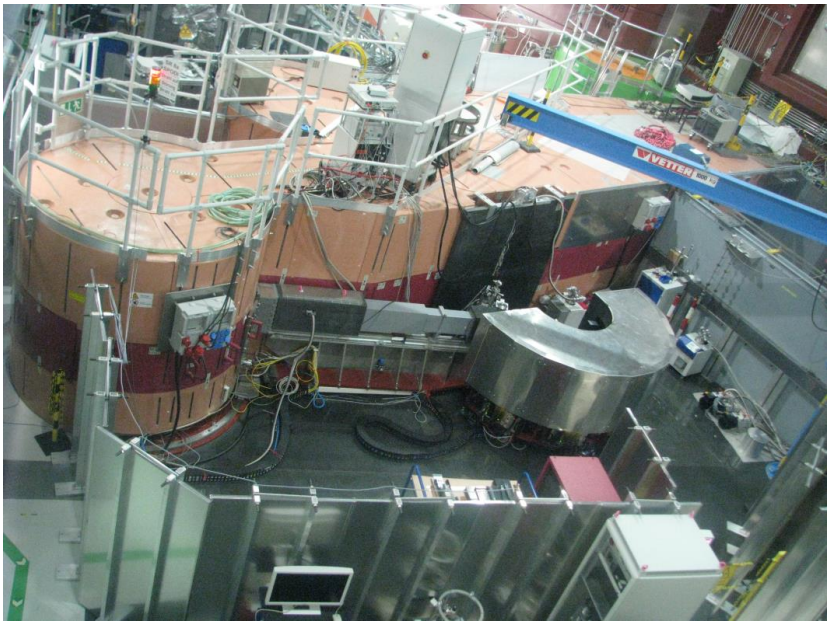

Manual of the JCNS Laboratory Course Neutron Scattering

Content

1. Applications of neutron powder diffraction

Powder diffraction reveals information on the phase composition of a sample and the structural details of the phases. In particular, the positions of the atoms (crystallographic structure) and the ordering of magnetic moments (magnetic structure) can be obtained. In addition to the structural parameters, also some information on the microstructure (crystallite sizes/microstrains) can be obtained. The knowledge of the structure is crucial to understand structure – properties – relationships in any material. Thus, neutron powder diffraction can provide valuable information for the optimisation of modern materials.

Typical applications:

Material	**Task**
lithium-ion battery materials	positions of Li atoms, structural changes/phase transitions at the electrodes during operation, diffusion pathways of Li atoms
piezoelectric ceramics	structural changes during poling in electric field, positions of O atoms
hydrogen storage materials	positions of H atoms, phase transformations during hydrogen absorption/desorption
ionic conductors for fuel cells	positions of O/N atoms, thermal displacement parameters of the atoms and disorder at different temperatures, diffusion pathways of O/N atoms
shape memory alloys	stress-induced phase transformations, stress-induced texture development
materials with collosal magneto resistance effect	magnetic moment per atom at different temperatures
catalysers	structural changes during the uptake of sorbents
nickel superalloys	phase transformations at high temperatures, lattice mismatch between matrix and embedded particles as function of temperature
magnetic shape memory alloys	magneto-elastic effects, magnetic moment per atom at different temperatures and magnetic fields

2. Basics of powder diffraction

Diffraction can be regarded as detection of interference phenomena resulting from coherent elastic scattering of neutron waves from crystalline matter. Crystals can be imagined by a three-dimensional periodic arrangement of unit cells. The unit cell is characterised by the lattice parameters (dimensions and angles) and the positions of atoms or molecules inside the unit cell.
For diffraction experiments the probe should have a wavelength comparable to interatomic distances: this is possible for X-rays, electrons or neutrons.

Structure factor

The structure factor describes the intensity of Bragg reflections with Miller indexes (*hkl*), based on the particular arrangement of all atoms *j* in the unit cell

$$F_{hkl} = \sum_{j=1}^{n} b_j T_j \exp\left\{2\pi i \vec{H}\vec{R}_j\right\}$$

where
F_{hkl}: structure factor of Bragg reflection with Miller indexes *hkl*.
n: number of atoms in unit cell
b_j: scattering lengths (in case of neutron scattering) or atomic form factor (in case of X-ray diffraction) of atom *j*
T_j: Debye Waller factor of atom *j*

The scalar product $\vec{H}\vec{R}_j$ consists of the reciprocal lattice vector $\vec{H}$ and the vector $\vec{R}_j$, revealing the fractional atomic coordinates of atom j in the unit cell.

$$\vec{H}\vec{R}_j = \begin{pmatrix} h \\ k \\ l \end{pmatrix} \cdot \begin{pmatrix} x_j \\ y_j \\ z_j \end{pmatrix} = hx_j + ky_j + lz_j$$

Thus, the structure factor can also be given as follows:

$$F_{hkl} = \sum_{j=1}^{n} b_j T_j \exp 2\pi i\left\{hx_j + ky_j + lz_j\right\}$$

The intensity of a Bragg reflection is proportional to the square of the absolute value of the structure factor: $I \propto \left|F_{hkl}\right|^2$

Debye-Waller Factor

The Debye-Waller Factor describes the decrease in the intensity of Bragg reflections due to atomic thermal vibrations.

$$T_j(Q) = \exp\left\{-\frac{1}{2}\left\langle\left(\vec{Q}\vec{u}_j\right)\right\rangle\right\}$$

vector $\boldsymbol{u_j}$ reflects the thermal displacements of atom j

Braggs' Law

Braggs' Law provides a relation between distances of lattice planes with Miller indexes *hkl,* i.e. d_{hkl}, and the scattering angle 2θ of the corresponding Bragg peak. Braggs' law can be illustrated in a simplified picture of diffraction as reflection of neutron waves at lattice planes (Fig. 1). The waves which are reflected from different lattice planes interfere, If the path difference between the reflected waves corresponds to an integer multiple of the wavelength, constructive interference occurs.
The condition for constructive interference (= Braggs' law) is given by:

$$2d_{hkl}\sin\theta = n\lambda$$

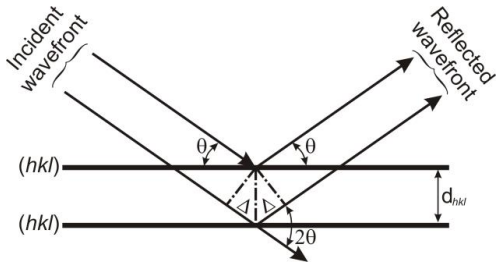

Figure 1: Illustration of Bragg's law: constructive interference of neutron waves, reflected from lattice planes, where θ, 2θ are Bragg angles, $2\Delta=2d_{hkl}sin\theta$ is the path difference and $2\Delta=n\lambda$ is the constructive interference.

The result of constructive interferences can be observed as so called Bragg reflections at a neutron detector. Applying Bragg's law one can derive the lattice spacings ("d-values") from the scattering angle positions of the Bragg peaks in a constant-wavelength diffraction experiment. With the help of d-values a qualitative phase analysis can be carried out.

Ewald's sphere

The Ewald's sphere provides a description of diffraction with help of the reciprocal lattice. At first, we introduce the scattering vector ***Q*** and the scattering triangle (Figure 2). The incident neutron wave is described by a propagation vector $\boldsymbol{k_i}$, the scattered wave is given by $\boldsymbol{k_f}$. In the case of elastic scattering (no energy transfer) both vectors $\boldsymbol{k_i}$ and $\boldsymbol{k_f}$ have the same length which is reciprocal to the wavelength.

$$\left|\vec{k}_i\right| = \left|\vec{k}_f\right| = \frac{2\pi}{\lambda}$$

remark:

The length of the wave vectors are sometimes given as $\left|k_i\right| = \left|k_f\right| = \frac{1}{\lambda}$ *(This definition is found esp. in crystallographic literature, while the other one is more common in physics textbooks).*

The angle between vectors $\boldsymbol{k_i}$ and $\boldsymbol{k_f}$ is the scattering angle 2θ. The scattering vector ***Q*** is the given by the difference between $\boldsymbol{k_i}$ and $\boldsymbol{k_f}$:

$$\boldsymbol{Q} = \boldsymbol{k_f} - \boldsymbol{k_i} \quad |Q| = 4\pi \frac{\sin\theta}{\lambda}$$

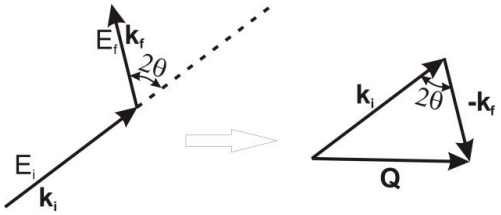

Figure 2: Illustration of scattering vector and scattering angle resulting from incident and scattered waves.

In the visualisation of the diffraction phenomena by Ewald the scattering triangle is implemented into the reciprocal lattice of the sample crystal – at first, we consider diffraction at a single crystal (Figure 3). Note that the end of the incident wave vector coincides with the origin of the reciprocal lattice. Ewald revealed the following condition for diffraction: we have diffraction in the direction of $\boldsymbol{k_f}$, if its end point (equivalently: the end point of scattering vector ***Q***) lies at a reciprocal lattice point *hkl*. All possible $\boldsymbol{k_f}$, which fulfil this condition, describe a sphere with radius 2π/λ, the so called Ewald's sphere. Thus we obtain a *hkl* reflection if the reciprocal lattice point *hkl* is on the surface of the Ewald's sphere.

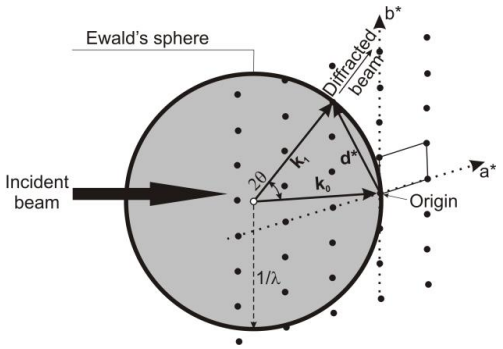

Figure 3: Illustration of diffraction using the Ewald's sphere (in crystallographic notation).

In figure 3 the radius of Ewald's sphere is given by 1/λ (For $|k_i| = \frac{2\pi}{\lambda}$ we obtain a radius of $2\pi/\lambda$).

We receive the following condition for diffraction: the scattering vector $\boldsymbol{Q}$ should coincide with a reciprocal lattice vector $\boldsymbol{H_{hkl}}$ (* 2π):

$$\vec{Q} = 2\pi\vec{H}_{hkl};\ \vec{H}_{hkl} = h\vec{a}^{\,x} + k\vec{b}^{\,x} + l\vec{c}^{\,x};\ \left|\vec{H}_{hkl}\right| = d^{x}_{hkl} = \frac{1}{d_{hkl}}$$

From this diffraction condition based on the reciprocal lattice we can derive Bragg's law:

$$\left|\vec{Q}\right| = 2\pi\left|\vec{H}_{hkl}\right| \rightarrow 4\pi\frac{\sin\theta}{\lambda} = \frac{2\pi}{d_{hkl}} \rightarrow 2d_{hkl}\sin\theta = \lambda$$

The Ewald's sphere is an important tool to visualize the method of single crystal diffraction: At a random orientation of a single crystalline sample a few reciprocal lattice points might match the surface of Ewald's sphere, thus fulfil the condition for diffraction. If we rotate the crystal, we rotate the reciprocal lattice with respect to the Ewald's sphere. Thus by a stepwise rotation of the crystal we receive corresponding reflections.

Powder Diffraction in Debye-Scherrer Geometry

For a powder sample one can assume a random orientation of all crystallites. Correspondingly, there is a random orientation of the reciprocal lattices of the crystallites as well. The reciprocal lattice vectors for the same *hkl*, i.e. $\boldsymbol{H_{hkl}}$, describe a sphere around the origin of the reciprocal lattice. In the picture of Ewald's sphere we observe diffraction, if the surface of the Ewald's sphere intersects with the spheres of $\boldsymbol{H_{hkl}}$ vectors. For a sufficient number of crystallites in the sample and a random distribution of grain orientations, the scattered wave vectors $\boldsymbol{k_f}$ describe a cone with opening angle 2θ with respect to the inident beam $\boldsymbol{k_i}$.
In the so called Debye-Scherrer geometry a monochromatic beam is scattered at a cylindrical sample (Fig. 4). The scattered neutrons (or X-rays) are collected at a cylindrical detector in the scattering plane. The intersection between cones (scattered neutrons) and a cylinder (detector area) results in segments of rings (= Debye-Scherrer rings) on the detector (Fig 5). By integration of the data along the Debye-Scherrer rings one derives the conventional constant-wavelength powder diffraction pa
angle 2θ.

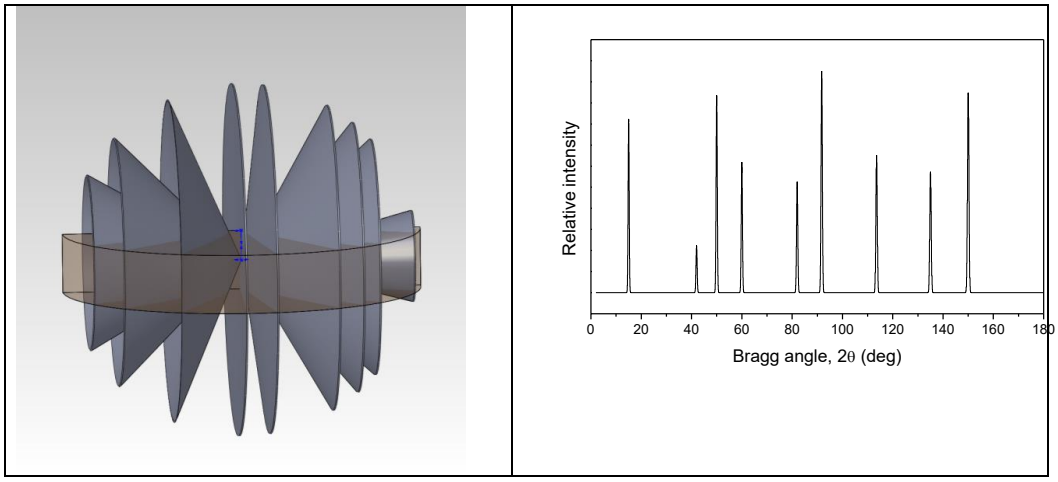

Figure 4: Illustration of powder diffraction using Debye-Scherrer geometry. On the left: cones of neutrons scattered from a polycrystalline sample are detected in the scattering plane. On the right: resulting powder diffraction pattern (after data integration along the Debye-Scherrer rings).

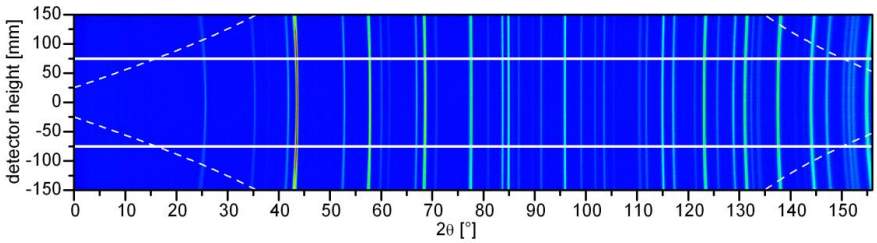

Figure 5: Two dimensional diffraction data (detector height vs. scattering angle 2θ), collected at high-resolution powder diffractometer SPODI, illustrating the Debye-Scherrer rings of a corundum sample.

Relations between Bragg positions and lattice parameters

With the help of Braggs law one can derive the lattice spacings “d-values” directly from the positions of the Bragg reflections. The d-values are related with the lattice parameters of the unit cell (the cell dimensions *a,b,c* and the cell angles α,β,γ) and the Miller indexes (*hkl*) of the corresponding reflections. In the following, the relations are provided for the different crystal systems.

cubic $$\frac{1}{d_{hkl}^2} = \frac{h^2+k^2+l^2}{a^2}$$

hexagonal $$\frac{1}{d_{hkl}^2} = \frac{4}{3}\frac{h^2+hk+k^2}{a^2} + \frac{l^2}{c^2}$$

tetragonal $$\frac{1}{d_{hkl}^2} = \frac{h^2+k^2}{a^2} + \frac{l^2}{c^2}$$

orthorhombic $$\frac{1}{d_{hkl}^2} = \frac{h^2}{a^2} + \frac{k^2}{b^2} + \frac{l^2}{c^2}$$

monoclinic $$\frac{1}{d_{hkl}^2} = \frac{h^2}{a^2\sin^2\beta} + \frac{k^2}{b^2} + \frac{l^2}{c^2\sin^2\beta} + \frac{2hl\cos\beta}{ac\sin^2\beta}$$

3. Information from powder diffraction experiments

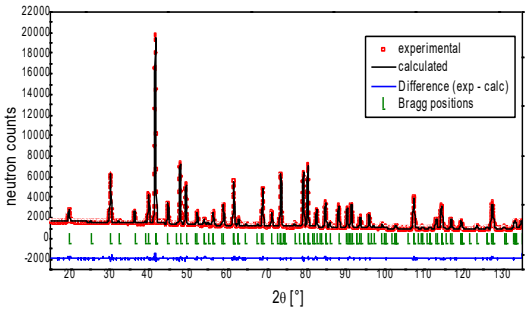

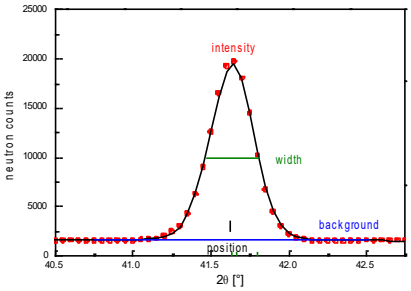

F n.
p

I w
p

Positions (scattering angles) of Bragg reflections

- phase identification (from d-values)
- lattice parameters of the phases
- symmetry information (space group) by lattice parameters and selection rules (systematic extinction of reflections)

Intensity of Bragg reflections

- crystallographic structure
  - positions of atoms (fractional atomic coordinates)
  - occupancies of atoms on their sites
  - thermal displacement parameters
- magnetic structure
  - magnetic lattice (propagation vector)
  - magnetic symmetry (space group)
  - magnetic moment per atom
- quantitative phase analysis
- preferred orientation effects

Profiles of reflections

The reflection profiles result in a convolution of the instrumental resolution function with possible broadening effects of the sample

- microstructural information from peak broadening
  - microstrains
  - crystallite sizes

Modulation/Profile of Background

- short range order
- disorder
- amorphous contents

4. Evaluation of powder diffraction data

Powder diffraction data are used for qualitative or quantitative phase analysis, investigations of phase transformations, refinement of structural parameters or a structural solution.

Qualitative phase analysis is based on the determination of d-values and relative intensities (in particular intensities of strong reflections have to be considered). The phase identification requires crystallographic data bases (e.g. ICDD, ISCD, COD) and is supported by literature data and information from other methods (e.g. NMR, analysis of the chemical composition). Such kind of phase analysis is however typically carried out with laboratory X-ray diffraction.

The majority of neutron powder diffraction studies is carried out to observe structural changes – in particular structural phase transformations – as a function of temperature or other external parameters as pressure, magnetic field, electric field…In this respect, neutron diffraction allows to investigate technical materials under conditions close to their application. For instance, lithium ion batteries can be investigated during charging/discharging or piezoelectric materials during electric poling. Reaction pathways in chemical reactions can be observed at distinct gas atmospheres and temperatures.

Typically, powder diffraction data are analysed by the full-profile decomposition, the so called Rietveld method, for a refinement of structural parameters as lattice parameters, fractional atomic coordinates, atomic occupancies and atomic displacement parameters. In the Rietveld method, the full diffraction pattern is calculated based on a structure model, taking into account the above mentioned structural parameters, as well as reflection profile parameters, instrumental parameters and background parameters. Using least-squares method, a stepwise refinement of the model parameters is carried out to describe (“to fit”) the experimental data.

Powder diffractometers are often classified as “high-resolution” or “high-intensity” diffractometers. High-resolution powder diffractometers are designed for structure refinements on complex systems. High-intensity diffractometers allow fast kinetic measurements to investigate phase transitions at a short time scale or chemical reactions.

Besides structure refinement, also structure solution can be done based on powder diffraction. A structure solution reveals the determination of a formerly unknown structure of a compound, including the correct space group. This includes following steps:

- finding cell dimensions
- finding genuine symmetry
- localisation of atoms
- determination of site occupancies
- determination of thermal displacement parameters

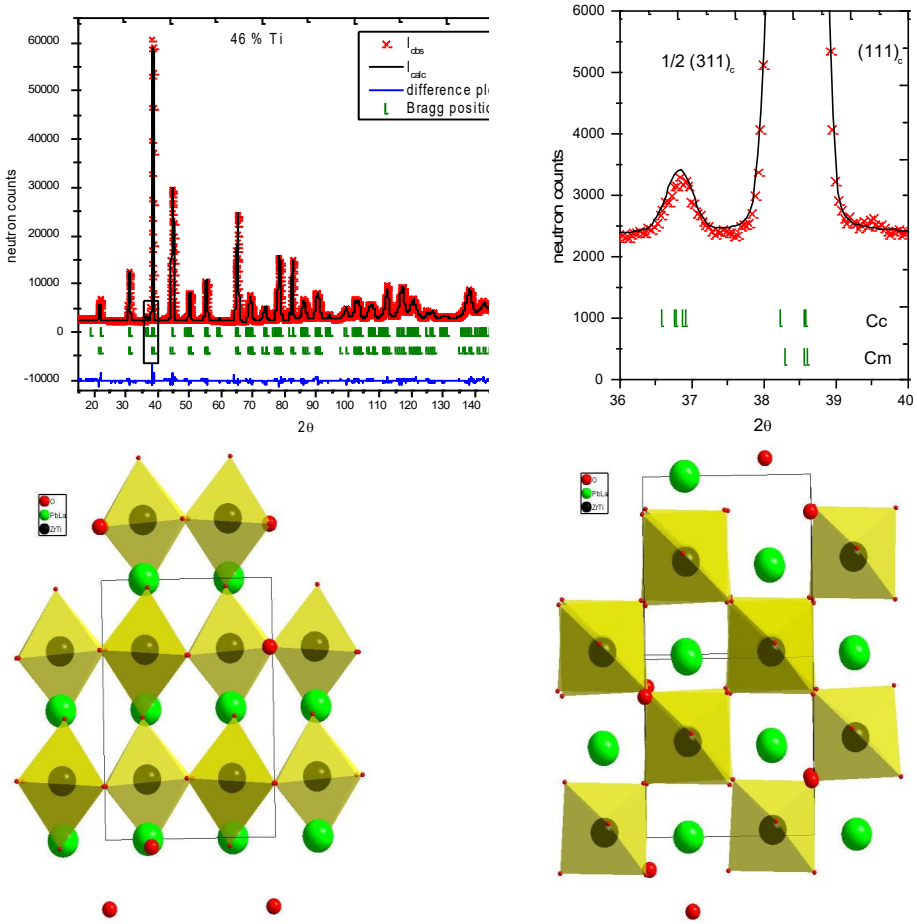

Figure 7: a) Data treatment of a measurement on the ferroelectric $Pb_{0.99}La_{0.01}Zr_{0.54}Ti_{0.46}O_3$, carried out at 5 K at diffractometer SPODI (FRM II): Diffraction pattern including experimental data, calculated data by Rietveld fit, Bragg reflection positions of the phases (space groups C_C *and* C_m) and difference plot (between experimental and calculated data). b) Zoom into the diffraction pattern, hightlighting a superlattice reflection of the C_C phase. c) structure model of the C_C phase, view in the $[001]_c$ direction. d) structure model of the C_C phase, view in the $[010]_c$ direction. In particular, the superstructure in the tiltings of oxygen octahedra can be seen in c) and d).

5. Comparison between neutron and X-ray diffraction

I) X-rays are scattered at electrons, neutrons are scattered at nuclei

In case of X-ray scattering, the scattering power of an atom (described by the atomic form factor *f*) is proportional to the number of electrons (or: charge density).
Neutrons are scattered at nuclei. Thus the interaction (described by the scattering length b) varies between different isotopes of an element. In contract to X-ray diffraction, the scattering power of neighbouring elements in the periodic system can be very different.

implications:

Localisation of light elements next to heavier ones

X-ray diffraction is a powerful tool to determine the positions of heavy atoms, but the localisation of light atoms in the vicinity of much heavier atoms is often difficult or related with high uncertainties. Neutron diffraction is advantageous to localise light atoms such as H, D, Li, C, N, O in the neighbourhood of heavy atoms.

Localisation of neighbouring elements in the periodic table

Neighbouring elements in the periodic table can hardly be distinguished by means of X-ray diffraction. Neutrons are advantageous for such cases: examples: Mn – Fe - Co – Ni or O – N.

Q-dependence of intensities

Since the size of electron clouds is comparable to the wavelength, the atomic form factor depends on $\sin\theta/\lambda$ or Q. Therefore the intensities of X-ray reflections decrease significantly for increasing Q (increasing scattering angles 2θ).
As the range of the neutron–nuclei–interaction is by orders of magnitude smaller than the wavelengths of thermal neutrons, scattering lengths do not depend on Q. As a consequence, neutron diffraction patterns do not show a decrease of Bragg reflection intensities for higher scattering angles, enabling the analysis of larger Q-ranges. In particular, neutron diffraction is advantageous for the analysis of thermal displacement parameters.

II) neutrons interact weakly with matter

implications:

sample volume

The flux (number of particles per time and space unit) from neutron sources is much lower compared to X-ray tubes or even synchrotrons. In addition, neutrons interact weakly with matter. Therefore, much larger sample amounts are required compared to X-ray diffraction ("grams instead of milligrams"). On the other hand this weak interaction results in much higher penetration depths of neutrons, compared to laboratory X-ray diffractometers. Thus, polycrystalline bulk samples can be investigated. Furthermore, the usage of large sample volumes avoid possible problems due to preferred orientation effects. In this respects, neutron diffraction is typically advantageous for coarse grained materials.

Sample environments

The large penetration depths of neutrons facilitates the usage of sample environments like cryostat, furnaces, magnets,... In general neutron scattering experiments are more versatile applying very high or low temperatures compared to X-ray instruments. On the other hand, synchrotron studies are advantageous for small samples amounts. Therefore high pressure studies are more challenging for neutron than X-ray diffraction.

III) neutrons exhibit a magnetic moment

Neutrons do not have an electric charge. However, they consist of three quarks causing an internal charge distribution. In combination with their spin this results in a magnetic moment of the neutron.

implications:

magnetic scattering

The dipole-dipole interaction between the magnetic moment of the neutron and a magnetic moment of an atom results in a magnetic scattering contribution. The magnetic scattering power is incidentally in the same order of magnitude as the nuclear scattering contribution. Magnetic scattering contribution can be easily detected by means of neutron diffraction. In synchrotron diffraction studies, possible magnetic scattering events are weaker by several orders of magnitude than the Thomson scattering.

6. Setup of the high-resolution neutron powder diffractometer SPODI at FRM II

The main components of a constant-wavelength neutron powder diffractometer are: source, monochromator, sample and detector (Fig. 8). Between these components collimation systems are installed which determine the instrumental resolution function and the neutron flux.

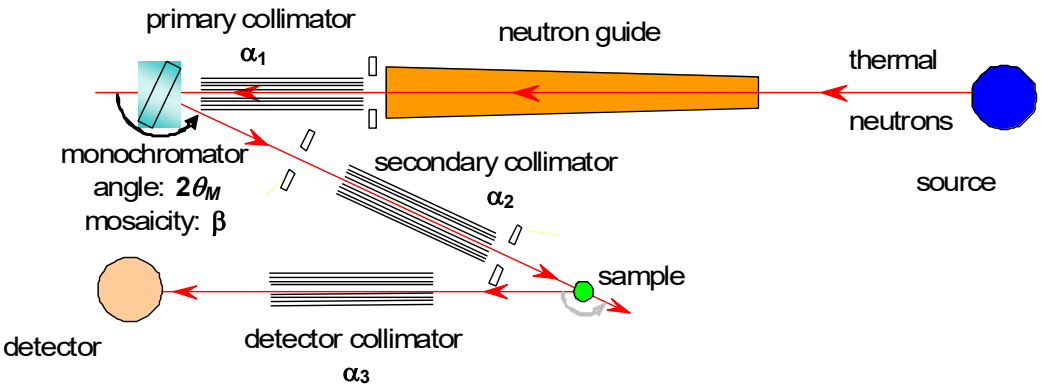

Figure 8: Illustration of a typical instrumental layout, introducing the parameters used by Caglioti to describe the instrumental resolution function.

Instrumental resolution function

The instrumental resolution function of a constant wavelength diffractometer can be expressed by a relation between the full-width at half maximum (FWHM) of the reflections as a function of the scattering angle 2θ. As shown by Calgioti, the instrumental resolution function (of a constant-wavelength powder diffractometer) can be approximated by:

$$FWHM = \sqrt{U \tan^2\theta + V \tan\theta + W}$$

with the Caglioti parameters:

$$U = \frac{4\left(\alpha_1^2\alpha_2^2 + \alpha_1^2\beta^2 + \alpha_2^2\beta^2\right)}{\tan^2\theta_m\left(\alpha_1^2 + \alpha_2^2 + 4\beta^2\right)}$$

$$V = \frac{-4\alpha_2^2\left(\alpha_1^2 + 2\beta^2\right)}{\tan\theta_m\left(\alpha_1^2 + \alpha_2^2 + 4\beta^2\right)}$$

$$W = \frac{\alpha_1^2\alpha_2^2 + \alpha_1^2\alpha_3^2 + \alpha_2^2\alpha_3^2 + 4\beta^2\left(\alpha_2^2 + \alpha_3^2\right)}{\left(\alpha_1^2 + \alpha_2^2 + 4\beta^2\right)}$$

In this approach it is assumed that all components have Gaussian transmission profiles. The resolution function is determined by the horizontal beam divergences α_1, α_2, α_3, the monochromator angle $2\theta_m$ and the mosaicity of the monochromator β (Figure 8). The Caglioti equations help to design an instrument to achieve a designated performance. However, it should be emphasised that in the approximations of Caglioti only the horizontal beam divergences are taken into account, neglecting vertical beam divergences caused by a vertical focusing monochromator or a vertical divergent neutron guide. Those effects are taken into account by ray-tracing methods (Monte-Carlo simulations), which allow a detailed modelling of the individual components.
The powder diffractometer SPODI has been designed to achieve both high resolution and good profile shape. In its standard configuration (highest resolution mode) SPODI uses a unique very high monochromator take-off angle of 155° along with a large monochromator-to-sample distance of 5 meters. An evacuated beam tube of about 4 m in length is located between the monochromator and the sample which also controls both vertical and horizontal neutron beam divergences at the sample position. Thus the natural neutron beam divergence in horizontal plane is 25' only.

Monochromator

At constant-wavelength diffractometers, the monochromatisation is perfomed using crystals followings Bragg's equation:

$2d_{hkl}\sin\theta = \lambda$, where the effective transmission band is determined by a derivative

$$\frac{\Delta\lambda}{\lambda} = \Delta\theta_M \cot\theta_M$$

The width of the wavelength band $\Delta\lambda/\lambda$ strongly depends on the monochromator angle $2\theta_m$ and the mosaicity of the monochromator β, i.e $\Delta\theta_m$. Thus these parameters have a major impact on the instrumental resolution function and the flux on the sample.
Typically, the monochromator crystals are installed at a vertical focusing unit of 200 – 300 mm, allowing optimization of the intensity distribution at the sample position with respect to the monochromator – sample distance or the sample height. On the other hand, the vertical beam divergence results in a smearing of the Debye-Scherrer rings along the detector height (this effect depends also on the sample height). At the high-resolution powder diffractometer SPODI, 15 Germanium wafer-stack crystals with a (551)-orientation are used. Different wavelengths between 1.0 Å and 2.6 Å can easily be selected by a rotation of the monochromator unit (without changing the monochromator take-off angle $2\theta_m$), i.e. by selecting different (*hkl)* reflection planes. In general, large wavelengths are advantageous to

investigate structures exhibiting large cell dimensions (or interatomic spacings). This is the case for large unit cells, but in particular for magnetic ordering. With decreasing wavelengths, larger Q-values can be achieved. Thus, with lower wavelengths, more reflections can be observed in the same scattering angle range. Low wavelengths are in particular advantageous for the analysis of thermal displacement parameters or static disorder phenomena.

Detector array

At constant-wavelength diffractometers the data are collected in an angle-dispersive manner at equidistant 2θ points. Detector systems based on ^{3}He have been most commonly used due to their very high efficiency. Nowadays, the world wide shortage of ^{3}He demands and promotes the development of alternatives, in particular scintillator based systems.
Classical high-resolution powder diffractometers, such as D2B (ILL), SPODI (FRM II), BT1 (NIST), ECHIDNA (ANSTO) use multidetector/multicollimator systems. The data are collected by ^{3}He tubes while the beam divergence is limited by Soller collimators. Such systems enable high Q-resolution over a broad scattering angle regime, while the resolution does not depend on the sample diameter. On the other hand, a multidetector concept requires a data collection by stepwise positioning of the detector array to collect the full diffraction pattern. Therefore, kinetic measurements are not feasible due to the fact that the sample must not change during the collection of a pattern.
The detector array of SPODI consists of 80 ^{3}He tubes, which are position sensitive in the vertical direction. Thus, two-dimensional raw data are obtained, which allow to rapidly check for sample crystallinity, alignment and possible preferred orientation effects. The conventional diffraction patterns (intensity vs. scattering angle 2θ) are derived from the two-dimensional raw data by integration along the Debye-Scherrer rings.

7. Experiment: Phase- and structure analysis of lead titanate at various temperatures

samples

Lead zirconate titanates $PbZr_{1-x}Ti_xO_3$ („PZT“) exhibit piezo-, pyro- and ferroelectric properties. Piezoelectricity describes the generation of an electric polarisation as a consequence of a mechanical deformation – or the other way round the development of a macroscopic strain by an electric field. The crystallographic condition of piezoelectricity is the lack of an inversion center: as the balance points of negative and positive charge do not coincide, the displacements of the ions in the electric field results in an electric polarization. Pyroelectrticity refers to a spontaneous polarization of a material as a function of temperature. Ferroelectrics belong to a special class of pyroelectric materials, in which the polarization can be switched by an electric field, resulting in a ferroelectric hysteresis.

The electromechanical properties of $PbZr_{1-x}Ti_xO_3$ can be understood by their phase transformation behaviour. At high temperatures they exhibit the perovskite crystal structure with simple cubic symmetry (space group Pm-3m). Because of its symmetry (inversion center) this phase is not piezoelectric but paraelectric. During cooling, titanium-rich samples undergo a phase transition to a tetragonal phase (space group P4mm). This phase transformation is accompanied by atomic displacements. In particular, the Ti^{4+}/Zr^{4+} are shifted in the opposite direction than O^{2-} ions, resulting in a dipole moment or a spontaneous polarisation. The material exhibits ferroelectric behaviour, with a polar axis in the direction of the pseudocubic c-axis, i.e. $[001]_c$. Zirconium-rich samples undergo a phase transition towards a rhombohedral phase (space group R3m) during cooling. In this case, the atomic displacements result in a polar axis in direction $[111]_c$ with respect to the parent pseudocubic lattice. Materials $PbZr_{1-x}Ti_xO_3$ with compositions (Zr/Ti ratios) close to the so called morphotropic phase boundary between rhombohedral and tetragonal phase, show the highest piezoelectric response, i.e. the largest macroscopic strain as a function of the applied electric field. These compositions are therefore most interesting for technological applications. The piezoelectric properties can be modified further by adding doping elements to substitute Pb^{2+} or Ti^{4+}/Zr^{4+} ions.

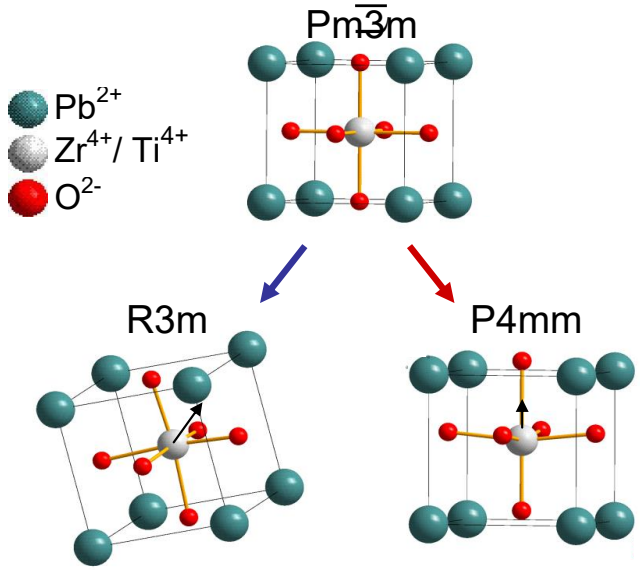

Figure 9: Structure models of the paraelectric cubic phase and the ferroelectric rhombohedral and tetragonal phases.

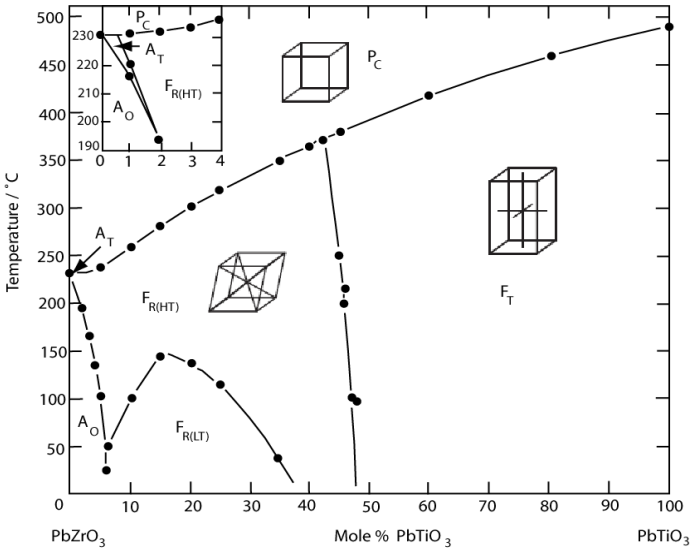

Figure 10: Phase diagram of $PbZr_{1-x}Ti_xO_3$, illustrating regions of phase stability for paraelectric cubic phase P_C, ferroelectric rhomboedral phases $F_{R(HT)}$ (= high temperature) and $F_{R(LT)}$ (= low temperature) and ferroelectric tetragonal phase F_T. From B. Jaffe, W. R. Cook, H. Jaffe, Piezoelectric Ceramics and Related Issues, Academic Press, London, 1971.

$PbZr_{1-x}Ti_xO_3$, find extensive applications

- transformation from mechanical in electric energy: ignition elements, lighters
- transformation from electric in mechanical energy (actuators): fuel injectors, loudspeakers, sonar transducers, active control of vibration, ink printers
- transformation from mechanical force in an electric signal (sensors): strain gauges, microphones
- data storage, information technology: capacitors, F-RAM

Experiment

In the frame of the practical course, the temperature-dependent phase transformation behavior of a $PbZr_{1-x}Ti_xO_3$ sample with tetragonal symmetry should be investigated. Diffraction patterns at different temperature steps between room temperature and 600 °C will be collected using a vacuum high-temperature furnace. The structural changes at different temperatures will be investigated by an analysis of the lattice parameters. Based on the experimental data, the relations between the structural changes and the corresponding physical properties can be discussed.

Following experimental procedures will be carried out

- sample preparation, filling the sample material into a sample can, adjustment of the sample stick, installation of the sample stick into the furnace
- short test measurement to check the sample adjustment and data quality
- programming the experiment to run the data collection at various temperatures and starting the scans
- data reduction: derivation of diffraction patterns from the two-dimensional raw data
- data analysis: analysis of the lattice parameter changes as a function of temperature
- discussing the results with respect to structure – properties relationships

Literature

[1] V. K. Pecharsky, P. Y. Zavalij, Fundamentals of Powder Diffraction and structural Characterisation of Materials (2003).
[2] G. L. Squires, Introduction to the Theory of Thermal Neutron Scattering, Dover Reprints (1978).
[3] C. Kittel, Einführung in die Festkörperphysik, 10. Edition, Oldenbourg (1993).
[4] H. Dachs, Neutron Diffraction, Springer Verlag (1978).
[5] H. Ibach und H. Lüth, Festkörperphysik, Einführung in die Grundlagen, 6. Edition, Springer Verlag (2002).
[6] J.R.D. Copley, The Fundamentals of Neutron Powder Diffraction (2001), http://www.nist.gov/public_affairs/practiceguides/SP960-2.pdf.
[7] A. D. Krawitz, Introduction to Diffraction in Materials Science and Engineering.
[8] W. Kleber, Einführung in die Kristallographie, Oldenbourg (1998).

Contact

Instrument SPODI

Web: https://mlz-garching.de/spodi

Dr. Markus Hoelzel

Forschungsneutronenquelle Heinz Maier-Leibnitz (FRM II)
Technische Universität München
Phone: 089/289-14314
e-Mail: markus.hoelzel@frm2.tum.de

Dr. Anatoliy Senyshyn

Forschungsneutronenquelle Heinz Maier-Leibnitz (FRM II)
Technische Universität München

Phone: 089/289-14316
e-Mail: anatoliy.senyshyn@frm2.tum.de

Dr. Volodymyr Baran

Forschungsneutronenquelle Heinz Maier-Leibnitz (FRM II)
Technische Universität München

Phone: 089/289-14373
e-Mail: volodymyr.baran@frm2.tum.de

POLI

Polarized hot neutron single crystal diffractometer

Jianhui Xu

Institute for Crystallography, RWTH Aachen University
Jülich Centre for Neutron Science
Forschungszentrum Jülich

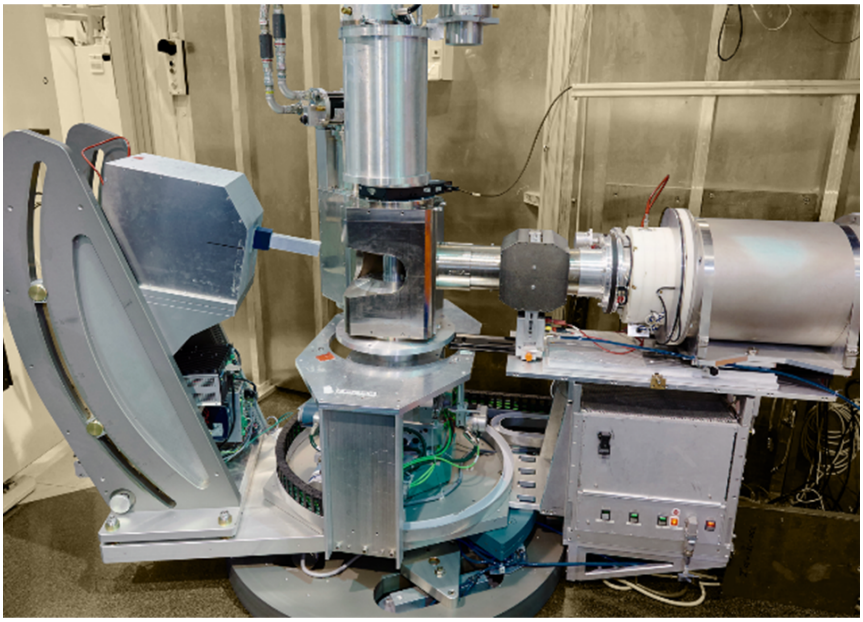

Contents

1 Introduction

In this practice, we will perform a polarized neutron single crystal diffraction experiment using the flipping ratio method. This is a unique method for precisely determining magnetic form factor [1] and magnetic anisotropy [2,3] taking advantage of nuclear-magnetic coherent scattering. The magnetic form factor is a Fourier transformation of the spacial distribution of magnetic electron clouds centred at magnetic ions in a crystal. By performing inverse Fourier transformations, a real space magnetic density can be obtained and then compared with theoretical calculations in quantum mechanics, which provides information on quantum states of magnetic ions in the crystal. For example, Fig. 1 illustrates the measured magnetic density of $Ba_2TGe_2O_7$ (T = Cu, Co and Mn) compounds where the different orbital occupations of the five $3d$ orbitals induce different density shapes for the three compounds [4].

In this experiment, you will first learn the normal devices and setups for performing such an experiment and then learn how to perform the experiment and analyse the collected data. For more details about polarized neutron diffraction techniques, the readers are referred to Refs. [5–7].

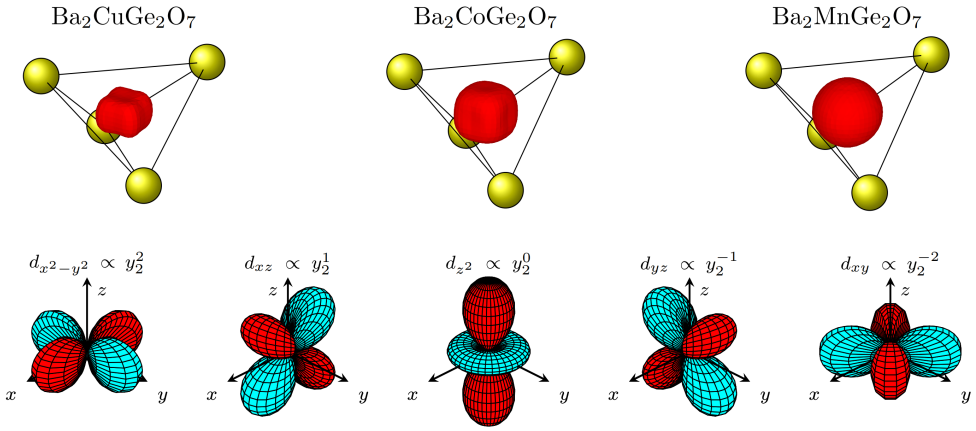

Fig. 1: (upper) Perspective views on the isosurface of the magnetic density of $Ba_2TGe_2O_7$ (T = Cu, Co, and Mn) compounds obtained by fitting the flipping ratio data with multipole models . There nine, seven, and five $3d$ electrons for the divalent Cu^{2+}, Co^{2+} and Mn^{2+} ions, corresponding to 1, 3 and 5 unpaired electrons with difference orbital filling schemes. The yellow balls are oxygen ions around the magnetic ions. (lower) The five $3d$ electron orbitals in cubic crystal electric fields represented by the isosurfaces showing the angular distribution probability for electrons in each orbital. Taken from Ref. [4].

2 Basic theory

The use of polarized neutrons adds an extra dimension to neutron diffraction studies on magnetic materials in comparison with using unpolarized neutrons. One important advantage is the

ability to obtain an unambiguous separation of magnetic and nuclear scattering. Another is the ability to resolve different directional components of magnetic structure factors. In the study of non-collinear magnetic structures, it is sometimes impossible to distinguish between two or more different viable magnetic structures without polarized neutrons. Here we briefly present the basic theory of polarized neutron diffraction related to this experiment.

Neutron carries a spin, an intrinsic angular momentum with a corresponding magnetic moment. The neutron spin has a quantum number 1/2 which allows $+1/2\hbar$ and $-1/2\hbar$ for the angular momentum along a quantization direction. In practical situations, the quantization direction is usually defined by an external magnetic field. A perfectly polarized neutron beam means that all the neutrons of the beam are in one of these two eigenstates, i.e., all "up" or all "down".

The neutrons have spin-dependent interactions with nuclei with nonzero spins and with the unpaired electrons with spin and orbital angular momenta. For example, the interactions between neutrons and unpaired electrons are magnetic dipole-dipole interactions between the magnetic moments of neutrons and electrons. The spin of neutron can be flipped during scattering by the nuclear spin perpendicular to the neutron spin or by the magnetic moment perpendicular to the neutron spin. Therefore, the final beam polarization can be changed by scattering which can be measured in experiments with polarization analyses.

The beam polarization can be changed in both direction and magnitude. The intensity and polarization of the scattered beam are given by the Blume-Maleyev equations [8–11]:

$$I = N^*N + \boldsymbol{M}_\perp^* \cdot \boldsymbol{M}_\perp + 2\boldsymbol{P}_\mathrm{i} \cdot \Re[N^*\boldsymbol{M}_\perp] + i\boldsymbol{P}_\mathrm{i} \cdot (\boldsymbol{M}_\perp^* \times \boldsymbol{M}_\perp), \tag{1}$$

$$\begin{aligned} \boldsymbol{P}_\mathrm{f} I = {} & \boldsymbol{P}_\mathrm{i} N^*N \\ & - \boldsymbol{P}_\mathrm{i}(\boldsymbol{M}_\perp^* \cdot \boldsymbol{M}_\perp) + 2\Re[\boldsymbol{M}_\perp^*(\boldsymbol{P}_\mathrm{i} \cdot \boldsymbol{M}_\perp)] \\ & + 2\Re[N^*\boldsymbol{M}_\perp] + 2\Im[N^*\boldsymbol{M}_\perp] \times \boldsymbol{P}_\mathrm{i} \\ & - i(\boldsymbol{M}_\perp^* \times \boldsymbol{M}_\perp). \end{aligned} \tag{2}$$

In the equations above, I and $\boldsymbol{P}_\mathrm{f}$ are the intensity and polarization of the scattered beam. $\boldsymbol{P}_\mathrm{i}$ is the polarization of the incident beam. N and $M_\perp$are nuclear structure factor and the component of the magnetic structure factor perpendicular to $\boldsymbol{Q}$ originating from magnetic electrons. There are four different types of terms in the equations: nuclear only, magnetic only, nuclear-magnetic interference and magnetic chirality or handedness. The nuclear-magnetic interference appears when the magnetic and nuclear periodicities are the same and the magnetic and nuclear scatterings coherently interfere at the same points in reciprocal space. Magnetic chirality means chirality in spin-ordered states or (atomic-scale or mesoscopic) spin textures. Fig. 2 shows the left-handed and right-handed chiral magnetic structure of $CsCuCl_3$ as an example [12].

There are four different types of neutron diffraction derived from the Blume-Maleyev equations:

- unpolarized diffraction
- half polarized diffraction (flipping ratio method)
- uniaxial polarization analysis
- three-dimensional polarization analysis (spherical neutron polarimetry)

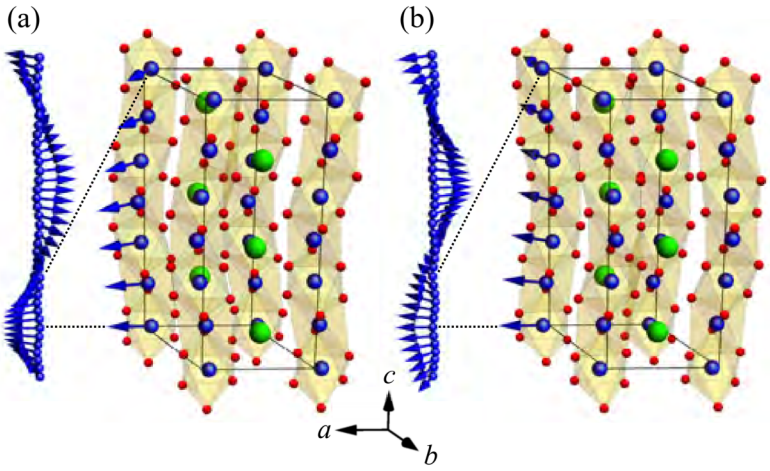

Fig. 2: Left-handed (a) and right-handed (b) chiral magnetic and crystal structure of $CsCuCl_3$. Taken from Ref. [12].

With unpolarized neutrons, the scattered intensity is simply the sum of the nuclear and magnetic intensities. Remarkably, the scattered beam could have non-zero polarization due to the nuclear-magnetic interference and the magnetic chirality irrespective to the unpolarized incident beam. Fox example, the (111) Bragg peak of the magnetized Cu_2MnAl crystal is $\sim 96\%$ polarized because nuclear and magnetic scattering have similar scattering amplitude and interfere destructively for neutrons of one spin state. Together with a relatively high scattering intensity, this makes it a widely used polarizing neutron monochromator.

Half polarized neutron diffraction (Fig. 3) is an experiment in which only a polarizer (or analyser) is used and the Bragg peak intensities (I^+ and I^-) for positive and negative incident polarizations are measured. Then, the two intensities are compared by taking the ratio I^+/I^- (the so-called flipping ratio). It is a very precise method to measure the magnetic structure factor and form factor for constructing magnetic density maps in the unit cell because many factors (except for the extinction factor) affecting the precision of the Bragg peak intensity are cancelled out by the intensity division.

In an experiment with uniaxial polarization analysis, the incident beam is polarized along a certain direction, and the spin-flip and spin-non-flip scattering intensities are measured. This is a powerful method for separating magnetic, nuclear, coherent, and incoherent scatterings.

Finally, the spherical neutron polarimetry method allows to measure both the longitudinal and the transverse components of the final polarization and thus to precisely determine the changes of the neutron polarization in direction and magnitude during the scattering process of the sample. This method provides the most comprehensive information than the methods mentioned above but has the cost of more measurements with polarization analyses.

On POLI, there are three setups implemented for single crystal measurements: unpolarized neutron diffraction under extreme sample environments, the flipping ratio method (Fig. 3), and the spherical neutron polarimetry method. In this experiment, we will perform a flipping ratio

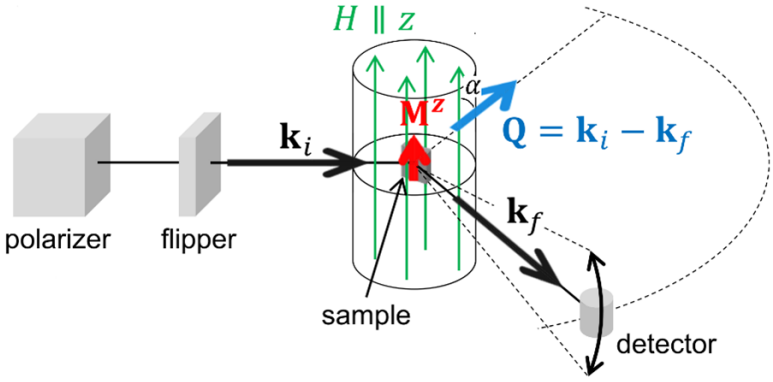

Fig. 3: Experimental setup for a polarized neutron diffraction experiment. Taken from Ref. [13].

measurement on a magnetic single crystal in high vertical magnetic fields. Here, we assume that $\boldsymbol{P}_\mathrm{i}$ is along the vertical axis z and the polarization is $\pm P$ when flipping the polarization of the incident beam. According to the Blume-Maleyev equations, the flipping ratio is,

$$\begin{aligned} R &= \frac{I^+}{I^-} \\ &= \frac{N^*N + \boldsymbol{M}_\perp^* \cdot \boldsymbol{M}_\perp + 2P\Re[N^* M_\perp^z] + iP(\boldsymbol{M}_\perp^* \times \boldsymbol{M}_\perp)^z}{N^*N + \boldsymbol{M}_\perp^* \cdot \boldsymbol{M}_\perp - 2P\Re[N^* M_\perp^z] - iP(\boldsymbol{M}_\perp^* \times \boldsymbol{M}_\perp)^z} \end{aligned} \tag{3}$$

where the superscripts z denote the vertical component of the vectors. If magnetic moments in the sample are perfectly aligned along the vertical field direction and there is no magnetic chirality, the flipping ratio is simplified to be,

$$R = \frac{N^2 + M^2 \sin^2\alpha + 2P \sin^2\alpha\, \Re[N^* M]}{N^2 + M^2 \sin^2\alpha - 2P \sin^2\alpha\, \Re[N^* M]} \tag{4}$$

where α is angle between the scattering vector and the vertical axis. Further, for centrosymmetric structures, both N and M are real and we have,

$$R = \frac{N^2 + M^2 \sin^2\alpha + 2P \sin^2\alpha\, MN}{N^2 + M^2 \sin^2\alpha - 2P \sin^2\alpha\, MN} \tag{5}$$

Once the nuclear structure factor N is known precisely, the magnetic structure factor can be deduced by solving a second-degree equation based on which the magnetization maps (e.g., Fig. 1) can be constructed by e.g., reverse Fourier transformations.

3 Overview of the instrument

POLI is two-axis single crystal diffractometer with a lifting counter detector using polarized and unpolarized neutrons. It is built on the hot neutron source of the FRM II reactor providing

Table 1: Useful instrument parameters for this experiment.

Components	Parameters	Description
Monochromator	`theta_m`	Monochromator θ
Sample	`omega` (ω)	Sample θ
	`gamma` (γ)	Sample 2θ
	`xtrans`, `ytrans`	Sample horizontal translations
Detector	`nu` (ν)	Detector lifting angle

a very high neutron flux at short wavelengths (0.5-1.0 Å). The SR-9a neutron guide leads the primary beam to the monochromator of POLI. The neutrons of the desired wavelength are reflected by the monochromator. After flying out of the shielding, they go through polarizer (optionally) and reach the sample on the sample table. The scattered neutrons can be directly detected by the detector at a 2θ angle or first pass through the polarization analyser between the sample and the detector. On the neutron flying path, there are magnetic guide fields, flippers, and procession coils to maintain and manipulate the neutron polarization. Table 1 shows a few useful instrument parameters for this experiment.

Monochromator
There are two monochromators made of Cu and Si single crystals on POLI and the (220) and (311) Bragg peaks are used, respectively. They are mounted back-to-back on a goniometer on the monochromator table inside the shielding. Two fixed channels on the monochromator shielding at $2\theta_{\text{mono}} = 14^\circ$ and 42° allow four different wavelengths to be used: 0.55, 0.70, 0.90 and 1.15 Å. The whole instrument outside the monochromator shielding can be moved using air cushion.

Polarizer and analyser
The incident monochromatic neutron beam can be polarized by a polarizer. There are two neutron polarizers on POLI of different types: a polarized ^{3}He spin filter cell and a Fe/Si supermirror bender.

The ^{3}He spin filter is a glass cell filled with polarized ^{3}He gas located in a magnetostatic cavity with magnetic shielding made of μ-metal of very high permeability. The nuclear spins of the ^{3}He gas are polarized in the laser lab at FRM II and the gas preferably absorbs the neutrons with spins anti-parallel with the ^{3}He nuclear spins. Electrical coils around the cavity generate a homogeneous horizontal magnetic field parallel with the ^{3}He nuclear polarization and the incident beam. This keeps the ^{3}He gas from being depolarized by the random stray fields from the environment.

The Fe/Si supermirror bender consists of a stack of the thin Si wafers (0.3 mm thick) coated with Fe/Si multi-layer supermirrors of a total reflection angle three times of that of the nature nickel (m=3). There are Gd absorbing layers on the top of the supermirror. The Fe/Si supermirrors are magnetized by permanent magnets on the top and at the bottom of the bender so that the supermirrors only reflect neutrons with one certain spin state. The stack is bent into a C-shape, closing the direct view through a Si wafer. As a result, only neutrons with one spin state are reflected by the supermirror, can travel inside the Si wafers, and finally exit the bender. Whereas the neutrons of the other spin state are not reflected, cannot follow the C-shape, and is absorbed

in the Gd layer.

The ^{3}He spin filter cell is normally used for experiments with zero-field sample environments or magnets with low stray fields (e.g., the $2.2\,\mathrm{T}$ magnet on POLI). Otherwise strong stray fields break the polarization of the ^{3}He gas and thus the neutron polarization. The Fe/Si supermirror bender is more robust to the stray fields and normally used in the experiments with strong magnets (e.g., the $8\,\mathrm{T}$ magnet on POLI).

Nutator (adiabatic spin-field rotator)
The nutator is located at the exit/entrance of the ^{3}He polarizer/analyser which changes the beam polarization direction. It is a magnetic tunnel parallel to the incident/scattered neutron beam. The nutator after the polarizer contains successively longitudinal and transverse static guide fields which adiabatically changes the polarization. By rotating the nutator after the polarizer about its axis, the neutron polarization can be set to be along any direction in the plane perpendicular to the incident beam.

Mezei coil spin flipper
The Mezei flipper uses a non-adiabatic field perpendicular to the guide field to flip the polarization. It consists of a compensation coil and a flipping coil which are perpendicularly winded. The compensation coil creates a field to cancel the guide field and the flipping coil generates a field perpendicular to the neutron polarization to rotate the polarization by $180°$. After the neutrons exit the flipper, they enter the guide field region immediately. It is useful for a monochromatic beam of a fixed neutron velocity.

Sample table
The sample is built with an air cushion for positioning. It has a goniometer for mounting relatively light sample environments, e.g., a cryostat. The goniometer has horizontal translations and can tilt sample by up to $\pm5°$. The goniometer can be rotated about the vertical axis which is the sample θ angle. The goniometer could not hold heavy sample environments, e.g., the $8\,\mathrm{T}$ magnet. Therefore, the heavy sample environments are directly mounted on the sample table and the sample stick inside can be rotated as the sample θ angle.

Lifting counter detector
The detector is an aluminium tube which is filled with high pressure ^{3}He gas. It is inside a shielding box and mounted on the sample 2θ arm. The sample 2θ range is from $-20°$ to $130°$ (depending on the sample environment used). The vertical lifting angle is from $-4°$ to $30°$.

Neutron camera
A neutron camera can be mounted facing the direct beam after the sample for checking the sample position in the beam.

4 Experiment procedure

Finding the orientation of a single crystal with a single detector on POLI is difficult, especially when the sample orientation is not known. Generally, the quality and orientation of the single crystal are first checked with a X-ray/neutron Laue camera. The reciprocal planes interested are aligned close to the horizontal plane, making it easily accessible because the sample is only rotated in the horizontal plane and the lifting angle for the detector is limited. An initial

crystal structure determined from other experiments will be used to calculate a list of reflections. The stronger reflections are first measured and used for finding the orientation matrix and for refining the lattice parameters which are very critical for locating and measuring the Bragg peaks interested afterwards.

1. Shifting the sample to the centre of the ω rotation for a homogeneous illumination
   (a) Mount sample inside the magnet on the sample table.
   (b) Take images of the sample in the beam using the neutron camera at ω_0, $\omega_0 + 180°$, $\omega_0 + 90°$ and $\omega_0 + 270°$ (ω_0 is the current sample theta angle).
   (c) Compare the images and shift the sample to the centre of the rotation.
2. Correcting the sample height by measuring $\pm\boldsymbol{Q}$ Bragg peaks. This will bring the sample to the rotation centre of the lifting detector.
3. Centring a list of strong Bragg peaks and refining the orientation matrix and the sample lattice parameters. Centring for a Bragg peak means finding the optimal ω, γ and ν values at which the Bragg peak shows the strongest intensity. This is done by iteratively performing successively ω, γ and ν scans for a Bragg peak and finding the peak centre until the optimal angular values for the centre do not change much.
4. Perform flipping ratio measurements for a list of Bragg peaks.
5. Extract the magnetic structure factors from the measured flipping ratios.
6. Calculate the magnetic density map using inverse Fourier transformation.

5 Preparatory exercises

1. What is neutron polarization? How to polarize neutrons? What are the three types of neutron polarizers?
2. How does the neutron spin react to magnetic fields? How to maintain and manipulate the neutron polarization during the experiment?
3. What are the necessary devices and their functions for performing neutron polarization analysis?
4. What are the four types of terms in the Blume-Maleev equations?
5. What is the difference between cold, thermal, and hot neutrons? Why are hot neutrons useful for detailed analyses of structures?
6. Why does a supermirror polarizer have a low performance for hot neutrons?

6 Experiment-related exercises

1. What are the magnetic electrons in materials? What is the magnetic form factor?
2. What type of magnetic structure do you know?
3. Why is a large Q-coverage important for doing a reverse Fourier transformation for constructing a real-space magnetic density map?
4. In the flipping ratio method, why do we apply a strong magnetic field?

(a) The monochromators on the table inside the shielding.

(b) Double focusing Si and Cu monochromators.

(c) The ^{3}He filter cell (upper) and the magnetic cavity (lower) of the ^{3}He polarizer. The ^{3}He cells are inserted into the hole.

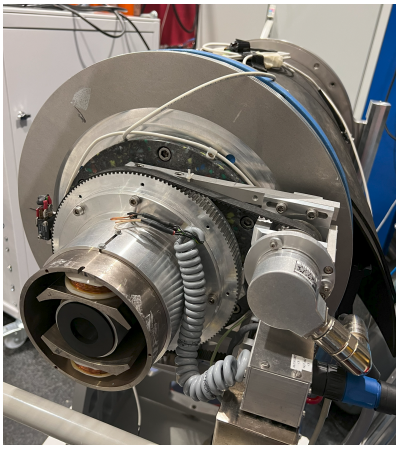

(d) The nutator at the exit of the ^{3}He polarizer.

Fig. 4: Overview of the POLI instrument components.

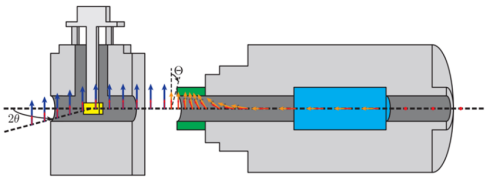

(e) Sectional view of the polarized neutron diffraction setup with the ^{3}He polarizer (in blue), the nutator (in green), the sample (in yellow) and a magnet (in grey at the sample position). The red arrows show the neutron polarization, orange arrows guide fields, and the blue arrows vertical fields from the magnet.

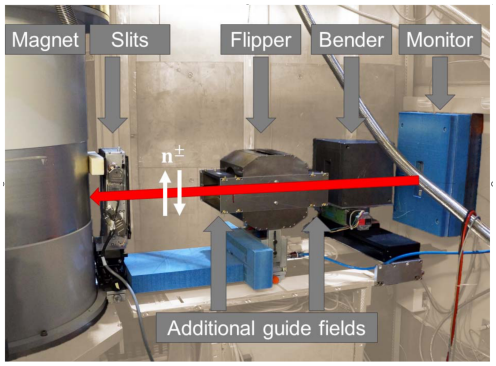

(f) The setup with the 8 T magnet, Mezei flipper and supermirror bender polarizer.

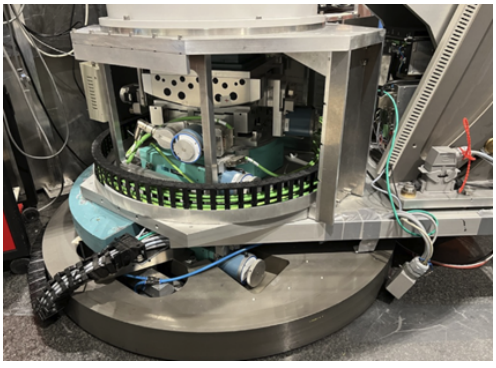

(g) Sample table.

(h) The lifting counter detector.

Fig. 4: (continued) Overview of the POLI instrument components.

References

[1] R. Nathans et al., J. Phys. Chem. Solids **10**, 138 (1959).

[2] A. Gukasov and P. J. Brown, J. Phys.: Condens. Matter **14**, 8831 (2002).

[3] A. Gukasov and P. J. Brown, J. Phys.: Condens. Matter **22**, 502201 (2010).

[4] H. Thoma, *Germanium-based multiferroiccompounds with melilite structure (PhD Thesis)* (RWTH Aachen University, Aachen, 2023).

[5] A. T. Boothroyd, *Principles of Neutron Scattering from Condensed Matter* (Oxford University Press, Oxford, 2020).

[6] T. Chatterji, *Neutron Scattering from Magnetic Materials* (Elsevier Science, , 2006).

[7] E. Ressouche, JDN **13**, 02002 (2014).

[8] M. Blume, Phys. Rev. **130**, 1670 (1963).

[9] M. Blume, Phys. Rev. **133**, A1366 (1964).

[10] S. V. Maleev, Soviet Phys.-JETP **34**, 89 (1958).

[11] S. V. Maleyev, Soviet Phys.-JETP **13**, 860 (1961).

[12] Y. Kousaka et al., Phys. Rev. Materials **1**, 071402 (2017).

[13] J. Jeong et al., Phys. Rev. Lett. **125**, 097202 (2020).

Contact

POLI

Phone: 089/158860-518
Web: https://mlz-garching.de/poli

Jianhui Xu

Outstation at MLZ of Institute for Crystallography, RWTH Aachen University
Jülich Centre for Neutron Science (JCNS)

Phone: 089/158860-825
e-Mail: jianhui.xu@frm2.tum.de

PANDA

Three-axis spectrometer

Peter Link (TUM), Astrid Schneidewind, Petr Cermak

Jülich Centre for Neutron Science
Forschungszentrum Jülich

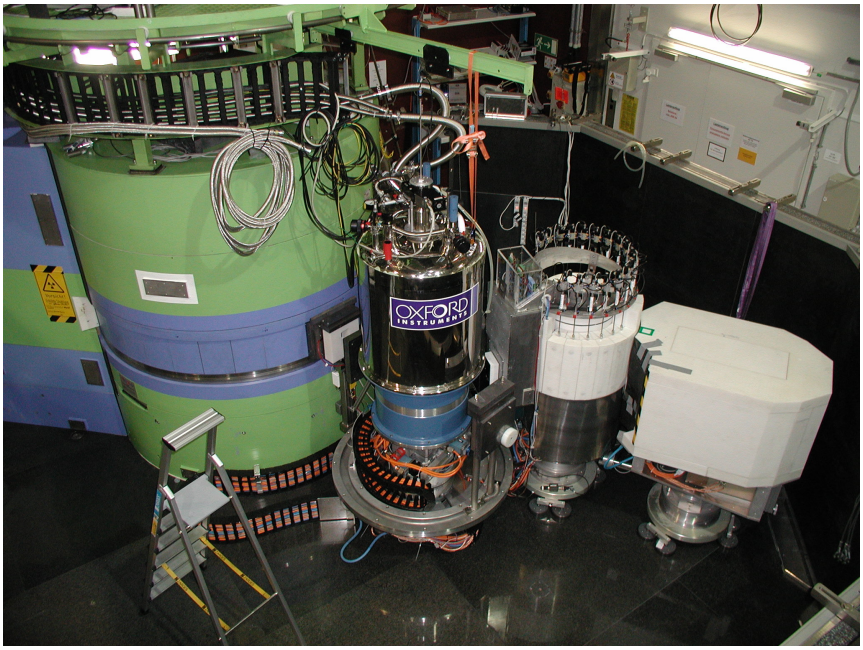

Contents

1 Introduction and theoretical basics

This short summary is thought as a repetition of the basic knowledge needed for this experiment. It is expected that you are familiar with the chapter 11 of the *Lectures*. You will need to know, that scattering vector Q is defined as

$$\boldsymbol{Q} = \boldsymbol{k}_i - \boldsymbol{k}_f, \tag{1}$$

where $\boldsymbol{k}_i$ and $\boldsymbol{k}_f$ are incident and final wavevectors. If $k_i = k_f$, we speak about elastic scattering. We can measure elastic scatterting on PANDA as well, but usually our users are interrested in inelastic case.

You should be also familiar with the concept of the reciprocal lattice introduced in chapter 4.8 of the *Lectures*. Reciprocal lattice represents the Fourier transform of a real Bravais lattice defining the crystalline arrangement in single crystal. It exists in reciprocal space (also known as momentum space) and it is much harder to imagine than the Bravais lattice (existing in real space). It can be shown that the reciprocal lattice of a Bravais lattice is a Bravais lattice again having all symmetry elements of the original lattice. Each point hkl in the reciprocal lattice refers to a set of planes (hkl) in real space. It is convinient to use reciprocal space to depict equation (1), as can be seen in Fig. 1.

You shoul also know different types of the crystal lattices, the terms of *unit cell* as well as the use of *Miller's indices*.

1.1 Brillouin-zone

To simplify description of periodic lattice, it is useful to construct so called Brillouin zones. For this, in the reciprocal lattice the perpendicular bisector planes of the vectors connecting one lattice point with all the others are created (see also Fig. 2).

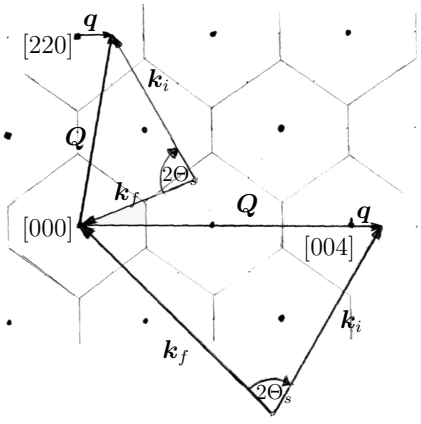

Figure 1: *Scattering diagrams for inelastic scattering of neutrons on a fcc crystal. The reciprocal* $[1\bar{1}0]$ *plane is drawn. Notation similar to the text. The energy transfer is represented by the different lengths of* $\mathsf{k_i}$ *and* $\mathsf{k_f}$

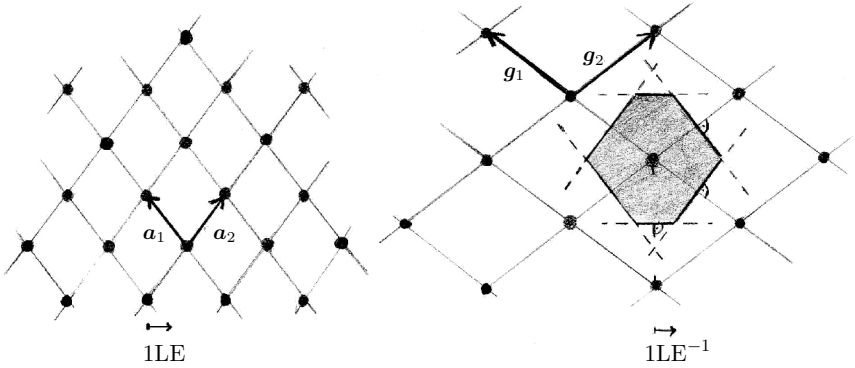

Figure 2: *2-dimensional point lattice in the real and reciprocal spaces. The first Brillouin zone is plotted around a reciprocal lattice point.*

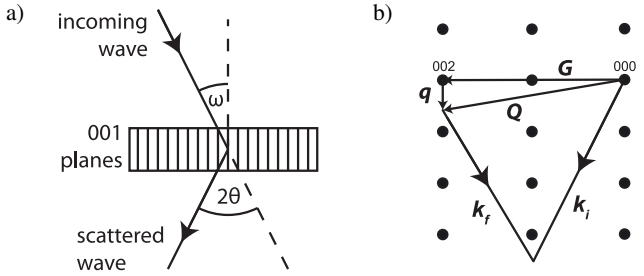

Figure 3: *Schematics of measurement in a) real space and in b) reciprocal space*

Remark: The construction of the Brillouin zones is on the basis Bravais lattice. I.e., Germanium and Silicon have a fcc lattice with a 2-atomic basis. The scattering function is influenced in a way that several refections vanish, others are amplified. The reciprocal lattice stays to be of fcc symmetry.

The first Brillouin zones around the points of the reciprocal lattice fill the reciprocal space. By this, points of high symmetry are easy to identify. They are used to be named by letters (see Fig. 4).

Because of the periodicity of the lattice, we define $\boldsymbol{q}$, which is measured from the center of the Brilluin zone:

$$\boldsymbol{Q} = \boldsymbol{G} \pm \boldsymbol{q} \tag{2}$$

where $\boldsymbol{G}$ is a Bragg point in reciprocal space (satisfying equation 4.16 in the *Lectures*). See Fig. 3 for example.

1.2 Inelastic scattering processes

Inelastic scattering was introduced to you on the example of vibrating atoms - phonons in chapter 11.2.2 of the *Lectures*. PANDA is cold triple axis instrument and it is most suited for study of energy transfers between 0.1 - 5 meV. This energy range is often too low for optical phonon study, but ideal for acoustic phonons, vibrations of ordered magnetic moments (magnons, spin waves), crystal field excitations and interaction between them.

To shortly summarize and visualize inelastic scattering one can assume that the neutron initiates an oscillation in the crystal. By this, the neutron looses energy or gains energy when scattered on an oscillating atom which results in the annihilation of this oscillation. For the energy gain, a decent mode has to be already excited in the crystal. Therefore at the temperature of absolute zero, there is no energy gain scattering and at room temperature, both energy gain and loose sides are almost equivalent.

What is now the advantage of neutrons for the study of lattice vibrations, compared to x-rays? You know, that x-rays are easier to handle and available with much higher flux, especially at synchrotron sources where in addition higher brilliance is achieved. The energy of thermal neutrons is in average circa $30\,\mathrm{meV}$ which is related to a wavevector of $3.8\,\mathrm{\AA}^{-1}$. The dimensions of the reciprocal lattice is circa $2\,\mathrm{\AA}^{-1}$ for Germanium. X-rays with similar wave vectors have energies of $\approx 10\,\mathrm{keV}$. The excitation of a lattice vibration with an energy of $10\,\mathrm{meV}$ would be according to a relative energy change of 10^{-6} for photons. For neutrons the change is in the order of kinetic energies.

1.3 Dispersion relation

Typical purpose of the PANDA experiment is to determine the correlation $\omega(\boldsymbol{q})$ experimentally. $\omega(\boldsymbol{q})$ is the dispersion relation of phonons or any other (quazi)particals in the crystal. It contains all information about the dynamic properties of the studied material. Physical quantities as velocity of sound (from phonons) or the contribution of the heat capacity can be deduced from it. But, also the dominating interaction potentials between the atoms can be derived. For the visualization the 3-dimensional relation is drawn for several directions of symmetry abreast (see Fig. 4).

The physical principle of dispersion relation $\omega(\boldsymbol{q})$ of phonons is shown on example of one-dimensional atomic chain in chapter 11.2.2 of the *Lectures*.

2 Triple axis basics

2.1 Typical measurement

At one time, clasical triple axis instrument did measure on point in reciprocal Q-energy space (e.g. one point in Fig. 4). We look now at the correlation between the configuration of the spectrometer and the variables $\boldsymbol{Q}$ and ΔE. The absolute values of $\boldsymbol{k}_i$ and $\boldsymbol{k}_f$ (incident and outgoing wave vectors) are determined by the scattering angles at the monochromator and the

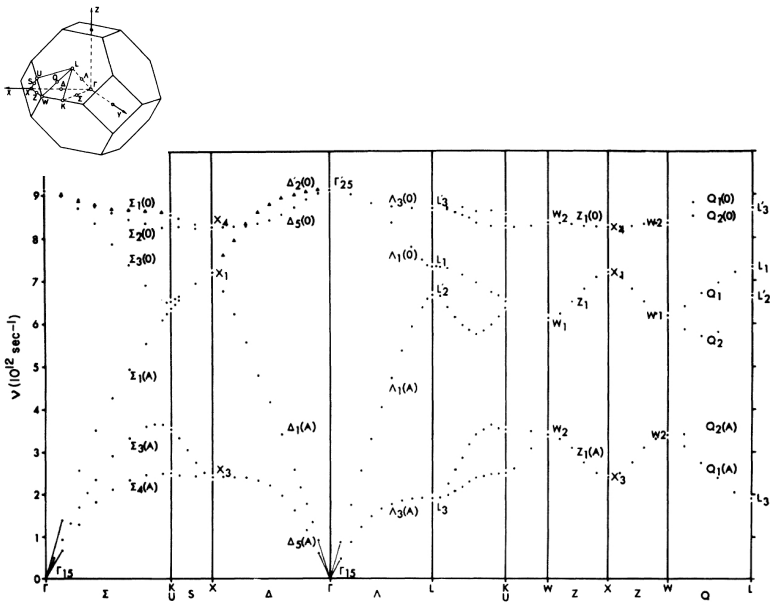

Figure 4: *Dispersion relation of Germanium at 80 K taken from [6]. Points of exceptionally high symmetry are indicated by letters. (small picture).*

analyzer crystals $2\Theta_m$ and $2\Theta_a$, respectively [1]. Having neutron waves we need

$$E_{\mathrm{kin}} = \frac{(\hbar\, k_{\mathrm{n}})^2}{2m}\ , \tag{3}$$

with $\boldsymbol{p}$ the momentum and m the mass of the neutron.
Thus, we know also

$$\omega = \frac{\Delta E}{\hbar} = \hbar\, \frac{|\boldsymbol{k}_i|^2 - |\boldsymbol{k}_f|^2}{2\, m_{\mathrm{n}}}. \tag{4}$$

The orientation of the sample determines the direction of $\boldsymbol{k}_i$ relatively to the crystal lattice (characterized by the sample rotation angle ω_s, `sth` in NICOS, see chapter 4.1) and the scattering plane. Within the scattering plane $2\Theta_s$ determines the direction of $\boldsymbol{k}_f$. $\boldsymbol{Q}$ results from eq. (1).

Conversely, we do not get the configuration of the instrument from ω and $\boldsymbol{Q}$.

In standard experiments, the scans are done at constant $\boldsymbol{Q}$ or constant energy transfer ΔE. While for very stiff dispersion modes, in the vicinity of the Brillouin zone center, constant-E is chosen (Fig. 5(b)), most of the Brillouin zone is normally measured with const.-$\boldsymbol{Q}$ (Fig. 5(a)). Please take time and think about the reason and how the different angles change during the two measurements shown in the figures.

As demonstrated in fig. 6, the lengths of $\boldsymbol{k}_i$ or $\boldsymbol{k}_f$ can be fixed. This is a way to change the resolution of the instrument optimizing the measurement for different problems.

[1] $2\Theta_m$ and $2\Theta_a$ are the relevant numbers. The rotation of the crystals Θ_m and Θ_a are fixed in relation to $2\Theta_m/2$ and $2\Theta_a/2$.

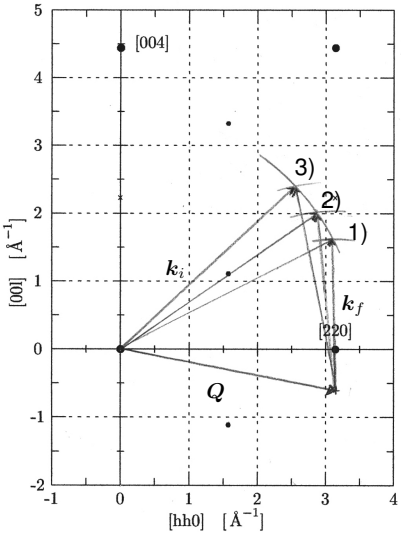

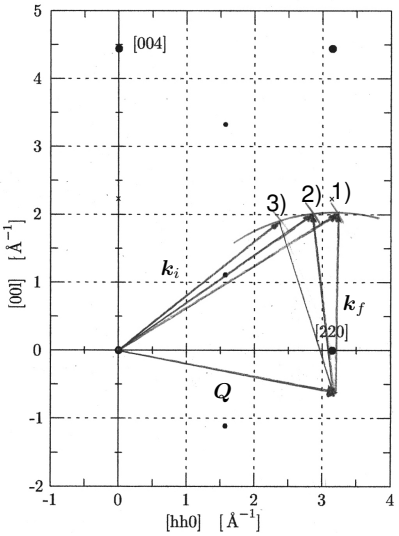

(a) Example for constant-Q scans

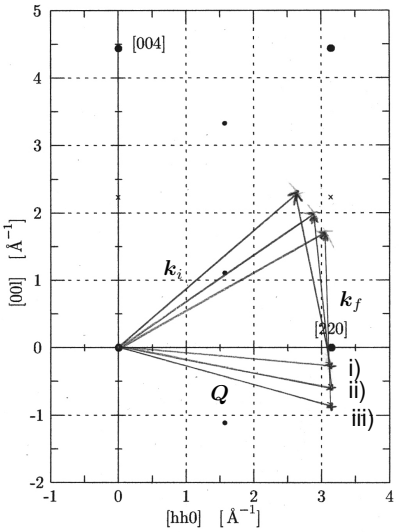

(b) A constant-E scan

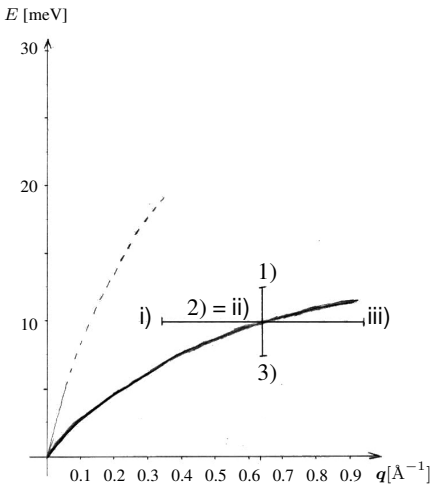

(c) corresponding points of the dispersion relation

Figure 5: *Examples for different scans (scattering triangles and dispersion relation.)*

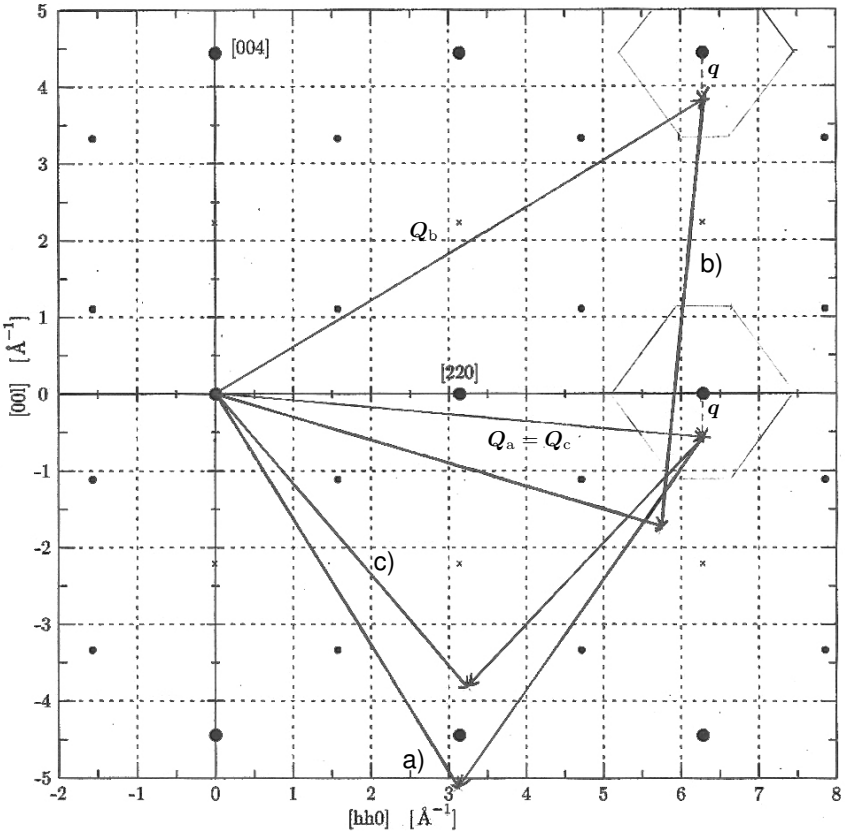

Figure 6: *The same phonon excitation measured in different ways:*
(a)↔(b): Measurements at different elastic peaks but with identical $|\boldsymbol{k}_i|$ and $|\boldsymbol{k}_f|$.
(a)↔(c): Identical position of the reciprocal space measured with different $\boldsymbol{k}_i$.

2.2 Normalization of the counting rates

Planning an experiment, it seems to be native to count the scattered neutrons in the detector at every point for a useful time. But, the counting rate Z_{Det} depends not only on the scattering cross section. It also depends on instrument parameters which possibly change during the measurement or within a scan.

$$Z_{\mathrm{Det}} \propto I_{\mathrm{prim}}(\boldsymbol{k}_i) \cdot R_{\mathrm{Mono}}(|\boldsymbol{k}_i|)\ \frac{1}{|\boldsymbol{k}_i|}\ S(\boldsymbol{Q},\omega)\ R_{\mathrm{Anal}}(|\boldsymbol{k}_f|) \cdot P_{\mathrm{Det.}}(|\boldsymbol{k}_f|). \tag{5}$$

with $R(|\boldsymbol{k}|)$ the reflectivities of the Bragg crystals (on analyzer and detector), $P_{\mathrm{Det.}}(|\boldsymbol{k}_f|)$ the efficiency of the detector and $I_{\mathrm{prim.}}(|\boldsymbol{k}_i|)$ the incident intensity at the used energy. $S(\boldsymbol{Q},\omega)$ is the scattering cross section of your crystal, which you want to measure.

In order to get that quantity we use a monitor detector usually mounted after the monochromator and before the sample. The probability to be detected is for neutrons with a velocity v proportional to the time t the neutrons stay in a monitor of the width d:

$$t = \frac{d}{v} = \frac{d\, m_{\mathrm{n}}}{\hbar\, |\boldsymbol{k}|} \tag{6}$$

One expects as monitor count-rate:

$$Z_{\mathrm{monitor}} \propto I_{\mathrm{prim}}(\boldsymbol{k}_i) \cdot R_{\mathrm{Mono}}(|\boldsymbol{k}_i|)\frac{1}{|\boldsymbol{k}_i|} \tag{7}$$

To perform a measurement, events are counted in the detector until a particular number of monitor counts is reached. The real count rate in the detector with monitor Z'_{Det} is:

$$Z'_{\mathrm{Det}} = \frac{Z_{\mathrm{Det}}}{Z_{\mathrm{Moni}}} \propto S(\boldsymbol{Q},\omega)\ R_{\mathrm{Anal}}(|\boldsymbol{k}_f|) \cdot P_{\mathrm{Det.}}(|\boldsymbol{k}_f|). \tag{8}$$

As you have seen in previous chapter, every point in reciprocal space $\boldsymbol{Q}$ can be achieved with infinite number of combinations of $\boldsymbol{k}_i$ and $\boldsymbol{k}_f$. Because the measured count rate normalized by the monitor depends only on $|\boldsymbol{k}_f|$, it make sense to perform all measurements in constant $|\boldsymbol{k}_f|$ mode, where dependence (8) vanishes. If $|\boldsymbol{k}_f|$ is varied by any reasons during the scan, the corresponding corrections have to be done for the data analysis.

2.3 Resolution function

Up to now we did not consider the fact that at every point of the $\boldsymbol{Q}$-ω-space the spectrometer is pointing to the measured intensity is scattered in a finite volume around this point. A sharp (δ-) peak in the scattering function at $(\boldsymbol{Q}_0, \omega_0)$ gives a measured signal of the form:

$$Z_{\mathrm{Det}}(\boldsymbol{Q},\omega) \propto R(\boldsymbol{Q}-\boldsymbol{Q}_0, \omega-\omega_0). \tag{9}$$

R is the *resolution function* and depends on the configuration of the spectrometer only. Ordinary R is assumed to be Gaussian in its components.

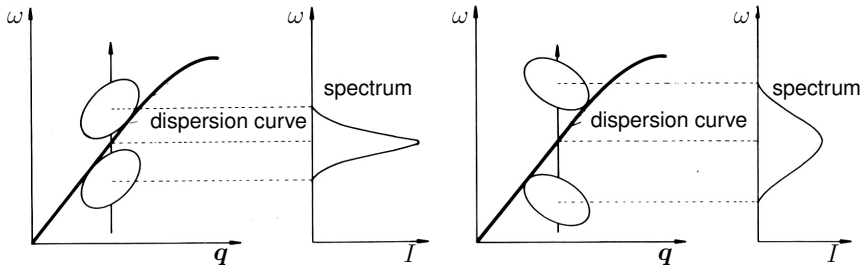

Figure 7: *Focused vs. unfocused measurement.*

The measured signal results from the convolution:

$$Z_{\mathrm{Det}}(\boldsymbol{Q},\omega) \propto \int S(\boldsymbol{Q}',\omega')\; R(\boldsymbol{Q}'-\boldsymbol{Q},\omega'-\omega)\; d\boldsymbol{Q}' d\omega'. \tag{10}$$

For illustration take a contour line of the resolution function (exactly: the 2-dimensional projection of the resolution function). It is normally elliptically and shows the region of the scattering function 'seen' by the instrument. In fig. 7 the projections of the resolution function are plotted into the dispersion relation, at the right the intensities to be expected, respectively. A measurement is characterized to be *focused* if the short axes of the resolution ellipsoid is perpendicular to the dispersion surface (to be measured).

It is important to understand in which cases a sharp resolution function is helpful or not. E. g., see a const.-Q-scan through a sharp 'horizontal' dispersion surface:

$$S(\boldsymbol{Q},\omega) = S_0\,\delta(\omega-\omega_0). \tag{11}$$

The measurement is focused, i.e.

$$R(\boldsymbol{Q},\omega) = e^{-\frac{\omega^2}{\sigma_\omega}} \cdot R(\boldsymbol{Q}). \tag{12}$$

Eq.(10) gives:

$$Z(\omega) \propto e^{-\frac{\omega^2}{\sigma_\omega}} \int R(\boldsymbol{Q}) d\boldsymbol{Q}. \tag{13}$$

Expanding the resolution ellipsoid in the momentum coordinates, the measured intensity increases. The line width depends only on $e^{-\frac{\omega^2}{\sigma_\omega}}$.

Reference: [7] Chap.4

The real form of the resolution function is influenced now by several effects: The Bragg-crystals are not of perfect lattices but have a finite mosaicity (which means it consists of several small single crystals, and their lattice parameters have weak deviations from the average). This 'mosaicity spread' - given by the angle η_m - broadens the Bragg peaks e.g. at the monochromator. Further influences are the finite angle resolution of the detectors, a finite size of the sample and diverging beams.

The beam reflected at the monochromator is a bunch of wave-vectors with a distribution $p_m(\boldsymbol{k}_i)$, the transmission function of the monochromator. The analyzer has to be described in analogy. To calculate the resolution function of the spectrometer, the two transmission functions have to be convoluted with respect to $2\Theta_s$. This simulation can be done by software Takin [8]. You will get some qualitative ideas about this within the experiment.

Reference: [3]

2.4 Peak forms

We learned: For sharp peaks in the scattering function we get a Gaussian signal in the measurement. This will be found in most of the experiments. However, some compounds exhibit broadened phonon resonances, so-called *soft modes*. They are originated by phonon-phonon- and phonon-electron-interactions [2] and result in a finite lifetime τ of the single oscillation states. Calculating the damped harmonic oscillator the line shape is identified to be Lorentzian:

$$S(\omega) \propto \frac{\omega^2}{\left(\omega_0^2 - \omega^2\right)^2 + \left(\frac{\omega}{\tau}\right)^2} \tag{14}$$

with the line width (FWHM):

$$\delta\omega = \frac{1}{2\tau}. \tag{15}$$

The resulting signal of such a 'soft' peak is the convolution of a Lorentzian with a Gaussian curve called Voigt profile. This profile is not easy to be calculated mathematically. In the case of comparable widths of the single profiles it can be sufficient to take the width of the Voigt curve as the sum of the widths of the Gaussian and the Lorentzian contributions.

If it is necessary for the data analysis to determine the peak *widths*, the resolution function has to be deconvoluted from the measured signal. This can be done by software.

References: [2], [4]

3 Description of the PANDA

PANDA is a three axis spectrometer (TAS) at the cold source of FRM II reactor at MLZ. The first thermal TAS was built 1954 and generally improved 1959 by Bertram N. Brockhouse at NRU Reactor in Chalk River. For his merit in the field of inelastic neutron scattering he got the Nobel price 1994. Even if the intensities at the detector were increased by magnitudes, the instrument is remote controlled and the safety is improved today, the general principle of the method is still the same:

The beam of cold neutrons (energy $E \approx 5(30)\,\mathrm{meV}$, momentum $p \approx 1.5(4) \cdot 10^{-24}\,\mathrm{kg\,m/s}$), which has de Broglie wavelength

[2] These effects are neglected by the assumption of harmonic oscillations.

$$\lambda = \frac{h}{p}, \tag{16}$$

or a wavevector of the length $k = \frac{2\pi}{\lambda}$, exits the moderator tank of the reactor through a beam port. The neutrons enter a monochromator being of single crystals with a d-spacing d.

By the Bragg equation

$$n\lambda = 2d \sin \Theta_m \tag{17}$$

the angle $2\Theta_m$ defines the energy of a monochromatic neutron beam (wave vector $\boldsymbol{k}_i$, energy E_i), which points to the sample to be investigated.

Direction and energy of the neutrons are changed at the sample following the inelastic scattering laws. At the secondary spectrometer (analyzer) neutrons with the wave vector $\boldsymbol{k}_f$ and the energy E_f are selected by Bragg reflection at a second crystal and are counted in the detector. By this, the momentum transfer ($\boldsymbol{Q}$) of the neutrons to the sample as well as the energy transfer (ΔE) from the sample to the neutrons can be determined.

$$\boldsymbol{Q} = \boldsymbol{k}_i - \boldsymbol{k}_f, \qquad \Delta E = E_i - E_f. \tag{18}$$

For useful statistics normally a fixed configuration of the instrument - related to a decent energy and momentum transfer - is taken for counting at the detector. The scattering function of the sample is therefore taken pointwise. These scans are measured at constant $\boldsymbol{Q}$ or at constant energy E, depending on the experimental strategy (see below).

PANDA is located at the beamport SR2 in the experimental hall of FRM II and has a comparably large neutron flux at low background. For more detail see:
`http://www.mlz-garching.de/panda`.

We now discuss the components of the three axis spectrometer. Photos of the main components are collected at the gallery 16 for better understanding.

Shielding Since neutrons damage biological matter the region of the primary beam has to be shielded. This is done by a so-called drum (in the case of PANDA blue / green colored) with the monochromator in its centre. The drum is made of heavy concrete with a large amount of chemically combined water, boron added. Also used are boron-treated (PE) sheets. Chemically combined water and PE contain a large amount of hydrogen which is able to decelerate fast neutrons. Boron as a large absorption coefficient for cold and thermal neutrons [3], and the isotope emerging at the neutron capture is not radioactive. But, normally materials are activated by the nuclear reactions and therefore activated (and the reactor emits hard Gamma radiation also if the primary shutter is closed), so the shielding has to be opened only after measurements of the remaining radiation even if the reactor is down. A part of the installation is shown here at the photos. The drum is made to shield γ-radiation as well as neutrons.

During the movement of the monochromator axes a ring of the shielding which contains the beam channel for the beam scatered at the monochromator is entrained. To avoid a closing of the primary beam during the ongoing rotation, the ring partially consists of 11 so-called mobile

[3] Typical reaction: ${}^{10}_{5}\mathrm{B} + {}^{1}_{0}\mathrm{n} \rightarrow {}^{7}_{3}\mathrm{Li} + {}^{4}_{2}\mathrm{He} + 2.8\,\mathrm{Mev}$

Notation:

$\mathcal{Q}$	Neutron source
$\mathcal{M}$	Monochromator
$\mathcal{S}$	Sample table
$\mathcal{A}$	Analyzer
$\mathcal{D}$	Detector
$\alpha 1$ $\alpha 2$ $\alpha 3$ $\alpha 4$	collimators
$2\Theta_m$ $2\Theta_s$ $2\Theta_a$	angles of the Spectrometer-axis
Abs	Shielding
Sel	Selector
Mob	Mobile blocks
Sh	Primary shutter

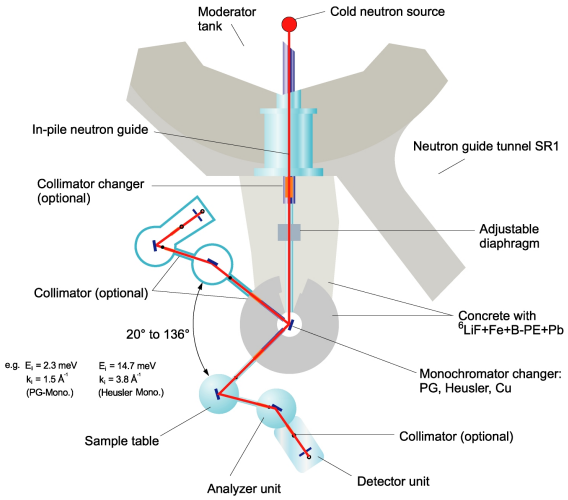

Figure 8: *Schematic design of a three axis spectrometer.*
Remark: all angles are counted in the region $[-180°, 180°]$. ($0°$ is directed in beam, positive angles are counter-clockwise.) $2\Theta_s$ is therefore positive.

blocks (made of the same concrete as the ring) which are moved by an automatic control from one side of the opening to the the other. The geometry and the control ensure a proper shielding where necessary (see fig.8).

Monochromator In the rotation centre of the shielding the monochromator is positioned. It consists of 121 single crystals of pyrolytic graphite (PG) mounted on a crystal holder. The crystal holder and therfore the grapite lattice planes are rotated by the angle Θ_m to the primary beam. The intensity of the monochromatic beam scattered at the angle $2\Theta_m$[4] depends on the lattice parameter of the monochromator material (here PG) and on the incoming angle..

To avoid contamination of higher-order Bragg reflection in the incoming beam, $n = 2, 3 \ldots$ (Gl. (17)), filter materials are positioned between monochromator and sample. In the case of PANDA this is polycrystalline boron or, sometimes, pyrolytic graphite.

Maximum intensity at sample and detector can be achieved by focusing the monochromator and the analyzer in horizontal and vertical direction. Here the 121 monochromator (55 analyzer) crystals are curved in both directions by complex mechanics to get the crystal surfaces into a paraboloid-like shape. The radius of the curvature depends on the neutron wavelength. By taking into account the distances also a focus of the momentums is possible.

Sample table The sample is mounted on a table which can be moved on air-pressure. In addition to motors rotating the sample and the analyzer/detector around the sample - giving Θ_s and the scattering angle $2\Theta_s$, the sample orientation can be adjusted by goniometers and

[4] Remark: Sometimes the angles Θ_m, Θ_s and Θ_a are named α_1 to α_3.

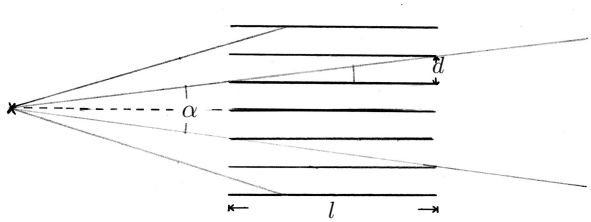

Figure 9: *Drawing of a Soller collimator. The divergence of the outgoing beam is* $\tan(\alpha/2) = \mathsf{d}/\mathsf{l}$*, which is in the example ca.* 18°*. On PANDA the collimation can be chosen between 15 and 80 minutes.*

translation stages. For studies of magnetism, the sample is normally positioned in a cryostat or a cryomagnet - cooling down to temperatures of 0.03 K and appying fields up to 13.2 T.

Analyzer The analyzer is also located in a shielding, but here the reason is to decrease the background in the detector. The crystal holder located again on a goniometer and translation stages allows a horizontal focus of the analyzer, the crystals are mounted to have a fixed vertical focus. The crystals are at the angle Θ_a to the beam, the detector is rotated by $2\Theta_a$.

Detector The neutrons are counted by a beamtube, filled with $^3\mathrm{He}$ under high pressure (ca 10 bar). A neutron can be trapped by a $^3\mathrm{He}$ nucleus and converted to $^4\mathrm{He}$. The emitted γ quant ionizate the gas and is detected like in a Geiger-Müller counter. This allows to count ca. 90% of the incoming neutrons.

Diaphragms, collimators and attenuators In addition to the already described parts several components are needed in the beam path dor beam conditioning. For example variable diaphragms (slits) are installed before and after the sample which are adjusted to the sample size to decrease the background. A secondary shutter is mounted after the monochromator. More diaphragms are with the primary shutter in the reactor wall and between the primary shutter and the monochromator.

Beyond that in every part of the beam path so-called Soller collimators can be applied. It contains of ca. 20 cm long, coated with white $\mathrm{GdO_2}$ foils, which are exactly parallel and therefore limit the divergence of the beam . The value of the divergence is described by the angle α (see fig. 9). Collimators with $\alpha = 15'$ to $\alpha = 60'$ are available. Small divergence corresponds with high resolution but small intensity. The primary collimators are placed in the primary shielding and are changed automatically, the others have to be changed by hand (motorization planned). The beam size is limited only horizontally, i.e. within the scattering plane. For increase of intensity we normally allow a large divergence of the beam in the direction perpendicular to the scattering plane.

Sometimes, e.g. for alignment, the detector is in the straight beam or Bragg reflections have a very large intensity. To avoid a saturation of the detectors, the incoming beam ist attenuated

by PE-plates of different thicknesses which can moved into the beam (and combined) automatically.

Monitor To compare or to combine data from different scans or measurements the intensities are normalized to an intensity counted by the monitor in the primary beam. Its signal is proportional to the incoming intensity. This is also important for energy scans, where the incoming intensity changes with $2\Theta_m$ due to the energy-dependent spectrum. Also different reactor power can be corrected in this way (see paragraph 8).

Goniometer Monochromator, analyzer and sample are placed on 2-axis goniometers. This allows tilts around two perpendicular to each other which meet in the centre of the beam. So the sample does not move out of the beam centre during the tilt. The available angles are limited ($\pm 15^\circ$), the sample can be adjusted but has to be pre-oriented before measuring on the three-axis instrument. It is also possible to translate the sample a few millimeters horizontally and vertically.

Cover page: Overview over PANDA
From left: Monochromator shielding, sample table with 15T cryomagnet, analyzer box and detector shielding.

Figure 10: *(Following page) Components of PANDA taken in different phases of the construction.*

(a) Side view into the (opened) Monochromator shielding onto the PG-monochromator.

(b) PG-analyzer in the (opened) analyzer box. The horizontal curvature is changed by rotating the individual segments.

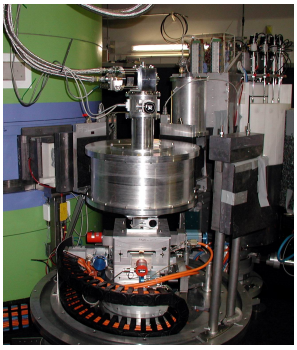

(c) Detailed view onto the sample table with vacuum chamber. From bottom: Rotation table, xy-stage, goniometer, z-stage

(d) Soller collimators in the automatic changer for $\alpha 1$ (in the primary beam.)

(e) Typical sample mounting for use of cryostat.

(f) Detector tubes to be built into the detector shielding

4 Experiment

PANDA is a complex research instrument, where normally measurements on samples at very low temperature, high magnetic fields and / or high pressure are performed. Phonons for example are measured to learn about the interaction potentials in solids. Measurements of spin wave dispersions contribute to determine magnetic interactions.

The goal of this practice is to give inside to the potential of neutron scattering on a three-axis spectrometer. To get results, you have to understand the functionality of the instrument and measure resolution function of the instrument. Because of limited time of this practice, you will not be able to measure and evaluate any dispersion realation, a normal experiment on PANDA needs 7-10 days. Your PANDA labcourse will be going on like

1. Preparation
   - Gather theoretical basics (lecture room).
   - Talk about a strategy for the measurements and a plan of the experiment (lecture room).
   - Pass the security to the experimental hall.
   - Safety instruction at the instrument PANDA.
2. Alignment
   - Proof of the instrument alignment by scans of the monochromator or analyzer axis.
   - Alignment of the sample, define the scattering plane, optimize background.
3. Measurements
   - Determine the resolution elipsoid of the spectrometer for two different wave vectors by measuring sets of scans around the Bragg peaks.
   - Do the same for the horizontally flat geometry of PANDA.
   - Do the same for different $\boldsymbol{k}_f$.
   - Compare intensities and resolution in all cases.
4. Data analysis
   - Learn how to plot the measured data (1D and 2D plots)
   - Compare measured results with theoretical predictions in Takin software [8].
   - Fit the dispersion relation of prepared dataset end evaluate the results.

4.1 NICOS basics - sample alignment

Our instrument control software is NICOS. It is written in Python and also all commands and scriptings is done in Python. We will now illustrate how to use basic NICOS commands on the procedure of sample alignment.

(a) Put the sample on the sample table / in the cryo and enter the sample parameters to nicos:

```
# define the name of the sample
Sample.samplename = 'NaCl'
# define the unit cell parameters and symmetry
Sample.lattice = (5.64, 5.64, 5.64)
Sample.angles = (90.0, 90.0, 90.0)
Sample.spacegroup = 225
# define the sample orientation, to have HHL plane
# within the scattering plane of the instrument
Sample.orient1 = (1.0, 1.0, 0.0)
Sample.orient2 = (0.0, 0.0, 1.0)
```

(b) Calculate the sample 2θ angle of the desired Bragg peak and drive the instrument there.

```
# set the variable peak to hkl indices
# on which we will align PANDA
peak = (0,0,2)
# just calculate instrument angles
calpos(peak)
# drive sample 2theta to 50 (calculated position)
stt(50)
```

(c) Scan the sample rotation to find the peak:

```
# run continous scan of an axis (sample rotation)
# from 10 to 200 degrees)
contscan(sth, 10, 200)
```

(d) Perform a finer scan and rotate the sample to the fitted peak position:

```
# run scan (stop at every point) of sth
# from 53, 20 points, step 0.2, count 1s
scan(sth, 53, 0.2, 20, 1)
# move to the fitted value
sth(54.2)
# tell NICOS, that this is my 002 reflection
setalign(peak)
```

(e) Scan the goniometer on which the peak lies and move it to the fitted maximum position:

```
# centered scan around 0,
# step size: 1 deg.
# 5 points on each side
# time: 1s per point
cscan(sgy, 0, 1, 5, 1)
# move to fitted value
sgy(0.2)
```

(f) Perform a longitudinal scan to correct the sample lattice constants:

```
# perform centered scan around position "peak"
# step is 0.003 in l direction
qcscan(peak, (0,0,0.003), 12, 1)
# Question:
# center of the scan was at 1.984,
# how should we adjust lattice parameters?
```

(g) Repeat the procedure on a peak with $\theta \pm 90°$ to get the scattering plane aligned.

(h) Adjust the sample slits (by running prepared script in NICOS)

```
run('slits.py')
```

5 Conclusions

Congratulations, you just finished reading of the PANDA tutorial! If something was not clear, we will be happy to answer your questions during the tutorial.

Have you ever thinked, why is our instrument called PANDA? Do you thing it is an abbreviation of something else? Try to think about it! Most original solution could get some small reward :)

Looking forward to see you,
PANDA Team

References

[1] B. N. Brockhouse and P. K. Iyengar. Normal modes of germanium by neutron spektrometry. *Phys. Rev.*, 111(3):747, Aug 1958.

[2] W. Demtröder. *Laserspektroskopie*, Kapitel 3 (Linienbreiten und Profile von Spektrallinien). Springer, 4. edition, 2000.

[3] B. Dorner. *Coherent Inelastic Neutron Scattering in Lattice dynamics*. Springer-Verlag, 1982.

[4] K. Dransfeld, P. Kienle, and G. M. Kalvius. *Physik I*, Kapitel 8. Oldenbourg, 8. edition, 1998.

[5] J. Kauppinen and J. Partanen. *Fourier Transforms in Spectroscopy*. Wiley-VCH, Berlin, 2001.

[6] G. Nillson and G. Nellin. Normal vibrations of germanium by neutron spektrometry. *Phys. Rev. B*, 3(2):364, Jan 1971.

[7] G. Shirane, S. m. Shapiro, and J. M. Tranquada. *Neutron scattering with a triple-axis Spektrometer*. Oxford University Press, 2002.

[8] T. Weber, R. Georgii, and P. Böni. Takin: An open-source software for experiment planning, visualisation, and data analysis. *SoftwareX*, 5:121 – 126, 2016.

[9] R. Zorn. Fourier transforms. In *Neutron Scattering*. T. Brückel, G. Heger, D. Richter and R. Zorn, 2006.

Internet resources

`http://www.mlz-garching.de/panda`
: PANDA homepage.

`http://wiki.mlz-garching.de/panda`
: PANDA public wiki page.

`http://wiki.mlz-garching.de/takin`
: Takin - software for instrument resolution simulation.

`http://wiki.mlz-garching.de/ufit`
: ufit - software for treting triple axis data.

Contact

PANDA

Phone: 089/289-14749
Web: http://www.mlz-garching.de/panda

Astrid Schneidewind

JCNS at Maier-Leibnitz Zentrum Garching, Forschungszentrum Jülich GmbH

Phone: 089/289-14749
e-Mail: astrid.schneidewind@frm2.tum.de

Petr Cermak

Phone: 089/289-11773
e-Mail: p.cermak@fz-juelich.de

SPHERES

Backscattering spectrometer

Joachim Wuttke, Daria Noferini, Marina Appel, and Michaela Zamponi

Jülich Centre for Neutron Science
Forschungszentrum Jülich

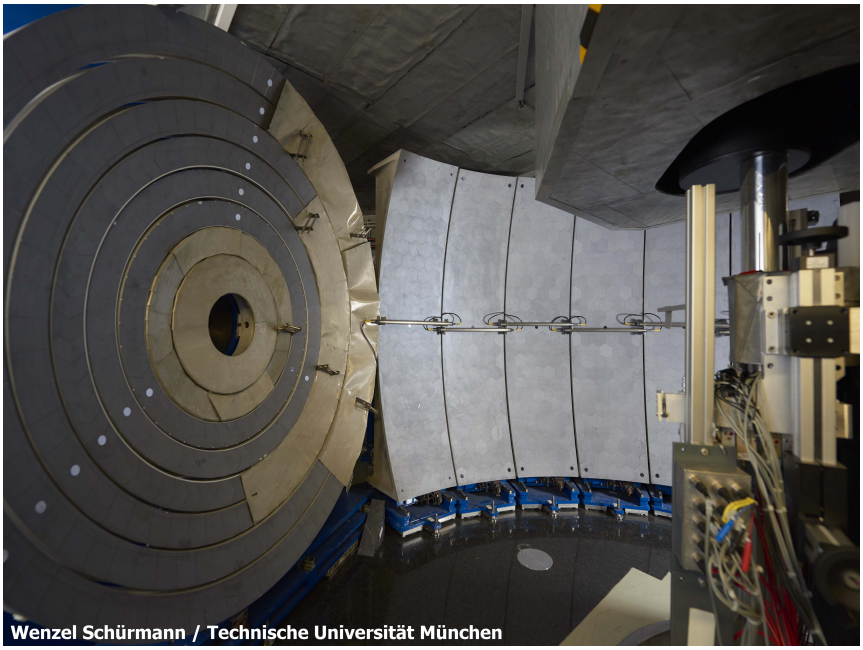

Contents

1 Introduction

Neutron *backscattering spectrometers* are used to measure *inelastic scattering* with very high *energy resolution*. What does this mean?

In inelastic scattering, scattering intensity is measured as function of the energy exchanged between the scattered neutron and the sample. As in other areas of physics, a data set of the form intensity-versus-energy is called a *spectrum*. An instrument that resolves inelastic scattering is therefore called a *spectrometer*.

While elastic scattering experiments yield information about *structure* or *texture* of a sample, inelastic scattering is used to investigate its *dynamics*. Specifically, inelastic neutron scattering yields information about the thermal motion of atomic nuclei.

The most common instrument for inelastic neutron scattering is the triple-axis spectrometer. It is routinely used to measure phonon and magnon dispersions, with energy exchanges of the order of meV. In contrast, the *high resolution* of a backscattering spectrometer allows to resolve very *small energy shifts* of the order of μeV. By the time-energy uncertainty relation, small energy means long times. Hence, backscattering addresses relatively *slow* nuclear motion — much slower than the lattice vibrations typically seen in triple-axis spectrometry. Depending on their nature, such motions can appear in the spectra as a broadening of the elastic line (quasielastic broadening) or as distinct features at certain transferred energies (inelastic peaks).

What processes take place on the energy or time scale made accessible by neutron backscattering? For instance the following:

- hyperfine splitting of nuclear spin orientations in a magnetic field,
- rotations or hindered reorientations of molecules or molecular side groups,
- quantum tunneling,
- hydrogen diffusion in ionic conductors,
- diffusion of water confined in small pores or at different surfaces,
- relaxation in viscous liquids and glasses,
- innermolecular rearrangements in polymers and biological systems such as proteins.

During your lab course day, you will use the backscattering spectrometer SPHERES (SPectrometer for High Energy RESolution) to study one example of these applications.

2 Spectrometer Physics

2.1 Energy Selection by Backscattering

In crystal spectrometers, neutron energies are selected by Bragg reflection from crystals, according to the *Bragg condition*

$$n\lambda_n = 2d_{hkl}\sin\Theta \tag{1}$$

where d_{hkl} is the distance of lattice planes $[hkl]$, and Θ is the glancing angle of reflection from these planes. The index n indicates that along with a fundamental wavelength λ_1, integer

fractions $\lambda_n = \lambda_1/n$ are transmitted as well. To suppress these unwanted higher orders, experimental setups include either a mechanical neutron velocity selector (Fig. 1), or a beryllium filter.

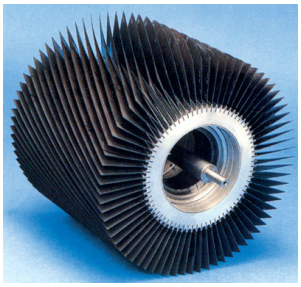

Fig. 1: Rotor of a mechanical neutron velocity selector. The blades are coated with neutron absorbing material. In SPHERES, such a selector is used as a pre-monochromator that reduces the incoming white spectrum to about $\pm 6\%$. © Astrium GmbH.

In practice, the parameters d and Θ on the right-hand side of Eq. (1) are not sharp: Imperfections of the crystal lead to a distribution of lattice constants, characterized by a width δd. And similarly, imperfections of the neutron optics (inevitable because the incoming beam, the sample, and the detector all have finite size) lead to a distribution of reflection angles, characterized by a width $\delta\Theta$. By differentiating the Bragg equation (1), one obtains the relative width of the wavelength distribution reflected by a crystal monochromator:

$$\frac{\delta\lambda}{\lambda} = \frac{\delta d}{d} + \cot\Theta\,\delta\Theta. \tag{2}$$

In usual crystal spectrometers, the second term is the dominant one. However, by choosing $\Theta = 90°$, the prefactor $\cot\Theta$ can be sent to zero. This is the fundamental idea of the backscattering spectrometer. If a monochromator crystal is used in backscattering geometry, with $\Theta \simeq 90°$, then the reflected wavelength distribution is in first order insensitive to the geometric imperfection $\delta\Theta$; it depends only on the crystal imperfection δd and on a second-order $(\delta\Theta)^2$ term.

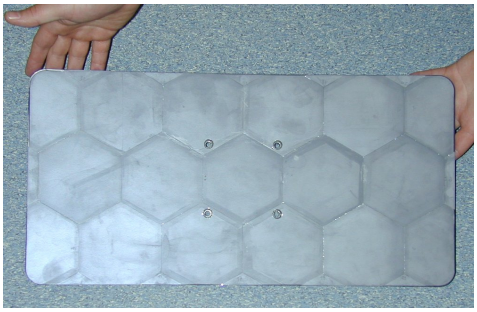

Fig. 2: The monochromator of SPHERES consists of hexagonal Si(111) wafers of 750 µm thickness, glued onto a spherical support made of carbon fiber.

The monochromator of SPHERES is made of silicon crystals in (111) orientation (Fig. 2). The backscattered wavelength is $\lambda = 2d_{111} = 6.27$ Å, corresponding to a neutron energy of

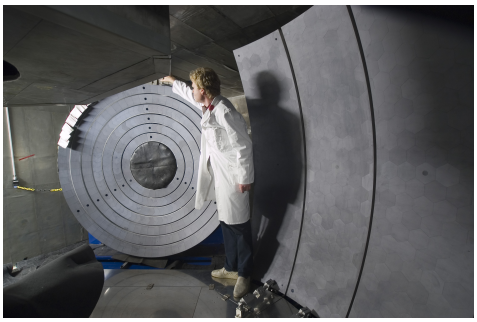

Fig. 3: The analyzers of SPHERES are made of the same Si(111) as the monochromator. For small scattering angles, they are shaped as rings; for large scattering angles, they are approximately rectangular sections of a sphere.

2.08 meV. The crystals are cut from wafers produced by the semiconductor industry. They are perfectly monocrystalline, so that their intrinsic resolution[1] of $\delta d/d \simeq 10^{-6}$ is actually too good because it does not match the spectrometer's second-order geometric imperfection $(\delta\Theta)^2 \lesssim 10^{-4}$. As a remedy, the crystals are glued to a spherical support so that the resulting strain induces a lattice constant gradient of the order $\delta d/d \simeq 10^{-4}$.

2.2 Spectrometer Layout

In a crystal spectrometer, a *monochromator* is used to send a neutron beam with a narrow energy distribution $E_\mathrm{i} \pm \delta E$ onto the sample. After the sample, a second monochromator, called *analyzer*, is used to select a narrow energy distribution $E_\mathrm{f} \pm \delta E$ out of the scattered spectrum. In SPHERES, we actually have a huge array of analyzers (Fig. 3), covering a solid angle of about 2.5, which is 20% of 4π. These analyzers send energy-selected neutrons towards 14 different detectors, depending on the scattering angle ϑ.

Fig. 4 shows the complete layout of SPHERES. The incoming beam is pre-monochromatized by a mechanical velocity selector. Then, it is transported by a focussing neutron guide into the instrument housing where it passes trough the open position of a first rotating chopper (background [bg] chopper)[2] and then hits a second rotating chopper (PST chopper). The PST chopper rotor (Fig. 5) carries mosaic crystals made of pyrolitic graphite on half of its circumference. When the incoming neutrons hit these crystals, they undergo a Bragg reflection towards the monochromator.[3] Otherwise, they are transmitted towards a beamstop.

The backscattering monochromator selects a neutron band $E_\mathrm{i} \pm \delta E$ as described above. Neu-

[1] In perfect crystals, the intrinsic resolution $\delta d/d$ is limited by *primary extinction*: Say, each crystalline layer has a reflectivity of about 10^{-6}. Then only about 10^6 layers contribute to the Bragg reflection. This limits $\delta\lambda/\lambda$ to about 10^{-6}.

[2] The role of this device is to reduce the background during the counting of the scattered neutrons.

[3] As a side effect, the Bragg deflection by rotating mosaic crystals achieves a favorable *phase-space transform* (PST): the incoming wavevector distribution is spread in angle, but compressed in modulus. This results in a higher spectral flux in the acceptance range of the monochromator.

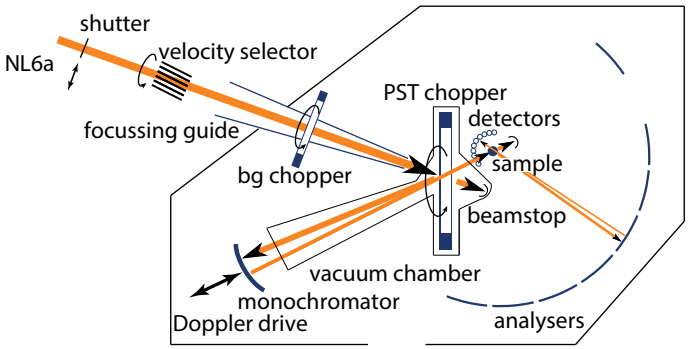

Fig. 4: Layout of the Jülich backscattering spectrometer SPHERES at MLZ

Fig. 5: Schematic front view of the PST chopper rotor of SPHERES. The yellow band indicates the mosaic crystals that deflect the incident beam towards the monochromator.

trons within this band are sent back towards the PST chopper. When they reach the PST chopper, the rotor has turned to its open position: the mosic crystals have moved out of the way; the neutrons coming from the monochromator are transmitted towards the sample.

The sample scatters neutrons into 4π. About 20% of this is covered by analyzers. If a scattered neutron hits an analyzer and fullfills the backscattering Bragg condition, it is sent back towards the sample. It traverses the sample[4] and reaches a detector. To discriminate energy-selected neutrons from neutrons that are directly scattered from the sample into a detector, the time of arrival is put in relation to the chopper phase.

While the primary spectrometer (everything before the sample) is mainly in vacuum, the secondary spectrometer is not. To minimize neutron losses in the secondary spectrometer, the entire instrument housing can be flooded with argon. However, for the labcourse we preferentially remove the argon, so that participants can enter into the housing.

2.3 Measuring Spectra

So far we have introduced a static arrangement with fixed energies $E_\mathrm{i} = E_\mathrm{f}$. Such an arrangement is actually used to measure the fraction of elastic versus total scattering, called the *Debye-Waller factor* for coherent scattering and the *Lamb-Mössbauer factor* for incoherent scattering.

[4] Of course not all neutrons are transmitted: some are lost, some are scattered into a wrong detector. This inaccuracy is inevitable in neutron backscattering. We strive to keep it small by using rather thin samples with typical transmissions of 90% to 95%.

More often, however, one wants to measure full spectra $S(Q, \omega)$. Therefore, one must find a way to modify the energy transfer

$$\hbar\omega = E_\mathrm{i} - E_\mathrm{f}. \tag{3}$$

This can be done using the *Doppler effect*: The monochromator is mounted on a linear drive that performs a cyclic motion. In the monochromator's rest frame, the backscattered energy is always the value $E_0 = 2.08$ meV given by the lattice constant of Si(111). Depending on the monochromator's velocity v, the value in the laboratory frame is

$$E_\mathrm{i}(v) = \frac{m_\mathrm{n}}{2}\,(v_0 + v)^2 \tag{4}$$

where $v_0 = 631$ m/s is the neutron velocity at $E_0 = m_\mathrm{n}/2\,v_0^2$. The Doppler drive of SPHERES has a linear amplitude of ± 75 mm and achieves a velocity amplitude of ± 4.7 m/s, resulting in an energy range

$$-30.7\ \mu\mathrm{eV} < \hbar\omega < 30.9\ \mu\mathrm{eV}. \tag{5}$$

This is called the *dynamic range* of the spectrometer.

When a scattered neutron is detected, its time of flight is traced back to the moment when it has been backscattered by the monochromator. From the recorded trace of the linear drive, the monochromator velocity at that moment is infered, ω is computed from (4) and (3), and the corresponding histogram channel is incremented. To determine $S(Q, \omega)$, one needs to normalize to the time spent in channel ω. This normalization is routinely done by the instrument's raw-data reduction program SLAW.

2.4 Instrument Characteristics

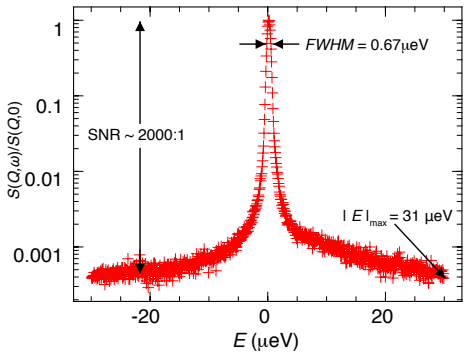

Fig. 6: Resolution function of SPHERES, measured on a standard sample at a low temperature where the scattering is purely elastic.

The performance of a spectrometer can be characterized by its *resolution function*. To obtain the resolution function, one measures the spectrum of a purely elastic scatterer. Fig. 6 shows the result of a resolution measurement from a user experiment on SPHERES. Note the logarithmic intensity scale.

Conventionally, the resolution of an instrument is characterized by the *full width at half maximum* (FWHM). For SPHERES, a typical value is 0.65 μeV. Note however that the FWHM is not the full story: the quality of an instrument also depends on the *shape* of the resolution functions, especially of the deep wings. The resolution of SPHERES is slightly asymmetric. This is related to the $(\delta\Theta)^2$ term in the wavelength spread of a backscattering analyzer: all deviations from the perfect $\Theta = 90^\circ$ geometry lead to the transmission of longer wavelengths, never of shorter ones.

Another important figure of merit is the *signal-to-noise ratio* (SNR). It depends strongly on the ratio of scattering to absorption cross sections and on the thickness and geometry of the sample. With argon filling SNR for a typical sample with good scattering can exceed 2000:1, whereas without argon it is decreased by *ca* 35%. On the other hand, for strongly absorbing samples it is sometimes less than 100:1. The SNR can be further substantially enhanced by operating the background chopper at half the frequency of the PST chopper, albeit at the cost of intensity.

3 Applications

In the following, two different applications of neutron backscattering are explained: hyperfine splitting in a magnetic material, and methyl group tunneling.

3.1 Hyperfine Splitting

The measurement of hyperfine splitting has been historically the first application of neutron backscattering,[5] and to this day, it is the conceptually simplest one.

Since the neutron has spin $S = 1/2$, its magnetic quantum number can take the values $S_z = \pm 1/2$. In a scattering event, this quantum number can change. In more pictorial words: when a neutron is scattered, it may or may not undergo a *spin flip*.

As angular momentum is conserved, a change of S_z must be accompanied by an opposite change of the magnetic quantum number I_z of the nucleus by which the neutron is scattered, $\Delta I_z = -\Delta S_z$. Therefore, spin-flip scattering is only possible if the sample contains nuclei with nonzero spin I.

Nuclei with nonzero spin quantum number I possess a magnetic moment

$$\mu = I g \mu_\mathrm{N} \tag{6}$$

with the nuclear magneton

$$\mu_\mathrm{N} = \frac{e\hbar}{2m_\mathrm{p}} = 3.153 \cdot 10^{-8}\ \mathrm{eV/T}. \tag{7}$$

The g factor is different for each nucleus.[6]

[5] A. Heidemann, Z. Phys. 238, 208 (1970).

[6] Tabulation: http://ie.lbl.gov/toipdf/mometbl.pdf.

A local magnetic field B leads to a splitting of energy levels,

$$E = I_z g \mu_N B, \tag{8}$$

called *hyperfine splitting*. Consequently spin-flip scattering is accompanied by an energy exchange $\Delta E = \pm g\mu_N B$. By measuring the neutron energy gain or loss $\pm\Delta E$, one can accurately determine the local field B in ferromagnetic or antiferromagnetic materials.

3.2 Molecular Rotation and Quantum Tunneling

Rotational motion of molecules or molecular side groups is one of the most important applications of neutron backscattering. Here, we specialize on the rotation of methyl (CH_3) groups. We consider these groups as stiff, with fixed[7] CH bond length 1.097 Å and HCH angle 106.5.°

The only degree of freedom is then a rotation around the RC bond that connects the methyl group to the remainder R of the molecule. This RC bond coincides with the symmetry axis of the CH_3 group. The rotational motion can therefore be described by a wave function ψ that depends on one single coordinate, the rotation angle ϕ.

The Schrödinger equation is

$$\left\{ B\frac{\partial^2}{\partial\phi^2} - V(\phi) + E \right\} \psi(\phi) = 0. \tag{9}$$

For free rotation ($V = 0$), solutions that possess the requested periodicity are sine and cosine functions of argument $J\phi$, with integer J. Accordingly, the energy levels are $E = BJ^2$.

Given the value $B = 670$ μeV, it is obvious that free rotor excitations occur only far outside the dynamic range of neutron backscattering. Conversely, if we observe an inelastic signal from methyl groups on a backscattering spectrometer, then we must conclude that $V \neq 0$: the methyl group rotation is *hindered* by a rotational potential. This potential can be caused by the remainder R of the molecule as well as by neighbouring molecules.

Due to the symmetry of the CH_3 group, the Fourier expansion of $V(\phi)$ contains only sine and cosine functions with argument $3m\phi$, with integer m. In most applications, it is sufficient to retain only one term,

$$V(\phi) \doteq V_3 \cos(3\phi). \tag{10}$$

The strength of the potential can then be expressed by the dimensionless number V_3/B. In the following we specialize to the case of a *strong potential*, $V_3/B \gg 10$, which is by far the most frequent one.

In a strong potential of form (10), the CH_3 group has three preferential orientations, separated by potential walls. The motion of the CH_3 group consists mainly of small excursions from the preferred orientations, called *librations*. Essentially, they are harmonic vibrations.

At low temperatures, almost exclusively the vibrational ground state is occupied. Yet reorientational motion beyond librations is possible by means of quantum mechanical tunneling: the wave functions of the three localised *pocket states* ψ_m ($m = 1, 2, 3$) have nonzero overlap.

[7] Ignoring the variations of empirical values, which are of the order of ± 0.004 Å and $\pm 1.5°$.

Therefore, the ground state is a linear combination of pocket states.[8] Periodicity and threefold symmetry allow three such combinations: a plain additive one

$$\psi_1 + \psi_2 + \psi_3, \tag{11}$$

and two superpositions with phase rotations

$$\psi_1 + \mathrm{e}^{\pm i2\pi/3}\psi_2 + \mathrm{e}^{\pm i4\pi/3}\psi_3. \tag{12}$$

In the language of group theory, state (11) has symmetry A, the degenerate states (12) are labelled E^a, E^b. It is found that A is the ground state. The *tunneling splitting* $\hbar\omega_\mathrm{t}$ between the states A and E is determined by the overlap integral $\langle\psi_m|V|\psi_n\rangle$ ($m \neq n$). It depends exponentially on the height of the potential wall. Provided it falls into the dynamic range of neutron scattering, it leads to a pair of inelastic lines at at $\pm\hbar\omega_\mathrm{t}$.

With rising temperatures, the occupancy of excited vibrational levels increase. This facilitates transitions between A and E sublevels and results in a decrease of $\hbar\omega_\mathrm{t}$ and a broadening of the inelastic lines.

Upon further temperature increase, thermal motion of neighbouring molecules causes so strong potential fluctuations that the picture of quantum tunneling is no longer applicable. Instead, the motion between different pocket states can be described as *stochastic jump diffusion*.

Let $p_m(t)$ be the probability of being in pocket state m ($m = 1, 2, 3$). Assume that jumps between the three main orientations occur with a constant rate τ^{-1}. Then, the p_m obey rate equations

$$\frac{\mathrm{d}}{\mathrm{d}t}p_m(t) = \frac{1}{\tau}\left\{-p_m + \sum_{n\neq m}\frac{1}{2}p_n\right\}. \tag{13}$$

The stationary equilibrium solution is just $p_m = 1/3$ for all m. When perturbed, the system relaxes into equilibrium with a time dependence of $\exp(-t/\tilde{\tau})$. Explicit solution of the linear differential equation system (13) yields $\tilde{\tau} = 2\tau/3$.

According to a fundamental theorem of statistical mechanics (the *fluctation dissipation theorem*), the relaxation by which a slightly perturbed system returns *into* equilibrium has the same time dependence as the pair correlation function *in* equilibrium. Therefore, we can employ the solution of (13) to write down the self-correlation function of the protons that constitute our methyl group. Fourier transform yields then the incoherent scattering function

$$S(Q\omega) = a(Q)\delta(\omega) + b(Q)\frac{\Gamma}{\omega^2 + \Gamma^2}. \tag{14}$$

The first term describes elastic scattering. The second term, the Fourier transform of the exponential $\exp(-t/\tilde{\tau})$, is a Lorentzian with linewidth $\Gamma = \tilde{\tau}^{-1}$; such *broadening* of the elastic line is often called *quasielastic*.

[8] This is an extremely simplified outline of the theory. In a serious treatment, to get all symmetry requirements right, one must also take into account the nuclear spins of the H atoms. See W. Press, Single-Particle Rotations in Molecular Crystals, Springer: Berlin 1981.

4 Preparatory Exercises

1. Relate the relative wavelength spread $\delta\lambda/\lambda$ to the relative energy spread $\delta E/E$.

2. In SPHERES, useable detectors are located at scattering angles 2θ ranging from 12.5° to 134°. Calculate the corresponding wavenumbers in Å^{-1}. Recommendation: use the following constants in *atomic units*: $\hbar c = 1973$ eVÅ and $m_n c^2 = 940$ MeV.

3. Convert dynamic range and resolution of SPHERES into GHz. To make contact with optical spectroscopy, you might also wish to convert into cm^{-1}.

4. Empirically, it is found that the centre of the resolution function can be fitted by a Gaussian $a\exp(-E^2/2/\sigma^2)$. Derive an expression that relates the Gaussian standard deviation σ to the FWHM.

5. Note that the above mentioned fit applies only to the very centre of the resolution function. How does a Gaussian look like on the lin-log representation of Fig. 6? And a Lorentzian?

6. In SPHERES, the distance sample-analyzer is 2 m. Calculate the time neutrons need for a round trip sample-analyzer-sample.

7. Assume that the monochromator motion is perfectly sinusoidal. Sketch how the measuring time per energy channel varies with $\hbar\omega$.

8. Draw a sketch of the expected backscattering spectrum $S(Q,\omega)$ of a ferromagnetic material with $I \neq 0$.

9. A good example to observe rotational tunneling is the benzene-derived molecule xylene (dimethylbenzene, C_8H_{10}). What is the required thickness to obtain 90% transmission for a flat xylene sample?

10. Sketch the expected spectra for different temperatures.

5 Experiment Procedure

5.1 The experiment itself

First, the key components and working principles of the instrument are revised and discussed with the tutor.

The proposed experiment consists in the observation of methyl group tunneling in xylene, in its *meta-* or *para-* isomeric form. An alternative experiment is the observation of hyperfine splitting in a magnetic material. The tutor shows how to insert the sample in the instrument's cryostat and how to launch the measurements using the instrument's graphical user interface. Log entries are written to the instrument log wiki. The details of the experimental procedure are discussed with the group.

5.2 Data reduction

The program SLAW is used to convert raw neutron counts into $S(Q, \omega)$. It is parametrized by a script, called `Slawfile`. The tutor provides a sample script, which is then modified to convert the results of the current experiment.

SLAW can save $S(Q, \omega)$ in a variety of output formats. Most relevant are plain tabular formats `recttab` and `spectab`, and a self-documenting format `y08` required by our standard data-analysis software FRIDA.

5.3 Data evaluation

The data evaluation is done using the data-analysis package FRIDA. For a tutorial and help, refer to the FRIDA webpages. [9]

1. Plot a representative selection of measured spectra and observe how the signal change at different temperatures and Q-values.
2. With the help of the tutor, fit the signal for one of the temperatures using the convolution of a theoretical model with a measured resolution function. For convenience, a simplified model will be employed.
3. Use the same model to fit the other temperatures and evaluate the temperature dependence of the relevant fit parameters.
4. Select one spectrum and try to fit the elastic line and a chosen inelastic line, if there are any, with a Gaussian and with a Lorentzian.

6 Experiment-Related Exercises

Use the obtained results from data evaluation to answer the following questions and discuss them with the tutor.

1. How does the signal qualitatively change with different temperatures? And with different Q-values?
2. Summarize the temperature dependence of the fit parameters.
3. How could you improve the simplified model to better describe the data?
4. Why is it important to measure the resolution function?

[9] Follow the link at `https://jugit.fz-juelich.de/mlz/frida`.

Contact

SPHERES

Phone: 089/158860-522
Web: http://www.mlz-garching.de/spheres

Michaela Zamponi

Jülich Centre for Neutron Science at MLZ, Forschungszentrum Jülich GmbH

Phone: 089/158860-793
e-Mail: m.zamponi@fz-juelich.de

DNS

Neutron Polarization Analysis

Yixi Su and Thomas Müller

Jülich Centre for Neutron Science
Forschungszentrum Jülich

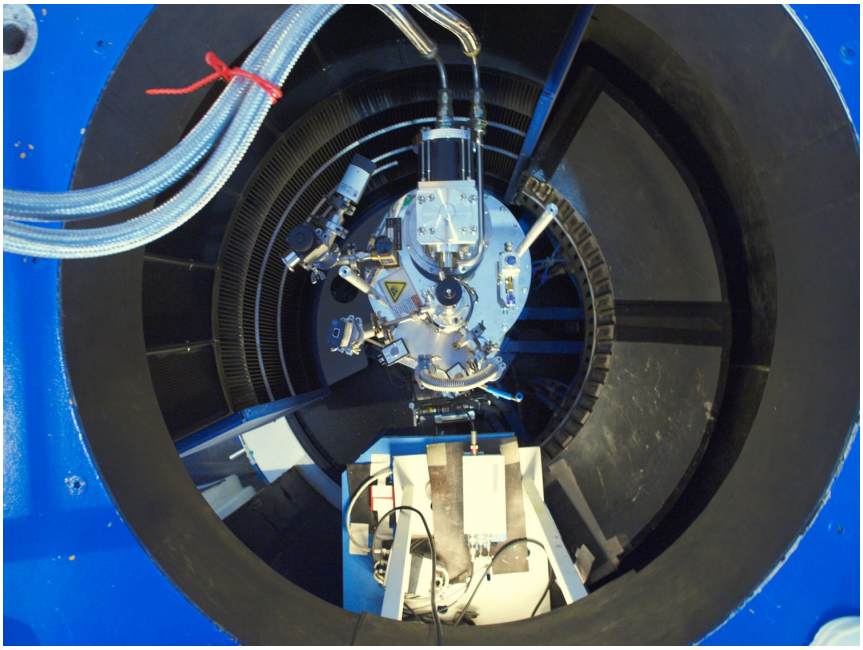

Contents

1 Introduction

Polarized neutron scattering and polarization analysis represent powerful techniques for the studies of complex ordering phenomena and dynamics of condensed matter. The elements of this technique and its advanced applications in particular in magnetism have been comprehensively covered in a number of lecture notes and papers [1–5]. The aim of this exercise on *Neutron Polarization Analysis* is to provide you with some hands-on experience on the practical aspects of polarized neutron scattering based on the multi-detector time-of-flight spectrometer DNS at MLZ [6]. The details on the handling of polarized neutrons and the fundamentals of polarization analysis will be demonstrated from a range of experiments and exercises.

In Section 2 of this manual, an overview of the instrument DNS as well as its unique capabilities will be given. Section 3 consists of necessary preparatory exercises and questions which can be studied before the experiment. Section 4 describes the experiment procedure and Section 5 provides the experiment-related exercises.

2 Overview of the DNS Instrument

DNS is a versatile diffuse scattering cold neutron time-of-flight spectrometer with polarization analysis at the neutron guide NL6 at MLZ. DNS has the capability to allow unambiguous separations of nuclear coherent, spin incoherent and magnetic scattering contributions simultaneously over a large range of scattering vector Q and energy transfer E. A schematic layout of DNS is shown in Fig. 1.

DNS features wide-angle polarization analysis, a large position-sensitive detector array and a high frequency disc chopper system. With its compact design and the powerful double-focusing PG(002) monochromator, DNS is optimized as a high intensity instrument with medium resolution. A monochromatic neutron beams with a wavelength between 2.4 to 6 Å is available at DNS. A neutron velocity selector suppresses higher orders or allows to select $\lambda/2$ without the need to move the secondary spectrometer. The polarizer is a solid-state C-bender with Fe/Si

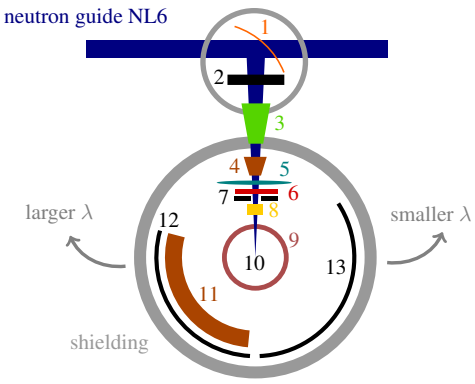

1. Double focusing PG(002) monochromator
2. Beamshutter
3. Velocity selector
4. Polarizer (supermirror benders)
5. Disk chopper
6. Pi-flipper
7. Slits
8. Monitor
9. XYZ-coils
10. Sample
11. Polarization analysers
12. Detectors 24 tubes
13. Position sensitive detectors 128 tubes

Fig. 1: Schematic sketch of DNS instrument.

coated polarizing supermirrors m = 3.5 [7] and the polarization analyzers use m = 3 Schärpf bender-type focusing supermirrors. A polarized neutron flux as high as 5×10^6 n/(s·cm^2) has been achieved at 4.74 Å. The polarization rate of the incident neutron beams is nearly 96%. The wide-angle polarization analysis in the horizontal scattering plane is achieved by the simultaneous use of 24 analyzers separated by 5° in 2θ. The neutron spins are manipulated using a Mezei-type π-flipper, followed by a set of orthogonal XYZ-coils situated around the sample position for providing guide fields. In addition to the high polarized flux, the unique strength of DNS lies in its extreme versatility. DNS can be operated in a number of modes for a wide range of samples. There are three polarization analysis (PA) modes at DNS: uniaxial-PA for separation of coherent and spin-incoherent scattering in non-magnetic samples; longitudinal-PA for separation of magnetic scattering in paramagnetic and antiferromagnetic samples; and vector-PA for the determination of complex magnetic structures.

Time-of-flight (TOF) spectroscopy is another important application at DNS. Additional to the polarization analysis detectors a set of 128 position-sensitive ^{3}He tubes of 1 m height and half inch diameter without polarization analysis increases the covered solid angle up to 1.9 sr. For TOF measurements the beam is pulsed with a three slit titanium disc chopper with a frequency up to 300 Hz, shown in Fig. 2a. DNS is targeted as a high count-rate cold neutron time-of-flight spectrometer with medium resolution. It is thus ideal for the studies of spin dynamics in many novel magnetic materials. Fig. 2b shows a TOF measurement of Vanadium with an achieved elastic-line resolution of 0.3 meV. The technical details of DNS are given in Table 1.

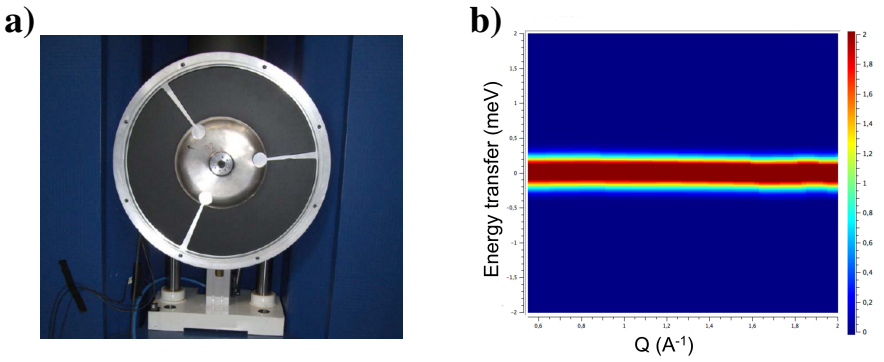

Fig. 2: **(a)** Opened chopper housing, with visible titanium three slit chopper. **(b)** TOF measurement of Vanadium f = 250 Hz, λ = 4.2 Å, elastic-line resolution $\approx$ 0.3 meV

Monochromator	horizontal- and vertically adjustable double-focusing crystal dimensions: wavelengths:	PG(002), d = 3.355 Å (at NL6) 2.5 × 2.5 cm^2 (5 × 7 crystals) 2.4 Å ≤ λ ≤ 6 Å
Velocity selector	minimum wavelength wavelength bandwith $\Delta\lambda/\lambda$:	1.5 Å at 2200 rpm 30 – 40 %
Chopper system	chopper disk: chopper frequency:	Titanium, 3 slits, ∅ = 420 mm ≤ 300 Hz
Expected flux at sample (n/cm^{2}s)	non-polarized polarized (polarizer: m = 3.5 supermirror benders)	≈ 10^8 ≈ 5×10^6–10^7
Detector banks for non-polarized neutrons	position sensitive ^{3}He detector tubes total solid angle covered: horizontal covered scattering angle:	128 units, ∅ = 1.27 cm, height ≈ 100 cm 1.9 sr $0° \leq 2\theta \leq 135°$
Detector banks for polarized neutrons	polarization analyzers: ^{3}He detector tubes: horizontal covered scattering angle:	24 units, m = 3 supermirror benders 24 units, ∅ = 2.54 cm, height 15 cm $5° \leq 2\theta \leq 135°$
Q$_{max}$	λ_i = 2.4 Å (E$_i$ = 14.2 meV) λ_i = 6 Å (E_i = 2.28 meV)	4.84 Å^{-1} 1.93,Å^{-1}
Energy resolution	λ_i = 2.4 Å (E$_i$ = 14.2 meV) λ_i = 6 Å (E_i = 2.28 meV)	≈ 1 meV ≈ 0.1 meV
Suitable samples	single crystals, powders, soft matter (e.g. polymers, liquids etc.)	
Sample environments	top-loading CCR, closed-cycle cold head, orange cryostat, cryofurnace, ^{3}He/^{4}He dilution cryostat (∼20mK), cryomagnet (self-shielding, vertical field up to 5T)	

Table 1: The technical details of the DNS instrument.

Typical scientific applications at DNS are the studies of complex magnetic correlations, such as in highly frustrated magnets and strongly correlated electron systems, as well as the structures of soft condensed matter, such as the nanoscale confined polymers and proteins, via polarization analysis. Beside the separation of the magnetic cross section from nuclear and spin-incoherent ones, polarization analysis can also be used to explore possible anisotropy of spin correlations in complex materials. Polarized powder diffraction carried out at DNS is complementary to standard neutron powder diffraction and may be extremely useful for magnetic structure refinements, particularly in case of small magnetic moments by improving the signal to background ratio. Fig. 2(a) shows the magnetic and nuclear scattering of iron-based superconductor Sr_2CrO_3FeAs measured at DNS with polarization analysis and the corresponding Rietveld refinements [8].

The exploration of unusual magnetic properties can also be efficiently undertaken on single crystals by reciprocal space mapping. Fig. 2(b) shows an example of the measured magnetic

diffuse scattering patterns originating from the spiral spin-liquid state of $MnSc_2S_4$. The diffuse magnetic scattering separated by polarization analysis forms a squared-ringpattern close to the Brillouin zone boundaries characteristic for the predicted spiral surface [9]. Fig. 2(c) shows the magnetic diffuse scattering derived with the same approach on the molecule magnet $\{Mo_{72}Fe_{30}\}$ [10]. DNS also represents a powerful instrument for the soft condensed matter community for the separation of nuclear coherent scattering from often dominating spin incoherent scattering background in hydrogenous materials.

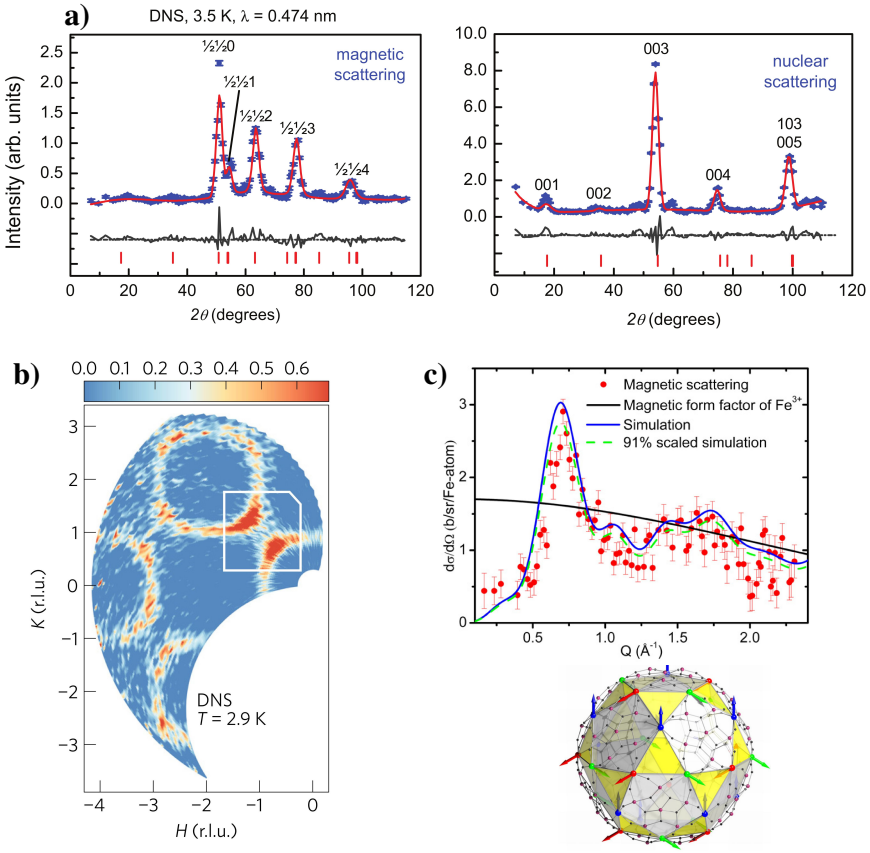

Fig. 3: Examples of the scientific applications at DNS: **(a)** magnetic and nuclear scattering of iron-based superconductor Sr_2CrO_3FeAs at 3.5 K as measured (blue) at DNS via polarization analysis and the Rietveld refinements (red) [9]; **(b)** Diffuse magnetic scattering from the spiral spin-liquid state of $MnSc_2S_4$ **(c)** differential magnetic scattering cross section measured at 1.5 K and the theoretical simulation with the three-sublattice spin model of the citation$\{Mo_{72}Fe_{30}\}$ molecule magnet [10].

3 Preparatory Exercises

The practical aspects and the experimental setup of DNS with respect to polarization analysis have been addressed and discussed in great details in the lecture [1]. Therefore, it is strongly recommended to go through the relevant sections of the lecture notes thoroughly before the exercises. Try to answer the following general questions, it would greatly improve your understandings:

1. What is the Larmor precession? How to calculate the Larmor frequency (ω_L)?
2. How do neutron spins respond to changing magnetic fields? What are adiabatic and non-adiabatic behavior?
3. How to are polarized neutrons produced and how is the spin state of the neutrons after the scattering process analyzed?
4. What is a spin flipper and how does it work?
5. What is the flipping ratio? What is the polarization rate of the neutron beams?
6. What are nuclear coherent, spin incoherent, isotopic incoherent and magnetic scattering processes? Whether and how are the spin states of the scattered neutrons changed in those scattering processes?

In addition to these general questions, the following exercises are provided:

1. How strong should the magnetic field $\mathbf{H}_y$ be in a coil of length L = 100 mm to perform a 90° turn for neutrons with $\lambda = 4$ Å (see Fig. 4a)
2. A magnetic field $\mathbf{H}$ changes its space direction by 90° over a distance of L = 20 mm (as shown in Fig. 4b). How strong should the field $\mathbf{H}$ be to achieve an adiabatic evolution of the neutron spins? The neutrons wavelength is $\lambda = 4$ Å.

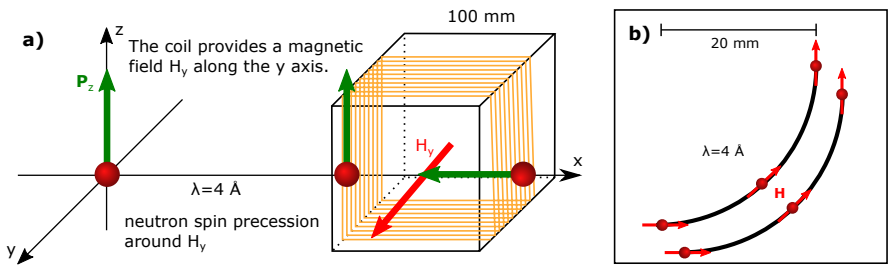

Fig. 4: Prepatory exercises

4 Experiment Procedure

After the DNS instrument and its major instrument components are briefly introduced by the tutor, the first task for students is to learn how to manipulate neutron spins via Larmor precession and properly set guide fields.

The experiment will start with a measurement of two standard samples, which are used to correct for detector efficiency and finite flipping ratio. The students will change the samples in the cryostat and will learn how to move the sample, detectors, fields and slits by the python based instrument control software Nicos. Afterwards a polycrystalline magnetic sample and a single crystal will be examined.

1. Vanadium hollow-cylinder: nuclear spin-incoherent scattering
2. Non-magnetic alloy $Ni_{0.89}Cr_{0.11}$: isotopic incoherent scattering
3. Antiferromagnetic powder NiO
4. Single crystal sample - from an actual research project at the point of the lab course
5. Alternatively D_2O could be measured

The students are expected to perform the experiment to measure the spin-flip and non-spin-flip scattering intensities of each sample via wide-angle polarization analysis at DNS and understand the differences between nuclear, magnetic, spin-incoherent and isotopic incoherent scattering.

The $Ni_{0.89}Cr_{0.11}$ sample will further be used for the alignment of the π-flipper and z-compensation field strengths.

For detailed information about the instrument components and data analysis software the students are referred to the DNS intranet wiki (only accessible from MLZ network):
`https://wiki.frm2.tum.de/dns:index`

5 Data Evaluation and Experiment-related Exercises

After the experiment the students will learn how to plot the data using instrument specific software and how to separate the different scattering cross sections. The polarization efficiency can never achieve 100% due to polarization losses by depolarizations in the polarizer, the analyzer and the guide fields and the imperfections of the polarizer, the analyzer and the flipper, this always leads to a finite flipping ratio. The correction for finite flipping ratio thus becomes an important and always necessary practical issue in order to obtain a precise separation. Therefore, the following exercise related to the flipping ratio correction is provided

1. For neutrons with a wavelength λ=4.74 Å and a flight path of 10 mm through the flipper coil, how strong the flipping field would be required to achieve a π-flip?

2. Which measurement would you use to determine the flipping ratio at DNS. How large is the flipping ratio and the polarization rate of the incident neutron beam at DNS?

3. With the measured finite flipping ratio, how would you correct the spin-flip scattering intensity I_{sf} and the non-spin-flip scattering intensity I_{nsf}?

4. How can polarization analysis be used to separate nuclear coherent scattering from spin-incoherent scattering in soft condensed matter?

5. How is the scattering cross section obtained via the XYZ-method? Which necessary corrections need to be done for a precise separation?

6. What ratio between the spin-flip and non-spin-flip intensities do you expect for Vanadium and $Ni_{0.89}Cr_{0.11}$ and what is the physical origin?

References

[1] W. Schweika, "Neutron scattering: lectures on the JCNS laboratory course held at Forschungszentrum Jülich and at the Heinz Maier-Leibnitz Zentrum Garching; in cooperation with RWTH Aachen", in *Spin-dependent and magnetic scattering of polarized neutrons*, edited by T. Brückel, S. Förster, G. Roth, and R. Zorn (Jülich : Forschungszentrum, Zentralbibliothek, 2018).

[2] J. Schweiza, "Polarized neutron and polarization analysis", in *Neutron scattering from magnetic materials*, edited by T. Chatterji (Elsevier Science, 2006).

[3] O. Schärpf, "The spin of the neutron as a measuring probe. Application of spin polarized neutrons to measure electronic (including magnetic) properties of metals, semiconductors, superconductors." (2010).

[4] W. Schweika, "XYZ-polarisation analysis of diffuse magnetic neutron scattering from single crystals", Journal of Physics: Conference Series **211**, 012026 (2010).

[5] O. Schärpf and H. Capellmann, "The XYZ-difference method with polarized neutrons and the separation of coherent, spin incoherent, and magnetic scattering cross sections in a multidetector", Physica Status Solidi (a) **135**, 359 (1993).

[6] Y. Su, K. Nemkovskiy, and S. Demirdiş, "DNS: diffuse scattering neutron time-of-flight spectrometer", Journal of large-scale research facilities JLSRF **1**, A27 (2015).

[7] K. Nemkovski et al., "Simulation and optimization of a new focusing polarizing bender for the diffuse neutrons scattering spectrometer DNS at MLZ", Journal of Physics: Conference Series **862**, 012018 (2017).

[8] M. Tegel et al., "Non-stoichometry and the magnetic structure of Sr_2CrO_3FeAs", EPL (Europhysics Letters) **89**, 37006 (2010).

[9] S. Gao et al., "Spiral spin-liquid and the emergence of a vortex-like state in $MnSc_2S_4$", Nature Physics **13**, 157 (2016).

[10] Z.-D. Fu et al., "An approach to the magnetic ground state of the molecular magnet $\{Mo_{72}Fe_{30}\}$", New Journal of Physics **12**, 083044 (2010).

Contact

DNS

Phone: 089/289-14339
Web: https://www.mlz-garching.de/instrumente-und-labore/spektroskopie/dns.html

Dr. Yixi Su

Forschungszentrum Jülich GmbH
Jülich Centre for Neutron Science at MLZ
Lichtenbergstr. 1
85748 Garching
Germany

Phone: 089/289-10714
e-Mail: y.su@fz-juelich.de
Web: http://www.fz-juelich.de/SharedDocs/Personen/JCNS/EN/Su_Y.html?nn=820902

Dr. Thomas Müller

Phone: 089/289-10730
e-Mail: t.mueller@fz-juelich.de
Web: http://www.fz-juelich.de/SharedDocs/Personen/JCNS/EN/Mueller_T.html?nn=964128

J-NSE “PHOENIX”

Neutron Spin Echo Spectrometer

Olaf Holderer

Jülich Centre for Neutron Science
Forschungszentrum Jülich

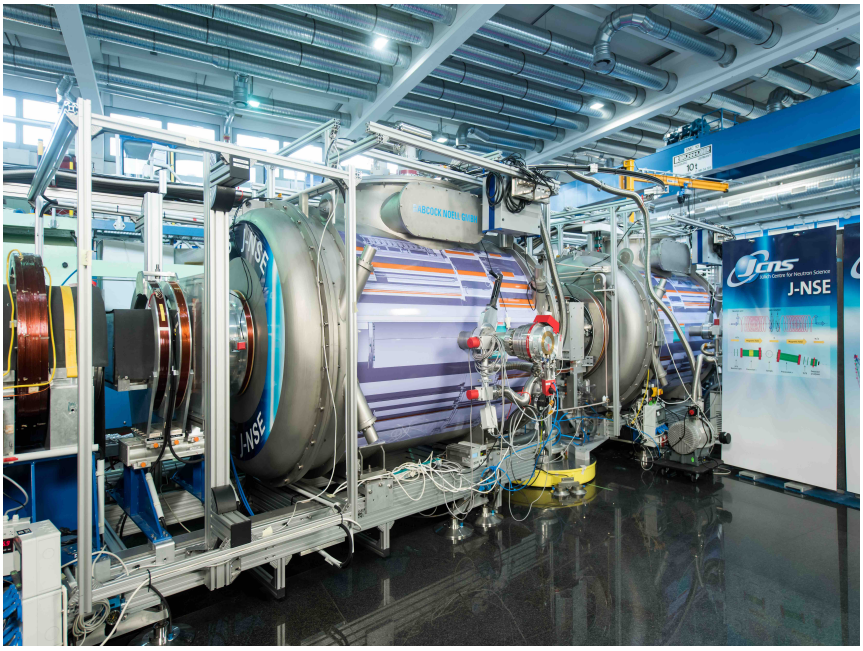

Contents

1 Introduction

Neutron spin echo spectroscopy provides the highest energy resolution in neutron scattering. The covered energy range (or Fourier time range) matches excellently thermally driven motions in soft matter systems such as polymer chains in solution, in the melt, domain motions of proteins, phospholipid membrane fluctuations to mention just a few. This experiment aims to study the dynamics of a polymer chain in solution. Poly(ethylene propylene) (PEP) with a molecular weight of 100 kg/mol is dissolved in deuterated decane with a concentration of 3%. The dynamics of PEP polymer in solution will be studied at room temperature. The results will be interpreted in terms of the Zimm model, which allows to draw conclusions about the internal motions of the polymer chains.

2 Neutron Spin Echo Spectroscopy

The neutron spin echo technique uses the neutron spin as an indicator of the individual velocity change the neutron suffered when scattered by the sample. Due to this trick NSE accepts a broad wavelength band and at the same time is sensitive to the velocity changes down to 10^{-5}. However, the information carried by the spins can only be retrieved modulo an integer number of spin precessions and thus it is retrieved as intensity modulation proportional to the cosine of a precession angle difference. *The measured signal is the cosine transform $I(Q,t)$ of the scattering function $S(Q,\omega)$.* All spin manipulations only serve to establish this special type of velocity analysis. For details see Reference [1].

Due to the intrinsic Fourier transform property of the NSE instrument it is especially suited for the investigation of relaxation-type motions, which contribute at least several percent to the entire scattering intensity at the momentum transfer of interest. The Fourier transform property yields the desired relaxation function directly without numerical transformation and tedious resolution deconvolution. The resolution of the NSE may be corrected by a simple division.

The NSE instrument (see Figure 1) consists mainly of two large solenoids that generate the magnetic field that causes the precession of neutron spin (precession field). The precession of the spin is limited by π/2-flippers, which are in front of the entrance and respectively exit of the first and second main solenoids; the π-flipper is located near the sample position. The embedding fields for the flippers are generated by Helmholtz-type coil pairs around the flipper locations. After leaving the last flipper the neutrons enter an analyzer containing 60 (30 x 30 cm^2) magnetized CoTi supermirrors located in a solenoid set. These mirrors reflect only neutrons of one spin direction into the multidetector. Figure 1 (middle) shows the layout of the solenoids, the bottom part the engineering design of the J-NSE spectrometer. The main precession coils providing the strong precession region, are superconducting and fully compensated (no dipolar stray fields) in order to minimize the mutual influence of the different spectrometer components.

Depending on its velocity, each neutron undergoes a number of precessions in the first solenoid before hitting the sample. After the scattering process the π-flipper inverts the spin orientation so that the rotation in the second solenoid exactly compensates the first if the speed of the neutrons is not changed by the scattering (purely elastic process), whereas inelasti-

cally scattered neutrons collect a different phase angle of rotation, $\Delta\Psi \simeq \Delta v/v^2\,\gamma\,J$, with $\gamma = 2\pi \times 2913.06598 \times 10^4\,\mathrm{s}^{-1}\,\mathrm{T}^{-1}$ and J being the magnetic field integral (the integrated magnetic field a neutron experiences during its flight through the field). The distribution of the velocity changes Δv of neutrons that experienced an energy transfer during scattering at the sample – in terms of its cos-Fourier transform – is measured as polarization of the neutron beam at the end of the second solenoid after the last $\pi/2$-flipper. *Small velocity changes are proportional to the small energy changes* $\hbar\omega$, ω being the frequency of the Fourier transform. The time parameter (Fourier time) is proportional to $\lambda^3 J$ and here in first instance is controlled by the current setting of the main coils, which determins the field integral J.

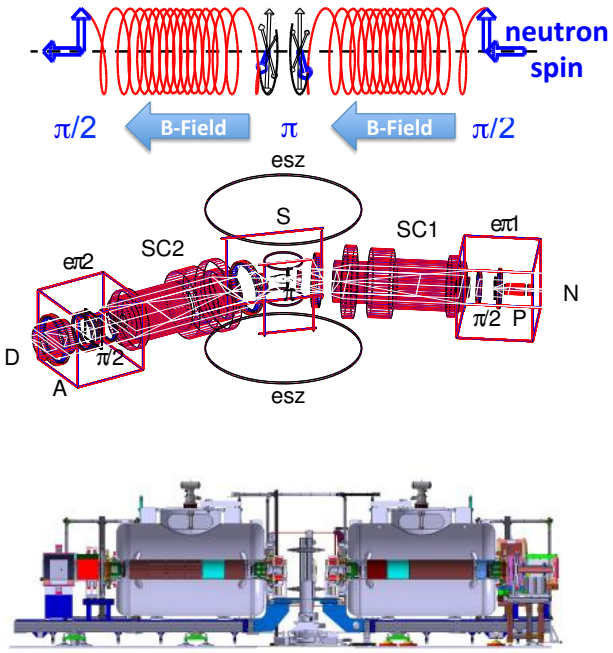

Fig. 1: Working principle of the NSE spectrometer showing the spin precessions along the flight path for the velocity encoding/decoding (top), the magnetic layout of the actual J-NSE spectrometer with all solenoids (middle) and the engineering design of the actual J-NSE spectrometer (bottom) [2, 3].

The polarization is determined by scanning the magnetic field in one of the main coils with the so-called phase coil. If first and second arm are symmetric, a maximum of the polarization is measured. However, if the phase of the spins is shifted by 180 degree by variation of the field of one coil, one gets to a minimum of intensity. With a 360 degree variation one gets to the next maximum and so on. These oscillations are shown in Figure 2. The amplitude of such an echo is normalized to the difference between maximum intensity (up-value), where all flippers are switched off, and the minimum intensity where only the π-flipper is switched on (down-value). Assuming that this normalization accounts for all imperfections of the polarization analysis in the instrument, the result yields the desired degree of polarization reduction due to

inelastic/quasielastic scattering of the sample. Since the thus determined polarization reduction also contains the effects due to field integral inhomogeneity a further normalization step is needed, which is equivalent to a resolution deconvolution in a spectroscopic instrument as e.g. the backscattering spectrometer. In order to be able to perform this resolution correction the same experimental and data treatment procedure has to be carried out with an elastic scatterer.

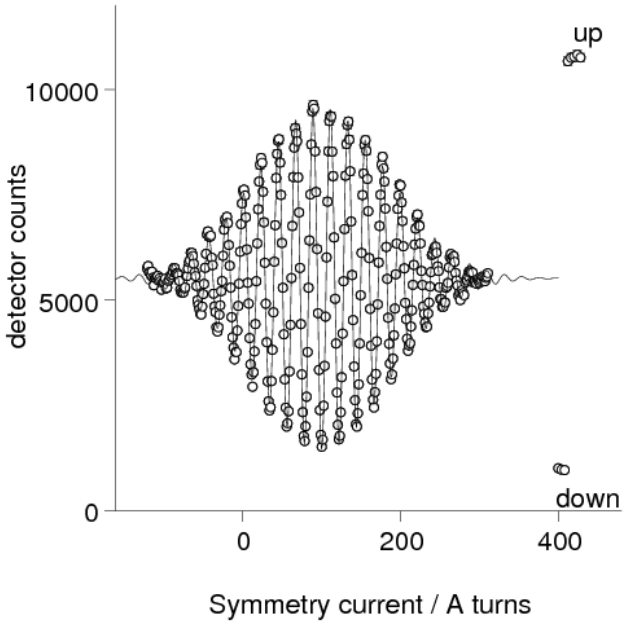

Fig. 2: Echo group measured with the NSE instrument.

For a given wavelength the Fourier time range is limited to the short times (about 3 ps for J-NSE instrument @ MLZ) by the lower limit of the field integral and to long times by the maximum achievable field integral $J = \int Bdl$. The lower limit results from the lowest field values that are needed as “guide” field in order to prevent neutrons from depolarization effects. The upper limit results either from the maximum field that can be produced by the main solenoid, or by the maximum field integral inhomogeniety ($\rightarrow$ variation of precession angle between different paths within the neutron beam) that can be tolerated respectively corrected for, depending which condition applies first. The J-NSE may achieve a $J = 1$ Tm corresponding to t = 96 ns at λ = 8 Å.

The scattering vector Q is determined by the angle 2θ of the second arm of the spectrometer with respect to the first one by $Q = 4\pi/\lambda \sin(\theta)$ (Bragg equation). The Fourier time t is proportional to the magnetic field of the main solenoids. At a given scattering vector Q, the magnetic field is successively increased and an echo group is recorded for each setting to obtain $I(Q, t)$ as a function of t.

2.1 Separation of coherent and incoherent scattering

By the use of polarized neutrons it is possible to separate the coherent and spin incoherent part of the scattering, since the incoherent scattering changes the polarisation to $-1/3$. For different scattering vectors Q the scattering intensity is measured, once in the spin-up configuration and once in the spin-down setup. In the spin-up configuration all spin flippers are switched off and the longitudinal, in forward direction (i.e. parallel to the magnetic field) polarized beam can pass through the spectrometer. The analyzer in front of the detector transmits those polarized neutrons. The measured intensity at the detector in this configuration is the maximum possible intensity. In the spin-down configuration only the π flipper at the sample position is switched on, which rotates the neutron spin orientation by $180°$. The spin direction is now against the magnetic field direction and in the ideal case the analyzer completely absorbs the neutrons, so that the minimal possible detector intensity is measured. Omitting background effects and assuming perfect flipping ratio (ratio spin-up/spin-down = ∞ in the direct beam) coherent and incoherent scattering contributions can be separated as follow (with Up: detector intensity in the diffraction run with all flippers off, $Down$: detector intensity in the diffraction run with only π flipper at sample position on, I_{coh}: coherent scattered intensity, I_{inc}: incoherent scattered intensity):

$$Up + Down = I_{coh} + I_{inc} \tag{1}$$

$$Up - Down = I_{coh} - 1/3 I_{inc} \tag{2}$$

which gives

$$Up = I_{coh} + 1/3 I_{inc} \tag{3}$$

$$Down = 2/3 I_{inc} \tag{4}$$

respectively

$$I_{inc} = 3/2 Down \tag{5}$$

$$I_{coh} = Up - 1/2 Down \tag{6}$$

To include non-ideal flipping ratio and background count rate the calculation is more difficult.

3 Polymer dynamics

There are different models to describe the dynamics of large molecules. A nice overview is given in the book "Neutron Spin Echo in Polymer Systems", which is also available online [4], as well as in laboratory course lectures, chapter 13.

The conformation of a linear polymer chain follows a random walk, this means a chain segment of length l can move freely around the neighboring segment (within the limitation of chemical

bonds). With a set of segment vectors $\mathbf{r}_n = \mathbf{R}_n - \mathbf{R}_{n-1}$, where $\mathbf{R}_n$ is the position vector of segment n, the distance between segments, which are n steps apart, follows a Gaussian distribution [4]:

$$\Phi(R,n) = \left(\frac{3}{2\pi n l^2}\right)^{3/2} \exp\left(-\frac{3R^2}{2nl^2}\right) \tag{7}$$

with l the segment length.

By summing up the scattering amplitudes of the centres of the segments of a polymer chain with the correct phases, one obtains the scattering function of the polymer chain (see Lecture on Dynamics of Macromolecules for more details):

$$I(Q,t) = \langle \sum_{n,m=1}^{N} \exp[i\mathbf{Q}\cdot(\mathbf{R}_n(t) - \mathbf{R}_m(t))]\rangle \tag{8}$$

A snapshot of the chain, i.e. the static structure factor, is obtained for $t = 0$. One gets the well known Debye funktion:

$$I(Q) = N f_{Debye}(Q^2 R_g^2) \tag{9}$$

$$f_{Debye}(x) = \frac{2}{x^2}(e^{-x} - 1 + x) \tag{10}$$

with R_g the radius of gyration of the chain.

3.1 Rouse dynamics

In the Rouse model the Gausssian polymer chain is described as beads connected by springs. The springs correspond to the entropic forces between the beads and the distance between the beads corresponds to the segment length of the polymer. The polymer chain is in a heat bath. The Rouse model describes the movement of the single chain segments of such a polymer chain as Brownian movement. Thermally activated fluctuations (by the stochastic force $\mathbf{f}_n(t)$ with $< \mathbf{f}_n(t) >= 0$), friction force (with friction coefficient ζ) and the entropic force determine the relaxation of polymer chains.

The movement of the chain segments is described by a Langevin equation:

$$\zeta\frac{d\mathbf{R}_n}{dt} + \frac{\partial U}{\partial \mathbf{R}_n} = \mathbf{f}_n(t) \tag{11}$$

The Langevin equation can be solved and one can calculate with equation 8 the intermediate scattering function, which is measured by NSE (for details, see the lecture on "Dynamics of Macromolecules"):

$$I(Q,t) = \exp(-Q^2 Dt) I_{intern}(Q,t) \tag{12}$$

with a diffusive part with a relaxation rate proportional to Q^2 and the part describing the internal relaxation, which can be written for $QR_G >> 1$:

$$I_{intern}(Q,t) = \frac{12}{Q^2 l^2}\int_0^\infty du \exp(-u - \sqrt{(\Gamma_Q t)}h(u/\sqrt{(\Gamma_Q t)})) \tag{13}$$

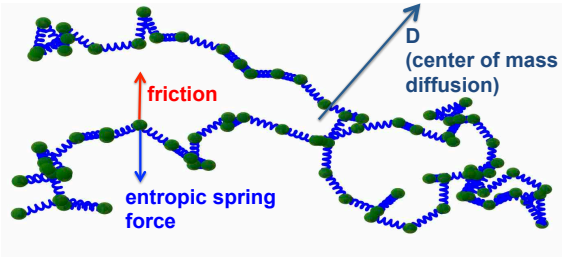

Fig. 3: Schematic representation of the polymer chain in the Rouse model [4] as a Gaussian chain with beads connected by springs.

with the relaxation rate

$$\Gamma_Q = \frac{k_B T}{12\zeta} Q^4 l^2 \tag{14}$$

and

$$h(u) = \frac{2}{\pi} \int dx \cos(xu)(1 - e^{-x^2})/x^2 \tag{15}$$

Note that the local relaxation rate depends on Q^4. When $I(Q,t)/I(Q,0)$ is plotted against the Rouse variable $\sqrt{\Gamma_Q t}$, all curves collapse onto a master curve if the Rouse model holds.

With this model, for example, the dynamics of short polymer chains in the melt can be described. With increasing molecular weight some other effects like the constraints imposed by mutual entanglements of the polymer chains become important, which are described in the reptation model by de Gennes (Nobel prize 1991). In this experiment polymers in solution, not in the melt, are considered. The Rouse model then needs to be extended by hydrodynamic interactions as will be described in the following section.

3.2 Zimm dynamics

Polymers in solution can be described by the Zimm model, where hydrodynamic interaction between the chain segments mediated by the solvent are dominant. Moving chain segments exert forces on other segments due to the flow of the surrounding solvent. Within some approximations the system can be described by a Langevin equation analogous to that of the Rouse model which includes the friction coefficient $\xi = 6\pi\eta a_{seg}$ with η the viscosity of the solvent. The main modification is the inclusion of the hydrodynamic interaction represented by an Oseen tensor to account for the forces acting to neighbouring beads via the flow field of the solvent. More details can be found in Reference [4].

The intermediate scattering function can be written again in the form of Equation 12, with a global diffusion of the whole particle, and the internal polymer fluctuations $I_{intern}(Q,t)$. An approximation to $I_{intern}(Q,t)$ of the Zimm model is a stretched exponential function which reads

$$I_{intern}(Q,t) = \exp\left(-\left(\frac{k_B T Q^3 t}{6\pi\eta b}\right)^{\beta}\right) \tag{16}$$

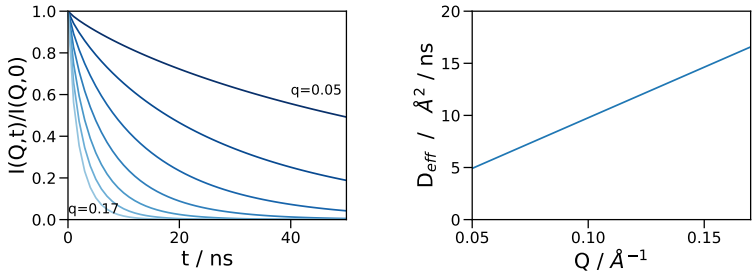

Fig. 4: Calculated I(Q,t) with the Zimm model (left) and resulting effective diffusion (Γ/Q^2).

with $b \simeq 1.354$ and $\beta \simeq 0.85$. The relaxation rate of a polymer chain in this model, $\Gamma = k_B T Q^3/(6\pi\eta)$, is mainly determined by the viscosity of the solvent. Internal dynamics is dominant at higher scattering vectors Q, where also the typical Q^3 dependence of the relaxation rate can be observed. At smaller scattering vectors the contribution from the center of mass diffusion is more prominent so that rather a Q^2 dependence of the relaxation rate is expected.

Figure 3.2 shows the calculated I(Q,t) for a series of Q-values (i.e. scattering angles instrument) which will be measured in the labcourse with the NSE spectrometer, together with the resulting relaxation rate divided by Q^2. This should be constant for simple diffusing processes. The linear increase indicates the Q^3-depencence which is characteristic for Zimm dynamcis.

3.3 Center of mass diffusion

With NSE spectroscopy the movements on length scales in the order of nanometer and time scales in the order of nanoseconds can be observed. This matches e.g. the center of mass diffusion of macromolecules in solution or micelles. The mean square displacement of a particle is $< r^2(t) >= 6 D_{CM} t$ with the diffusion constant $D_{CM} = k_B T/(6\pi\eta R_G)$, where R_G is the hydrodynamic particle radius and η the viscosity (Stokes-Einstein-relation). The dynamic structure factor which is measured by NSE is then

$$I(Q,t)/I(Q,0) = \exp\left(-1/6 < r^2(t) > Q^2\right) = \exp\left(-D_{CM} Q^2 t\right) \tag{17}$$

This result can be obtained again by the Langevin equation of a particle undergoing Brownian motion in a solvent. A simple diffusion process therefore has a quadratic dependence on the the scattering vector Q.

4 Preparatory exercises

1. How fast do neutrons with a wavelength of 8 Å fly?
2. What is the value of the earth’s magnetic field?

3. What is the magnetic field at the surface of a common permanent magnet?
4. How many mm fall neutrons on their way from the entrance of the spectrometer to the detector (about 7 m) due to gravity?
5. How many precessions does a neutron of $\lambda = 8$ Å perform in the main coils if the Fourier time is set to 20 ns? (Angle $\Psi = \gamma/v \int Bdl$).

5 Experiment procedure

5.1 The experiment itself

First, the function of the key components of the neutron spin-echo spectrometer will be explained and demonstrated.

The generation of the "Spin Echo" will be demonstrated with an auxiliary phase coil, wound around one of the main precession coils with a simple wire. With a laboratory DC-powersupply connected to this coil, the magnetic field inside this main coil is slightly varied. A fully symmetrical setup with identical magnetic path integrals in both main coils results in a maximum count rate at the detector. Increasing the current in the auxiliary coil from this point results in an additional phase shift of the neutron spin and thus the intensity varies from the maximum to a minimum and further to the next maximum and so on. In this way, the echo group is scanned.

- The frequency of the oscillation (i.e. the current needed to go from one intensity maximum to the next maximum), depends on the field integral and on the wavelength of the neutrons. Approximating the field integral of a current loop allows thus to determine the wavelength of the neutrons in this experiment. This will be done with the recorded data.

The experimental sample under investigation is a polymer chain (PEP, polyethylenepropylene) with a molecular weight of 100 kg/mol in solution (deuterated decane). The PEP concentration is 3 wt %. The first experiment with the sample is to measure the elastic scattering by recording the spin-up and spin-down intensity at the detector.

- The coherent and incoherent scattering of the sample shall be extracted from this reading and plotted versus the scattering vector Q.

The dynamics of the sample is measured. For some selected scattering vectors Q, a series of Fourier times is measured for the sample, for a background sample containing everything but the objects under investigation, in this case the pure deuterated solvent (d-decane), and for an elastic scatterer as reference.

5.2 Data reduction

Each Fourier time is determined by measuring 2-3 oscillations of the echo bunch and fitting the theoretical curve (a cosine oscillation with a gaussian envelope) to the measured points.

In short, the normalized amplitude of the fitted curve is the degree of polarization obtained in this measurement. This elaborated fitting procedure is done with a program called `drspine`, which creates the files containing the intermediate scattering function $I(Q,t)/I(Q,0)$.

5.3 Data evaluation

The $I(Q,t)$ vs. t is contained in the files report_XXXXX.dtr as ascii-data.

- Read in the data with some data treatment program (e.g. free software `qtisas`: `https://www.qtisas.com`).
- Try to fit the data. First use a simple exponential function $I(Q,t) = A\exp(-\Gamma t)$ and determine the relaxation rate Γ. For diffusion like behaviour with the Stokes-Einstein diffusion coefficient, $\Gamma = DQ^2$ should be valid. Plot Γ/Q^2 vs. Q to check the validity of the model. It also allows for the determiation of the hydrodynamic radius of the particle assuming a viscosity of d-decane of $\eta = 0.954 \times 10^{-3}$ kg/(ms).
- Use a stretched exponential function as model function: $I(Q,t) = A\exp(-[\Gamma t]^{\beta})$ and determine the relaxation rate Γ and the stretching exponent β. The Zimm model would predict that the rate depends on the viscosity η as $\Gamma = k_B T/(6\pi\eta)Q^3$. What is the viscosity of d-decane? Does the Q-dependence of the model describes that of the data correctly (i.e. is $\Gamma/Q^3 = const.$)?

6 Experiment related exercises

Data evaluation (the bullet points in section 5):

1. Separate coherent and incoherent scattering from the elastic scan (diffrun) and plot it.
2. Evaluate the data containing $I(Q,t)/I(Q,0)$ vs t with the models as described in the previous section and discuss the results.

General questions:

1. Why are no iron yoke magnets used in the construction of a NSE spectrometer?
2. What is the maximum field inside the main precession coils of the J-NSE?
3. What determines the resolution of the spin echo spectrometer?
4. How does the signal look like if the scattering is spin-incoherent? (Hint: in this case 2/3 of all neutron spins get flipped in the scattering process.)
5. What is the measured effect of the spin echo spectrometer?
6. What is measured finally?

7 J-NSE Training environment

Data reduction and evaluation of the NSE labcourse experiment can be done in the training environment at `https://training.mlz-garching.de/jcns/` where the j-nse relevant data and evaluation software is available in a linux container running in the browser.

The following section describes the basics of the j-nse data structure, data reduction and evaluation and serves as a guideline for the practical part of the labcourse.

7.1 Log into the labcourse training environment

Training environment: http://training.mlz-garching.de/jcns/ User name: will be given during labcourse pwd: will be given during labcourse

1) open terminal emulator (top: Applications -> terminal emulator)
2) `cd` brings you to home directory
3) `cd data` brings you to the directory with the labcourse data
4) `jupyter lab` starts jupyter lab in a web browser.
5) Start the two notebooks `DrSpineMacroGenerator.ipynb` and `pep100_labtest.ipynb`
6) Inside the notebooks: execute the cells with code with shift-ENTER

The notebooks and data reduction tools available here and described in more detail below can be used to get a deeper insight into the working principle of neutron spin echo spectroscopy and in the workflow of data reduction.

7.2 Look at the raw data

In the file browser of the jupyter lab on the left, you can click on the different files and view them in a jupyter sub-tab.

Look at

- `m20104.echo`: raw ascii data of a scan: a single scattering vector q, multiple Fourier times t (=B-Field-setting), at each Fourier time t a scan of the phase coil to record the echo. At each point of the phase coil scan, a detector image (32x32 pixels = 1024 pixels).
- `m20104_ActC4mmQ0.10t0.989ns.dat`: extract of one Fourier time for quick plotting. First column: current in phase coil, then anode signal (detector sum), different sensors (B, Temp) and detector areas.
- `mxx.echo.directory`: Short description of all scans at the instrument (here, extract of the full mxx.echo.directory file). “Electronic labbook”.
- `diffract.run`: diffraction only, with ‘spin up’ (column 7) and ‘spin down’ (column 12) configuation as a function of q (second column). Can serve as polarized diffraction to extract coherent and incoherent intensity (*one labcourse task, see above*). Mainly for assessing the required measurement time.

7.3 Data reduction: From Detector Images to I(Q,t)

1) Prepare macro for drspine data reduction programm:

   - go to `DrSpineMacroGenerator.ipynb` tab in jupyter lab. Select refs, sample, bgr according to the entries in the mxx.echo.directory (refs: 19968-70, sample 19971-73, bgr 19974-76).
   - “Create macro”
   - possibly execute it right away within the script, BUT: more insight with separate execution
   - if you execute it, also execute the two cells at the end with the pdflatex and the qpdfview command to get the pdf report.

2) open another Terminal, `cd`, `cd data`, then call `$HOME/local/bin/drspine` and within the program then the created macro `macname1` (or the name you gave). Already prepared macro: `drpep` in case the macro generation fails.

3) A pdf with the report of the evaluation opens with details concerning the fits, but also some “standard evaluation” of the intermediate scattering function I(q,t).

If the pdf report does not open (for the macro generator this is the case) call `pdflatex report19971_1.tex` followed by `qpdfview-qt5 report19971_1.pdf` in the terminal window or directly in drspine. -BUT BEFORE: Study the details below:

7.3.1 Details of data reduction

First check: required python environment installation? Call

`sh $HOME/local/bin/drspine_create_env.sh` and
`source $HOME/local/bin/drspine_activate.sh`
in a Terminal window.

These two commands are in `cd`, `cd drspine`, `tail -15 INSTALL.md`

(If you changed to the drspine directory, don’t forget to navigate back to the data directory with `cd`, `cd data`)

With
`alias drspine='$HOME/local/bin/drspine'`
starting drspine gets a bit easier (just `drspine` instead of the path.

Details which can be studied: with the drspine program: call
`dump`
to save all fitting details.

Echo fits across the 2D detector, e.g. for the reference:
`drspine --> plot fits run 19969 tau 1`
(then the python command line opens, from there, the same things can be called with:)

```
plot_fits('./fits_19969',tau=1,npix=8,)
```

Troubleshooting in case the fits do not work: Reinstall the ipython environment with the following commands:
`cd, cd .ipython rm -rf profile_drspine/`
Then reinstall the profile with
`sh $HOME/local/bin/drspine_create_env.sh`
`source $HOME/local/bin/drspine_activate.sh`
see above. Then it should work.

High fourier time (good echos throughout the detector, since it is an elastic scatterer, with some reduction in polarization due to imperfections of the instrument):

```
drspine/plot [2]: plot_fits('./fits_19969',tau=10,npix=8,)
```

PEP polymer in deuterated decane, low fourier time (good echos throughout the detector):

```
drspine/plot [2]: plot_fits('./fits_19972',tau=1,npix=8,)
```

Hig fourier time: (already fainted echos throughout the detector due to the decay in I(q,t)):

```
drspine/plot [2]: plot_fits('./fits_19972',tau=10,npix=8,)
```

Deuterated decane, low fourier time: Already almost no echco, dynamics so fast that everything already decayed; much weaker intensity:

```
drspine/plot [2]: plot_fits('./fits_19975',tau=1,npix=8,)
```

Close python command line with ctrl-d, quit drspine with `quit`.

create pdf report (if not done automatically): 1) pdflatex report...tex 2) qpdfview-qt5 report...pdf

7.4 Final data: I(q,t)

Ascii results of I(q,t) vs t for different sets of q are in the .dtr files and also in last_sqt.dat. The pdf report contains a tentative “standard” analysis. Further analysis can then be done by fitting the datasets with some model, e.g. with jupyter notebooks, origin, qtisas (a free origin clone adapted to scattering).

Follow data evaluation suggestions from section .

7.5 Data evaluation and fitting example

The notebook `pep100_labtest.ipynb` gives an example of some fits with different models to the data.

Note: if there are remaining calls to dpd (commands starting with dpd.xxx), just delete “dpd.” and re-execute the cell.

References

[1] F. Mezei, *The principles of neutron spin echo*, in *Neutron spin echo*, pp. 1–26 (Springer, 1980).

[2] M. Monkenbusch, R. Schätzler, D. Richter, *The Jülich neutron spin-echo spectrometer—Design and performance*, Nuclear Instruments and Methods in Physics Research Section A: Accelerators, Spectrometers, Detectors and Associated Equipment **399**, 301 (1997).

[3] S. Pasini, O. Holderer, T. Kozielewski, D. Richter, M. Monkenbusch, *J-NSE-Phoenix, a neutron spin-echo spectrometer with optimized superconducting precession coils at the MLZ in Garching*, Review of Scientific Instruments **90**, doi:10.1063/1.5084303 (2019).

[4] D. Richter, M. Monkenbusch, A. Arbe, J. Colmenero, *Neutron spin echo in polymer systems*, in *Neutron Spin Echo in Polymer Systems*, pp. 1–221 (Springer, 2005).

Contact

J-NSE “PHOENIX”

Phone: 089/158860-506
Web: https://mlz-garching.de/j-nse

Olaf Holderer

Jülich Centre for Neutron Science
at Heinz Maier-Leibnitz Zentrum
Phone: +49 89/158860-707
e-Mail: o.holderer@fz-juelich.de

KWS-1 & KWS-2

Small Angle Neutron Scattering

Henrich Frielinghaus, Marie-Sousai Appavou

Jülich Centre for Neutron Science
Forschungszentrum Jülich

Manual of the JCNS Laboratory Course Neutron Scattering

Contents

Fig. 1: *Representation of the protein lysozyme, which has a very compact form.*

Fig. 2: *A spherical colloidal particle is the second sample of choice.*

1 Introduction

The objective of this lab course is to clarify the essential concepts of small-angle neutron scattering. Structures are only visible by a scattering experiment if there is an appropriate contrast. For neutrons one often uses the exchange of ^{1}H by ^{2}H = D, i.e. deuterium. The chosen contrast of this lab course is achieved by using heavy water (D_2O) as solvent. The materials (solutes) are natural ones having normal protons.

The globular, compact lysozyme (Fig. 1) appears in chicken eggs and has anti-bacterial function. The molecule is charged, which leads to repulsive interactions. So there is a short range order, and the distance between the molecules can be determined.

The other sample is a dispersion of colloidal, spherical particles. The sample will be diluted such that there is no interaction between the particles. So we can determine the size of the particles by the Guinier approximation, and secondly by the first “minimum”. More details are given below.

2 Preparing solutions in Water

A lysozyme solution of 0.02g per ml of water must be prepared. We will weigh 0.02g of Lysozyme and put it into a new Packard glas. With an Eppendorf pipette we will add exactly 1 ml D_2O. These pipettes are extremely accurate with respect to the volume. From the solution about 0.5 to 0.6ml are transferred to Hellma quartz cuvettes, which are 1mm thick. For the later evaluation we need a highly accurate concentration. So all weights need to be written down as exactly as possible.

For the colloidal suspension, we will prepare a 1% solution. So we will weigh 0.01 g or polystyrene particles. Then we will again add 1 ml of D_2O.

If some samples have been already prepared (possibly from earlier groups), we may also use those without own preparation.

3 The Measurement at KWS-1 and/or KWS-2

These two solutions (suspensions) are now being measured in the small-angle neutron scattering instrument KWS-1 (or KWS-2). The wavelength of neutrons is set to 7Å. The collimation is fixed to 8m. The samples are placed as close as possible to the detector, to measure the largest Q values possible. Both samples will be measured at detector distances 2m and 8m. The offset between the sample position and the detector of about 30cm leads to effective detector distances of about 1.7m and 7.7m.

The sample holder will be filled with the two samples. In addition, the empty beam and a plexiglass plate are measured for absolute calibration. For a good statistical measurement the following times are set: 8m detector distance for 20min, and 2m detector distance 10min. The total measuring time for the 4 positions will be about 2 hours. The measurement is typically started before lunch, and can be evaluated in the afternoon. It is quite likely that an internal employee will start separate measurements during the afternoon until the next morning in order to use the valuable measuring time overnight.

4 Evaluation of the Scattering Data: Absolute Calibration

The measured data is raw data at first and describes the intensity on the detector. The data has to be corrected for the effectiveness of the different detector channels. Then the empty beam measurement is subtracted to account for the zero effect of the instrument. Then the intensities are expressed as absolute units using Eq. 5.5 and are radially averaged, because for the isotropic scattering samples, the intensity does not depend on the polar angle. To perform all these steps we will be using a software available in our institute, called QtiKWS. However, since the understanding of the Eq. 5.5, as such, is more important than the exact technical understanding of the evaluation, the results are produced relatively quickly by the software, namely, $\mathrm{d}\Sigma/d\Omega$ as a function of the scattering vector Q for our samples. This data will be provided for the students to do the final evaluation. In the following, this evaluation is described.

5 Evaluation of Lysozyme Scattering Curves

The position of the maximum $Q_{\max}$ provides information on the typical distance of the proteins in solution. This can be calculated to $\ell = 2\pi/Q_{\max}$. Knowing the weight of the protein in water (0.02g/cm^3) there is an alternative way to calculate the average distance. The molar mass of the protein is 1.43×10^4g/mol. The number density of the protein is therefore $n/V = 0.02\text{g/cm}^3/(1.43 \times 10^4\text{g/mol}) = 1.40 \times 10^{-6}\text{mol/cm}^3 = 8.42 \times 10^{-7}\text{Å}^{-3}$. For a simple cubic packing the typical distance is given by $\ell = \sqrt[3]{V/n}$. For a hexagonal close packed lattice the typical distance is $\ell = \sqrt[6]{16/27}\sqrt[3]{V/n}$. This distance is the minimum distance of the planes

important for the scattering experiment, and the next neighbor distance of the hexagonal c.p. lattice is $\sqrt{3/2}\,\ell = \sqrt[6]{2}\sqrt[3]{V/n}$. Both calculated distances of the cubic and hexagonal structure are to be compared with the measured one.

6 Evaluation of the Scattering from Colloidal Particles

In a first step we have to prepare the scattering data for background subtraction. We plot the original data of the two detector distances in a log-log plot, i.e. $\log_{10}(d\Sigma/d\Omega) \rightarrow \log_{10} Q$. After this, we will see a plateau at high Q which indicates the constant incoherent scattering. Taking the average of the last (say 10) points will give us the estimate of the background. A new column with the background subtracted will be generated for the 8m and 2m measurements. Finally, the two data sets should be combined to yield a single data set.

Now, we will aim at the overall appearance of the colloids, i.e. we will determine the particle dimension. For this purpose the Guinier approximation can be applied. The general appearance of the Gunier scattering law was already given in eq. 5.35 and reads:

$$\frac{d\Sigma}{d\Omega}(\mathbf{Q}\rightarrow 0) = \frac{d\Sigma}{d\Omega}(0) \cdot \exp\left(-\frac{1}{3}Q^2 R_g^2\right) \tag{1}$$

For this purpose we plot the logarithm of the background corrected intensity against the square of the scattering vector, i.e. $\ln(d\Sigma/d\Omega) \rightarrow Q^2$. The highest Q will lead to large values that we are not interested in. So the plot has to be truncated to the rather small Q, say $Q^2 = 0..4 \times 10^{-4}\text{Å}^{-2}$. Here, we do a linear regression and take the slope S as a result only. It has the units Å^2. From this we can calculate the radius of gyration using $R_g = \sqrt{-3S}$. Then, the relation to the full radius is used, i.e. $R = \sqrt{\frac{5}{3}} R_g$.

If the concentration was too high, or there are weak electrostatic repulsive interactions, we will try to apply the structure and formfactor fit. The presence of a structure factor can be seen by lower scattering intensities at smallest Q compared to slightly higher Q, i.e. there is a maximum in the scattering that would not be there without interactions. We will then have:

$$\frac{d\Sigma}{d\Omega}(\mathbf{Q}) = \frac{d\Sigma}{d\Omega}(0) \cdot S(Q) \cdot F(Q) \tag{2}$$

For the formfactor, we will take the ideal sphere expression:

$$F(Q) = \left[3\frac{\sin(QR) - QR\cos(QR)}{(QR)^3}\right]^2 \tag{3}$$

For the two particle structure factor we will then find the approximation:

$$S(Q) = 1 - 8\phi \cdot \left[3\frac{\sin(2QR) - 2QR\cos(2QR)}{(2QR)^3}\right] \tag{4}$$

The full expression will then be fitted to the whole scattering curve, and the radius will be one parameter that we obtain.

Then, we will try to read the Q-value of the first “minimum”. Due to smearing effects of the reolution and polydispersity, the “minimum” may only weakly be formed as a weak dip. The radius is now obtained from $R = 4.493/Q_{\min}$.

The last evaluation method will be the Porod scattering at high Q. It applies for any shape of particles with a smooth surface. Here the many heavily oscillating fringes are smeared out, such that the scattering has a simple power law:

$$\frac{d\Sigma}{d\Omega}(\mathbf{Q}) = P \cdot Q^{-4} = \frac{9}{2} \cdot \frac{d\Sigma}{d\Omega}(0) \cdot (QR)^{-4} \tag{5}$$

So, we need to determine the forward scattering from our previous evaluations, and read the coefficient P from a log-log plot of the intensity versus the scattering vector Q.

After we have obtained three different versions of the radius R, they should be compared and discussed. The imperfections of the different evaluations should have become clear by the use of the different approaches.

7 Preparatory Exercises

(I) Lysozyme in D_2O

The first sample of the Neutron Lab Course at the SANS instrument KWS-1 (KWS-2) will be Lysozyme in heavy water (D_2O). This protein is rather globular (diameter ca. 5 nm). The Coulomb interactions of this charged molecule lead to liquid-like short-range-ordering. This will be observed in the SANS scattering experiment by a correlation peak. Simple estimations will be made now:

1. Give the connection between the number density ϕ and the unit cell parameter assuming a simple cubic lattice!
2. The chemical concentration c is usually given in g/L or mg/ml. The molar mass of the molecule is 14307g/mol. What is the connection between the chemical concentration and the number density?
3. The correlation peak appears at a scattering vector $Q_{\max}$. How would it relate to the unit cell parameter of a simple cubic lattice? What is the dependence of $Q_{\max}$ as a function of the chemical concentration c?
4. Please rationalize the relations of the hexagonal close packed lattice with respect to the cubic packing! The spacing of the planes is shorter by a value of rougly 0.916 (larger Q value compared to cubic). The nearest neighbor has a larger distance of ca. 1.122 times the cubic packing.

(II) Colloidal Dispersion

The different approaches for the size determination is the main subject here.

1. The Appendix B derived the Guinier scattering law for any shape of particles while in the main manuscript the first application was the compact sphere. What is the general meaning of the radius of gyration R_g? What is the general understanding for other shapes of particles?
2. At large Q we observe a constant background from incoherent scattering. The hydrogen atom has a incoherent cross section of 80×10^{-24}cm^2, and the deuterium atom 2×10^{-24}cm^2. The concentration of hydrogen from the particles is roughly 100 times smaller than the concentration of deuterium from the heavy water. On the basis of these numbers estimate the ratio of background from the particles and the solvent!
3. We came across the Porod scattering at high Q for the spheres with smooth surfaces. The original expression for the scattering would describe heavy oscillations at high Q. Why does this part of the scattering curve smear out such that a simple power law is remaining? This reason holds for any type of power law at high Q.

Contact

KWS-1 & KWS-2

Phone: +49-89-158860-324 & +49-89-158860-326
Web: http://www.mlz-garching.de/kws-1
http://www.mlz-garching.de/kws-2

Henrich Frielinghaus

Jülich Centre for Neutron Science
Forschungszentrum Jülich GmbH
at Heinz Maier-Leibnitz Zentrum
Lichtenbergstrasse 1
D-85747 Garching, Germany

Phone: +49-89-158860-706
e-Mail: H.Frielinghaus@fz-juelich.de

Aurel Radulescu

Phone: +49-89-158860-712
e-Mail: A.Radulescu@fz-juelich.de

Artem Feoktystov

Phone: +49-89-158860-746
e-Mail: A.Feoktystov@fz-juelich.de

Marie-Sousai Appavou

Phone: +49-89-158860-747
e-Mail: M.S.Appavou@fz-juelich.de

Zakaria Mahhouti

Phone: +49-89-158860-805
e-Mail: Z.Mahhouti@fz-juelich.de

Jia-Jhen Kang

Phone: +49-89-158860-739
e-Mail: J.Kang@fz-juelich.de

KWS-3

Very Small Angle Neutron Scattering Diffractometer with Focusing Mirror

Vitaliy Pipich and Baohu Wu

Jülich Centre for Neutron Science
Forschungszentrum Jülich

Contents

1 Introduction

KWS-3 is a very small angle neutron scattering (VSANS) diffractometer using focusing mirror to achieve a high Q-resolution $3 \cdot 10^{-5} Å^{-1}$. In "standard mode" with Q-range between 10^{-4} and $2.5 \cdot 10^{-3} Å^{-1}$ KWS-3 demonstrates worldwide best performance: flux much higher than any pinhole SANS instrument and measurement time much shorter than at any double crystal diffractometer (Ultra-SANS=USANS). The high brilliance FRM-II reactor in Garching allowed for the increase in neutron flux by more than forty times in comparison to flux in Jülich before relocation. A number of improvements have been carried out during the last years. Integration of the second detector with almost three times better space resolution and of second sample position at 1.3m sample-to-detector distance extended Q-range in both directions. Currently, Q-range of KWS-3 covers almost three decays from $3 \cdot 10^{-5}$ to $2.5 \cdot 10^{-2}$ $Å^{-1}$ with polarized or non-polarized neutrons.

USANS and SANS experiments are performed by two different types of instruments to cover a combined Q-range from 10^{-5} $Å^{-1}$ up to 1 $Å^{-1}$. In principle, the Q-ranges of both instrument classes are overlapped. Typical USANS instruments like S18 (ILL) or PCD (NIST) may reach maximum Q-vectors of $5 \cdot 10^{-3}$ $Å^{-1}$. The disadvantage of these instruments is that they do not allow taking a full area image on a 2D position sensitive detector. On the other hand, the well-known pinhole instrument D11 at Institute Laue-Langevin (ILL) reaches a minimum Q-vector of $4 \cdot 10^{-4}$ $Å^{-1}$ by use of largest possible wavelength 22 Å and sample-to-detector distances (> 40 m). But the required instrumental settings push both types of instruments to their limits, mainly due to signal-to-noise level and the reduced flux at sample position. To overcome this intensity problem several VSANS technics were introduced as additional elements of a pinhole SANS instrument like neutron lenses (material and magnetic), multi-beam collimators (pinhole and slit geometry; single- and multi-point) [1]. An alternative design is realized by the KWS-3 instrument [2]. KWS-3 is designed from scratch as a VSANS instrument without default pinhole option. In Figure 1(a) optimal Q-ranges for different small angle technics are shown. Figure 1(b) demonstrates neutron intensity gain of VSANS (KWS-3) instrument in comparison to best SANS and USANS diffractometers.

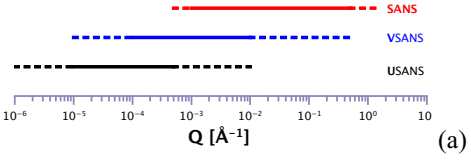

(a)

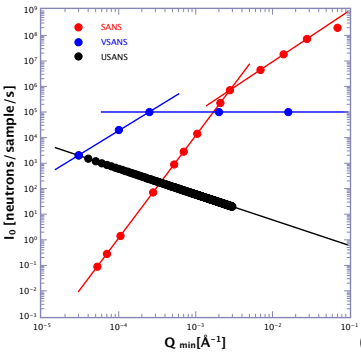

(b)

Figure 1: (a) optimal Q-ranges of different small angle technics; solid lines correspond to optimal configurations and dashed lines to "reachable" Q-ranges where only strongly scattered samples could be measured; (b) "illustrative" plot of neutron intensities per sample for given minimum Q.

The increasing need for these intermediate Q-vectors arises from the growing interest in biological and colloidal samples, which partially deal with length scales in the μm range. An investigation of the multilevel structures in partially crystalline polymer solutions performed using a combination of those three above depicted types of SANS instruments can be found in [3].

The principle of KWS-3 instrument is an one-to-one image of an entrance aperture onto a 2D position-sensitive detector by neutron reflection from a double-focusing toroidal mirror as shown in Figure 2(left). The main innovation and challenge of KWS-3 was to build a large mirror having a shape as close as possible to an ellipsoid and surface roughness less than 5 Å. The dimension of the toroidal mirror is 120×12×5 cm^3 thick double focusing mirror of 11 m focal length. At such a short mirror length with respect to the focal length, the toroidal shape is a good enough approximation to an elliptical shape. The reflection plane has been chosen to be horizontal, reducing the deterioration of the image due to gravity. Photo of the mirror is shown in Figure 2 (right).

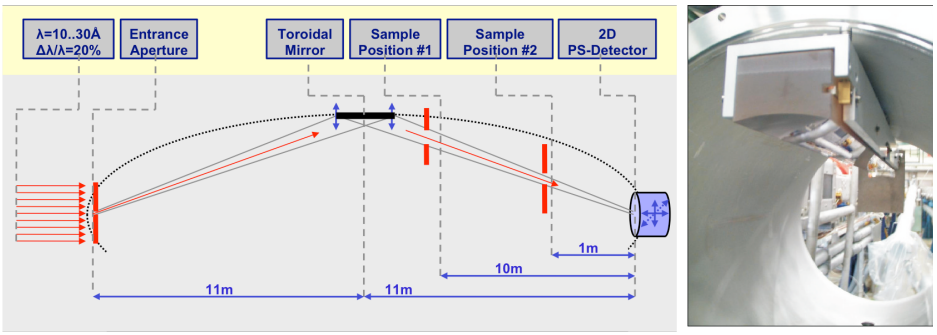

Figure 2: (left) layout of KWS-3; (right) toroidal mirror installed in the vacuum chamber.

KWS-3 is optimized for VSANS range from $3.0 \cdot 10^{-5}$ to $2.5 \cdot 10^{-2}$ $Å^{-1}$. For last cold source filling and instrument configuration the flux at the sample position (and detector) is near **25000** counts per full sample (λ = 12.8 Å , $\Delta\lambda/\lambda$ =16%, 2x2 mm^2 entrance aperture, 20x80 mm^2 beam size and sample-to-detector distance is around 9.5 m). The instrument's standard configuration with a 9.5 m sample-to-detector distance (SD) allows performing scattering experiments with Q range between $3.0 \cdot 10^{-5}$ and $2.5 \cdot 10^{-3}$ $Å^{-1}$. A second sample position at 1.3 m SD reaches the Q-range to $1.5 \cdot 10^{-3}$ – $2 \cdot 10^{-2}$ $Å^{-1}$ and can overlap with the classical pinhole SANS instruments (KWS-1/2). Another "mobile" sample position could be installed to adapt a sophisticated sample environment between 8 and 2 m SD. Thus the length scale that can be analyzed by VSANS at KWS-3 goes beyond 20 μm.

2 VSANS applications

All applications of the classical SANS could be investigated by VSANS by taking into account Q-resolution of VSANS. The conventional fields of application of very small angle scattering studies are:

- particles in solution [protein & colloidal aggregates, polymers, micelles, ceramics];
- porous materials [cement, paste, rocks, coal etc.];
- inhomogeneous metallic alloys;
- bulk samples with artificial regular structure [phase gratings];
- hierarchical structures of biominerals hydrogels and aerogels;
- rheology and structure/morphology of complex fluids;
- magnetic scattering [with polarized and non-polarized neutrons];

and other inhomogeneities on a size range from 30 nm to 20 μm, often in addition to SANS spectra, but also diffraction, reflection and refraction studies on surfaces.

3 Preparatory Exercises

1. The contrast variation (CV) is a very important feature of the neutron scattering. What is the scattering length density (SLD) ρ? How to calculate the SLD? What is the definition of the scattering contrast Δρ? How to carry out the contrast variation experiment in case of an aqueous solution of particles?
2. The standard Q-range of KWS-3 is from $4.0 \cdot 10^{-5}$ to $2 \cdot 10^{-2}$ $Å^{-1}$. What the size of particles could be investigated in this Q-range? What are the form factor P(Q) and structure factor S(Q)? In which case the scattering intensity $d\Sigma/d\Omega(Q)$ could be represented as a product of the structure factor and form factor $d\Sigma/d\Omega(Q) = d\Sigma/d\Omega(0) \cdot P(Q) \cdot S(Q)$? What is the physical "content" of the forward scattering $d\Sigma/d\Omega(0)$ [I(0)]?
3. The standard wavelength at KWS-3 is 12.8 Å. What are disadvantages of this wavelength? What should we correctly select before sample preparation?
4. What is the difference between pine-hole SANS and focused SANS? Could you estimate the length of a pine-hole SANS instrument with Q-resolution from 10^{-4} to $3 \cdot 10^{-3}$ $Å^{-1}$ and the beam-size 16 cm^2?

4 Experiment Procedure

Before the VSANS experiment: The key to a successful VSANS experiment is to know the detailed information of the system studied. For example, for the solution samples, one may need to know the concentration, scattering contrast, the size range of the scattering, the sample volume.

During the experiment: Depending on the particle size studied, the sample volume available, the temperature and pressure required, the instrument needs to be set up specifically. After setting the optimum instrument configuration (Collimator-sample and detector-sample distances, irradiation time, sample temperature etc.), samples are measured on the sample holder with specific sample environment.

After the experiment: The raw data from an experiment of an anisotropic sample should represent the scattering of this scatterer. The data are generally corrected for the

sample and instrument geometry, detector efficiency, electronic and backgrounds, and averaged isotopically by the software QtiKWS [4].

The following experiments marked with '*' are optional. You can select the experiments considering on your background.

4.1 Suspensions of Spherical Colloidal Polystyrene Particles in Water

The measured SANS intensity (corrected for background and put on an absolute scale) for many 'particulate' systems can be expressed as

$$\frac{d\Sigma}{d\Omega}(Q) = \frac{N}{V} \tag{1}$$

Where N is the number of the particles, V is the sample irradiation volume, Δρ is the scattering contrast, V_p is the volume of the scatterer. P(Q) is the scattering form factor which describes the size and shape of the scatterers. S(Q) is the scattering structure factor (the inter-particle correlation factor) which represents the interference of neutrons scattered from different objects. In many cases when the particles concentration are very low, it is reasonable to analyse the scattering in terms of randomly oriented, non-interacting particles (i.e. we neglect the structure factor in this case and set S(Q)=1). Thus from equation 1 we can obtain the structure factor and form factor when measure several samples with different conditions, e.g. different concentration, Δρ.

Within the frame of this practicum we will explore aqueous solution of monodisperse polystyrene (PS) microspheres with diameter 8000/6000 Å and the initial concentration 1%/ 0.02%/ 0.01% of particles in H_2O. From this experiment we want to know the shape and average dimension of the particles and the particle interactions. In future, this sample will be used at KWS-3 as "a standard sample" to check the performance of instrument, absolute calibration, instrument resolution.

Table 1. Suspensions of Spherical Colloidal Polystyrene Particles in Water for practicum 4.1.

	S1	S2	S3	S4	S5
Concentration / wt%	1	0.5	0.2	0.1	1
Size / Å	8000	8000	8000	8000	6000

4.2 *Contrast Variation Experiment on Polystyrene Particles in H_2O/D_2O

In Table 2 there is collected information about PS microspheres obtained from the producer; additionally all necessary information about H_2O and D_2O is listed there.

Table 2. Parameters of used components

	Polystyrene Spheres	H_2O	D_2O
Scattering Length Density [Å^{-2}]	$1.41 \cdot 10^{-8}$	$-0.56 \cdot 10^{-8}$	$6.50 \cdot 10^{-8}$
Density, 20°C [g/cm^3]	1.05	1.0	1.05
Radius [Å]	4000±45		

The contrast variation is proposed to proceed simply by step-by-step adding of D_2O to the initial H_2O solution of spheres. To estimate how much of D_2O we should add, the simulation of the forward scattering should be done as function of D_2O concentration:

$$\frac{dS}{d\Omega}(0) = F_{\text{Spheres}} V_{\text{Spheres}} \left(\rho_{\text{Spheres}} - \rho_{\text{Water}}\right)^2,$$

where V_{Spheres} is volume of PS spheres, ρ_{Spheres} SLD of PS spheres, ρ_{Water} SLD of D_2O/H_2O mixture, Φ_{Spheres} volume fraction of PS spheres in D_2O/H_2O mixture. We could rewrite the above mentioned equation in terms of Φ_0 and Φ_{D2O}, the volume fraction of PS spheres in the initial H_2O solution and volume fraction of D_2O in D_2O/H_2O mixture respectively:

$$\frac{dS}{d\Omega}(0) = \frac{F_0(1-F_{D2O})}{1-F_0 F_{D2O}} V_{\text{Spheres}} \left[\rho_{\text{Spheres}} - \rho_{H2O} - F_{D2O}(\rho_{D2O} - \rho_{H2O})\right]^2.$$

In Figure 3 the forward scattering $d\Sigma/d\Omega(0)$ as a function of Φ_{D2O} and Φ is plotted. At the starting point of the experiment (Φ_{D2O}=0) we have PS spheres in pure H_2O and maximal volume fraction of spheres $\Phi_{\text{Spheres}} = \Phi_0 = 1\%$. Minimum of the plotted curve corresponds to the matching point of PS spheres in water. In Table 3 seven points around matching concentration are labelled with "CV" mark. In case of CV, from the scattering curves of above-mentioned samples we need to extract only "integral" parameter forward scattering to extract information about minimum of the forward scattering, and plot it as function of D_2O content.

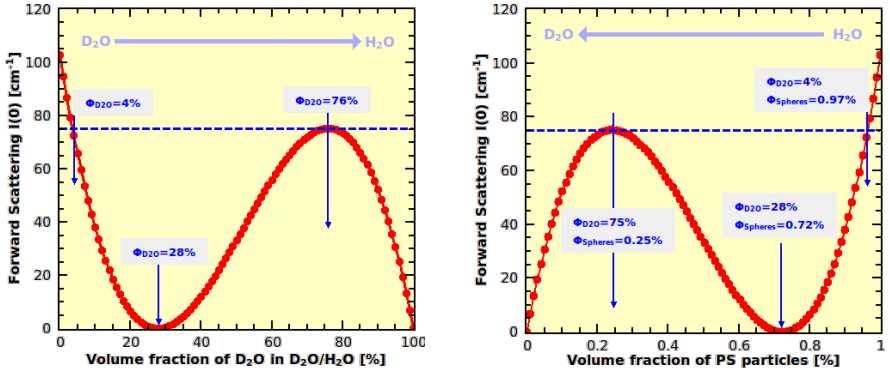

Figure 3. Forward scattering as a function of Φ_{D2O} and Φ.

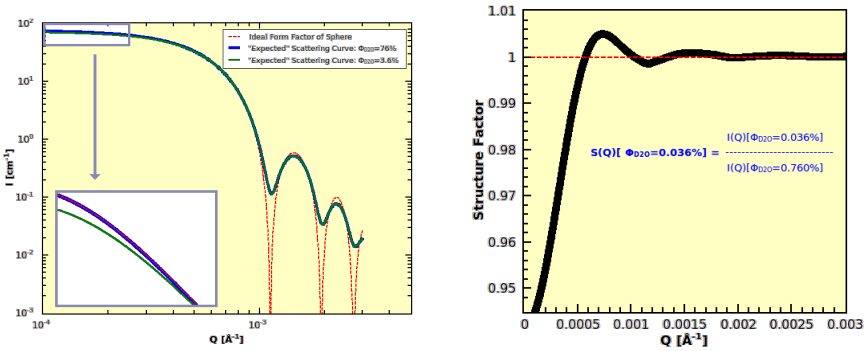

Figure 4: Expected results. (Left) the scattering signal in case of Φ_{D2O}=0.04 and 0.76. In the amplified inset is the small angle part of the calculated scattering curves. In case of Φ_{D2O}=0.04 there is clear suppression of the forward scattering due to the hard sphere interactions. Calculated scattering curve in case of the sample with Φ_{D2O}=0.76 shows no interaction term. Red curve is pure form factor of PS spheres without taking into account instrumental resolution function. (Right) Ration between Φ_{D2O}=0.04 and Φ_{D2O}=0.76 is plotted here. So the forward scattering and form factor of both sample are the same, and in case of Φ_{D2O}=0.76 sample S(Q)=1, therefore this ratio is the structure factor of Φ_{D2O}=0.04 sample.

Next step is the investigation PS spheres in case of sample with D_2O content 76% [PS content 0.25%]. This point is located at the local maximum (see Figure 3). At this level of the dilution the structure factor is definitely undetectable. Please read carefully caption of Figure 4 to understand the logic of planned experiment.

Table 3. Samples for practicum; CV: samples for the contrast variation; FF, SF: sample for form and structure factor determination.

Φ_{D2O}	0 CV	3.6 FF, SF	10 CV	20 CV	30 CV	40 CV	50 CV	60 CV	76 FF
$\Phi_{Spheres}$	1.00	0.96	0.9	0.8	0.7	0.6	0.5	0.4	0.24
I(0) [cm^{-1}]	103	75.2	38	6.5	0.47	12.01	33.2	55.9	75.2

4.3 *VSANS for Anisotropic and Periodic Samples

From the experiment 4.2 and 4.3, we discussed isotropic samples in the solution where the scattering is isotropic at the same Q value. The scattering patterns depend on the shape, size (P(Q), form factor) and ordering (S(Q), structure factor) of the scattering particles resulting in different shaped neutron scattering, mostly in circles (isotropic scattering) on the 2D detector. However, anisotropic scattering arises if the studied system contains anisotropic inhomogeneities, elongated or flattened, or certain predominant arrangement of molecules. The scattering pattern is the reciprocal “image” (Fourier transform) of the size and the arrangement of the particles (real space). If the particles in the sample are randomly oriented, the 2D scattering pattern of such a system would be a circular average and isotropic. While the particles have more or less orientation, the 2D scattering pattern becomes anisotropic. The pattern contains

additional information related to the structure which makes the small angle scattering analysis quite complicated.

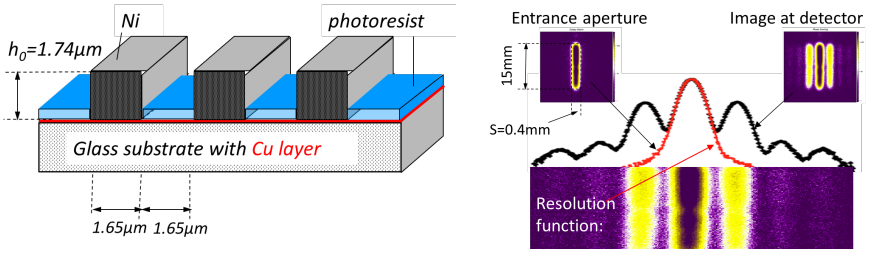

Figure 5: (Left) Electrolytic deposition of Ni on Cu coated glass substrate through photoresist mask: stripes 1.65 µm, separation 1.65 µm => period d=3.3 µm. (Right) Slit geometry of the neutron entrance aperture and 2D image at detector.

A model of Ni Grating sample is shown in Figure 5. During the experiment, we want to measure the sample using neutron beam with different geometry. From the experiment we want to measure the distance of the Ni slit in the grating. We try to understand the anisotropic and periodic samples scattering and compare to the sample measured in solutions.

5 The experiment and data reduction

All samples listed in Table1/2 we will measure without beamstop (Sample). Additionally, the empty cell (EC) and the dark current (DC) run will be measured and used for data reduction of all datasets.

What to measure?

I_{Sample}, I_{EC}, I_{DC} [counts per current pixel, normalized by monitor]

Sample transmission T (by corresponding mask we consider only primary beam):

$$T = I_{Sample}/I_{EC}$$

Empty cell and black current subtraction (for every pixel of the detector):

$$I = \left(I_{Sample} - I_{DC}\right) - T \cdot (I_{EC} - I_{DC})$$

Absolute calibration:

$$\frac{d\Sigma}{d\Omega} = \frac{I}{d \cdot T \cdot \varepsilon_D \cdot \langle I_{EC} \rangle \cdot \Delta\Omega}$$

where d sample thickness, T sample transmission, εD detector efficiency, ΔΩ solid angle per current pixel, <IEC> normalized neutron intensity at sample.

Radial averaging of the obtained matrix:

$$\frac{d\Sigma}{d\Omega} \rightarrow \frac{d\Sigma}{d\Omega}(Q)$$

6 Experiment-Related Exercises

Within our "one-day-experiment" at KWS-3 it would be nice to get as much as possible information about above mentioned sample, like:

a) in the first experiment, why it is not necessary to measure H_2O as background?
b) the form factor P(Q) of PS spheres from sample with Φ_{D2O}=0.76; "real" radius R and polydispersity of the PS microspheres;
c) the structure factor S(Q) in case of Φ_{D2O}=0.04 and decide about the interactions between spheres: could we neglect the structure factor S(Q) during data analysis?
d) the scattering length density of PS spheres by H_2O/D_2O contrast variation. At matching point, the SLD of microspheres and water are equal. Polystyrene in microspheres is amorphous or crystalline?

References

Eskilden, M. R. et al., Nature 391, 563 (2000);

Frielinghaus, H. et al., J. Appl. Cryst. 42, 681 (2009);

Alefeld, B. et al., Physica B 283, 330 (2000);

Kentzinger, E. et al., Physica B 350, e779 (2004);

Goerigk, G. et al., J. Appl. Cryst. 44, 337 (2011);

Pipich, V.; Fu, Z., *Journal of large-scale research facilities JLSRF* **2015,** *1*, A31.

Radulescu A. et al., Macromolecules 39, 6142 (2006)

V.Pipich, QtiKWS, http://www.qtikws.de.

Contact

KWS-3

Phone: 089/289-14325; 089/289-11677
Web: https://www.mlz-garching.de/kws-3

Vitaliy Pipich

Jülich Centre for Neutron Science JCNS
Forschungszentrum Jülich GmbH
Outstation at FRM II
Phone: 089/289-10710
e-Mail: v.pipich@fz-juelich.de
Web: http:// iffwww.iff.kfa-juelich.de/~pipich/

Baohu Wu

Jülich Centre for Neutron Science JCNS
Forschungszentrum Jülich GmbH
Outstation at FRM II
Phone: 089/289-11687
e-Mail: ba.wu@fz-juelich.de

TREFF

Reflectometer

Stefan Mattauch and Ulrich Rücker

Jülich Centre for Neutron Science
Forschungszentrum Jülich

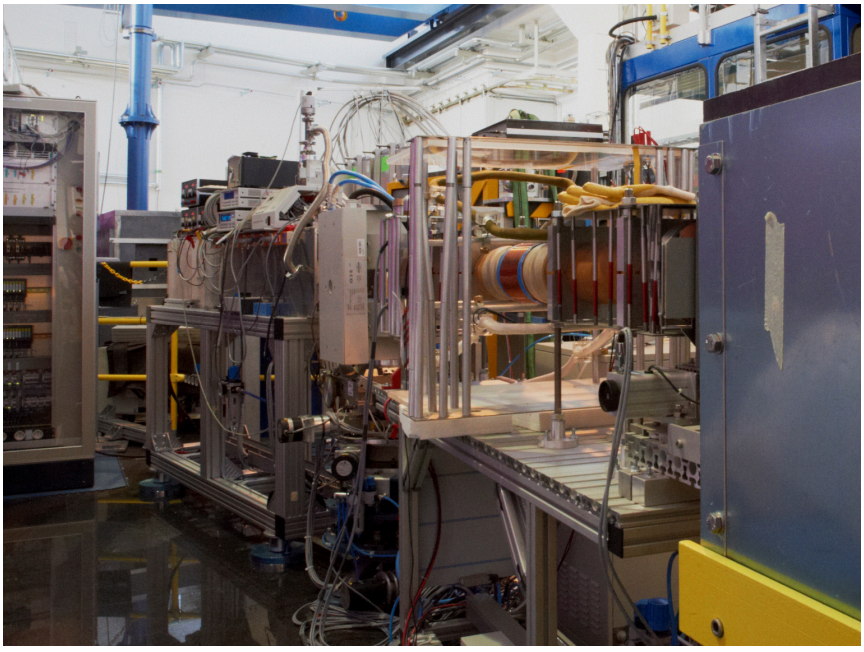

Manual of the JCNS Laboratory Course Neutron Scattering

Contents

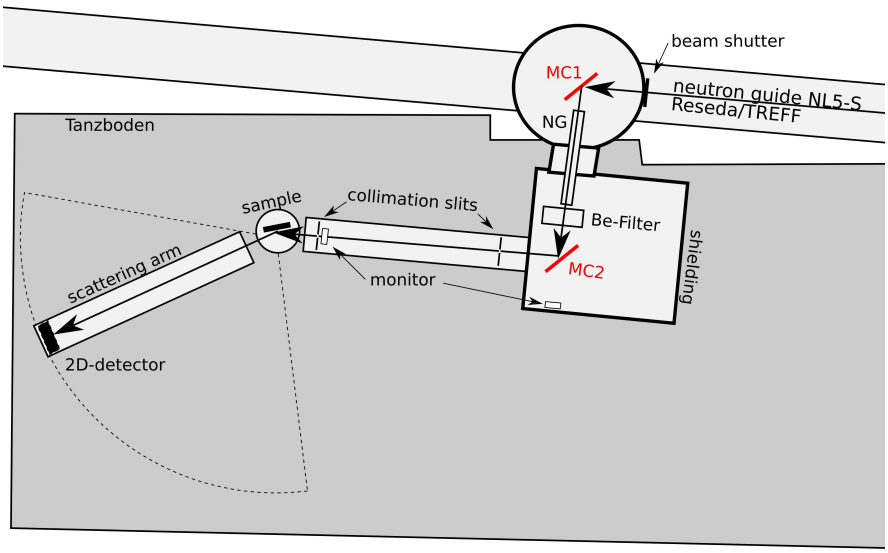

Fig. 1: *Sketch of the reflectometer TREFF@NOSPEC in top view.*

1 Introduction

The neutron reflectometry TREFF@NOSPEC at the neutron guide NL5-S is part of the neutron guide laboratory at the research reactor FRM II in Garching. TREFF is a joint facility of JCNS and the neutron optics group of FRM II. It is used for the investigation of magnetic layered structures as well as neutron optical components for the installation and improvement of neutron scattering instruments.

Figure 1 depicts the neutron reflectometer TREFF in the neutron guide hall of the FRM II research reactor. Essentially, it consists out of a double monochromator, the collimation path, the sample table with several stages of translation and rotation and, finally, the scattering arm with a position sensitive detector. The distance between the collimation slits is 1820mm and 450mm between the second slit and the centre of rotation of the sample table. For this experiment the wavelength is set to λ=4.73 Å.

2 Preparatory Exercises

The following questions will be asked during the practical course at TREFF:

1. In the sketch (Figure 1 of the instrument you will find a Be-filter and a NG (neutron guide) between the MC1 and MC2. What are they used for?

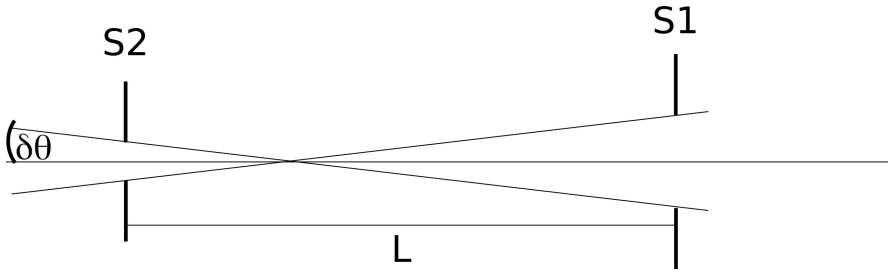

Fig. 2: *This drawing should help you to solve question 5.*

2. In the introduction the used wavelength was given with λ=4.73 Å. Which other wavelength are possible and how do you achieve these?
3. Depict a reflectivity curve of a substrate only
4. Depict a reflectivity curve of a substrate plus a layer
5. Calculate the divergence of a beam passing two slits S1 and S2 in a distance of L (see Figure 2)
6. Calculate the angle of collimation of the neutron beam to sufficiently resolve reflectivity oscillations of a 80nm thick monolayer on a substrate. What slit sizes follow for this reflectometer

3 Experiment Procedure

The aim of this experiment is the investigation of a nickel monolayer deposited on a glass substrate with unknown composition. Using neutron reflectometry the thickness of the nickel layer should be determined.

1. Perform a reflectivity experiment on the sample's back side and analyse the critical angle. To get sufficient collimation of the neutron beam, 0.6mm slit size for S1 and S2 should be taken.
2. Take the reflectivity curve of the Ni-monolayer system with the suitable collimation angles, so speaking the slit size for S1 and S2 calculated in the section before
3. Do like 3) but with a slit size of 3mm for S1 and S2.

3.1 The experiment itself

We (in the end it will be you) will mount the sample on the sample table and pre-align it with an appropriate tool (what could it be) parallel to the neutron beam. After some alignment scans

with the neutron beam we will measure the reflectivity curve step by step of the sample (see chapter Experiment Procedure).

3.2 Data reduction

The instrument saves the number of counts as a function of scattering angle.

3.3 Data evaluation

For systems such as multilayers the scattered intensity is determined by the difference in the potential of each layer (contrast). The potential is given by the **scattering length density** $\rho_{sld} = \sum_j b_j \rho_j$ with the scattering lengths b_j and the particle number densities ρ_j. The index j runs over all kind of atoms of the layer. The scattering length density is comparable to the optical density in light optics.
The **refraction index** of each layer is given by

$$n \gg 1 - \frac{\lambda^2}{2\pi}\rho_{sld} = 1 - \delta$$

.
With the **angle of total external reflection** $\Theta_c \sim \sqrt{2\delta}$, which is usually small, it follows

$$k_{c,z} = k\sin(q_c) \gg kq_c = \frac{2\pi}{\lambda}\sqrt{2\frac{\lambda^2}{2\pi}\rho_{sld}} = \sqrt{4\pi\rho_{sld}}$$

for the **critical wave vector**. For a monolayer system the **reflected amplitude** of each interface $r_{f,1}$ and $r_{f,2}$ can be calculated by the Fresnel formulae (Equation 16 in chapter 12 of the lectures book).
Neglecting roughness at the sample surface and at the interface between layer and substrate, for the amplitude at the surface one gets

$$r_{f,1} = \frac{k_{z,vac} - k_{z,lay}}{k_{z,vac} + k_{z,lay}} \quad \text{and at the interface} \quad r_{f,2} = \frac{k_{z,lay} - k_{z,sub}}{k_{z,lay} + k_{z,sub}}$$

with

$$k_{z,vac} = k\sin(q) \quad , \quad k_{z,lay} = \sqrt{k_{z,vac}^2 - 4\pi\rho_{sld,lay}} \quad \text{and} \quad k_{z,sub} = \sqrt{k_{z,vac}^2 - 4\pi\rho_{sld,sub}}$$

.
The superposition of both amplitudes yields the reflected amplitude of a monolayer sample

$$R = [r_{f,1} + r_{f,2}\exp(2ik_{z,lay}d)]\,\frac{\exp(-2ik_{z,vac}d)}{[1 + r_{f,1}r_{f,2}\exp(2ik_{z,lay}d)]}$$

with the film thickness d. The **reflected intensity** is given by re mean square of R. For $k_{z,vac} > 3k_{c,z}$ the intensity can be calculated in **Born approximation** by

$$|R|^2 \gg \frac{\pi^2}{k_{z,vac}^4}\left[\rho_{sld,lay}^2 + (\rho_{sld,lay} - \rho_{sld,sub})^2 + 2\rho_{sld,lay}(\rho_{sld,lay} - \rho_{sld,sub})\cos(2k_{z,vac}d)\right]$$

4 Experiment-Related Exercises

1. calculate from the reflectivity curve of the glass substrate the scattering length density $\rho_{sld,sub}$
2. Describe the differences and explain them between the measurement of the Ni monolayer with the 3mm slit and the slit size you have calculated.
3. Calculate the scattering length density $\rho_{sld,sub}$ of the Ni monolayer using:

molar volume	V_{Ni}=6.59 cm^3 mol^{-1}
Avogadro number	N_L=6.02 10^{23} mol^{-1}
coherent scattering length	b_{Ni}=10.3 fm

4. Determination of the thickness d of the Ni monolayer using the reflectivity formula in Born approximation. At first, estimate d based on the distance of the fringes of the reflectivity (see Data evaluation chapter).

References

Your lecture book of the year

Contact

TREFF

Phone: 089/289-10768

Alexandros Koutsioumpas

Jülich Centre for Neutron Science
at Heinz Maier-Leibnitz Zentrum
Phone: 089/289-11674
e-Mail: a.koutsioumpas@fz-juelich.de

Kirill Zhernenkov

Phone: 089/289-10705
e-Mail: k.zhernenkov@fz-juelich.de

Sabine Pütter

Phone: 089/289-10742
e-Mail: s.puetter@fz-juelich.de

TOFTOF

Time-of-flight spectrometer

Marcell Wolf and Christopher Garvey

Forschungsneutronenquelle Heinz-Meier-Leibnitz (FRM II)
Technische Universität München

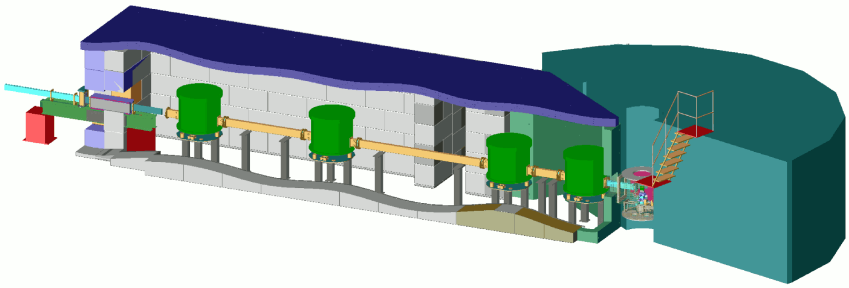

Contents

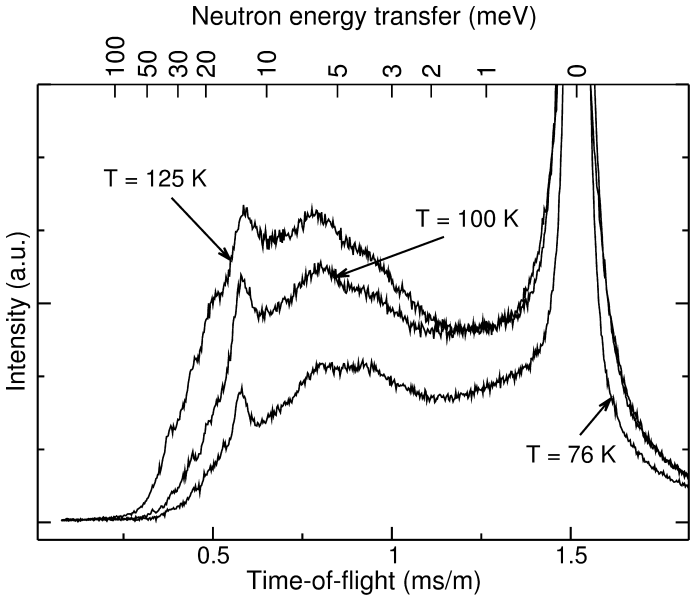

Fig. 1: Neutron time-of-flight spectrum of pentafluorotoluene, taken from [1]. Elastic scattering happens at energy transfer zero, quasielastic scattering in a region of approximately 0 ± 1 meV, inelastic scattering at larger energy transfers.

Scattering experiments are carried out in order to obtain information about the structure and dynamics of the studied systems (e. g. crystals, liquids, nanoparticles). Optical microscopes are simpler to understand and operate but their resolution is limited by the wavelength of light. There are only few techniques which give access to the length scale of molecules and atoms. Of those, one of the most important is scattering which gives direct information on the disposition and motions of atoms weighted according to the scattering probability, or cross-section [3].

There are several kinds of scattering experiments, depending on the subject matter. In this experiment we want to introduce you to *quasielastic neutron scattering* (QENS). Quasielastic scattering is referring to a broadening of the elastic line in a spectrum. The extend of this broadening is approximately 1 meV. Whereas in inelastic scattering (which will not be further discussed in this experiment), discrete maxima or bands appear clearly separated from the elastic line. While one can gain information about the structure or periodic motions (i. e. phonons) of the sample using *diffraction* or *inelastic scattering*, respectively, it is possible to analyse non-periodic motions (e. g. diffusion) with quasielastic scattering.

Prior to the experiment, you should read and understand these instructions you won't have much time to do so during the experiment. You should also work out the question section. In the following discussion we will follow the path of the neutrons from the source over the sample to the detector. Then theory of scattering will be introduced, so that one can understand which information can be obtained from the scattered neutrons. Thereon the specific experiment will be explained.

To carry out the experiment you should bring: this introduction; your answers to the ques-

tions; paper and a pen. After having started the measurement of the reference sample, we will show you the spectrometer TOFTOF. Afterwards we will prepare a sample, which we then will measure. Finally, we will evaluate the data together.

1 Basics

1.1 The neutron source FRM II

In general there are two techniques produce neutrons for a scattering experiment – spallation and nuclear fission. During spallation, huge nuclei (e. g. lead) are bombarded with protons, subsequently split and, among others, emit neutrons. The FRM II is a nuclear reactor optimized for use as a neutron source. Here, ^{235}U captures a thermal neutron and thereby becomes unstable. The nucleus fissures and, among others, emits three fast neutrons.

These fast neutrons must be slowed down (moderated) to thermal energies, that is room temperature, in order to initiate a new fission. One neutron is needed for the fission, while the others will be used for the neutron scattering experiments. The moderation occurs in D_2O of about 300 K which encloses the core.

In order to further slow down the neutrons, and thereby match their energies to the ones of atomic motions, a tank containing liquid D_2 at 25 K is located close to the fuel element. From this *cold source* several neutron guides lead the neutrons to the instruments. Inside these guides, the neutrons are transported by total reflection at the inner walls. The time of flight spectrometer TOFTOF is located at the end of neutron guide 2a in the neutron guide hall.

1.2 The time-of-flight spectrometer TOFTOF

Cold neutrons move with a velocity of several hundred m/s. Hence one can determine the kinetic energy of the neutrons comfortably by a time of flight (TOF) measurement along a certain distance. If one sets the initial energy of the neutrons before the scattering event to a well-known value and measures the final energy (or velocity) after the scattering process, the energy transfer can be determined. Since the position of the detectors is fixed, the scattering angle is also known.

During time of flight spectroscopy the energy transfer is measured by a time of flight measurement of the neutrons. The advantage of the time of flight technique is that a huge range of momentum and energy transfer can be captured simultaneously.

TOFTOF is a multi chopper time of flight spectrometer with direct geometry [4]. This means that all neutrons have (more or less) the same energy before interacting with the sample. After being scattered by the sample, the energy transfer can be determined. Both, the tuning of the energy of the incident neutrons (their wavelength) and the determination of the energy of the scattered neutrons is done by time of flight.

The neutrons are directed to the spectrometer through a neutron guide, which has a supermirror coating. The end of the guide is double focusing.

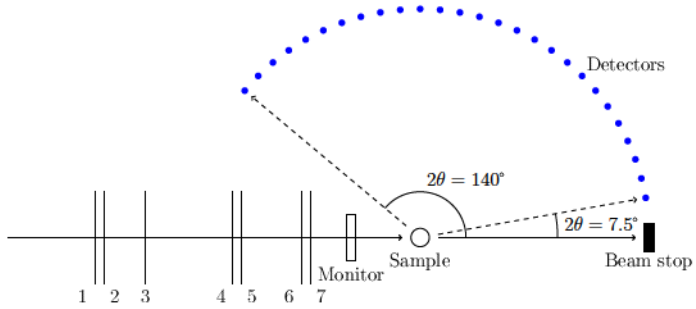

Fig. 2: Schematic drawing of TOFTOF. Following the neutron guide, first are paired choppers 1 & 2 which work together with 6 & 7 as velocity selector. Choppers 3 & 4 remove higher orders, 5 is the frame overlap chopper. The time needed for the neutrons to get from the sample to the detectors encodes their energy.

The primary spectrometer consists of seven rotating chopper discs which are placed in evacuated vessels (colored green on the cover page). The discs are made of carbon fiber composites and are coated with neutron-absorbing boron. On opposing sides, slits have been manufactured into the discs through which neutrons can pass. The first and last pair of choppers rotate in opposite direction each.

The incoming white neutron beam is pulsed by the first pair of choppers (choppers 1 and 2, pulsing choppers). This pulse still consists of neutrons with all velocities (or wavelength). Thus the pulse spreads along the way to the last chopper pair. These last two choppers (choppers 6 and 7, monochromating choppers) select a narrow range of wavelengths out of the pulse. The third and fourth chopper filter out higher orders (higher order removal choppers).

The fifth chopper is the frame overlap chopper. After the scattering process some neutrons fly towards the detectors, where they will be registered as a function of arrival time. It is essential that all scattered neutrons of one pulse are detected before the neutrons from the next pulse arrive. The overlap of slow neutrons from a pulse with fast neutrons of the following pulse inside the secondary spectrometer is called frame overlap. The frame-overlap-chopper blocks out several pulses, in order to avoid such an overlap.

The energy resolution (i.e. the width of the elastic line) is mainly determined by the chosen wavelength and the length of the neutron pulse that impinges on the sample. A good energy resolution can be achieved with a high rotational speed of the chopper discs (up to 22000 revolutions/minute). The energy resolution of the spectrometer can be changed continuously in the range from roughly 5 μeV to 5 meV (Fig. 3). By defining the energy uncertainty one can modify the time of observation in the range from roughly 1 ps to 1 ns.

The intensity of the incident neutron beam is recorded with a monitor, which is located between the primary spectrometer and the sample. An ionization chamber is used as a monitor, filled with fissile matter (^{235}U). The incoming neutrons trigger a fission and the high-energy nuclear fission products generate a clear voltage pulse, due to their high ionization density.

After passing the monitor, the neutrons hit the sample. Most of the neutrons are transmitted and are captured in the beamstop, but about 10 % of the neutrons are scattered in all possible directions. The neutrons that are scattered in the direction of the detector enter the flight chamber,

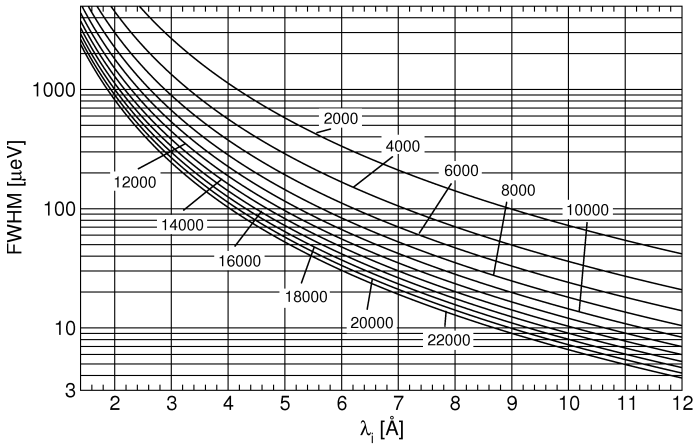

Fig. 3: Calculated energy resolution of the TOFTOF spectrometer shown for several chopper rotation speeds as function of the initial neutron wavelength. The chopper rotation speeds are given in rounds per minute (rpm) [4].

which occupies the space between the sample and detectors. The chamber is filled with argon in order to avoid unwanted scattering with air molecules.

Altogether 1000 ^{3}He-detectors (40 cm long and 3 cm in diameter) are placed tangential to the Debye-Scherrer-circle and also tangential to an imaginary spherical surface with a radius of 4 m around the position of the sample. Thus the flightpath from the sample to the detectors is 4 m long. The scattering angle 2θ covers a region from 7.5° to 140°. The detection of the scattered neutrons inside the ^{3}He-detectors occurs via a (n,p)-reaction. Hereby the neutrons are registered and tagged with a time stamp. The amount of detected neutrons is saved in time of flight bins for each detector in raw data files.

2 Theory

2.1 Cross sections

The probability that a neutron is scattered by a nucleus is denoted by the scattering cross section σ. It depends on:

1. the element
2. the isotope
3. the relative spin orientation of neutron and nucleus

Imagine a single crystal. The scattering cross section of every nucleus i can be decomposed into $\overline{\sigma} \pm \Delta\sigma_i$ where $\overline{\sigma}$ is the average over the whole crystal. This averaged part of the scattering cross section is called the *coherent scattering cross section*: scattered neutrons which can be

nuclide / element	σ_{coh} (barn)	σ_{inc} (barn)	σ_{abs} (barn)
^{1}H	1.758	80.27	0.3326
^{2}H	5.592	2.05	0.0005
H	1.760	80.26	0.3326
C	5.551	0.001	0.0035
N	11.01	0.5	11.51
O	4.232	0.001	0.0002
F	4.017	0.001	0.0096
Al	1.495	0.01	0.231
P	3.307	0.005	0.172
V	0.02	5.08	5.08

Table 1: Coherent and incoherent scattering cross sections as well as absorption cross sections of some selected nuclei or elements in their natural isotope composition, 1 barn = 100 fm^2. Source: [3].

described by this part of the scattering cross section "see" a regular lattice and interfere to a regular scattering pattern.

In contrast, the $\Delta\sigma$ are distributed randomly throughout the crystal and the scattering of the neutrons which can be described by the $\Delta\sigma$ does not interfere to a special pattern. This effect is attributed to an artificial quantity, the *incoherent scattering cross section*.

The proton (^{1}H) has the biggest incoherent cross section of all nuclei we study normally (about 80 barn, cf. Tab. 1). For practical purposes, the big difference between the incoherent scattering cross section of the proton and the deuteron (^{2}H) is of enormous importance. Using isotope exchange, i. e. (partial) deuteration of molecules, specific parts of the sample can be masked.

Vanadium scatters at the employed wavelengths also mainly incoherently although not as strong as the proton.

2.2 Principle of a scattering experiment

At a scattering experiment, two important values are recorded (cf. Fig. 4):

- The scattering vector $\mathbf{Q}$ is defined as the difference between the wave vector $\mathbf{k}_f$ of the scattered wave (f as "final") and the wave vektor $\mathbf{k}_i$ of the incident wave (i as "initial"). The momentum gained or lost during the scattering process can be calculated by

$$\Delta\mathbf{p} = \hbar\mathbf{Q} = \hbar(\mathbf{k}_f - \mathbf{k}_i) \; . \tag{1}$$

  However, the momentum transfer is commonly not noted. Instead, the scattering vector is commonly stated in units of inverse Ångstrom.

- The energy transfer ΔE is defined as the energy of the neutron after E_f and before E_i the

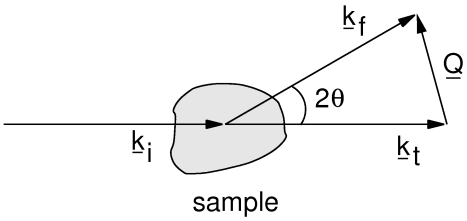

Fig. 4: Schematic representation of a scattering experiment. $\mathbf{k}_{i,f,t}$ are the wave vectors of the initial (incoming), final (scattered) and transmitted neutrons, respectively. $\mathbf{Q}$ is the scattering vector.

scattering process:

$$\Delta E = \hbar\omega = \hbar(\omega_f - \omega_i) = \frac{\hbar^2(|\mathbf{k}_f|^2 - |\mathbf{k}_i|^2)}{2m_n} \,. \tag{2}$$

The energy transfer is measured in meV. Often, ω is written incorrectly instead of $\hbar\omega$.

The absolute value of the wave vectors $\mathbf{k}$ is defined as $|\mathbf{k}| = 2\pi/\lambda$, with an refractive index $n \approx 1$ (which is a very good approximation for neutrons). However, the scattering vector cannot be measured directly, only the wave vector of the incident and scattered neutrons. Using the law of cosine one obtains a general equation for converting k_i and k_f to Q:

$$|\mathbf{Q}|^2 = |\mathbf{k}_i|^2 + |\mathbf{k}_f|^2 - 2|\mathbf{k}_i||\mathbf{k}_f|\cos(2\theta) \,. \tag{3}$$

In the case of elastic scattering, the energy transfer is zero. Hence $|\mathbf{k}_i| = |\mathbf{k}_f|$ simplifies the equation to

$$Q = \frac{4\pi}{\lambda}\sin\left(\frac{2\theta}{2}\right) \tag{4}$$

where $Q = |\mathbf{Q}|$. Roughly speaking a distance d in direct space corresponds to a Q value

$$Q = \frac{2\pi}{d} \,. \tag{5}$$

Therefore one can extract information about the physical configuration of the nuclei in the sample by analyzing the intensity of the elastic scattering as a function of Q (the diffractogram), cf. Fig. 6. Furthermore the intensity at a certain value of Q as a function of energy (a spectrum) provides information about the motion of the nuclei (see Fig. 6).

2.3 Correlation & scattering functions

The position and the motions of the nuclei in any system can be described using correlation functions. It can be shown that these correlation functions are what is measured with scattering methods.

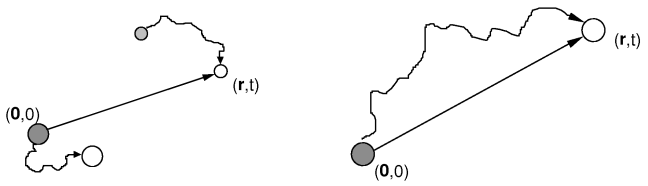

Fig. 5: Left: Pair correlation, right: self correlation. In the case of pair correlation, the second particle may be a different one than the first one but it doesn't have to.

The *pair correlation function* $G_{\text{pair}}(\mathbf{r}, t)$ gives the probability to find a particle j at time t at the place $\mathbf{r}$ if this or another particle i was at time $t = 0$ at the origin $\mathbf{r} = \mathbf{0}$, as shown in Fig. 5. The pair correlation function is

$$G_{\text{pair}}(\mathbf{r}, t) = \frac{1}{N} \sum_{i=1}^{N} \sum_{j=1}^{N} \int \langle \delta\{\tilde{\mathbf{r}} - \mathbf{R}_i(0)\} \cdot \delta\{\tilde{\mathbf{r}} + \mathbf{r} - \mathbf{R}_j(t)\} \rangle \, \mathrm{d}\tilde{\mathbf{r}} \,, \tag{6}$$

with the number of particles N, an integration variable $\tilde{\mathbf{r}}$ and the place $\mathbf{R}_j(t)$ of particle j at time t. The angle brackets $\langle\rangle$ denote an ensemble average.

The *self correlation function* or *auto correlation function* $G_{\text{self}}(\mathbf{r}, t)$ gives the probability to find one particle at time t at place $\mathbf{r}$ if this very particle was at time $t = 0$ at the place $\mathbf{r} = \mathbf{0}$, see again Fig. 5. It is defined as

$$G_{\text{self}}(\mathbf{r}, t) = \frac{1}{N} \sum_{i=1}^{N} \int \langle \delta\{\tilde{\mathbf{r}} - \mathbf{R}_i(0)\} \cdot \delta\{\tilde{\mathbf{r}} + \mathbf{r} - \mathbf{R}_i(t)\} \rangle \, \mathrm{d}\tilde{\mathbf{r}} \,. \tag{7}$$

In the following, we will assume that the samples are powder samples or liquids (i. e. not single crystals) and will therefore use the absolute value of $\mathbf{r}$, r, instead of the vector.

It is possible to calculate the pair and self correlation function from the scattered intensities. Roughly, the calculation is as follows:

From the intensity of the scattered neutrons measured as function of momentum and energy change, one obtains the *double differential scattering cross section* which can be seen as the sum of a coherent and an incoherent part:

$$\frac{\mathrm{d}^2\sigma}{\mathrm{d}\Omega \mathrm{d}E'} = \frac{k_f}{k_i} \frac{N}{4\pi} \big(\sigma_{\text{coh}} S_{\text{coh}}(Q, \omega) + \sigma_{\text{inc}} S_{\text{inc}}(Q, \omega) \big) \,. \tag{8}$$

It denotes the probability that a neutron is scattered into the solid angle $\mathrm{d}\Omega$ with an energy change $\mathrm{d}E'$. N is the number of scattering nuclei and $S(Q, \omega)$ is called the *scattering function*.

The Fourier transform in time and space of the coherent scattering function $S_{\text{coh}}(Q, \omega)$ is nothing but the pair correlation function $G_{\text{pair}}(r, t)$ and the Fourier transform in time and space of $S_{\text{inc}}(Q, \omega)$ is the self correlation function $G_{\text{self}}(r, t)$.

Three functions are important:

1. the *correlation function* $G(r,t)$
2. the *intermediate scattering function* $I(Q,t)$ which is the Fourier transform (from r to Q) of $G(r,t)$
3. the *scattering function* $S(Q,\omega)$ which is the Fourier transform (from t to ω) of $I(Q,t)$

All of them exist in two versions, considering pairs of particles (pair correlation function) or only one particle (self correlation function).

For the intermediate scattering function $I(\mathbf{Q},t)$ one can obtain further expressions – for a pair correlation

$$I_{\text{coh}}(\mathbf{Q},t) = \frac{1}{N}\sum_{i=1}^{N}\sum_{j=1}^{N}\left\langle \mathrm{e}^{-\mathrm{i}\mathbf{Q}\mathbf{R}_i(0)}\mathrm{e}^{\mathrm{i}\mathbf{Q}\mathbf{R}_j(t)}\right\rangle \tag{9}$$

and for the self correlation function

$$I_{\text{inc}}(\mathbf{Q},t) = \frac{1}{N}\sum_{i=1}^{N}\left\langle \mathrm{e}^{-\mathrm{i}\mathbf{Q}\mathbf{R}_i(0)}\mathrm{e}^{\mathrm{i}\mathbf{Q}\mathbf{R}_i(t)}\right\rangle \ . \tag{10}$$

At neutron spin echo spectrometers, the intermediate scattering function is measured – all other neutron scattering spectrometers, including TOFTOF, measure the scattering function.

At TOFTOF, we mainly probe the non-periodic motions in disorded materials, for instance diffusion processes in liquids. If a scatterer performs several motions simultaneously (but independently from each other), the resulting incoherent scattering function is a convolution in energy space of the single scattering functions, for example

$$S_{\text{total}}(Q,\omega) = S_{\text{diffusion}}(Q,\omega) \otimes S_{\text{internal motion}}(Q,\omega) \ . \tag{11}$$

As a convolution corresponds to a multiplication after Fourier transform, one can also write

$$I_{\text{total}}(Q,t) = I_{\text{diffusion}}(Q,t) \cdot I_{\text{internal motion}}(Q,t) \ . \tag{12}$$

If two scatterers perform two motions independently from each other and both cause incoherent scattering, the recorded total incoherent scattering function is simply the sum of the two scattering functions, for example

$$S_{\text{total}}(Q,\omega) = S_{\text{solute}}(Q,\omega) + S_{\text{solvent}}(Q,\omega) \ , \tag{13}$$

which is also a sum after Fourier transform to the intermediate scattering function.

This decomposition of the scattering functions into parts is *very* important.

Due to the limited number of supporting points it is not possible to obtain the correlation function by numerical Fourier transform of the measured scattering function. Therefore, one proceeds the other way round: After inventing a plausible correlation function, one performs a Fourier transform of this theoretical function to a scattering function and checks if this can describe the data.

The hereby obtained theoretical scattering function $S_{\text{theor}}(Q,\omega)$ is fitted to the measured scattering function $S_{\text{meas}}(Q,\omega)$ after convolving the theoretical scattering function with the measured instrumental resolution. The instrumental resolution is often determined using a vanadium sample which is an elastic, incoherent scatterer.

3 Experiment

3.1 The system

In this experiment we will study the diffusive motions of molecules, e.g. *n*-alkanes or salt solutions. By analyzing this system we want to learn more about the mechanism of molecular self-diffusion, i.e. internal motions of the molecules and long-range diffusion processes.

3.2 Modelling the motions

Molecules in general are by far too complex to come up with a scattering function which describes all the motions correctly. Therefore, very simplified models are used. Assuming that the molecule itself is rigid and moves as a whole, one obtains the scattering function

$$S_{\text{diffusion}}(Q,\omega) = \frac{1}{\pi}\frac{|\Gamma_d(Q)|}{\omega^2 + \Gamma_d(Q)^2}\ , \tag{14}$$

a Lorentzian with a Q-dependent width $|\Gamma_d(Q)|$. If the diffusion follows exactly Fick's law, one obtains

$$|\Gamma_d(Q)| = D \cdot Q^2 \tag{15}$$

with the diffusion coefficient D which is normally given in m^2/s.

Deviations from this ideal $\propto Q^2$ law indicate that the observed process is not ideal Fickian diffusion. A constant (too large) value of Γ_d at small Q can be a sign of *confinement*: the molecule cannot escape from a cage formed by the neighbouring molecules. If the width Γ_d goes towards a constant value at large Q, this can be a sign of *jump diffusion* which should rather be named *stop-and-go diffusion*: the molecule sits for some time at a certain place, then diffuses for a while, gets trapped again, ...

Try to fit the data with one Lorentzian. If this model does not describe the data satisfactorily, the assumption of a rigid molecule was probably not justified. The scattering function for a localized motion can be written as:

$$S_{\text{intern}}(Q,\omega) = A_0(Q)\cdot\delta(\omega) + (1 - A_0(Q))\cdot\frac{1}{\pi}\frac{|\Gamma_i|}{\omega^2 + \Gamma_i^2}\ , \tag{16}$$

that is the sum of a delta-function and a Lorentzian (confer also figure 6). $|\Gamma_i|$ gives the frequency of the motion, $A_0(Q)$ is called the *elastic incoherent structure factor* (EISF) and it gives information on the long time average position of the scatterer, in first approximation the size of the localized motion.

As we assume that the molecule performs a local motion and long-range diffusion simultaneously but independently from each other, we have to convolve the two functions with each other. The result is the sum of two Lorentzians:

$$S(Q,\omega) = F(Q)\cdot\left\{\frac{A_0(Q)}{\pi}\frac{|\Gamma_d(Q)|}{\omega^2 + \Gamma_d(Q)^2} + \frac{1 - A_0(Q)}{\pi}\frac{|\Gamma_d(Q)| + |\Gamma_i|}{\omega^2 + (|\Gamma_d(Q)| + |\Gamma_i|)^2}\right\}\ . \tag{17}$$

3.3 The experiment itself

We might either produce a sample together or fill an existing sample into the aluminium hollow cylindrical container or a flat aluminium container. This sample is then measured at TOFTOF, additionally a vanadium standard and the empty aluminum container will be measured. The length and number of measurements will have to be adjusted to the available time, it will be necessary to use some measurements of the preceding groups.

You will do all sample changes in the presence of a tutor who explains the procedure in detail.

3.4 Data reduction

The instrument saves the number of counts as a function of scattering angle and time-of-flight, $N(2\theta, \text{tof})$. The next step is the data reduction which applies several corrections and transforms to get rid of many instrument-specific properties of the data and convert them to a scattering function $S(Q, \omega)$.

Data reduction (and later on also data evaluation) is done using the program Mantid Workbench [5]. On the Desktop lauch the icon `Mantid Workbench`. Mantid Workbench is used in many large scale facilities and it includes a variety of instrument routines, including a TOFTOF data reduction routine. A detailed description of how to launch and run the routine is available at the instrument.

Mantid Workbench is structured in *workspaces*. A workspace contains all necessary data like the time of flight/energy transfer of the neutron, its 2θ/Q - values and the intensity. It also contains so called metadata, i.e. information about the measurement settings or sample conditions (e.g. temperature). Any operation on the data takes as an input a workspace and the output is stored in another workspace.

Raw data files that have been measured under the same conditions (e.g. temperature) can be added and treated as one data set. This will be done in the loading routine. After reading the data files, the raw data $N(2\theta, \text{tof})$ are normalized to the incoming neutron flux. The empty can measurement is subtracted from the data and the sensitivity of each detector is calibrated using the vanadium standard measurement. As vanadium is an incoherent scatterer, it should scatter the same intensity in all directions. The only effect which causes deviations from an isotropic scattering is the Debye-Waller-factor (DWF) which is well-known and can be corrected. This is followed by the calculation of the energy transfer from the time-of-flight so that one obtains $S(2\theta, \omega)$.

The next step is to calculate the momentum transfer Q from the scattering angle 2θ and the energy transfer ω using equation (3). During this step, we obtain about 1000 spectra with relatively low statistics each and a varying value of Q as the energy transfer varies. To get a better statistics and to have spectra which have the same Q for all values of energy transfer, the 1000 spectra are grouped into about n spectra of constant ΔQ in the same routine. The binning parameters can be set in TOFTOF data reduction routine.

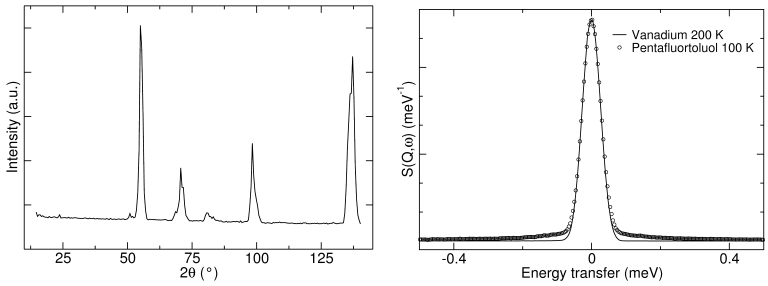

Fig. 6: Left: Neutron diffraction patterns of solid pentafluortoluene at 100 K ($\lambda_i = 6$ Å), taken from [1]. If the scattering vector is a reciprocal lattice vector, the positive interference of neutron waves yields a maximum in the scattered intensity. The sharp features in the diffraction pattern indicate an ordered lattice. Right: The spectra $S(Q, \omega)$ of pentafluortoluene (∘) and vanadium (–) at a momentum transfer of $Q = 1.1$ Å^{-1}, cf. also [1]. The solid sample shows only an internal motion, can therefore be described by equation 16.

3.5 Data evaluation

For a quantitative analysis, fit the spectra with the functions given in section 3.2. For this purpose, a fit-routine in Mantid Workbench can be used. For the fit, the binned data sets of $S(Q, \omega)$ for both the sample and the vanadium resolution measurement are required since the theoretical functions have to be convolved with the experimental resolution. Both data sets will have been created during the data reduction routine. Plot the data set you want to fit, and evoke the Fit Function Routine (for a single spectra) in Mantid Workbench. Using the *Add Function* command, you can build the appropriate fit function, e.g.

$$S(Q,\omega) = Convolution\,[Resolution; (DeltaFunction + Lorentzian)] + LinearBackground \tag{18}$$

The *Multi data set fitting* interface can be used to do a (sequential) fit for all Q-values in the data set. Judge the fit quality by the reduced χ^2 and by visually inspecting the fits together with the data. Plot the obtained parameters for the width, Γ, as function of Q^2 and determine the diffusion coefficient.

If you measured the sample at different temperatures, repeat the procedure for all of them.

4 Questions to be answered *before* the experiment

1. Do you expect the vanadium sample to be activated by the neutron beam? What about the aluminium container with the real sample? (2 min)

2. The vanadium standard sample at TOFTOF is a hollow cylinder with an outer diameter of 22.5 mm and a height of 65 mm. The wall thickness is 0.6 mm. Which fraction of the neutrons that hit the vanadium will be scattered? How big is the transmission?

3. Why do the samples measured at TOFTOF mostly have a transmission of about 90 %? How can the transmission be adjusted? (3 min)

4. The substance to be measured is filled in a gap between the inner and the outer cylinder of the sample container. The inner diameter of the outer cylinder is always 22.5 mm, the inner cylinder can be chosen to have either 22.1 mm or 22.3 mm outer diameter. The height of the cylinders is 65 mm. How large is the sample volume for the two different inner cylinders? Which inner cylinder would you use? (5 min)

5. Please note where this handout could need improvement. (5 min)

5 Questions to be answered *during* the experiment

1. When measuring water-based samples, H_2O is most often replaced by D_2O when the water is not the subject of the study. Why? The signal of the solvent has to be subtracted in both cases! (2 min)

2. Why is the sample container made of aluminum? (2 min)

3. The Vanadium standard sample at TOFTOF (hollow cylinder, 2 cm outer diameter, 0.6 mm thickness) is a "7% scatterer", meaning that it transmits 93% of the neutrons. In the moment, TOFTOF has 1000 neutron detectors with an active area of 40x3 cm each in 4 m distance from the sample. Estimate the efficiency of the monitor detector using the *Monitor rate* and *Signal Rate* given by the control program. (5 min)

4. To calculate the energy of neutrons in meV with a well-known wavelength given in Å, one can use a formula
$$E \approx \frac{a}{\lambda^2} \,. \tag{19}$$
Determine a numerical value for a. How big is the initial energy E_i of the neutrons in the current experiment? (5 min)

5. What is the maximal energy transfer from the neutron to the sample? (1 min)

6. What is the maximal energy transfer from the sample to the neutron? (1 min)

7. Draw at least six scattering triangles (as shown in Fig. 4) for these points in the dynamical range:

   - Elastic scattering with a scattering angle of 7.5°; with a scattering angle of 140° (the first & last detector at TOFTOF)
   - Same scattering angles with neutron energy gain
   - Same scattering angles with neutron energy loss

   (6 min)

8. Locate those points in this dynamic range plot and determine which area in this plot is accessible in the current scattering experiment. (5 min)

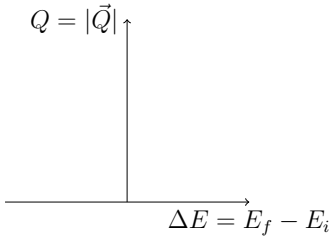

Fig. 7: Dynamic range plot.

9. How can you distinguish coherent and incoherent scattering in the diffraction pattern? Which information can you extract from the spectra when they are caused by coherent or incoherent scattering, respectively? (2 min)

10. Why do we measure Vanadium? (three reasons; for one it is important that Vanadium scatters neutrons incoherently, for two it is important that the Vanadium signal does not have a quasielastic broadening) (6 min)

11. Assume that the scatterers in your sample are partially trapped. They diffuse inside a "cage" until they find a hole through which they can escape. How do the intermediate scattering function $I(Q,t)$ and the scattering function $S(Q,\omega)$ look like? (5 min)

6 Constants

$$m_n = 1.675 \cdot 10^{-27}\,\mathrm{kg} \tag{20}$$

$$h = 6.626 \cdot 10^{-34}\,\mathrm{J}\cdot\mathrm{s} = 4.136 \cdot 10^{-15}\,\mathrm{eV}\cdot\mathrm{s} \tag{21}$$

$$\hbar = 1.055 \cdot 10^{-34}\,\mathrm{J}\cdot\mathrm{s} = 6.582 \cdot 10^{-16}\,\mathrm{eV}\cdot\mathrm{s} \tag{22}$$

$$e = 1.602 \cdot 10^{-19}\,\mathrm{C} \tag{23}$$

References

[1] C. Smuda, G. Gemmecker, and T. Unruh, Journal of Chemical Physics **128**, 194502 (2008).

[2] S. König, W. Pfeiffer, T. Bayerl, D. Richter, and E. Sackmann, Journal de Physique II **2**, 1589 (1992).

[3] National Institute of Standards and Technology, Neutron scattering lengths and cross sections , http://www.ncnr.nist.gov/resources/n-lengths/list.html (1992).

[4] T. Unruh, Jürgen Neuhaus, and Winfried Petry, Nucl. Instrum. Methods Phys. Res. A **580**, 1414 (2007).

[5] Manipulation and Analysis Toolkit for Instrument Data, Mantid Project, http://dx.doi.org/10.5286/SOFTWARE/MANTID , (2013).

Contact

TOFTOF

Phone: 089/289-14881
Web: http://www.mlz-garching.de/toftof

Marcell Wolf

Heinz Maier-Leibnitz Zentrum (MLZ)
Technische Universität München
Phone: 089/289-14975
e-Mail: marcell.wolf@frm2.tum.de

Christopher Garvey

Phone: 089/289-12697
e-Mail: christopher.garvey@frm2.tum.de

REFSANS.

Horizontal Time-of-Flight Reflectometer with GISANS Option

Gaetano Mangiapia, Sebastian Busch, Martin Haese, Nebojša Zec, Jean-François Moulin

German Engineering Material Science am Heinz Maier-Leibnitz Zentrum Helmholtz-Zentrum Hereon

© Technische Universität München

Contents

1 Introduction

REFSANS is the horizontal reflectometer with GISANS option operated by Helmholtz-Zentrum Hereon at the Heinz Maier-Leibnitz Zentrum (MLZ) in Garching.[1] It has been conceived to measure both specular and off-specular reflectivity for solid/liquid, solid/gas, and liquid/gas interfaces. Moreover, it allows performing Grazing-Incidence Small Angle Scattering experiments to investigate lateral correlations at the interfaces.

Differently from other reflectometers installed at MLZ, REFSANS uses a pulsed polychromatic incident neutron beam and determines the neutron wavelengths through the analysis of their Time-of-Flight (ToF). Although technically more demanding, ToF-analysis has many advantages, such as the possibility to have access to a large Q range with a single angle of incidence, which is very important for investigations of kinetic phenomena occurring at interfaces.

Figure 1 shows a sketch of REFSANS. The instrument consists of three pairs of chopper disks to define the wavelength resolution and the wavelength band; a collimation system and optical components which are able to bend the incident beam, if necessary. The neutrons are recorded by a 2-D detector, which can be lifted up to 5 deg.

Typical reflectivity curves are recorded using two or three incident angles to cover the range $0.005 \leq Q_z \big/ \text{Å}^{-1} \leq 0.25$, where Q_z is the component of the momentum transfer which is perpendicular to the interface.

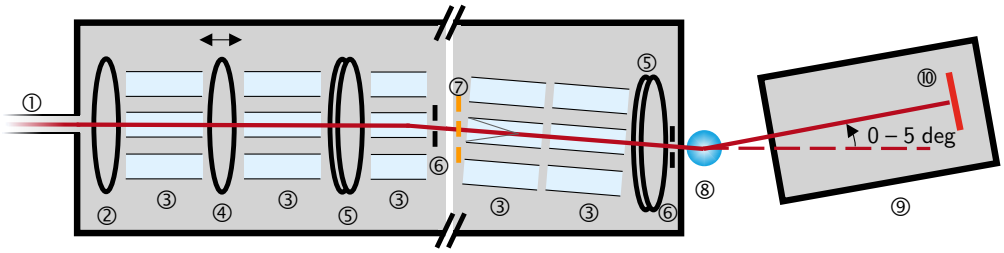

① Neutron Guide NL2b
② Master Chopper
③ Tiltable Neutron Guide Elements
④ Movable Slave Chopper
⑤ Additional Chopper Pairs
⑥ Slits
⑦ Polarizer and Spin Flipper
⑧ Sample
⑨ Liftable Scattering Tube
⑩ Detector

Figure 1. Sketch of REFSANS as seen from the side.

2 Preparatory exercises

The following questions will be helpful during your experiment at REFSANS

1. As mentioned in the introduction, REFSANS is an instrument working in Time-of-Flight mode. The horizontal distance between the first chopper disk and the detector can reach up to 21.5 m. Try to estimate the time it takes for neutrons to travel between these two points. Perform such evaluation for the fastest and slowest neutrons typically used at the instrument, namely $\cong 2$Å and $\cong 21$Å. All the necessary fundamental physical constants may be found on the NIST website.[2]

2. The duration of a neutron pulse has to be comparable to the interval of time required for the slowest neutrons to reach the detector. Based on the estimations performed in the previous point, try to evaluate at what rotation speed (expressed in revolutions per minute, rpm) the chopper disks have to rotate to provide the wavelength band $2 \leq \lambda/\text{Å} \leq 21$.

3. When a pulse starts traveling towards the detector, (part of) the neutrons inside the region enclosed between the first and second disks (master and slave choppers, respectively; see Figure 1) are recorded by the detector. It is normally assumed that the uncertainty affecting the measurement of the Time-of-Flight is negligible (indeed it is really small, 0.1μs). Based on this assumption, what can be said about wavelength uncertainty?

4. The neutron beam has to be collimated in order to define its direction as precisely as possible. Figure 2 shows the most used principle used to collimate a beam: a system composed of two slits. The dashed line represents the path of an ideal infinitely collimated beam, whereas the solid lines the effective beam divergence. The uncertainty on the angle that the beam forms with the sample is given by $\Delta\theta$, as represented in the figure. If the vertical apertures of the slits are b_1 and b_3, and if the distances between the slits is l, show that the angular uncertainty $\Delta\theta$ is given by

$$\Delta\theta = \arctan\frac{b_1 + b_3}{2l}$$

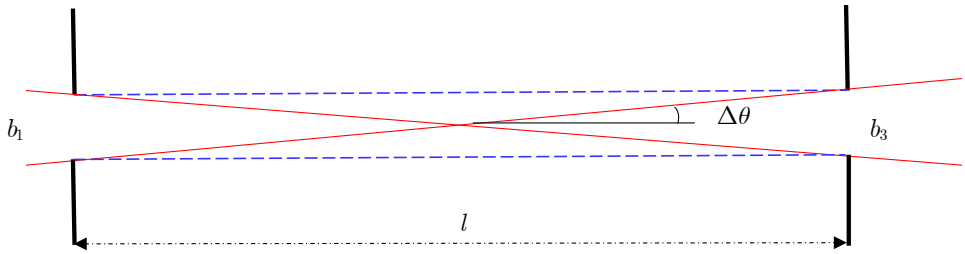

Figure 2. Principle of the REFSANS collimation system, from a lateral view.

5. Because of the Time-of-Flight mode, at REFSANS it is possible to cover a large Q_z range with a single or few angles of incidence. Suppose to use a wavelength band of $2 \leq \lambda/\text{Å} \leq 21$ and two incident angles of 0.50 deg and 2.50 deg to cover

the necessary Q_z range. Try to calculate this range and to imagine how the incident angles can be set.

6. For the analysis of the experiment (see Sections 3 and 4) you will need to estimate the Scattering Length Density (SLD) of Aluminum, Silicon and Titanium: their mass density of at room temperature are $2.7\ \mathrm{g \cdot cm^{-3}}$, $2.33\ \mathrm{g \cdot cm^{-3}}$ and $4.506\ \mathrm{g \cdot cm^{-3}}$, respectively. Try to perform this estimation. Try also to calculate the SLD of air, in normal conditions and compare it with the values obtained for the other three elements. Scattering lengths may be found on the NIST webpage.[3] Try also to list all other information you need, to perform the requested estimation.

3 Experimental procedure

In this experiment, a Silicon block coated with a layer of Titanium and an additional layer of Aluminum will be measured, to get information about the thickness and the quality of the coating layers. The two metallic layers have been deposited through the sputtering technique.[4]

Blocks like the one to be tested can be used as electrode in an electrochemical cell, to study corrosion phenomena occurring at the surface: The Aluminum surface is put in contact with a corrosive liquid and counter/reference electrodes. Then the Al/liquid interface is probed by neutron reflectometry. During the experiment, the potential between the electrodes or a certain current may be imposed through the use of a potentiostat/galvanostat.

This is a typical description of a so-called "*in-operando*" experiment: an experiment where a certain phenomenon is promoted imposing some quantities (such as the electrical current), and is investigated during its occurrence, at its site ("*in-situ*").

In our experiment we will limit ourselves to simply investigate the surface of the block: for investigations with neutron reflectometry, and even more so for electrochemical experiments, it is important that the surface is as smooth as possible to prevent the occurrence of off-specular scattering and low reflectivity.

3.1 The experiment itself

A short overview of REFSANS will take place, and the main characteristics of the TOF-analysis will be shortly discussed.

A silicon block with Ti/Al layers will be provided. The thicknesses requested from the manufacturer were $\tau = 100$Å for the Titanium layer and $\tau = 500$Å for the Aluminum layer. The participants will mount the block over a cell holder and install it at the instrument. After a short discussion about the order of the interfaces to be probed, the sample will be aligned.

To cover a Q_z interval ranged between $6 \cdot 10^{-3}\ \mathrm{Å^{-1}}$ and $0.15\ \mathrm{Å^{-1}}$ we will use the a wide

wavelength range (from 2 to 21 Å) and two incident angles, namely 0.50 deg and 2.50 deg. After a short discussion on the beam size to use and on the detector position, the measurement will be started. The measurement times can be set as 20 min for the primary beam, 30 min for the low angle measurement, and 1.5 h for the 2.50 deg measurement.

3.2 Data reduction

The data reduction will be performed with the instrument scientist, who will explain the fundamental steps and provide the reflectivity, R, *vs.* the vertical momentum transfer Q_z.

3.3 Data evaluation

Data evaluation of the measured reflectivities strongly depends on the system under investigation. For a simple system composed of a single interface or two interfaces, some of the characteristics may be obtained through a simple analysis of the pattern, such as position of maxima, distance between two consecutive maxima, position of the critical angle, *etc.*

For more complex systems, or even for gaining more details on simple systems, a full analysis of the results has to be performed. If the system can be approximated to a sequence of distinct layers, reflectivities may be analyzed through the Parratt recursion algorithm:[5] the system is divided in a certain sequence of layers. Applying the condition according to which the wave function and its first derivative must be continuous at each interface, a series of recurrence relations is constructed from which it is possible to calculate the theoretical reflectivity. This reflectivity depends on the thickness of the layers, as well as on their roughness and composition (SLD). An equivalent treatment is due to Abeles,[6] which takes advantage from the matrix formalism. Many programs are available for the analysis of reflectivity data. One good example is Motofit,[7-8] a package working in the IGOR Pro environment.[9] Motofit co-refines neutron reflectivity data, using the Abeles approach and least squares fitting. Another valid alternative is GenX [10]. These programs may also perform simultaneous fittings of systems in which the contrast have been changed by replacing some elements with different isotopes (*e.g.* -H with -D): this is very important because the mathematical procedure that allows us to obtain thicknesses, roughness *etc.* from reflectivity data is ill-posed: erroneous or physically meaningless values can have a trend of R as a function of Q_z very similar to that of the system under examination. Multiple measurements on the same system performed with suitably isotope replacement of some elements (the so-called *contrast variation method*) can reduce the appearance of unacceptable datasets.

For a very basic analysis, like the one concerning the sample which will be measured, Parratt32 may also be used: this program was formerly developed at the BErlin Neutron Scattering Center (now known as Helmholtz-Zentrum Berlin).

All programs for analyzing reflectivity data ask for the number of layers existing in the system to be analyzed, their SLD, thickness and roughness of the interfaces.

4 Experiment-related exercises

1. Observe the reflectivity data and try to qualitatively determine the main characteristics.
2. For the neutron reflection between two semi-infinite slabs, the critical value of Q_z is given by $Q_z \cong 4\sqrt{\Delta\rho \cdot \pi}$, where $\Delta\rho$ is the difference between the scattering length density (SLD) of the two media.[11] Compare this theoretical value with the experimental value observed.
3. Try to make an approximate sketch of the trend of the SLD *vs.* the vertical distance from the interface Si/Ti. How do you expect the SLD to change across the various interfaces?
4. The maxima and minima are due to the presence of the Al and Ti layers, which influence the neutron wave exercising a different potential and creating the conditions for constructive interference along proper directions. Thus, the position of the maxima depends on the (constructive) interference occurring between the neutron waves reflected from the different layers. A (broad) maximum at high Q_z should correspond to the thinner layer (Ti): therefore, its position should give a very rough estimation (the order of magnitude) of the Ti layer. Use the Bragg equation to estimate if the corresponding thickness agrees with the expected value. Also, discuss why this estimation might not give a proper value for the thickness.
5. Assume to have installed Motofit, to perform a full analysis of the reflectivity data. The program starts with a simple three-interface system, namely Air/SiO_2/Si: a thin layer of SiO_2 ($SLD = 3.47 \cdot 10^{-6}$ Å^{-2}) is always present on top of Si substrates. The roughness of the Si surface is, according to the manufacturer, ranged between 5 and 10 Å. Set 10 Å as starting value for this interface. Set also 15 Å as thickness for the SiO_2 layer. Afterwards the total number of layers have to be defined: in principle, besides the SiO_2, Ti, and Al layers, an additional layer of Al_2O_3 and, possibly, a layer of TiO_2 should be added on top of the correspondent metallic layers. Anyway, since these layers are most likely very thin (< 2-3Å), they can be neglected for a first analysis. Thus, add the layers of Al and Ti along with the SLD evaluated in Section 2 and the expected thicknesses. Also set a value of 9% for $\Delta Q_z / Q_z$ and try to fix all the values except the thicknesses of Ti and Al. Fit and judge the fitting. Roughness smears the minima and maxima and decrease the specular reflectivity: try to leave free the roughness for the Ti, Al and SiO_2 interfaces and re-fit. Finally, if the fitting is not satisfactory, try to leave free the SLD of Ti and re-fit. Judge the results and try also to understand if some values are different from those expected and why.
6. As general rule, for investigations with reflectometry, the roughness should not exceed 10 Å. Based on the results obtained, try to judge the quality of the layers sputtered on the Silicon crystal.

References

1. Moulin, J.-F.; Haese, M., REFSANS: Reflectometer and evanescent wave small angle neutron spectrometer. *Journal of large-scale research facilities JLSRF* **2015,** *1* (A9), 1-3.
2. Mohr, P. J.; Newell, D. B.; Taylor, B. N. Fundamental Physical Constants from NIST. https://physics.nist.gov/cuu/Constants/.
3. NIST Center for Neutron Research, Neutron scattering lengths and cross sections. https://www.ncnr.nist.gov/resources/n-lengths/.
4. Stuart, R. V., *Vacuum technology, thin films, and sputtering : an introduction*. Academic Press: New York, 1983; p viii, 151 p.
5. Parratt, L. G., Solid Surface Studies by Total Reflection of X-Rays. *Phys Rev* **1954,** *95* (2), 617-617.
6. Abeles, F., La Theorie Generale Des Couches Minces. *J Phys-Paris* **1950,** *11* (7), 307-309.
7. Nelson, A. Motofit and Reflectometry(scattering) resources Wiki. http://motofit.sourceforge.net/wiki/index.php/Main_Page.
8. Nelson, A. Motofit Files. https://sourceforge.net/projects/motofit/files/motofit/.
9. Current Download Releases by Software Family | Igor Pro by WaveMetrics. https://www.wavemetrics.com/downloads/current.
10. Björck, M.; Glavic, A. GenX - Home. https://aglavic.github.io/genx/.
11. Daillant, J.; Gibaud, A., *X-ray and neutron reflectivity : principles and applications*. 2nd ed.; Springer: Berlin, 2009; p xiv, 348 p.

Contacts

REFSANS

Phone: +49-89-289-14880; +49-89-289-11880

Web: https://mlz-garching.de/refsans

Jean-François Moulin

Helmholtz Zentrum Hereon, German Engineering Material Science (GEMS) am Maier-Leibnitz Zentrum (MLZ), Lichtenbergstraße 1, D-85747 Garching

Phone: +49-89-158860-762

e-mail: Jean-Francois.Moulin@hereon.de

Gaetano Mangiapia

Phone: +49-89-158860-839

e-mail: Gaetano.Mangiapia@hereon.de

Sebastian Busch

Phone: +49-89-158860-764

e-mail: Sebastian.Busch@hereon.de

Martin Haese

Phone: +49-89-158860-763

e-mail: Martin.Haese@hereon.de

Nebojša Zec

Phone: +49-89-158860-748

e-mail: Nebojsa.Zec@hereon.de

Matthias Pomm (Engineer)

Phone: +49-89-158860-761

e-mail: Matthias.Pomm@hereon.de

BIODIFF

A neutron diffractometer optimized for large unit cell sizes

Tobias E. Schrader[1] and Andreas Ostermann[2]

[1]Jülich Centre for Neutron Science,
Forschungszentrum Jülich
[2] Technische Universität München,
Heinz Maier-Leibnitz Zentrum (MLZ)

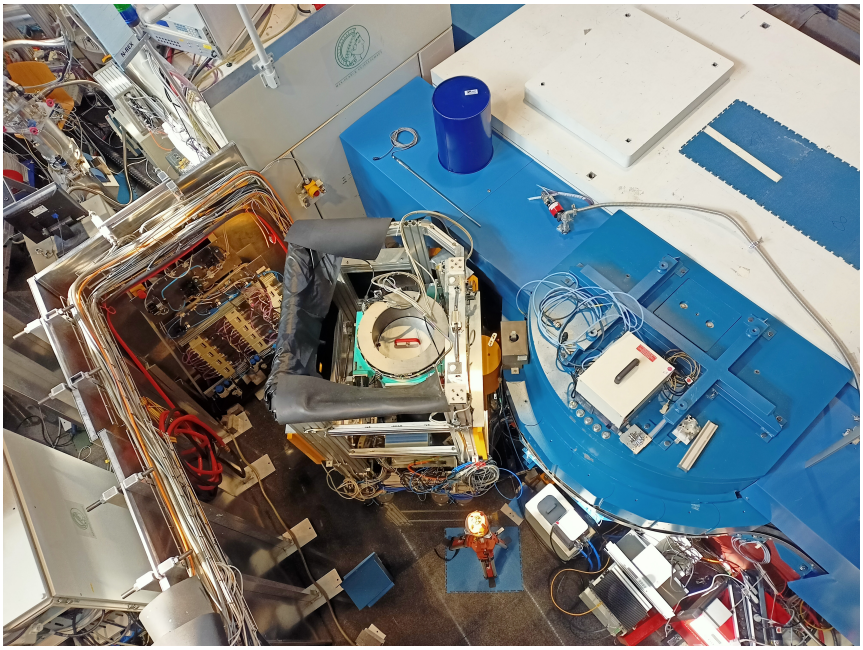

Contents

1 Introduction

Apart from water, proteins are the most abundant molecules in living cells. They are constantly synthesized in the cell by the well known transcription and translation mechanism where first the DNA is read out to produce a messenger RNA which encodes the proteins and in the subsequent translation process the protein is synthesized by the ribosomes which itself is a protein/RNA-complex. Proteins fulfil numerous functions in the cell, for example enzymatic catalysis which enhances the speed with which molecules like fatty acids are synthesized or transport and storage of important molecules like oxygen or they are involved in immunology, just to name a few [1] . In order to fulfill these functions proteins adopt a unique three dimensional structure with a carefully controlled mixture of flexibility and stiffness. For an understanding of their function knowledge of this three dimensional structure is a prerequisite. Ideally one would like to produce a movie where one can follow the functioning protein in action in slow motion with atomic resolution. In practice, there are techniques available which have a sufficient time resolution (in the fs-regime) but do only provide very limited structural information like time resolved infrared spectroscopy. On the other hand there are methods which provide full atomic resolution but with essentially no time resolution. With those methods one often stops the functioning process of a protein under investigation in an intermediate state by trapping methods using inhibitor molecules which stop the catalytic process of the protein leaving it trapped it in a certain intermediate state. This article will focus on the latter static techniques among which X-ray protein crystallography is the most widely used one. It will also introduce the method of neutron protein crystallography since there are some similarities but also some differences to X-rays as probes. Finally an example case study is discussed where both techniques give complimentary information. But at first a short introduction into the basic structural properties of proteins is given.

2 Some Basics about Proteins

2.1 Amino acids as the building blocks of proteins

Proteins consist of a chain of amino acids. In that sense they are biopolymers and since they in general have charged side chains they can also be called polyelectrolytes. The first information about a protein is therefore the number of amino acid residues it contains. This number can span quite a wide range between 10 and 25 000. In a historical nomenclature often the term “polypeptide” is used for a small protein containing between 10 and 100 amino acids. Amino acid chains with a smaller number of amino acids than 10 are often named oligopeptides. Typically a protein contains 100 amino acids. The average molecular weight per amino acid is around 100 g/mol. This provides a possibility to calculate an estimate for the molecular weight of a protein from the number of its residues. Despite there are many different amino acids (or to be more exact: 2-amino carboxylic acids) present in living organisms not all of them are used to build up proteins. The proteinogenic amino acids are shown in Figure 1. Covalently attached to the central C-atom, the so called C_α-atom are an amino functional group, a carboxylic group, the side chain atoms and finally one hydrogen atom. Since the C_α-atom has a sp3 hybridization sterically all four constituents point into the corners of a tetrahedron. Since (apart from the amino acid glycine) this C_α-atom has four different constituents it forms a chiral

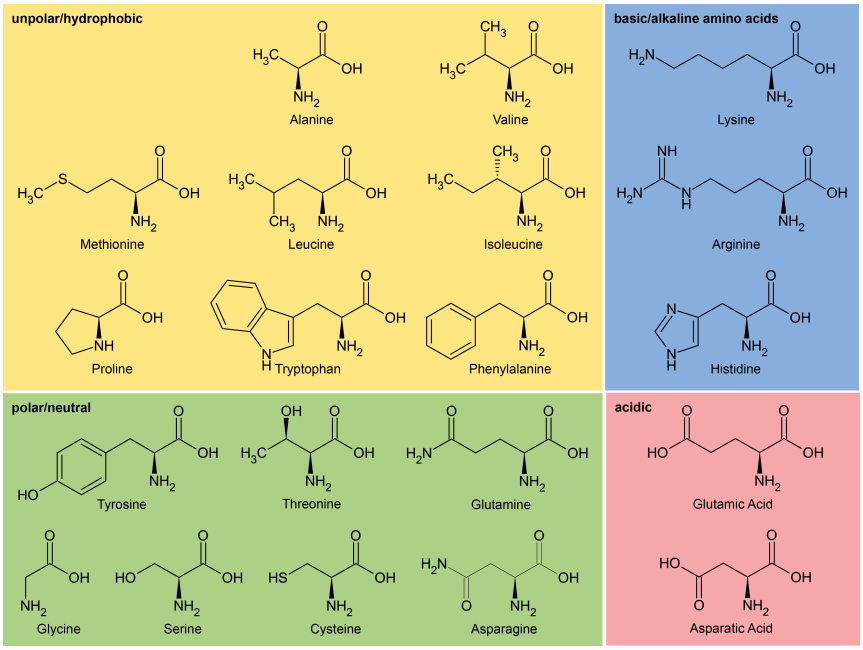

Fig. 1: A compilation of all 20 amino acids found in natural proteins. The N-terminal amino group is here shown in its neutral charge state pointing to the bottom of the page. Covalently attached to it is the C_α-atom which carries the corresponding side chain group $Adaptedfromhttp://upload.wikimedia.org/wikipedia/$.

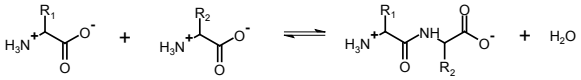

Fig. 2: A peptide bond forms between two amino acids. As a result a water molecule is released. The inverse process is called hydrolysis.

centre in the Fischer sense. So two different arrangements of these four constituents are possible which lead to the L- and D-enantiomers of the corresponding amino acid, according to Fischer's convention. But in nature only the L-enantiomers are found as building blocks of proteins.

The ribosomes in a living cell synthesize the proteins according to the code read from the messenger RNA. This process is called translation . Hereby in a step by step fashion one amino acid after the other is linked via a peptide bond between the carboxylic group of the existing amino acid chain and the amino functional group of the newly added amino acid. A water molecule is released per peptide bond formed (see Fig. 2). Hence, the peptide bond formation is a poly-condensation. The inverse process requires adding a water molecule and is named hydrolysis. Formation of a peptide bond requires free energy, so the inverse process is exothermic but happens on a very long time scale between 10 to 1000 years without enzymatic catalysis.

The sequence of amino acids is the primary structure of the protein. It can be displayed as a line

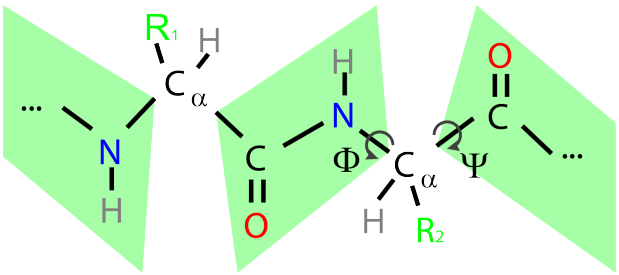

Fig. 3: Due to a partial double bond character of the C-N peptide bond the rotation around it is hindered by a steep potential. This causes the four atoms OCNH to form a planar structure (marked in green). The only remaining degrees of freedom per amino acid along the backbone are the two dihedral angles ψ and ϕ.

of text with a three letter code representing one amino acid. It is a common convention that the line of text starts at the N-terminal end of the amino acid chain i. e. with the amino acid with side chain R1 in the example given in Fig. 2 on the right.

Another specialty of the peptide bond is its partial double bond character of the chemical bond between the carbon and nitrogen atom. The lone electron pair at the nitrogen atom is delocalized and has some existence probability between the atoms forming the peptide bond. This causes the bond length to shrink below the value of a single bond. As a consequence, the rotation around the CN-bond is hindered and the four atoms OCNH form a planar geometry denoted by a green polygon in Fig. 3[1]. This is why one amino acid only contributes two degrees of freedom to the amino acid backbone which are denoted by the dihedral angles ϕ and χ, for their definition see Fig. 3. Another property of this planar set of atoms is their potential to from hydrogen bonds. Hereby, the oxygen atom is partly negatively charged and is a hydrogen bond acceptor. The hydrogen atom covalently linked to the backbone nitrogen atom carries a positive partial charge and is therefore a hydrogen bond donor. It is this hydrogen atom which can be easily replaced by a deuterium atom when the protein is dissolved in heavy water (D_2O) for a certain time. This can be seen as a proof for the hydrogen donor capabilities of this hydrogen atom.

2.2 The three dimensional structure of proteins

After leaving the exit tunnel of the ribosome the polypeptide chain folds into a unique three dimensional structure. This process is sometimes assisted by chaperones, which provide a special electrostatic environment, which helps the proteins to fold correctly. Since the backbone of all proteins is the same (i. e. the covalently linked atoms N- C_α-C-N- C_α-C and so forth) the side chains determine this unique three dimensional structure. This structure is stabilized by four different interactions. First of all there is the possibility of establishing hydrogen bonds between two parts of the backbone, but also between side chains or between a side chain

[1] Only in rare cases one finds a distorted planar geometry. The dihedral angle ω for the rotation around the CN-bond is in this case not equal to +180°. The potential for rotation around the CN-bond has a second local minimum at ω=0, which corresponds to the peptide bond in its cis configuration. This is frequently found in conjunction with the amino acid proline.

and a part of the backbone. Another stabilizing mechanism is a formed salt bridge between a negatively and a positively charged side chain, e. g. aspartic acid and lysine. The third interaction is the formation of a hydrophobic cluster or core. Hereby the surrounding water plays a major role which makes it a mostly entropic effect. It is more favorable for the water molecules to form hydrogen bonds with each other than to stick between some hydrophobic side chains. This is why those side chains tend to be packed together in the folding process resulting in van der Waals interactions among them. The fourth stabilizing moment of a three dimensional fold of a protein is a disulfide bridge between two cysteine residues. Often this is used to link two different amino acid chains to form one protein.

When the primary structure only gives the linear sequence of amino acids, the secondary structure of a protein denotes all arrangements of the protein backbone stabilized by a regular hydrogen bonding pattern. These hydrogen bonds are solely between different parts of the backbone. There are several structural motifs of that kind which occur frequently in proteins. Some of these motifs have been given a name e .g α-Helix or parallel β-sheet (Fig. 4).

The side chains of the amino acids forming an α-Helix point to the outside perpendicular to the helix axis. Per winding 3.6 amino acids form one winding. The hydrogen bonding pattern can be seen in Fig. 4 or taken from Table 1. Since all hydrogen bonds have a dipole moment which is aligned in parallel in an α-helix a large dipole moment is formed by an α-helix which makes it energetically unfavorable when the number of residues involved exceeds 40 [2]. The β-sheet comes in two flavors a parallel one and an anti-parallel one (shown in Fig. 4). They differ by the hydrogen bonding pattern, but in both cases the side chains point roughly perpendicular to the plane defined by the backbone alternatingly upwards and downwards.

The β-sheet comes in two flavors a parallel one and an anti-parallel one (shown in Fig. 4). They differ by the hydrogen bonding pattern, but in both cases the side chains point roughly perpendicular to the plane defined by the backbone alternatingly upwards and downwards.

Table 1: Geometric properties of some secondary structure elements (values taken from cite4).

Secondary structure	Frequency	H-bonding	Handedness	Typical ϕ	Typical ψ
α-helix (3.613)	abundant	i to i+4	right	-57°	-47°
310 helix	infrequent	i to i+3	right	-20°	-54°
α-helix (4.416)	rare	i to i+5	right	-57°	-80°
polyproline II	rare	-	left	-78°	+149°
polyglycine II	rare	i to i+3	left	-80°	+150°
parallel β-sheet	abundant	wide pair	-	-119°	+113°
antiparallel β-sheet	abundant	close pair	-	-139°	+135°

Apart from the structures mentioned in Table 1 certain turns form regular hydrogen bonding patterns such they can be considered secondary structural elements. On the bottom left of Fig. 4 with the backbone marked in blue a turn motif is visible. This is also an example of a secondary structure element of proteins. It allows for the amino acid chain to reverse its direction to form the anti-parallel β-sheet.

Ramachandran plots are especially suited to judge the secondary structure content of a protein. They consist of a scattered plot of all dihedral angles found per residue in the protein (see Fig. 5). On the x-axis all the dihedral angles of ϕ and on the y-axis the dihedral angle ψ is drawn for

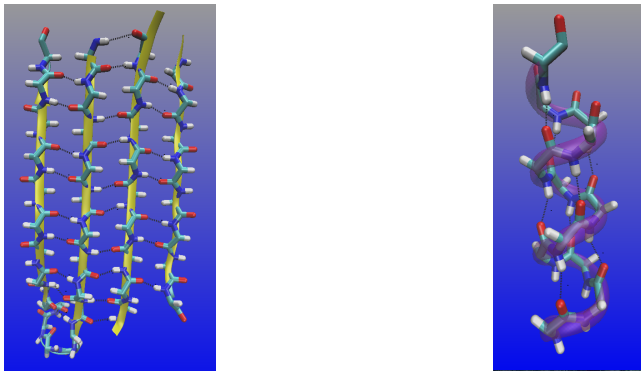

Fig. 4: On the left the residues 48 to 55, 107 to 130 and 187 to 196 of concanavalin A (pdb code 1XQN) are shown as an example of an anti-parallel β-sheet [3]. On the right residues 104 through 114 of sperm whale myoglobin (pdb code1L2K), are shown forming an α-helix [4] (Images made with VMD version 1.8.7).

each amino acid residue resulting in one black filled symbol per residue. Obviously, myoglobin is mostly an α-helical and concanavalin A a β-sheet rich protein. Due to steric hindrances because of the presence of the side chain many combinations of ϕ and ψ are unfavourable (white areas in Fig. 5).

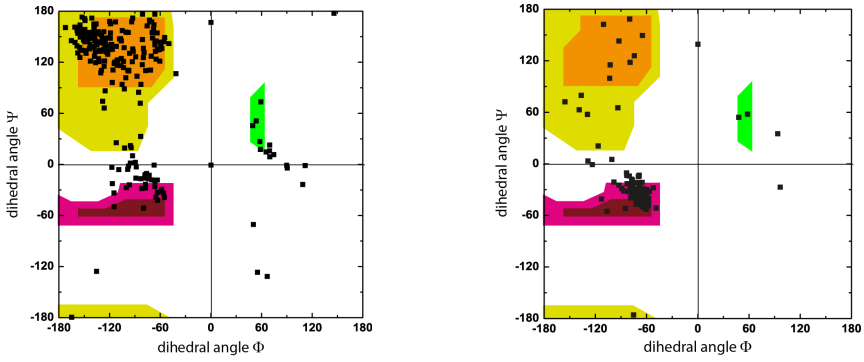

Fig. 5: Ramachandran plots of the protein concanavalin A on the left and myoglobin on the right. The red area shows dihedral angles typical for α-helices. In the yellow and orange areas dihedral angles typical for β-sheets can be found. The green region corresponds to rare left handed helical arrangements of the protein backbone (Images made with VMD version 1.8.7 [5]).

The tertiary structure of a protein denotes the three dimensional arrangement of all atoms of the protein in space, including the side chains. This information can be obtained by structural techniques like protein crystallography (will be discussed below), NMR. On that level all interactions mentioned above play a role. Super-secondary structural elements e. g. the α-helix bundle found in myoglobin and the $\beta\alpha\beta\alpha\beta$-structure found in dehydrogenases are often seen in a tertiary structure. Another concept to divide the tertiary structure into sub-motifs is to define certain domains which are parts of the protein which can fold to this domain structure

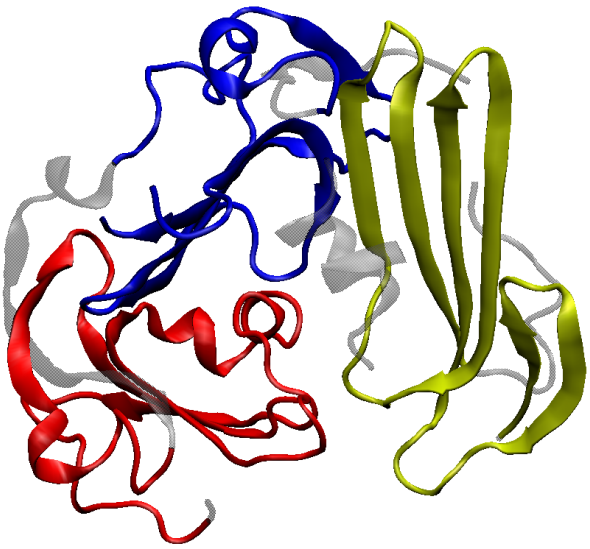

Fig. 6: Secondary structure plot of human urokinase plasminogen activator receptor citeXXX6, a complex protein (pdb code 1YWH). The domains DI (yellow), DII (blue) and DIII (red) are shown. Amino acids not belonging to any domain are depicted in grey.

without the context of the complete protein. Often these domains provide functional sub-units and their structure is highly conserved throughout the protein family. Figure 6 shows three domains DI to DIII of human urokinase plasminogen activator receptor protein as an example.

Some proteins need more than one amino acid chain to be functional. The arrangement of the different amino acid chains is then referred to as the protein's quarternary structure.

2.3 The protein folding problem

The process with which the proteins reach this three dimensional structure is called protein folding and is under intense investigations after C. B. Anfinsen has performed pioneering experiments on denaturation and re-folding [6]. Considering the time a typical protein needs for folding which is of the order of seconds there must be some directive force leading to the correct fold. An exhaustive search of the overall parameter space of all possible dihedral angles ϕ and ψ would take too long for proteins of a typical size of 100 amino acids (Levinthal's paradox). A possible mechanism for such a directive force is the hydrophobic collapse where all hydrophobic side chains move together to from a hydrophobic core inside the protein. In a different hypothesis secondary structure elements of proteins form first and lead then to the

final three dimensional fold.

3 Protein Crystallography

The previous chapter intended to define some technical terms which describe protein structure in general. The following chapter will show how most of this structural information has been obtained. The protein data bank (www.rcsb.org) is a well known source of structural information on proteins. Data from many different experimental techniques are entered in a standardized format, a .pdb file which essentially contains not only three dimensional coordinates of all observed atoms in a protein but also information on their mean square displacements. The number of stored entries exceeds 200 000. Among them X-ray crystallography has contributed more than 85 %. The next in line method with more than 15 000 entries in the data bank is electron microscopy. Solution NMR spectroscopy as a method was used in more than 12 000 entries. The remaining methods count less than 250 entries including neutron protein crystallography. Since the latter technique is represented by an instrument in the Jülich Centre for Neutron Science (JCNS) it is discussed in this experiment manual.

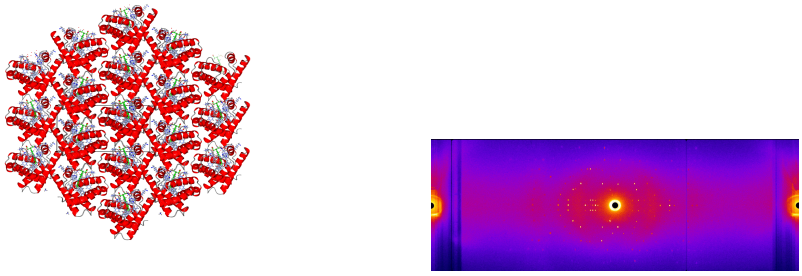

Fig. 7: Real space arrangement of myoglobin molecules in a crystal of space group $P2_1$ (on the left) versus diffraction pattern (right) of a myoglobin crystal.

For both techniques X-ray and neutron protein crystallography a single crystal of the protein of interest is required since the scattering of one protein molecule is very weak. Only using very bright X-ray sources in the future (e. g. XFEL) one might be able to gain enough information out of single protein molecules in solution, averaging many exposures and orientations. But in general a crystal has to be grown, especially large ones in case of neutron crystallography since the neutron luminosity of modern sources is much smaller than the X-ray flux reached by synchrotron sources. To grow sufficiently large crystals is a big challenge in the case of many proteins, especially membrane proteins. Here, one has to adjust a large parameter set of protein concentration, pH value, salt or precipitant concentration just to name a few. The crystal serves as a noiseless amplifier of the diffraction signal. But the arrangement of proteins in a crystals brings in another advantage, since the orientational averaging can be avoided, which is always present in the solution phase. Fig. 7 shows on the left the regular arrangement of myoglobin molecules in a crystal lattice. The unit cell of the monoclinic lattice (space group $P2_1$) is indicated by black lines. It bears one myoglobin molecule in the asymmetric unit and two myoglobin molecules in one unit cell. The picture on the right shows a diffraction pattern

Nucleus	atomic number	scattering length [10^{-12} cm]
^{1}H	1	-0.378
^{2}H	1	0.667
^{12}C	6	0.665
^{15}N	7	0.921
^{16}O	8	0.581

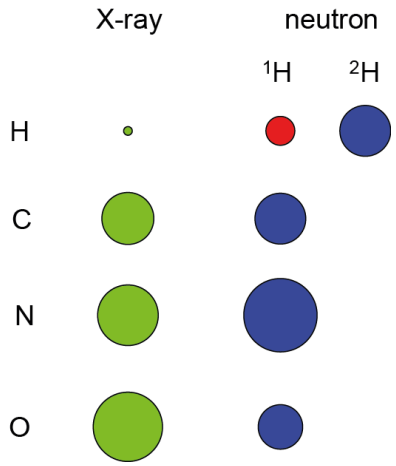

Fig. 8: The table on the left lists scattering lengths of selected atoms of biological relevance. On the right there is a comparison of X-ray scattering cross section with scattering lengths from neutron scattering. The circles are scaled to match at the carbon atom.

recorded with the instrument BioDiff on a myoglobin crystal. The crystal is rotated by ca. 0.3°while recording one diffraction pattern. In order to map the reciprocal space completely one has to put the crystal in many different orientations into the beam and record diffraction patterns as mentioned above. Fortunately, crystal symmetry helps that some orientations are equivalent to each other.

3.1 A neutron protein crystallography instrument

Since X-rays are scattered from the electrons in the crystal and neutrons from the nuclei, hydrogen atoms are hardly seen in X-ray crystallography experiments. Only at very high resolutions of 1 Åor less there is a chance to observe hydrogen atom positions. This resolution is often not within reach because of the crystal quality. Here neutron protein crystallography must be employed to retrieve the hydrogen atom positions. Moreover, neutron scattering can distinguish between different isotopes, especially between hydrogen and deuterium. Whereas from X-ray crystallography the electron density in the unit cell of the crystal can be calculated, neutron protein crystallography yields the nuclear scattering length density, which is a signed quantity. In fact, the coherent scattering length of hydrogen is negative and the one from deuterium is positive (cf. Fig. 8).

A major drawback of the method neutron protein crystallography is the required crystal size. Due to the much smaller neutron flux as compared to X-ray flux the crystals required for a neutron crystallography study must be much larger as compared to X-ray crystallography. Here, often crystal diagonals of 1 mm and more have to be reached. As an example of a neutron diffraction instrument optimised for protein crystallography the instrument BioDiff at the FRM II shall be introduced. It is a collaboration between the Forschungszentrum Jülich (FZJ) and the Forschungs-Neutronenquelle Heinz Maier-Leibnitz (FRM II).

Fig. 9: Schematic view of the BioDiff instrument (left) and a picture taken from a similar view point with the biological shielding removed (right).

Figure 9 shows a schematic view of the instrument from the top and a corresponding picture when the biological shielding has been removed. The neutron beam from the cold source of the FRM II reactor enters from the right. By Bragg reflection from a pyrolytic graphite crystal (002-reflex) neutrons are taken out from the white neutron spectrum of the neutron guide NL1 and pass a first boron carbide adjustable slit and a velocity selector. The velocity selector acts as a $\lambda/2$ filter. Together with the pyrolytic graphite crystal it forms a monochromator with a $\Delta\lambda/\lambda$ of ca. 2.5%. Behind the velocity selector the beam passes a second variable slit and the main instrument shutter, named γ-shutter. Additionally, a boron carbide neutron shutter is placed directly after the monochromator crystal for a faster shutter operation. Before entering the detector drum of the image plate detector through a Zirconium window a collimator made out of two manually exchangeable boron carbide apertures with fixed diameters between 3 mm and 5 mm shape the beam to fit to the sample size. At present the sample is usually contained in a glass tube (either a thin walled capillary or a NMR-tube for larger crystals). It is fixed to a standard goniometer which is mounted upside-down from the sample stage on top of the instrument. After passing the sample the main neutron beam exits the detector drum through a second Zirconium window and hits finally the beam stop which consists of a cavity of 4 mm thick boron carbide plates surrounded by a 13 cm thick wall of lead shielding bricks. The cylindrical image plate detector is covering roughly half of the total 4 π solid angle. It is 200 mm in diameter and 450 mm in height. It can be read out with three different resolutions of 125 µm, 250 µm and 500 µm. As an alternative, one can lower the image plate detector and swing in a neutron sensitive scintillator which is imaged onto a CCD-chip. This CCD-camera set up serves as a second detector. In particular it is used for a fast alignment of the sample crystal with respect to the neutron beam.

With the image plate detector the diffraction pattern shown in Fig. 7 on the right has been recorded. In fact, a complete crystallographic data set on a myoglobin crystal has been recorded allowing for the calculation of a nuclear scattering length density map. The exposure time was 17 minutes per frame and the crystal was rotated by 0.5°during exposure. 331 frames were recorded before the crystal was manually rotated by ca. 90°in the capillary and another set of 243 frames were recorded. Altogether ca. 9 days of beam time were necessary to record the complete data set. The achieved resolution with sufficient completeness was 1.7 Å. The required time to record this data set was much longer as the 30 minutes from X-ray diffraction.

3.2 Some general aspects of diffraction by a protein crystal

Having recorded a complete data set on a crystal some data treatment is necessary in order to calculate meaningful atom positions. Here only a brief introduction can be given more details can be found in text books [7, 8]. Assuming a number of n atoms per unit cell the structure factor of a single unit cell can be written as (see previous experiment manuals):

$$F(\boldsymbol{S}) = \sum_{j=1}^{n} f_j \exp(2\pi i \boldsymbol{r}_j \boldsymbol{S}) \tag{1}$$

Here $\boldsymbol{r}_j$ denote the atom position of atom j and $\boldsymbol{S}$ is the scattering vector perpendicular to the plane which reflects the incident beam. f_j can be seen here either as the scattering length of atom j in the neutron scattering case or the atomic scattering factor in case of X-ray diffraction. One can generalize this approach by switching form the summation to an integration to yield:

$$F(\boldsymbol{S}) = \int_{unitcell} \rho(\boldsymbol{r}) \exp(2\pi i \boldsymbol{r}\boldsymbol{S}) \, d^3\boldsymbol{r} \tag{2}$$

where $\rho(\boldsymbol{r})$ is the electron density distribution or the scattering length density respectively. Since a crystal consists of $AxBxC$ unit cells, the structure factor of the crystal can be composed as

$$F_{cryst.}(\boldsymbol{S}) = F(\boldsymbol{S}) \sum_{u=0}^{A} \exp(2\pi i u \boldsymbol{a}_j \boldsymbol{S}) \sum_{v=0}^{B} \exp(2\pi i v \boldsymbol{b}_j \boldsymbol{S}) \sum_{w=0}^{B} \exp(2\pi i w \boldsymbol{c}_j \boldsymbol{S}) \tag{3}$$

The vectors $\boldsymbol{a}$, $\boldsymbol{b}$ and $\boldsymbol{c}$ denote basis vectors of the unit cell. For an increasing number of unit cells the sums can be represented by delta functions leading to the Laue conditions for the structure factor being non-zero:

$$\boldsymbol{a}_j \boldsymbol{S} = h, \boldsymbol{b}_j \boldsymbol{S} = k, \boldsymbol{c}_j \boldsymbol{S} = l \tag{4}$$

Therefore, one only gets constructive interference, when the scattering vector is perpendicular to planes in the crystal which can be denoted by the index vector $\boldsymbol{h} = hkl$. For this reason the diffraction pattern of a single crystal shows distinct peaks, the so called Bragg peaks. The Bragg law can be easily derived from equation 4. Figure 10 shows the Ewald sphere construction. It is a tool to construct the direction of the diffracted beam. The Ewald sphere has its origin at the position of the crystal. Its radius is the reciprocal wavelength used in the scattering experiment. The origin of the reciprocal lattice is placed at the intersection of the sphere with the incident beam direction. Whenever the orientation of the reciprocal space is such that another point of the reciprocal space lies on the Ewald sphere a diffracted beam results in the direction of the line running from the centre of the Ewald sphere through that point.

When the crystal is rotated the reciprocal space rotates with it resulting in other lattice points to cause diffracted beams. In practice the incident beam is not strictly monochromatic but has a wavelength distribution which causes the Ewald sphere to be elongated to form a spherical shell of a certain thickness. This increases the number of diffracted beams observed. The beam

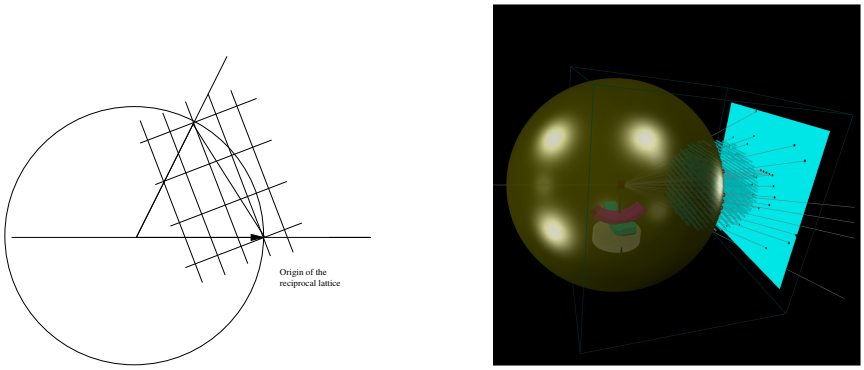

Fig. 10: Ewald sphere: On the left the schematic shows how to construct the Ewald sphere. On the right an Ewald sphere (golden colour) construction is shown in three dimensions. The blue square represents a flat two dimensional detector.

divergence adds also to its thickness. So, the positions of the diffracted beams on the detector only depend on the reciprocal lattice. The structure of the protein inside the unit cell is encoded in the amplitude and phase of the structure factor. To obtain the electron density or the nuclear scattering length density one has to perform the inverse Fourier transformation:

$$\rho\left(\boldsymbol{r}\right) = \frac{1}{V}\sum_{\boldsymbol{h}} F\left(\boldsymbol{h}\right)\exp\left(-2\pi i \boldsymbol{r}\boldsymbol{h}\right) \tag{5}$$

Here V is the volume of the unit cell. Unfortunately only the modulus squared of the structure factor is measured as intensity on the detector. The phase information is lost which is known as the phase problem of crystallography.

There are several solutions to the phase problem which are only applicable for the X-ray diffraction case:

1. isomorphous replacement: Several crystals of the same crystal structure have to be available for this method. First a crystallographic data set is recorded on an untreated crystal. Then crystals are soaked in at least two different heavy atom salt solutions. In the best case, the different heavy atom ions occupy different regular positions in the unit cell. From these (at least) two crystallographic data sets recorded on the heavy atom treated crystals phase information can be retrieved which is then used to determine the phases of the data set of the untreated crystal.

2. anomalous dispersion: Often it is possible to replace one distinct methionine amino acid with an artificial seleno-methionine one. The selenium atom has a suitable absorption edge on which anomalous scattering can be performed by tuning the wavelength of the beamline to the anomalous regime. Crystallographic data sets are then recorded at different wavelengths from with the phase information can be calculated. In some cases this approach can also be adopted for sulfur atoms present in naturally occurring cysteine residues.

3. molecular replacement: From the primary structure one can search the protein data base (pdb) for proteins with a similar amino acid sequence. If one finds enough fragments which seem to be sufficiently homologous to the unknown structure one can use those fragments for the calculation of initial phases. In further refinement steps these phases can be improved further. Since the number of unique structures entered in the protein data base is growing this method is increasingly favoured over other methods.

The phase problem of the neutron data sets is solved by using the X-ray structure and the molecular replacement technique.

3.3 Model building and refinement

With the data treatment one has now arrived at a contour map $\rho(\boldsymbol{r})$ be it either a nuclear scattering length density or an electron density. Now the information on the primary structure of the protein is used and either manually or employing software first the backbone is coarsely fitted into the contour map. Then from this model new amplitudes and phases of the structure factor are calculated using eq. 1. The modulus squared of the structure factor is again compared with the data. One could now think of a least square based fitting procedure to find the optimum arrangement of the protein atoms in the unit cell. In practice however maximum likelihood and simulated annealing molecular dynamics simulations are used because those are superior to the least square approach in terms of overcoming local minima. In these molecular dynamics simulations a lot of stereochemical information is used as restraints for example known bond lengths of Carbon to Carbon single bonds or bond angles. The agreement between model and observed contour map is often measured by calculating a so called R-factor:

$$R = \frac{\sum_{\boldsymbol{h}} ||F_{obs}(\boldsymbol{h})| - |F_{obs}(\boldsymbol{h})||}{\sum_{\boldsymbol{h}} |F_{obs}(\boldsymbol{h})|} \tag{6}$$

The index "obs" denotes the observed structure factors and the index "calc" the calculated structure factors from the model. The value of the R-factor lies in the limits between 0 and 1. A good agreement between model and measured data leads to an R-factor of about 0.2. R-factors of 0.5 and above are indicative for a random agreement between model and data.

But even a good R-factor does not guarantee that the model fits to the data. In fact, it is possible in special cases to obtain a reasonably low R-factor when using the amino acid chain in the wrong direction as a model [9]. Here, Brünger et al. [10] have suggested to divide the measured Bragg reflections into two subset one working set denoted by "A" and one test set denoted by "T". With the working set the fitting procedure is performed, whereas the test set only serves to control the model quality by calculating the R_{free} factor.

$$R_{free} = \frac{\sum_{\boldsymbol{h}\in T} ||F_{obs}(\boldsymbol{h})| - |F_{obs}(\boldsymbol{h})||}{\sum_{\boldsymbol{h}\in T} |F_{obs}(\boldsymbol{h})|} \tag{7}$$

The test set usually consists of 5 to 10 % of all structure factors, uniformly distributed over the resolution range.

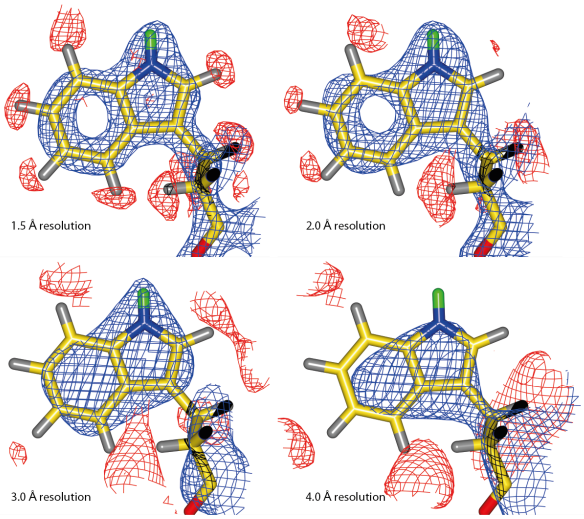

Fig. 11: The side chain of the amino acid tryptophan no. 7 of myoglobin measured with neutron diffraction at different resolutions. The contour level of the shown nuclear map is +1.5σ (blue) and -1.75σ (red). Exchangable hydrogen atoms (green) and Carbon- (yellow), Nitrogen- (blue) and Oxygen-atoms (red) appear on a positive contour level. Only not exchangable hydrogen atoms are seen on the negative contour level.

The R-factor and R_{free} factor should not differ too much from each other. In general, it is good practice to always look at the resulting model and its fit to the calculated map after each refinement step. Ramachandran plots can also be used to judge whether the amino acid backbone adopts a reasonable fold. With decreasing resolution (cf. Fig. 11) of the data it becomes more and more difficult to find the right orientations of side chains or even errors in the registry of the protein backbone can occur, whereby for example one amino acid is left out.

4 Example data set: Trypsin with the ligand aminopyridine

The enzyme trypsin is a protease. This means it cuts the protein chain of other proteins into two parts. The group of Prof. Gerhard Klebe from the University of Marburg has used this protein in order to show how neutron protein crystallography can contribute to a better understanding of drug fragment binding [11]. They measured a neutron structure of the ligand free enzyme as a reference. They used different small molecule ligands as examples for drug fragments with a drug consisting of typically 3-5 such fragments.

Here, we investigate how the fragment aminopyridine binds to trypsin.

The refinement is now the step where one adapts the model to the data. At BioDiff, the refinement program phenix.refine [13] is used in most cases. But also other programs can be chosen as for example the CCP4 suite or nCNS.

1. We use the sub-program from the phenix package called Xtriage to check the hkl-list file

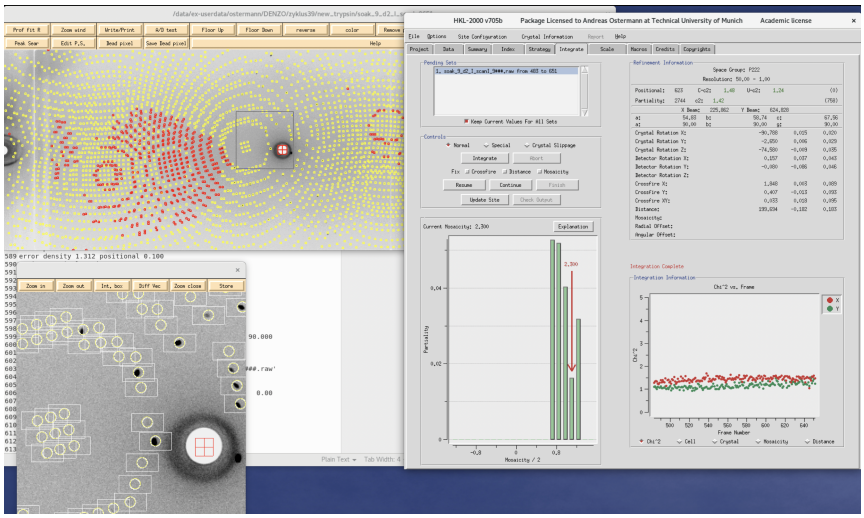

Fig. 12: A screenshot of the data integration software [12] at work: One detector image of the Trypsin data set is shown in black and white intensity encoding with the indexed Bragg reflexes encricled in yellow color. The red circles indicate when Bragg refelxes overlap. A magnified part of the detector image is shown in the bottom left corner. Here, the integration region is sown in a white circle and the background region is shown as a white rectangle. The χ^2 of the integration per image is plotted in the bottom right corner.

(*.sca) which was output from the software HKL2000 in the data reduction step.

2. For a starting model we use the x-ray structure of a ligand free trypsin enzyme which can be found in the protein data base with the name 5mne.pdb. To remove the lines which indicate the anisotropic refinement results, we use a linux command:

```
cat 5mne.pdb | grep ATOM > onlyATOM.pdb
```

3. The pdb-tools of phenix.refine are quite useful. We remove the hydrogen atoms from the model: Remove „name *H*“and we tick the box saying „Remove alternative conformations“

4. We skip the molecular replacement step which would normally follow now with the model we have produced so far. Instead we see that the ligand free model crystalized in the same space group and unit cell size as the data we have for the enzyme with the ligand aminopyridin. In this case we can use direktly phenix.refine to do a first rigid body refinement to get first phases from our ligand free model. We give the starting model onlyATOM.pdb and the hkl-list as input files. We use the following settings:

   - tick „generate new set of control reflections“
   - refinement settings: „rigid body“
   - refinement settings: „add hydrogen to model: H/D at exchangable site, H elsewhere“

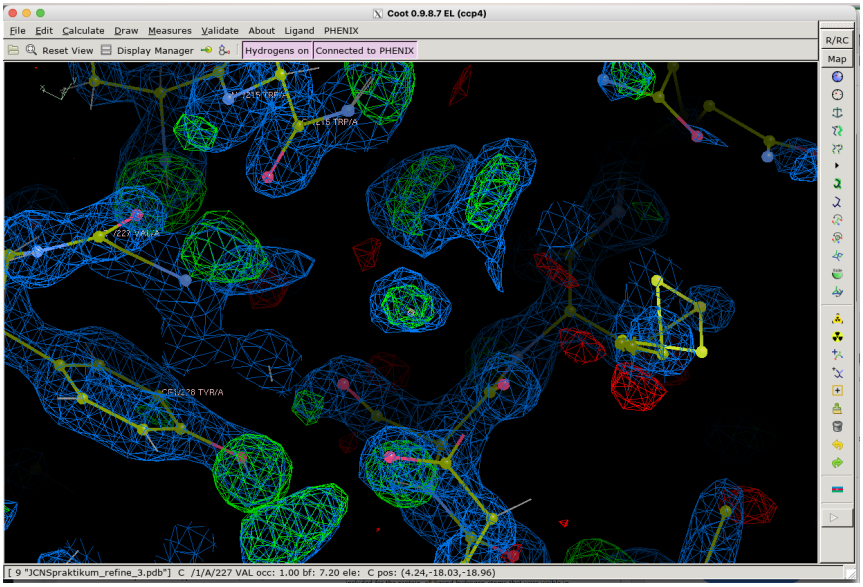

Fig. 13: A screenshot of the refinement in progress showing the aminopyridine density. Data taken from [11].

- refinement settings: scattering table „neutron“
- refinement settings: number of processors: 3

After three cycles of refinement the R-factors should drop to about 0.3. Can you make out, where the aminopyridine ligand is protonated?

5 Preparatory Exercises

In order to test your understanding of this experiment manual it is very helpful to solve the following problems:

1. How many protein molecules form one asymmetric unit in the given protein crystal (see specifications below)? Specifications of the protein crystal:
   - Frozen crystal with an orthorhombic unit cell (a≠b≠c and $\alpha = \beta = \gamma$=90°, space group P212121) with side lengths: a=57.96 Å, b=65.11 Å, c=86.51 Å
   - Molecular Weight of the protein: M_w=38770 Da (or g/mol)
   - Molecular Density of the protein: d=1.3g/cm3
   - Assumed water content in the crystal: Vs= 20%-50%
   - Z=4 (number of asymmetric units in the unit cell, i.e. the number of symmetry operators in the space group P212121)

2. Why is every second reflection missing/cancelled out on the main axis in the reciprocal space when using crystals with the space group P212121? Look into the structure factor equation 3!

6 Experiment Procedure

Each beamtime at BioDiff starts with mounting of crystals which have been brought by the users. When the first crystal has been aligned to the goniometer axis and the neutron beam, a first exposure can be made. From this first detector image one can judge already what the resolution of the data set will be when it is recorded using this crystal. Often one can already calculate the needed exposure time and the final completeness of the data set.

If the completeness and achievable resolution are good enough for the scientific question of the user to be answered, one can start data collection with this first crystal. But often one needs to mount some other crystals in order to see which crystal allows for the highest resolution and completeness in the shortest possible beamtime. This is often a delicate optimization process.

6.1 The experiment itself

After a short safety training, the instrument BioDiff will be explained in detail. As a first step we check the goniometer axis of the instrument with the use of the beam line camera. We will mount a protein crystal and align it on the goniometer axis using the cross hair of the beamline camera. After closing the drum of the instrument we can make an exposure with neutrons and collect a first detector image. From this image one try to deduce the resolution to which the crystal will scatter. Using the orientation matrix of the crystal inferred from this first diffraction image, we will develop a strategy for a collection of a full data set using the software HKL2000.

6.2 Data reduction

Using the example data set of trypsin or one data set recently measured at BioDiff, we will introduce the data reduction process. We will also discuss how one can optimize the integration of the Bragg reflexes. Time permitting we can also show our efforts to develop our own data reduction software called OpenHKL. The final outcome of this step of data processing is a list of intensities with their respective h, k and l value.

6.3 Data evaluation

Many users of BioDiff receive an hkl list file from the instrument responsibles of the respective diffractometer beam line. They choose then a refinement software to employ the fitting of the model to the hkl-list data. Here, the students can get hands on experience and perform their own refinement steps. The refinement of a neutron structure is never finished and a good quality refinment involves often a close look to the residual density and to the model it produced.

7 Experiment-Related Exercises

After performing the experiment one should be able to answer the following questions:

1. Why do hydrogen atoms appear on the negative contour of the scattering length density maps?
2. Why do the users often bring crystals where the water is exchanged with deuterated water?
3. What can you learn from a neutron structure of a protein which you cannot learn from an x-ray structure of the same protein?

Acknowledgement

The authors thank Andreas Heine and Gerhard Klebe for allowing us to use their data as a practical course.

References

[1] L. Stryer, *Biochemie* (Spektrum Akad. Verlag, Heidelberg Berlin New York, 1991), 4. edition.

[2] O. H. Weiergräber, *Proteins*, *Key Technologies*, volume 20, book section B7, p. 1000 (Forschungszentrum Jülich GmbH, Institute of Complex Systems, Jülich, 2011).

[3] M. P. Blakeley, A. J. Kalb, J. R. Helliwell, D. A. A. Myles, *The 15-K neutron structure of saccharide-free concanavalin A*, Proceedings of the National Academy of Sciences of the United States of America **101**, 16405, times Cited: 23 (2004).

[4] A. Ostermann, I. Tanaka, N. Engler, N. Niimura, F. G. Parak, *Hydrogen and deuterium in myoglobin as seen by a neutron structure determination at 1.5 angstrom resolution*, Biophysical Chemistry **95**, 183, times Cited: 38 (2002).

[5] W. Humphrey, A. Dalke, K. Schulten, *VMD: Visual molecular dynamics*, Journal of Molecular Graphics **14**, 33, times Cited: 6319 (1996).

[6] C. B. Anfinsen, *Some observations on the basic principles of design in protein molecules*, Comparative Biochemistry and Physiology **4**, 229, tY - JOUR (1962).

[7] J. Drenth, *Principles of Protein X-Ray Crystallography* (Springer Science+Business Media, LLC, New York, 2007).

[8] N. Niimura, A. Podjarny, *Neutron Protein Crystallography - Hydrogen, Protons, and Hydration in Bio-macromolecules*, IUCr Monographs on Crystallography (Oxford University Press, Oxford, New York, 2011).

[9] G. J. Kleywegt, T. A. Jones, *WHERE FREEDOM IS GIVEN, LIBERTIES ARE TAKEN*, Structure **3**, 535, times Cited: 170 (1995).

[10] A. T. Brunger, *FREE R-VALUE - A NOVEL STATISTICAL QUANTITY FOR ASSESSING THE ACCURACY OF CRYSTAL-STRUCTURES*, Nature **355**, 472, times Cited: 2956 (1992).

[11] J. Schiebel, R. Gaspari, A. Sandner, K. Ngo, H.-D. Gerber, A. Cavalli, A. Ostermann, A. Heine, G. Klebe, *Charges Shift Protonation: Neutron Diffraction Reveals that Aniline and 2-Aminopyridine Become Protonated Upon Binding to Trypsin*, Angewandte Chemie International Edition **56**, 4887 (2017).

[12] Z. Otwinowski, W. Minor, *[20] Processing of X-ray diffraction data collected in oscillation mode*, in *Macromolecular Crystallography Part A*, *Methods in Enzymology*, volume 276, pp. 307–326 (Academic Press, 1997).

[13] P. V. Afonine, R. W. Grosse-Kunstleve, N. Echols, J. J. Headd, N. W. Moriarty, M. Mustyakimov, T. C. Terwilliger, A. Urzhumtsev, P. H. Zwart, P. D. Adams, *Towards automated crystallographic structure refinement with phenix.refine*, Acta Crystallographica Section D **68**, 352 (2012).

Contact

BIODIFF

Phone: 089/158860-743
Web: http://www.mlz-garching.de/biodiff

Tobias E. Schrader

Jülich Centre for Neutron Science
at Heinz Maier-Leibnitz Zentrum
Phone: 089/158860-743
e-Mail: t.schrader@fz-juelich.de
Web: https://www.fz-juelich.de/profile/schrader_t

Andreas Ostermann

Heinz Maier-Leibnitz Zentrum (MLZ) und
Technische Universität München
Phone: 089/289-14702
e-Mail: Andreas.Ostermann@frm2.tum.de

PGAA

Prompt Gamma Activation Analysis

Zsolt Révay

Research Neutron Source Heinz Maier-Leibnitz (FRM II),
Technical University München

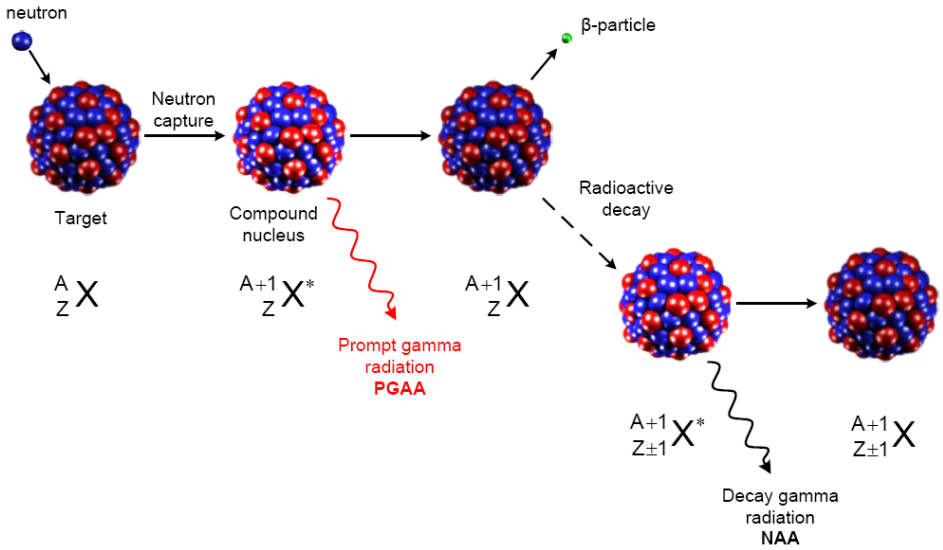

Contents

1 Introduction

The energy of **cold neutrons** is below 0.005 eV (i.e. much below the typical energies of chemical bonds), their wavelengths are around 5 Å (in the range of crystal lattices), and their velocities are a few hundred m s^{-1}. They are ideal for non-destructive investigations of atomic or nano-structures mainly based on neutron scattering. The neutron flux within the cold source is above 10^{14} cm^{-2} s^{-1}.

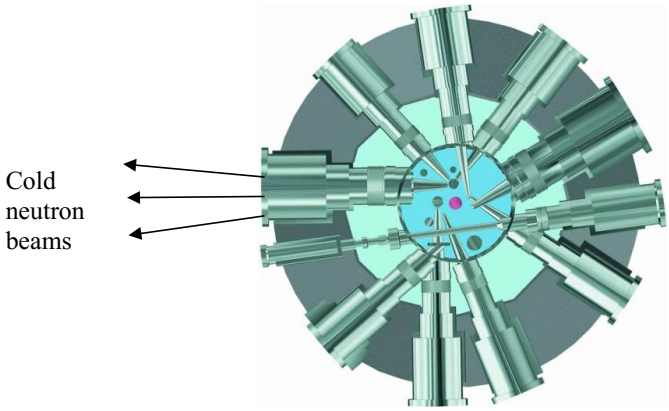

Figure 1. Beam tubes in FRM II reactor (source: FRM II webpage)

Cold neutrons can be transported away from the reactor core using **neutron guide**s. When using a simple flight tube, the intensity of the neutron beam decreases according to $1/r^2$. In guides, neutrons can be transmitted with just a very little loss, which is proportional to $1/r$. The inner surface of the guide tubes is covered with the so-called **supermirror** made of hundreds of sub-micron titanium and nickel layers. Each pair of metal layers reflects one wavelength with Bragg reflection, while the whole coating (with the total thickness of a few microns) reflects a whole wavelength range within ±2–3°. The guides can be as long as 50–100 m. The neutron flux at the end of a guide like this is still more than 10^9 cm^{-2} s^{-1}. The flux can be further increased with the use of elliptically tapered guides. At the PGAA facility at FRM II the flux at the focal point is about 5×10^{10} cm^{-2} s^{-1}.

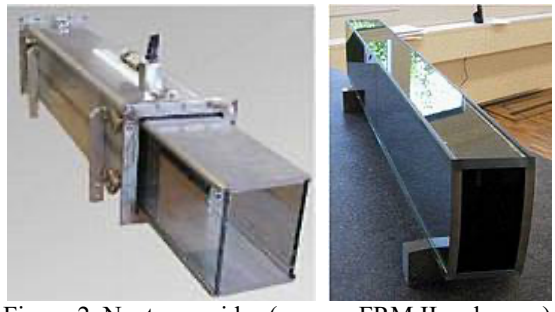

Figure 2. Neutron guides (source: FRM II web page)

2 Radiative neutron capture (or the (n,γ) reaction)

Neutrons have no electric charge; thus, they can interact with the positively charged atomic nucleus at any energy. (In contrast to charged particles, which need energies higher than a given threshold energy to interact with the nuclei.) Whenever a nucleus absorbs a slow (thermal or cold) neutron, a so-called compound nucleus is formed whose excitation energy equals the **binding energy** of the neutron. (For slow neutrons, the kinetic energy can be neglected.) The binding energy is in the range of 6–10 MeV for most nuclei, it tends to increase with the atomic number until Z = 22–28, then slowly decreases. Most compound nuclei get rid of the excitation energy with the emission of γ radiation. This is called radiative neutron capture, or (n,γ) reaction.

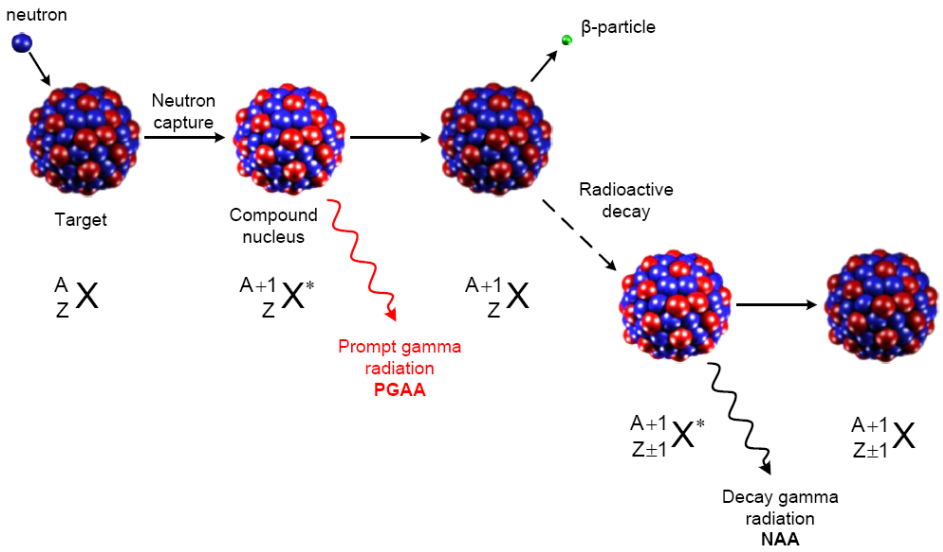

Figure 3. The process of the (n,γ) reaction

If the nucleus formed in the de-excitation is stable, then the process ends. If it is radioactive, then it decays away typically with β decay with a given half-life, during which **delayed γ radiation** is also emitted. The typical form is β^- decay, as these nuclides are neutron rich, but sometimes β^+ decay can also occur. As a result, we get a nucleus whose mass number is increased by one, and the atomic number is also increased by one, or in the case of β^+ decay, decreased by one.

After a neutron capture, certain nuclides emit charged particles: the most important reactions are the following: $^{3}He(n,p)^{3}H$, $^{6}Li(n,\alpha)^{3}H$, $^{10}B(n,\alpha)^{7}Li$, and $^{14}N(n,p)^{14}C$. In the case of neutron capture in ^{10}B, the first energy level above the ground state of ^{7}Li is also populated, that is why γ radiation with the energy of 478 keV is also emitted. These reactions have rather

high probabilities (cross sections), so they are applied in neutron detection or when shielding against neutrons.

The probability of the neutron capture is described by the **neutron capture cross section**. The SI unit of it is cm^2, but barn = 10^{-24} cm^2 is also accepted. The "real" cross section, as calculated from the sizes of protons and neutrons, is typically between 1–10 barns. While the scattering cross sections of the nuclei are not far from these values, the capture cross section can be several orders of magnitude smaller, or even higher. The nucleus of ^{4}He (i.e., the α particle) is so stable that it does not interact with neutrons at all. This is the only exception in the nature. Other stable nucleus formations typically have very low cross sections, like ^{12}C (0.0035 b), ^{16}O (0.00019 b), or the ones with closed neutron shells (e.g., ^{37}Cl, ^{40}Ca with $N = 20$, ^{90}Zr with $N = 50$, all less than 1 b). On the other hand, there are several nuclides, which "like" to absorb neutrons, i.e., they have high cross sections, such as ^{113}Cd (20,600 b), ^{157}Gd (257,000 b). These are typically heavy metals far from the magic numbers (meaning the nuclear shells), which have very dense level schemes, and an energy level slightly above the capture state is excited with a high probability (so-called low-energy resonances). Elemental cadmium and gadolinium (together with the above-mentioned boron) are also good neutron shielding materials.

The capture cross section highly depends on the neutron's kinetic energy. The most important rule that describes this correlation is the so-called **1/*v* law**, which means that the cross section is inversely proportional to the velocity (v), or the square root of the kinetic energy. This law is strictly valid for every nuclide at the cold neutron energies, and for most nuclides at thermal neutron energies. The light nuclides follow this rule up until the fast neutron energies. The simple explanation for this phenomenon is that the more time the neutron spends in the vicinity of the nucleus, the higher is the probability of its being absorbed.

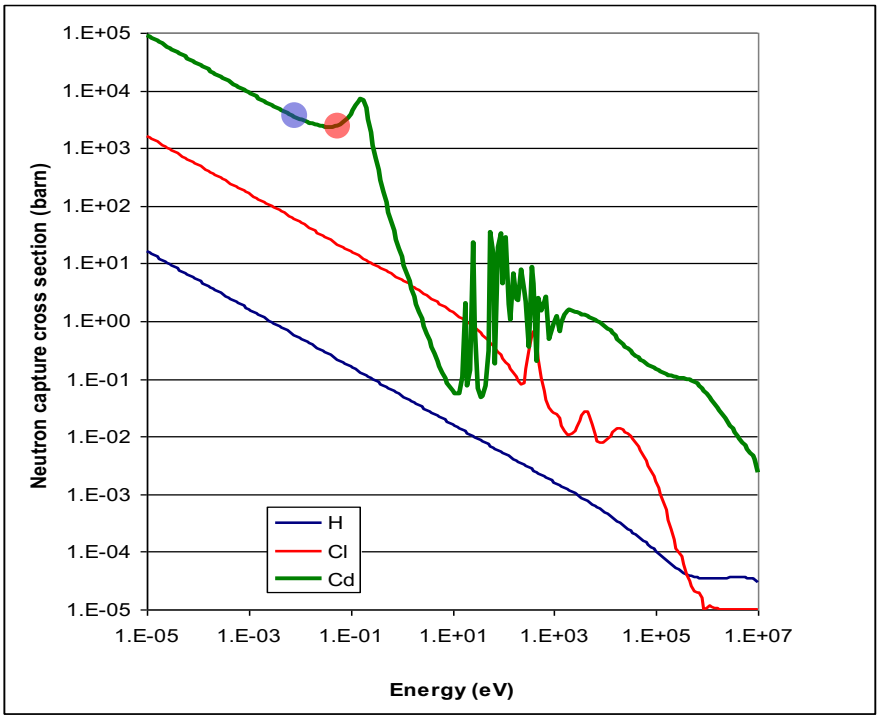

Figure 4. Capture cross sections of H, Cl and Cd as a function of energy.

As can be seen in the above figure, hydrogen (dominant isotope: ^{1}H) follows the $1/v$ law until about 1 MeV. Chlorine (^{35}Cl) has its first resonance above 100 eV, while in the case of cadmium (^{113}Cd) the first resonance is already at 0.17 eV, which is followed by broad region of unresolved resonances. This low-lying resonance overlaps with the thermal neutron energies. It can also be seen that in the cold-energy range, all cross-section curves are parallel on log-log scale, i.e., their ratios are independent from the neutron energies.

The capture state is not a state in the quantum mechanical sense, as it lives just for a very short time, decays in about 10^{-14} s, and de-excites in less than 10^{-10} s. This short live-time is still long enough that all the nucleons share equally the excitation energy (unlike in fast-neutron reactions, where the projectile runs through the nucleus kicking out one or more nucleons), but still far below the resolution times of the counting devices, and even more below the delayed γ radiation following β decay. The γ radiation emitted during the de-excitation is thus called **prompt gamma radiation**. The total energy released during the de-excitation always equals the binding energy.

There are a few nuclides, where no energy levels exist between the capture state and the ground state. These nuclides always emit their full excitation energy in the form one high-energy prompt gamma photon, like ^{1}H (2223 keV), ^{2}H (6250 keV). In all other cases, there is at least one energy level below the capture state; so, the de-excitation goes through an energy cascade.

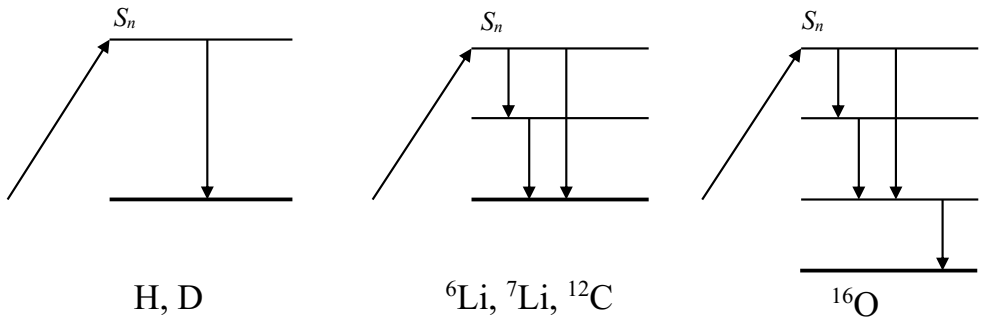

Figure 5. De-excitation from the capture state for a few light nuclides (S_n stands for the neutron binding energy).

The energies of the gamma photons correspond to the differences between the level energies; thus, they are characteristic to the emitter nuclide. (The gamma energy is slightly smaller than the energy of the transition due to the recoil of the nucleus, but the deviation is typically less than 1 keV.) The **branching ratios**, i.e., the probabilities of the transitions from a certain level depend on the nuclear properties of the states (spins, parities etc.).

The gamma rays appear in the spectra as peaks at certain energies. Heavier elements can have hundreds or thousands of levels below the capture state, at certain energy ranges sometimes they can be regarded as a continuum. The gamma spectra of these elements have **characteristic peaks** (close to the binding energy showing the primary transitions, and at low energies, showing the transitions to the ground state), but broad regions of irresolvable peaks also appear in them (see below).

The **emission probability** of a given γ photon is mainly determined by the branching ratio of the transition. At low energies, however, electrons might be emitted instead of gamma rays (electron conversion, EC).

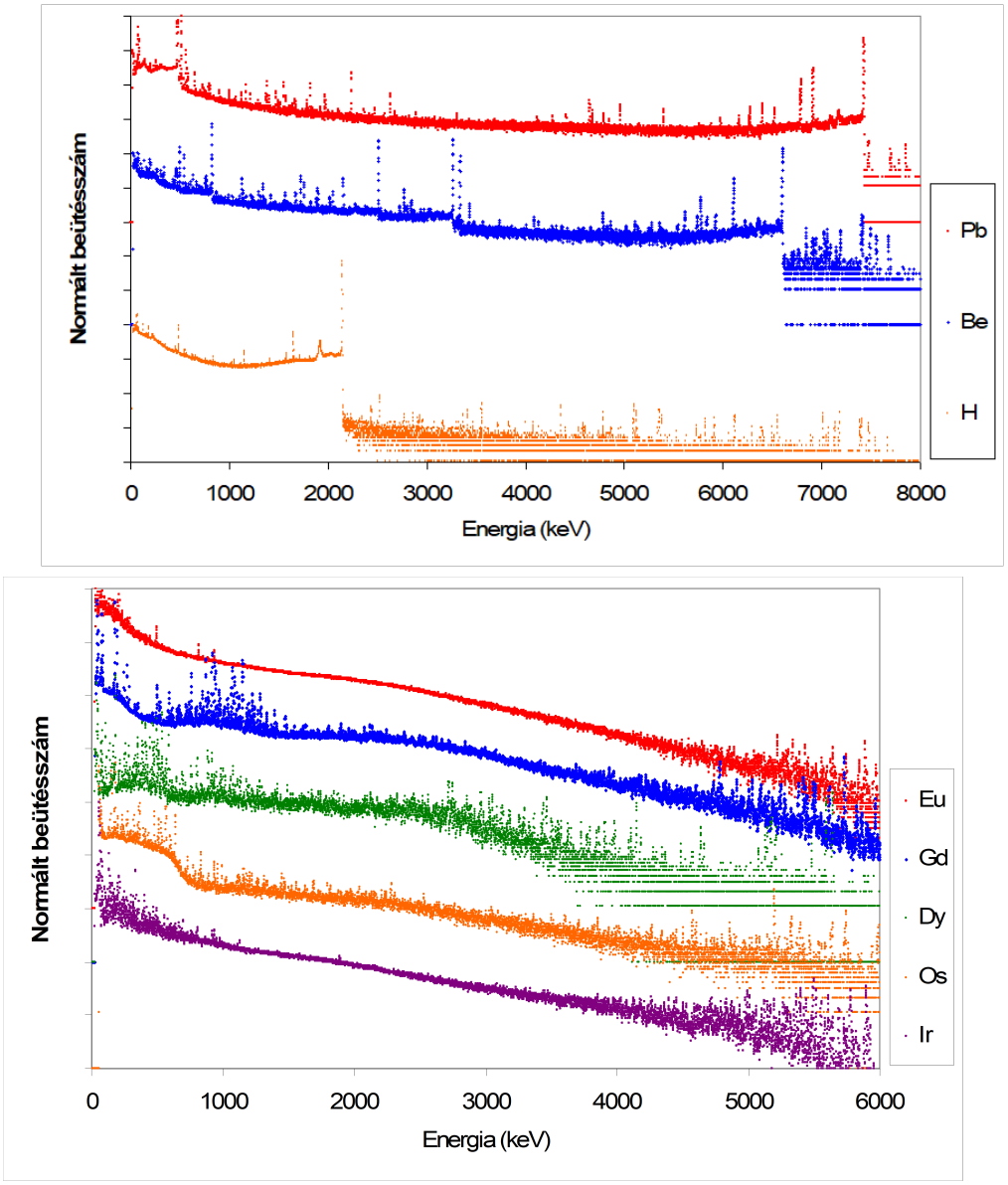

Figure 6. Spectra with strong characteristic peaks, with lower-intensity background peaks (above) and with many irresolvable peaks and broad continuum (below).

3 Chemical analysis based on radiative neutron capture

All the chemical elements emit a series of characteristic prompt gamma rays, based on which they can be identified in the gamma spectra. Because of the large number of peaks, interferences may disturb the identification. That is why, several of the strongest peaks need to be found to identify one element with a high certainty. Not just the energies, but also the **relative intensities** are characteristic. If we find a handful of peaks, whose energies agree with those of the element, and they also show the same intensity pattern, then we can regard the element as detected.

Once an element has been identified, the amount of it in the irradiated sample can be determined as follows:

$$\frac{A}{\varepsilon t} = aP_\gamma = n \;\; \Phi_0 \;\; \theta \sigma_0 P_\gamma = \frac{m}{M} N_A \;\; \Phi_0 \;\; \sigma_\gamma \tag{1}$$

where A is the peak area, ε is the counting efficiency, t is the measurement time (live time, s). The ratio $A/\varepsilon t$ shows the number of gamma photons emitted by the element in the irradiated sample in a second; it is sometimes called γ activity.
1) It equals the activity (*a,* number of decays per second) times the emission probability (P_γ).
2) When the activity is generated in a nuclear reaction, n is the number of atoms from the given element, which equals the mass m (g) over the molar mass M (g/mol) times the Avogadro constant N_A (mol^{-1}). Φ (cm^{-2} s^{-1}) is the flux of the neutron beam. At the end of the expression, the nuclear constants appear: θ is the isotopic abundance, σ_0 is the neutron capture cross section, while P_γ is the emission probability of the given gamma ray (mostly agrees with the branching ratio, discussed above).
3) The product of this three cannot be determined independently in this method, hence we use one unified quantity σ_γ, which is called the **partial gamma-ray production cross section**. The '0' index shows that the flux and the cross sections are regarded at thermal energies. The unit of the cross sections is cm^2 in this equation.

The activation equation in (1) is the basic equation for the **absolute method** of prompt gamma activation analysis (PGAA). Any quantity can be determined, if all the others are known. First, we have to calibrate our detection system with calibration sources of known activities and emission probabilities. Once we know the efficiency, with a flux monitor, whose mass and partial cross section are known, we can determine the flux. Then, if we know the partial cross section of an element for a given gamma peak, we can determine its mass. Alternatively, if we know the mass, then we can determine partial cross section for later analyses.

As the cross section is energy dependent, it seems important to differentiate between irradiations in cold and thermal beams. As mentioned above, the cross-section ratios are constant over the energy range of slow neutrons. This phenomenon can be used to simplify the flux determination. If we use the thermal cross section of a flux monitor to determine the flux, we use a number about 4-times too low, and thus we get an increased flux value. That is called the **thermal-equivalent flux**. If we use thermal-equivalent fluxes and thermal cross

sections, our calculations will always be consistent independent of the actual energy distribution of the neutron beam. (There is one exception, when a neutron beam's energy overlaps with the low-energy resonances. In this rare case, a special correction factor is taken into consideration to account for the discrepancy. In the frame of this lab practice, we do not deal with such cases.)

Sometimes we cannot be sure of the beam flux reaching the sample. The beam might be inhomogeneous, and we might not know the actual mass, either, because the sample itself can be larger than the beam. In such cases, we can still use the **relative method** of PGAA, i.e., we can use a simplified version of equation (1) as follows:

$$\frac{A_1 / \varepsilon_1}{A_2 / \varepsilon_2} = \frac{n_1}{n_2} \frac{\sigma_{\gamma,1}}{\sigma_{\gamma,2}} \tag{2}$$

where on the right-hand side, we can see the efficiency-corrected peak-area ratio which equals the molar ratio times the partial cross-section ratio. The measurement time and the flux cancel. The molar ratio can easily be converted into mass ratio, too: $m_1/m_2 = n_1/n_2 \times M_1/M_2$. The relative method can be regarded as using an internal flux monitor chosen from the components of the sample, while the flux is not explicitly expressed.

From the mass ratios or the molar ratios, the composition can be calculated either in weight percent or in molar percent. With the relative method, we do not get the actual mass of the element in the irradiated sample. It makes other simplifications possible, too. As we do not need the absolute efficiency, just the efficiency ratio, we do not need to use absolute activities during the calibration, which are sometimes known just with a relatively high uncertainty.

If we calculate the concentration from equation 1, and disregard the uncertainties from flux, time, and efficiency, then we also follow the relative method in the end.

The relative method makes it very simple to determine partial cross sections, too: one just needs to irradiate a simple compound, whose **stoichiometric coefficients** are very well known. Then, from the efficiency-corrected peak-area ratio, one can simply determine the unknown cross section relative to the other.

We can also use the delayed γ radiation for analysis as well, as the **delayed gammas** are also characteristic. The energy released after the activation is typically less than 3 MeV, which results in much simpler spectra. When the counting takes place after the irradiation, one has to correct for the decay using these three factors:

$$S = 1 - e^{-\lambda t_{act}} \tag{3}$$

$$D = e^{-\lambda t_{cool}} \tag{4}$$

$$C = \frac{1 - e^{-\lambda t_{count}}}{\lambda t_{count}} \tag{5}$$

where $\lambda = \ln 2 / T_{1/2}$ (the half-life in seconds), t_{act}, t_{cool}, and t_{count} mean the activation, cooling, and counting times, respectively. The **saturation activity** can be calculated from the dividing the activity on the left-hand side in equations 1 by the product of these three factors.

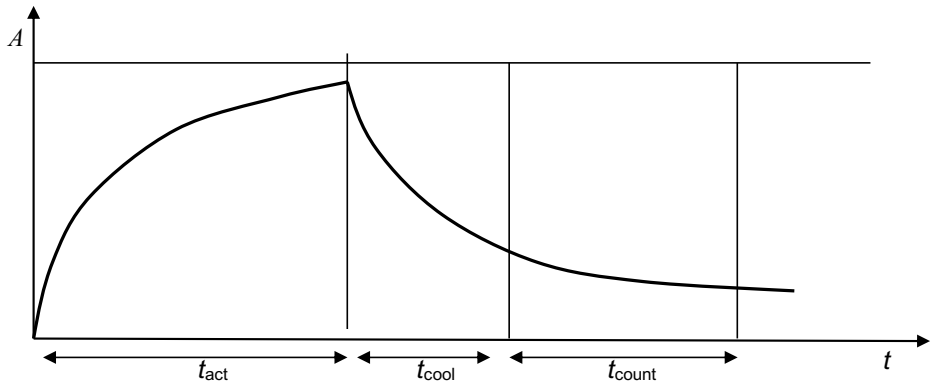

Figure 7. The change of activity in time during and after the activation. The thin horizontal line represents the saturation activity.

This method is called the **neutron activation analysis (NAA).** The irradiations take place in a near-core irradiation channel, while the counting is performed in low-background laboratories, where the samples are transferred with pneumatic (rabbit) systems. The high-flux cold beam at FRM II can be used for activation very efficiently, too.

If the counting is performed simultaneously with the irradiation, then we use the in-beam correction factor alone:

$$B = 1 - \frac{1 - e^{-\lambda t_{count}}}{\lambda t_{count}} \tag{6}$$

4 Gamma spectroscopy

Gamma radiation is acquired by a gamma spectrometer. The soul of this system is the **high-purity germanium (HPGe) semiconductor detector**.

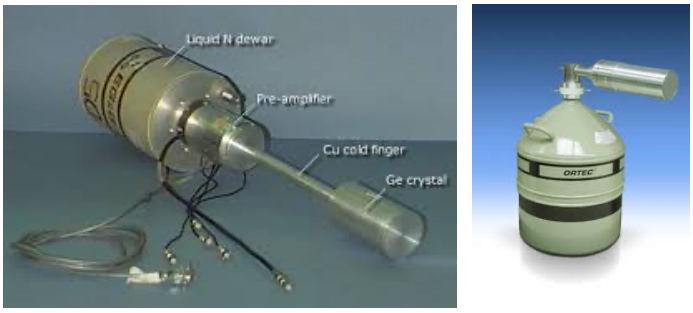

Figure 8. HPGe detectors

It can be regarded as a large (100–200 cm^3) diode, which is biased in the terminating direction, i.e., no electric current is flowing in it. Once ionizing radiation produces electron-hole pairs in its volume, a weak current can be observed. To minimize the disturbing effects from the thermal noise, the detector is kept at the temperature of liquid nitrogen. The detector signal is amplified and its height, that is proportional to the absorbed energy, is determined by a **digital spectrometer**. After the evaluation of one signal, the spectrometer adds one count to a channel proportional to this signal height (in the end to the gamma-ray energy) in the so-called **multi-channel analyzer (MCA)**. The spectra we use contain 16384 channels, we collect photons between about 30 keV and 11 MeV, thus one channel is about 0.7 keV broad. The total number of counts is typically many millions. The spectrometer handles **count rates** up to a few ten thousand counts per second (cps), but is typically operated at a few thousand cps.

The detector does not directly detect the γ photons. In the interaction of the photon with matter (see below), energetic charged particles (electrons, and sometimes also positrons) are produced. They generate a large number of electron-hole pairs in the semiconductor crystal. Counting is a statistical procedure, which results in a more-or-less Gaussian peak, whose Full Width at the Half of Maximum (FWHM) is 0.1–0.3% of the energy (at 1332 keV, large detectors, like the one at FRM II, have an FWHM of 1.9 keV, but using the low gain typical for PGAA it is somewhat worse: 2.3 keV).

The spectrum of a mono-energetic γ ray does not contain only one single line in the spectrum. The detector response function depends on the interactions of the photons with the germanium crystal, which are the following:

1. **Photo-electric effect.** In this interaction, the total energy of the γ photon is transmitted to an atomic electron, whose energy will be fully absorbed, and a signal proportional to this absorbed energy will be seen at the output. Photo-electric effect is typical for low-energy (max. few hundred keV) photons. If a photon is immediately absorbed in the crystal in one photo-electric interaction, we will see a count appearing at the energy of the photon (E).
2. **Compton scattering.** In Compton scattering, only a fraction of the photon energy will be transmitted to an atomic electron, and a lower-energy scattered photon will also be released. This photon may leave the crystal, or can interact with it again. Compton scattering is the typical interaction of medium-energy photons (max. a few MeV). If the photon undergoes only Compton scattering, then the respective count will appear somewhere below the photon energy. That is why we see a broad Compton plateau in each spectrum. Compton scattering is not isotropic. Its highest probability is for forward scattering, when there is no energy loss, and the backward scattering, when the energy loss is the greatest, and the back scattered photon has the energy of about 250 keV (a bit less than the half of the electron's rest mass). When this photon leaves the detector, a count will appear ~250 keV below E.
3. **Pair production.** This is typical for high-energy photons, i.e., with the energy of several MeV. In this case, an electron-positron pair is produced in the vicinity of an atom. Both charged particles lose their kinetic energies fully. After slowing down, the positron annihilates on an atomic electron producing (in most cases) two γ photons with the energy of exactly 511 keV (which is the rest mass of the electron), flying in the opposite directions. Any of the two photons may or may not interact and thus be detected in the detector. If one of them does not, but the other is fully

absorbed, then a peak will appear at the energy of $E - 511$, if none of them do, then a second peak appears also at $E - 1022$. They are called single and double escape peaks, respectively.

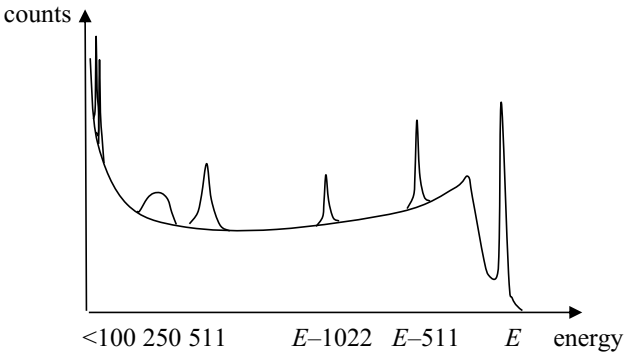

Figure 9. Schematic drawing of the detector response function.

The effects of all three interactions can be observed in the **detector response function** (see the figure above). The full-energy peak at E means the events, during which the whole photon energy is absorbed in the detector in one or several steps. The two escape peaks can be seen at the energies of E–511 and at E–1022. The so-called annihilation peak can be seen at 511 keV, which originate from escape photons from the structural materials. The energy of the Compton electrons is between 0 and $E - 250$, that is why the Compton plateau starts at very low energies and ends half way between the single escape peak and the full-energy peak in the form of the so-called Compton edge. Between this and the full-energy peak, events from multiple Compton scatterings appear. The photons back-scattered from the structural materials, produce a broad peak around 250 keV. Below 100 keV, one can see X-ray peaks induced by the gamma radiation in the structural materials and in the detector.

The Compton plateau can be significantly reduced by a solution called **Compton suppression.** A scintillator detector (in our case bismuth germanate, BGO, see figure below) surrounds the HPGe detector in order to catch the scattered photons.

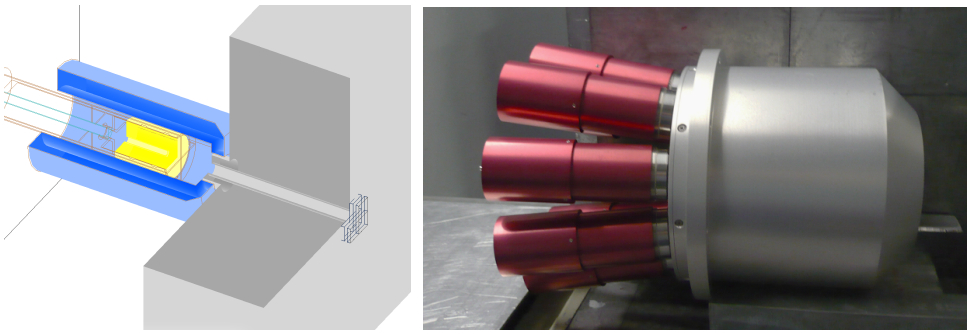

Figure 10. Bismuth germanate (BGO) scintillator surrounding the HPGe detector used for Compton suppression, design and photo.

Scintillators are another typical detector type in nuclear measurements. They emit a light flash in visible-ultraviolet range while being ionized. The light is collected by mirrors to a converter (so-called photo cathode) emitting electrons, and so-called photo-multiplier tubes amplify this weak current for further handling by electronics. The most well-known scintillators are zinc sulfide (ZnS), sodium iodide (NaI), and bismuth germanate (BGO).

The detector system is surrounded by a thick lead shielding, which also serves the purpose that the BGO does not see any other radiation, just the one scattered out from the HPGe.

Whenever the two detectors fire at the same time, a Compton event has just happened, meaning energy loss due to scattering. If those events are rejected, the spectrum will be much cleaner. Compton suppression can efficiently reduce the Compton plateau, thus smaller characteristic peaks can be detected all over the spectrum, as can be seen in the next figure.

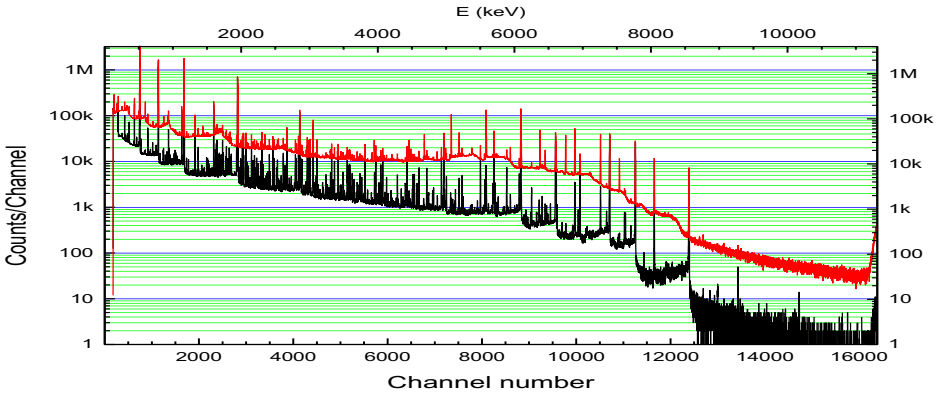

Figure 11. Normal and Compton-suppressed prompt gamma spectra of Cl (PVC).

The spectrum can be regarded as a vector, whose elements are integers. In our context, these numbers are counts in channels. To assign physical meaning to this set of counts, one has to calibrate the spectrum. The calibration remains valid until the system is changed, but it needs to be checked from time to time. (The PGAA instrument is calibrated at the beginning of each cycle.)

The spectrum peaks can then be fit using several programs, which determine the net peak areas, see below.

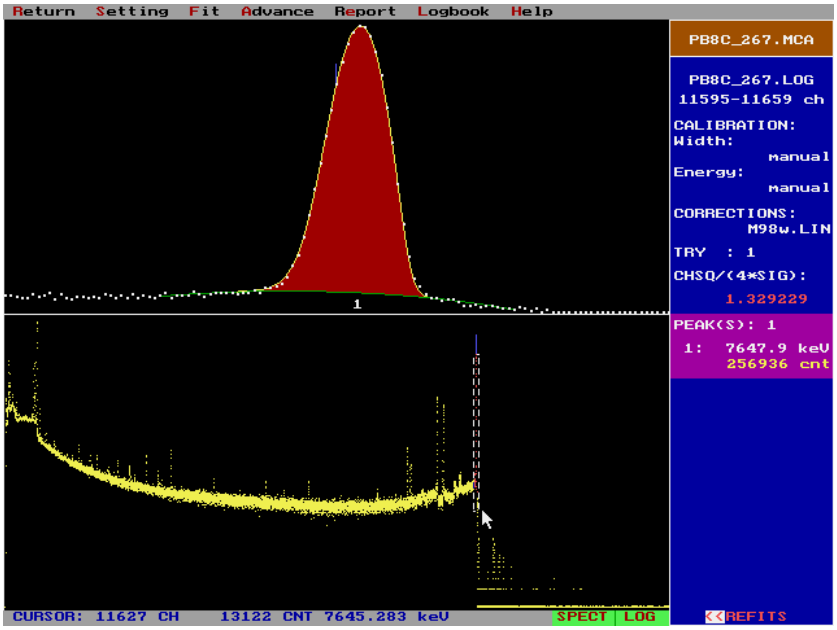

Figure 12. Peak fitting with Hypermet-PC.

To assign the channels to photon energy is called the **energy calibration**, when calibration sources are measured, whose photon energies are accurately known. Then we need to determine the detector efficiency, which shows the fraction of γ photons collected at a given energy compared to actual number of photons emitted by the sample. The detector at the PGAA facility is located at the distance of 330 mm from the sample, which means that we detect only a very small fraction (less than 0.1%) of the photons. At about 100 keV, the photons are detected for sure, once they reach the detector, but high-energy photons are detected with a much smaller probability. The detector efficiency involves both the geometric and the intrinsic efficiency. The **efficiency** curve for the PGAA detector at FRM II can be seen in the next figure.

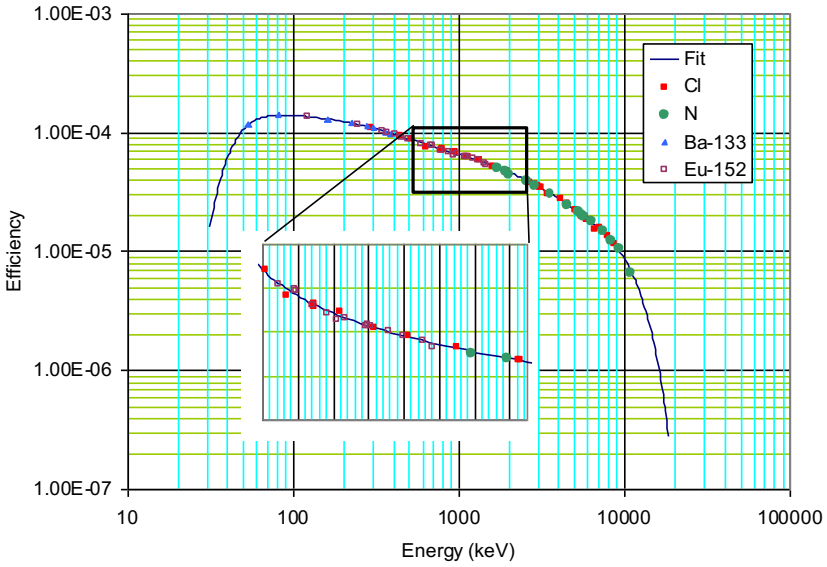

Figure 13. **Efficiency** of the HPGe detector. (Inset is linear.)

The **chemical analysis** is normally performed using a dedicated program. During the analysis, one has to identify all the chemical elements whose strongest lines appear in the spectrum (**qualitative analysis**). Then the masses have to be calculated according to equation 1 (**quantitative analysis**). In case of several strong lines, an average mass can be determined. The equivalent masses of the background components (lead from the shielding, fluorine from the Teflon sample holder, aluminum from sample chamber, etc.) have to be subtracted from the masses. These masses can be obtained from the chemical analysis of background spectra. From the net masses, one can then determine the composition of the sample using the relative method of chemical analysis.

5 PGAA instrument at FRM II

Neutron guides and collimators. The neutron beam arrives from the cold source through an approx. 55-m long, curved neutron guide, whose last 7 m is elliptically tapered. (The curvature filters out fast neutrons and gamma radiation arriving from the core.) The last 110-cm long section can be replaced with a collimator. In the first case one gets a strong focused beam (thermal-equivalent flux up to 6×10^{10} cm^{-2} s^{-1}), while in the second case, a weaker homogeneous beam is the result (flux up to 3×10^{9} cm^{-2} s^{-1}). The beam size is maximum 20×20 mm^2.

The **sample chamber** is made of aluminum and is lined with ^{6}Li-containing plastic (to absorb the scattered neutrons). It can be evacuated. It is equipped with a sample changer: a

carousel with 16 positions, from where aluminum sample frames can be moved into the beam. The samples are attached to the frames with Teflon string, and are typically sealed in Teflon (CF_2) bags.

The anti-Compton detector system (HPGe surrounded by BGO) is placed perpendicularly to the beam. The sample-to-detector distance is 330 mm. The radiation emitted by the sample reaches the HPGe detector through a lead collimator with a diameter of 20 mm.

Behind the sample chamber, a **beam stop** is located. It is made of boron carbide. It absorbs the thermal neutrons while emitting 478-keV γ photons, which are shielded against with lead. (1 cm of lead attenuates the 478-keV gamma rays from neutron capture on boron with about an order of magnitude.)

The whole instrument is covered with about 3 t of **lead** to **shield** against the strong radiation from the neutron guide, the beam stop, and the sample. The layout can be seen below.

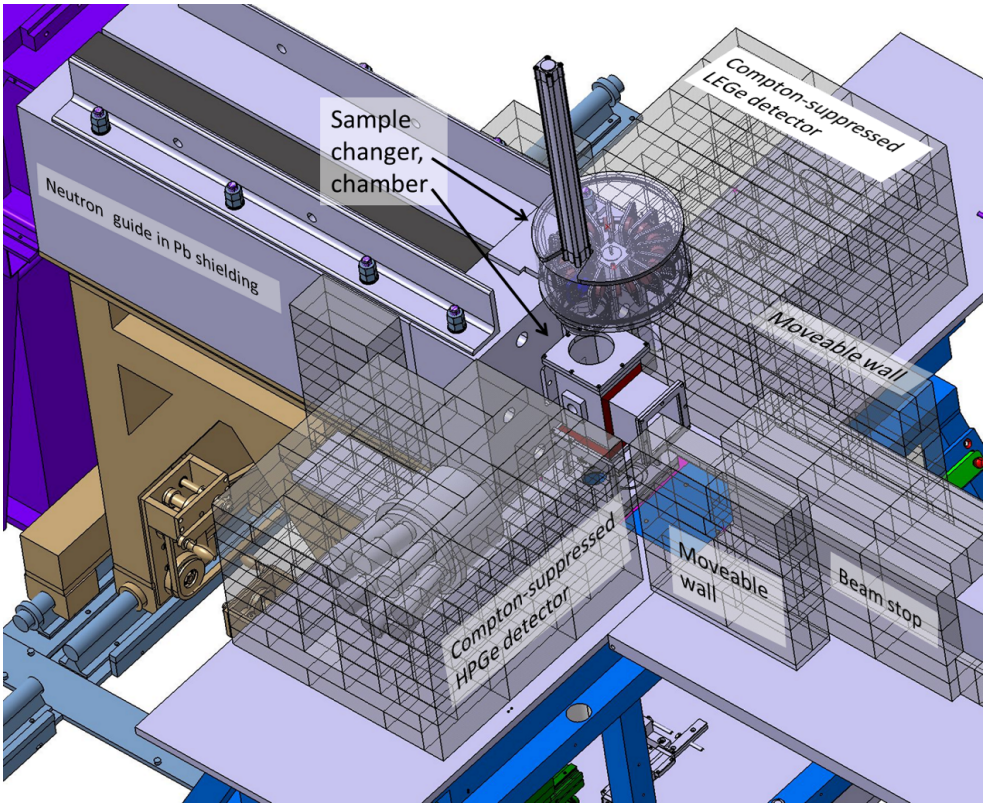

Figure 14. The layout of the PGAA facility. (Lead shielding and neutron guide removed around the neutron beam.)

6 Preparations

Read the description carefully.

Calculate the present activity of a radioactive source, whose activity was 393 kBq ±1.5% at 2008-03-01 (1st of March, 2008) and its half-life: 13.516 y. Use excel, so that it can be transferred to any other dates.

Check the rules of error propagation.

7 Experiment

7.1 Efficiency

Determine the efficiency of the detector at selected energies using a ^{152}Eu source.

Activity of the source: 393 kBq ±1.5% at 2008-03-01 (1st of March, 2008), its half-life: 13.516 y.

Plot the data points in log-log scale, then fit a straight line to it, and use this function in the later tasks.

Table 1. Energies and emission probabilities together with their uncertainties for ^{152}Eu (also available in an excel file).

Energy (keV)	Emission probability (%)
121.7817 (3)	28.41 (13)
244.6974 (8)	7.55 (4)
344.2785 (12)	26.58 (12)
411.1165 (12)	2.237 (10)
778.9045 (24)	12.96 (6)
867.380 (3)	4.241 (23)
964.079 (18)	14.49 (6)
1085.837 (10)	10.13 (6)
1089.737 (5)	1.73 (1)
1112.076 (3)	13.40 (6)
1212.948 (11)	1.415 (9)
1299.142 (8)	1.632 (9)
1408.013 (3)	20.84 (9)
1457.643 (11)	0.498 (4)

7.2 Flux

Determine the thermal-equivalent neutron flux at the sample position with a titanium flux-monitor foil using the efficiencies from task 1. (Take care of the units!)

mass: 0.00275g
molar mass: 47.87 g/mol
cross section at 342 keV: 1.84 barn ± 1.1%

cross section at 1381 keV: 5.18 barn ± 2.3%
(for comparison: efficiency at 342 keV in Feb 2019: 0.000161± 1.6%)
(for comparison: efficiency at 1381 keV in Feb 2019: $8.13 \times 10^{-5} \pm 1.8\%$)

7.3 Cross section

Determine the partial gamma-ray production cross section for 770-keV line of potassium from the PGAA spectrum of potassium chloride (KCl) using the relative method. Prepare and measure the sample, evaluate the lines at 770 keV and at 517 keV. Calculate the partial cross section and estimate the uncertainty of the result.

cross section: Cl 517 keV σ_γ: 7.58 ± 0.6%
(for comparison: efficiency ratio in Feb 2019: $\varepsilon(770)/\varepsilon(517) = 1.211 \pm 0.7\%$)

7.4 Analysis

Prepare a sample of cement, measure it with PGAA. Collect prompt (and decay) spectra. In the spectrum viewer, identify the major components of the sample (using the databases available at the instrument), i.e., make the qualitative analysis. Determine the composition based on the strongest lines of the identified elements, i.e., perform the quantitative analysis on the sample. Use Table 2 (and its excel-equivalent) for checking the characteristic peaks.

8 Exercises

Fit a function to the efficiency data points (e.g. linear on log-log scale) determined in Task 1. Use this function whenever the efficiency is needed.
Determine the flux from the prompt gamma spectrum of Ti foil (Task 2) using the areas of the Ti peaks at 341 and 1381 keVs.
Calculate the partial gamma-ray production cross section of K at the energy of 770 keV using the efficiency function and the spectrum from Task 3.
Based on the identified peaks of the detected elements from the spectrum of Task 4, please determine the composition of the sample.

Table 2. Molar masses of elements for Z<30, efficiencies at different energies (from Aug 2014, efficiency ratios are approximately valid at any time), partial gamma-ray production cross sections for the prompt (and certain decay) gamma lines. (Also available in Excel.)

Z	El	MW	E(keV)	dE	ε(b)	dε%	σ	dσ%	RI	T1/2 (s)
1	**H**	1.008	**2223.259**	0.019	5.76E-05	*1.2*	3.33E-01	*0.2*	100.0	
3	**Li**	6.941	**2032.31**	0.07	6.1E-05	*1.1*	3.98E-02	*5*	100.0	
3	**Li**	6.941	**980.559**	0.046	8.65E-05	*0.4*	4.36E-03	*5.1*	11.0	
3	**Li**	6.941	**1051.817**	0.048	8.43E-05	*0.4*	4.36E-03	*5.1*	11.0	
4	**Be**	9.012	**853.631**	0.011	9.1E-05	*0.5*	1.65E-03	*8.9*	26.7	
4	**Be**	9.012	**3367.484**	0.035	4.22E-05	*1.5*	2.92E-03	*8.9*	47.3	
4	**Be**	9.012	**2590.014**	0.025	5.17E-05	*1.3*	1.88E-03	*8.9*	30.4	
4	**Be**	9.012	**6809.579**	0.099	2.17E-05	*1.4*	6.18E-03	*9*	100.0	
5	**B**	10.811	**477.6**	5	0.000112	*0.6*	7.13E+02	*0.3*	100.0	
6	**C**	12.011	**1261.708**	0.057	7.82E-05	*0.5*	1.23E-03	*2.7*	45.6	
6	**C**	12.011	**4945.302**	0.066	3.01E-05	*1.4*	2.70E-03	*2.9*	100.0	
6	**C**	12.011	**3684.016**	0.069	3.91E-05	*1.5*	1.17E-03	*3.5*	43.5	
7	**N**	14.007	**1884.853**	0.031	6.38E-05	*1.0*	1.45E-02	*1.3*	61.1	
7	**N**	14.007	**5268.984**	0.072	2.83E-05	*1.4*	2.37E-02	*1.5*	100.0	
7	**N**	14.007	**5297.662**	0.153	2.81E-05	*1.4*	1.67E-02	*1.6*	70.5	
7	**N**	14.007	**5533.251**	0.076	2.7E-05	*1.3*	1.57E-02	*1.6*	66.0	
7	**N**	14.007	**6322.301**	0.088	2.35E-05	*1.3*	1.49E-02	*1.7*	62.8	
7	**N**	14.007	**10829.102**	0.208	1.04E-05	*4.8*	1.07E-02	*3.5*	44.9	
8	**O**	15.999	**870.682**	0.034	9.04E-05	*0.5*	1.75E-04	*6.2*	99.8	
8	**O**	15.999	**1087.714**	0.031	8.32E-05	*0.4*	1.51E-04	*6.3*	85.9	
8	**O**	15.999	**2184.381**	0.039	5.82E-05	*1.2*	1.50E-04	*6.2*	100.0	
8	**O**	15.999	**3272.109**	0.069	4.32E-05	*1.4*	3.53E-05	*7.1*	20.1	
9	**F**	18.998	**1633.602**	0.015	6.91E-05	*0.8*	9.60E-03	*4.3*	100.0	11.2
9	**F**	18.998	**583.493**	0.022	0.000104	*0.6*	3.52E-03	*4.3*	36.7	
9	**F**	18.998	**655.942**	0.022	9.98E-05	*0.6*	1.96E-03	*4.3*	20.5	
9	**F**	18.998	**6600.386**	0.11	2.25E-05	*1.3*	9.85E-04	*5.2*	10.3	
11	**Na**	22.99	**1368.633**	0.006	7.55E-05	*0.6*	5.30E-01	*1.6*	18.5	53852
11	**Na**	22.99	**90.979**	0.016	0.000176	*1.7*	2.65E-01	*1.3*	45.1	
11	**Na**	22.99	**869.221**	0.017	9.04E-05	*0.5*	1.13E-01	*1.2*	20.8	
11	**Na**	22.99	**6395.048**	0.126	2.33E-05	*1.3*	1.01E-01	*2*	19.3	
12	**Mg**	24.305	**584.936**	0.024	0.000104	*0.6*	3.16E-02	*4.7*	100.0	
12	**Mg**	24.305	**1808.616**	0.059	6.54E-05	*1.0*	1.81E-02	*4.7*	57.3	
12	**Mg**	24.305	**2828.117**	0.105	4.85E-05	*1.4*	2.39E-02	*4.7*	75.6	
12	**Mg**	24.305	**3916.653**	0.157	3.71E-05	*1.5*	3.14E-02	*4.7*	99.5	
12	**Mg**	24.305	**3053.85**	0.117	4.56E-05	*1.4*	8.27E-03	*4.8*	26.2	
13	**Al**	26.982	**1778.85**	0.03	6.6E-05	*1.0*	2.33E-01	*1.3*	99.4	134.5
13	**Al**	26.982	**7723.782**	0.255	1.86E-05	*1.5*	6.67E-02	*2*	28.7	
14	**Si**	28.086	**3538.976**	0.05	4.05E-05	*1.5*	1.18E-01	*1.7*	100.0	
14	**Si**	28.086	**4933.826**	0.074	3.01E-05	*1.4*	1.12E-01	*2*	95.3	
14	**Si**	28.086	**1273.383**	0.029	7.79E-05	*0.6*	2.89E-02	*1.9*	24.5	
14	**Si**	28.086	**2092.914**	0.032	5.99E-05	*1.1*	3.30E-02	*1.9*	28.0	
14	**Si**	28.086	**6379.747**	0.107	2.33E-05	*1.3*	2.10E-02	*2.8*	17.8	
14	**Si**	28.086	**7199.016**	0.127	2.04E-05	*1.4*	1.27E-02	*3.1*	10.8	
15	**P**	30.974	**77.992**	0.023	0.000171	*1.6*	5.89E-02	*4.8*	74.4	
15	**P**	30.974	**512.65**	0.018	0.000109	*0.6*	7.92E-02	*5*	100.0	
15	**P**	30.974	**636.57**	0.017	0.000101	*0.6*	3.10E-02	*4.6*	39.1	
15	**P**	30.974	**1071.154**	0.02	8.37E-05	*0.4*	2.48E-02	*4.7*	31.3	
15	**P**	30.974	**3899.648**	0.076	3.72E-05	*1.5*	3.01E-02	*4.7*	38.0	
16	**S**	32.066	**841.013**	0.014	9.15E-05	*0.5*	3.48E-01	*1.7*	100.0	
16	**S**	32.066	**2379.495**	0.035	5.5E-05	*1.3*	2.08E-01	*1.5*	59.9	
16	**S**	32.066	**5420.241**	0.1	2.75E-05	*1.4*	3.09E-01	*2.3*	88.9	
16	**S**	32.066	**3220.364**	0.057	4.37E-05	*1.4*	1.24E-01	*1.6*	35.8	
17	**Cl**	35.453	**517.077**	0.008	0.000109	*0.6*	7.43E+00	*0.9*	83.2	
17	**Cl**	35.453	**1164.831**	0.012	8.09E-05	*0.5*	8.92E+00	*0.7*	100.0	
17	**Cl**	35.453	**788.37**	0.212	9.36E-05	*0.5*	4.90E+00	*2*	55.0	
17	**Cl**	35.453	**786.182**	0.15	9.37E-05	*0.5*	3.61E+00	*2*	40.5	
17	**Cl**	35.453	**1951.15**	0.015	6.25E-05	*1.1*	6.49E+00	*0.8*	72.7	
17	**Cl**	35.453	**1959.359**	0.016	6.24E-05	*1.1*	4.18E+00	*0.9*	46.9	
17	**Cl**	35.453	**6110.711**	0.072	2.44E-05	*1.3*	7.37E+00	*1.4*	82.6	
17	**Cl**	35.453	**6619.576**	0.081	2.24E-05	*1.3*	2.75E+00	*1.6*	30.8	
17	**Cl**	35.453	**7790.277**	0.106	1.84E-05	*1.5*	2.89E+00	*2.1*	32.4	

Z	El	MW	E(keV)	dE	ε(b)	dε%	σ	dσ%	RI	T1/2 (s)
17	**Cl**	35.453	**6627.865**	0.084	2.24E-05	*1.3*	1.56E+00	*1.9*	17.5	
17	**Cl**	35.453	**8578.583**	0.153	1.61E-05	*1.8*	9.28E-01	*2.8*	10.4	
19	**K**	39.098	**770.325**	0.023	9.44E-05	*0.5*	9.03E-01	*1.3*	100.0	
19	**K**	39.098	**1158.88**	0.024	8.11E-05	*0.5*	1.60E-01	*1.6*	17.7	
19	**K**	39.098	**1618.976**	0.029	6.95E-05	*0.8*	1.30E-01	*1.6*	14.4	
20	**Ca**	40.078	**1942.677**	0.027	6.27E-05	*1.1*	3.52E-01	*2.1*	100.0	
20	**Ca**	40.078	**519.563**	0.075	0.000108	*0.6*	5.03E-02	*2.6*	14.3	
20	**Ca**	40.078	**2001.314**	0.029	6.16E-05	*1.1*	6.59E-02	*2.3*	18.7	
20	**Ca**	40.078	**6419.694**	0.213	2.32E-05	*1.3*	1.76E-01	*2.6*	50.0	
20	**Ca**	40.078	**4418.497**	0.12	3.33E-05	*1.4*	7.08E-02	*2.6*	20.1	
21	**Sc**	44.956	**147.114**	0.016	0.00017	*1.6*	6.08E+00	*1.4*	85.2	
21	**Sc**	44.956	**227.86**	0.016	0.000149	*1.0*	7.13E+00	*1.5*	100.0	
21	**Sc**	44.956	**142.627**	0.016	0.000171	*1.6*	4.88E+00	*1.5*	68.5	
21	**Sc**	44.956	**295.343**	0.019	0.000135	*0.7*	3.97E+00	*2.8*	55.6	
22	**Ti**	47.88	**1381.738**	0.027	7.51E-05	*0.6*	5.18E+00	*2.3*	100.0	
22	**Ti**	47.88	**341.689**	0.029	0.000127	*0.6*	1.84E+00	*1.1*	35.6	
22	**Ti**	47.88	**1585.952**	0.027	7.02E-05	*0.8*	6.24E-01	*1.2*	12.1	
22	**Ti**	47.88	**6760.011**	0.089	2.19E-05	*1.4*	2.97E+00	*2.9*	57.3	
22	**Ti**	47.88	**6418.353**	0.08	2.32E-05	*1.3*	1.96E+00	*2.9*	37.8	
23	**V**	50.942	**1434.06**	0.01	7.38E-05	*0.7*	4.95E+00	*2.1*	99.0	224.58
23	**V**	50.942	**125.234**	0.027	0.000175	*1.7*	1.61E+00	*2.6*	32.5	
23	**V**	50.942	**645.789**	0.022	0.0001	*0.6*	7.69E-01	*2.2*	15.6	
23	**V**	50.942	**6517.617**	0.148	2.28E-05	*1.3*	7.83E-01	*5.5*	15.8	
23	**V**	50.942	**7163.168**	0.181	2.05E-05	*1.4*	5.90E-01	*7.3*	11.9	
24	**Cr**	51.996	**834.803**	0.033	9.17E-05	*0.5*	1.38E+00	*1.9*	100.0	
24	**Cr**	51.996	**749.102**	0.032	9.53E-05	*0.5*	5.69E-01	*1.5*	41.3	
24	**Cr**	51.996	**7937.858**	0.117	1.8E-05	*1.6*	4.24E-01	*2.5*	30.8	
24	**Cr**	51.996	**8510.681**	0.137	1.63E-05	*1.8*	2.31E-01	*3.5*	16.7	
24	**Cr**	51.996	**8482.84**	0.14	1.64E-05	*1.8*	1.68E-01	*4.2*	12.2	
25	**Mn**	54.938	**846.754**	0.02	9.13E-05	*0.5*	1.28E+01	*1.2*	62.9	9280
25	**Mn**	54.938	**83.884**	0.023	0.000174	*1.6*	3.11E+00	*1.6*	24.2	
25	**Mn**	54.938	**1810.72**	0.04	6.53E-05	*1.0*	3.63E+00	*2.7*	17.8	9280
25	**Mn**	54.938	**7243.518**	0.092	2.02E-05	*1.4*	1.36E+00	*2.4*	10.6	
26	**Fe**	55.847	**352.332**	0.016	0.000126	*0.6*	2.73E-01	*1.2*	41.8	
26	**Fe**	55.847	**122.078**	0.022	0.000175	*1.8*	9.56E-02	*3.1*	14.7	
26	**Fe**	55.847	**691.914**	0.016	9.79E-05	*0.6*	1.37E-01	*1.3*	20.9	
26	**Fe**	55.847	**7631.051**	0.093	1.89E-05	*1.5*	6.53E-01	*1.9*	100.0	
26	**Fe**	55.847	**7645.485**	0.093	1.89E-05	*1.5*	5.49E-01	*2*	84.0	
26	**Fe**	55.847	**9297.903**	0.207	1.42E-05	*2.3*	7.47E-02	*3.3*	11.4	
27	**Co**	58.933	**229.811**	0.012	0.000148	*1.0*	7.18E+00	*1.2*	100.0	
27	**Co**	58.933	**277.199**	0.011	0.000138	*0.8*	6.77E+00	*1.2*	94.2	
27	**Co**	58.933	**555.941**	0.01	0.000106	*0.6*	5.76E+00	*1.1*	80.3	
27	**Co**	58.933	**447.717**	0.011	0.000115	*0.6*	3.41E+00	*1.1*	47.6	
27	**Co**	58.933	**7491.29**	0.121	1.94E-05	*1.5*	1.16E+00	*2.5*	16.1	
28	**Ni**	58.69	**464.972**	0.018	0.000113	*0.6*	8.43E-01	*1.2*	56.6	
28	**Ni**	58.69	**8998.31**	0.093	1.5E-05	*2.1*	1.49E+00	*1.9*	100.0	
28	**Ni**	58.69	**8533.453**	0.083	1.62E-05	*1.8*	7.21E-01	*1.9*	48.4	
28	**Ni**	58.69	**6837.437**	0.064	2.16E-05	*1.4*	4.58E-01	*1.7*	30.8	
28	**Ni**	58.69	**7819.547**	0.075	1.84E-05	*1.5*	3.37E-01	*1.9*	22.7	
29	**Cu**	63.546	**277.993**	0.025	0.000138	*0.8*	8.93E-01	*1.3*	100.0	
29	**Cu**	63.546	**159.018**	0.026	0.000167	*1.5*	6.49E-01	*1.2*	72.7	
29	**Cu**	63.546	**185.658**	0.026	0.00016	*1.3*	2.44E-01	*1.3*	27.3	
29	**Cu**	63.546	**202.689**	0.026	0.000155	*1.2*	1.94E-01	*1.3*	21.7	
29	**Cu**	63.546	**343.651**	0.025	0.000127	*0.6*	2.15E-01	*1.5*	24.1	
29	**Cu**	63.546	**7915**	0.088	1.81E-05	*1.5*	8.69E-01	*1.9*	97.3	
30	**Zn**	65.39	**115.256**	0.023	0.000176	*1.8*	1.67E-01	*1.6*	47.0	
30	**Zn**	65.39	**1077.336**	0.017	8.35E-05	*0.4*	3.56E-01	*1.4*	100.0	
30	**Zn**	65.39	**7863.545**	0.107	1.82E-05	*1.5*	1.41E-01	*3.5*	39.7	

References

Zs. Révay, T. Belgya: *Principles of PGAA method,* in: Handbook of Prompt Gamma Activation Analysis with Neutron Beams, (G.L. Molnár ed.), Kluwer Academic Publishers, Dordrecht/Boston/New York, 2004, pp.1–30.

Zs. Révay, P. Kudejova, K. Kleszcz, S. Söllradl, Ch. Genreith, *In-beam Activation Analysis Facility at MLZ, Garching,* Nucl. Instrum. Meth. A799 (2015) 114-123

Zs. Révay: Determining Elemental Composition Using Prompt Gamma Activation Analysis, Anal. Chem. 81 (2009) 6851-6859, DOI:10.1021/ac9011705

Zs Révay, R.B. Firestone, T. Belgya, G.L. Molnár: *Prompt Gamma-ray Spectrum Catalog,* in: Handbook of Prompt Gamma Activation Analysis with Neutron Beams, (G.L. Molnár ed.) , Kluwer Academic Publishers, Dordrecht/Boston/New York, 2004, pp.173–364.

Contact

PGAA

Phone: 089/289-14906

Web: https://mlz-garching.de/en/elementanalyse

Zsolt Révay

Forschungsneutronenquelle Heinz Maier-Leibnitz (FRM II)
Technische Universität München
Lichtenbergstr. 1
D-85748 Garching, Germany

Phone: 089/289-12694

e-Mail: zsolt.revay@frm2.tum.de

Band / Volume 260
Crystal and Magnetic Structure of CrAs under Extreme Conditions
A. Eich (2022), viii, 235 pp
ISBN: 978-3-95806-655-7

Band / Volume 261
Applications of transcription factor-based biosensors for strain development and evolutionary engineering
R. G. Stella (2022), x, 128 pp
ISBN: 978-3-95806-657-1

Band / Volume 262
Strömungsmechanische Simulation und experimentelle Validierung des kryogenen Wasserstoff-Moderators für die Europäische Spallationsneutronenquelle ESS
Y. Beßler (2022), XXIV, 154, xxxiii pp
ISBN: 978-3-95806-660-1

Band / Volume 263
9th Georgian-German School and Workshop in Basic Science September 12 – 16, 2022 | Kutaisi, Tbilisi | Georgia
A. Kacharava, E. Portius, N. J. Shah, H. Ströher (2022)
ISBN: 978-3-95806-664-9

Band / Volume 264
Self-assembly of Au-Fe_3O_4 dumbbell nanoparticles
N. Nandakumaran (2022), xiv, 234 pp
ISBN: 978-3-95806-666-3

Band / Volume 265
Time-resolved and three-dimensional characterisation of magnetic states in nanoscale materials in the transmission electron microscope
T. Weßels (2023), xx, 211 pp
ISBN: 978-3-95806-685-4

Band / Volume 266
Dissecting iron and heme regulatory networks and adaptation to heme stress in *Corynebacterium glutamicum*
A. Krüger (2023), IV, 274 pp
ISBN: 978-3-95806-686-1

Band / Volume 267
Morphological and functional characterization of layer 5 neurons in rat medial prefrontal cortex, their synaptic microcircuitry and serotonin modulation
R. Rama (2023), 116 pp
ISBN: 978-3-95806-688-5

Band / Volume 268
Magnetic and transport studies of the parent and Fe doped Hexagonal-Mn_3Ge Weyl semimetal
V. Rai (2023), xviii, 156 pp
ISBN: 978-3-95806-695-3

Band / Volume 269
The complex inositol metabolism of *Corynebacterium glutamicum* and its application for the production of rare inositols
P. Ramp (2023), VI, 161 pp
ISBN: 978-3-95806-699-1

Band / Volume 270
Spin- and orbital-dependent band structure of unconventional topological semimetals
K. Hagiwara (2023), v, 115 pp
ISBN: 978-3-95806-701-1

Band / Volume 271
Neutron scattering
Experimental Manuals of the JCNS Laboratory Course held at Forschungszentrum Jülich and at the Heinz-Maier-Leibnitz Zentrum Garching edited by T. Brückel, S. Förster, K. Friese, M. Kruteva**,** M. Zobel, and R. Zorn (2023), ca. 150 pp
ISBN: 978-3-95806-705-9

Schlüsseltechnologien / Key Technologies
Band / Volume 271
ISBN 978-3-95806-705-9

Mitglied der Helmholtz-Gemeinschaft